EPSRC
Engineering and Physical Sciences Research Council

Exova

UNIVERSITY OF BIRMINGHAM

SULPHIDE STRESS CRACKING TEST DEVELOPMENT FOR A WELDABLE 13%CR SUPERMARTENSITIC STAINLESS STEEL IN SIMULATED SEABED ENVIRONMENTS

by

MATTHEW WALTERS

A thesis submitted to the University of Birmingham for the degree of ENGINEERING DOCTORATE

School of Metallurgy and Materials
University of Birmingham
June 2014

ABSTRACT

Weldable 13%Cr supermartensitic stainless steels are commonly used for subsea pipelines in the oil and gas industry. Although classified as corrosion resistant alloys, these steels can be susceptible to Sulphide Stress Cracking (SSC) when exposed to wet environments containing chlorides, carbon dioxide and low levels of hydrogen sulphide. Standard guidelines stipulate that laboratory SSC tests are performed at 24 °C and at the maximum design temperature, however some studies suggest that the risk of SSC could be greater at temperatures below 24 °C. Seabed temperatures can be as low as 5 °C, so in-service cracking could occur following shut-down conditions even if the material has been qualified at 24 °C.

Four-point bend SSC tests performed at 5 °C and 24 °C in simulated seabed environments showed the material was more susceptible to SSC at 5 °C, but only when the as-received pipe surface was compromised. A supporting stress and strain investigation highlighted strain concentrations on the test surface which were coincident with the location of cracking observed in the SSC tests. Finite element simulations were used to demonstrate that tensile stress-strain data should be used over flexural bend data to load four-point bend specimens to the desired loading strain.

DEDICATION

This work is dedicated to the memory of my father, Anthony Walters

ACKNOWLEDGEMENTS

I would like to thank the EPSRC, the University of Birmingham and Exova (UK) Ltd for supporting and funding this EngD project. I also thank Nippon Steel & Sumitomo Metal Corporation for providing the test material used in this work and NACE Great Britain for travel assistance to the NACE 2013 Corrosion conference in Orlando, Florida.

I thank the Department of Metallurgy & Materials at the University of Birmingham and Exova Corrosion Centre for the provision of laboratory facilities. I am also very grateful to my academic supervisor Dr. Brian Connolly and my industrial supervisor Dr. Chris Fowler for their help and guidance during the course of this project.

I wish to thank the following people for their support over the last four years: Phil Dent, Dr. Kokloong Lee and Dr. Abhay Nadkarni from Exova, Dr. Chris Cooper, Dave Price, Jeff Sutton, Pr. Hanshan Dong and Dr. Xiaoying Li from the University of Birmingham, Dr. Masakatsu Ueda, Dr. Hisashi Amaya and Dr. Tomohiko Omura from Nippon Steel & Sumitomo Metal Corporation, Dr. Alan Turnbull from NPL, Dr. Richard John Greene from Strain Solutions Ltd and Dr. Anas Yaghi from the Manufacturing Technology Centre.

Finally, I would like to thank my wife Faye for your love, support and patience. I could not have done this without you.

CONTENTS

LIST OF FIGURES

LIST OF TABLES

LIST OF ABBREVIATIONS

AR	As-Received SSC test specimen (retains inner bore of pipe)
AYS	Actual Yield Strength
BCC	Body-Centred Cubic
BCT	Body-Centred Tetragonal
CCD	Charge-Coupled Device
CRA	Corrosion Resistant Alloy
CW	Condensed Water
DBTT	Ductile to Brittle Transition Temperature
DCB	Double-Cantilever Beam
DIC	Digital Image Correlation
DPI	Dye Penetrant Inspection
EDX	Energy Dispersive X-ray analysis
EFC	European Federation of Corrosion
FCC	Face-Centred Cubic
FEA	Finite Element Analysis
FEM	Finite Element Modelling
FM	Fully Machined SSC test specimen (surfaces ground to 600 grit)
HAZ	Heat-Affected Zone
HE	Hydrogen Embrittlement
HIC	Hydrogen Induced Cracking
IGSCC	Intergranular Stress Corrosion Cracking
ILS	Invariant-Line Strain
IPS	Invariant-Plane Strain
OCTG	Oil Country Tubular Goods
OES	Optical Emission Spectroscopy
OTI	Offshore Technology Information (HSE Publication)
PEEK	Polyetheretherketone
PID	Proportional-Integral-Derivative (control system)
PTFE	Polytetrafluoroethylene
PW	Produced Water
PWHT	Post-Weld Heat-Treatment
SEM	Scanning Electron Microscope
SCC	Stress Corrosion Cracking
SMYS	Specified Minimum Yield Strength
SOHIC	Stress Oriented Hydrogen Induced Cracking
SSC	Sulphide Stress Cracking
SSRT	Slow Strain Rate Test
UNS	Unified Numbering System
XRD	X-Ray Diffraction

CHAPTER 1: INTRODUCTION

1.1 Background

Weldable 13%Cr supermartensitic stainless steels are corrosion resistant alloys (CRAs) commonly used for welded pipelines in the oil and gas industry as an alternative to inhibited carbon steel or lined pipe. These pipelines are commonly used for transporting sweet (carbon-dioxide containing) and mildly-sour (carbon dioxide with low levels of hydrogen sulphide) production fluids from the wellhead to the platform. Figure 1.1 shows a diagram of the Woodside Echo Yodel field; a sweet-gas field located at a depth of 130 m on the North West Shelf of Western Australia. This field uses 12" diameter CRA pipeline for transporting raw gas over a distance of 23 km from fixed subsea wellheads to the Goodwyn A platform [1].

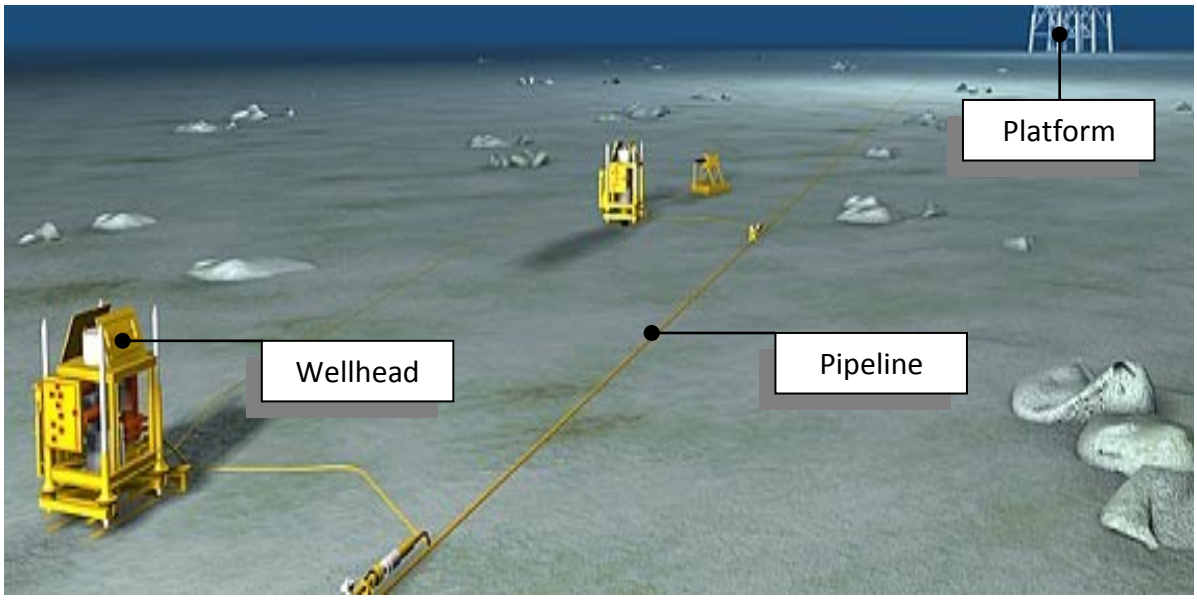

Figure 1.1 The Woodside Echo Yodel gas field located on the North-West Shelf of Australia uses corrosion resistant alloy subsea pipelines to transport raw gas from the wellheads to oil platform [1]

The oil or gas reservoir is connected to the wellhead via high strength down-hole tubular pipes. In operating conditions the internal pipe temperature can be as high as 130 °C, but during shut-down conditions the pipe will be at the same temperature as the seabed. Seabed temperatures generally decrease with increasing depth, and pressure increases by one atmosphere (approximately 100 kPa) for every 10 metre increase in water depth [2]. Temperature variation depends on latitude and region. Above about 500 m in mid-latitude, temperature varies seasonally but with diminishing amplitude with increasing depth (Figure 1.2). At depths below about 800 metres temperature is remarkably constant and reaches about 2 °C at the deep-sea floor (at a depth of approximately 5 km) [2].

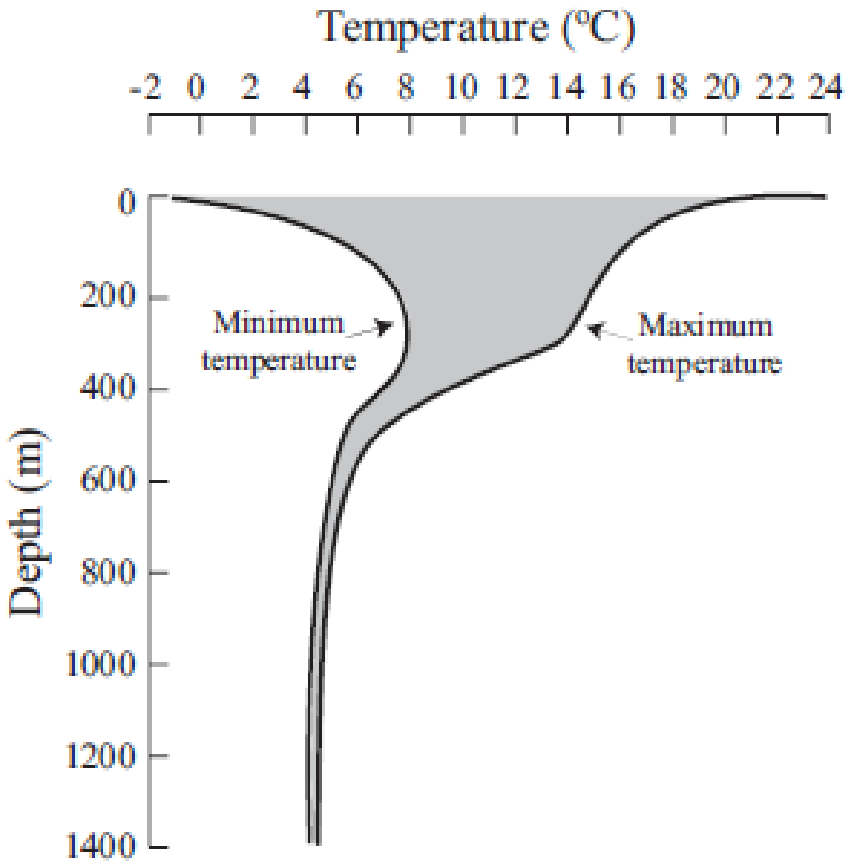

Figure 1.2 Annual temperature variations in the Western North Atlantic illustrating the diminishing amplitude of seasonal variation with depth [2]

1.2 Industrial Problem

In 2005 Exova Corrosion Centre conducted an investigation to determine the Sulphide Stress Cracking (SSC) resistance of a weldable 13%Cr supermartensitic stainless steel pipeline material for sour-service application at 7 °C, 24 °C and 115 °C. The tests were performed on root-intact welded specimens using the four-point bend loading method and the results indicated that SSC was more severe at 7 °C when compared to 24 °C and 115 °C [3]. Most sour-service qualification programmes are performed in accordance with NACE MR0175/ISO15156 [4] which stipulates that CRAs are only tested at room temperature and the maximum service operating temperature, with no provision for SSC testing at temperatures below room temperature. Since subsea pipelines are exposed to the seabed temperature during shut-down conditions, it is possible that a 13%Cr subsea pipeline could be qualified based on room temperature SSC tests but fail in service when exposed to low temperature conditions.

1.3 Project Objectives

Nippon Steel & Sumitomo Metal Corporation commissioned Exova Corrosion Centre and the University of Birmingham to investigate the low temperature SSC resistance of a commercially available weldable 13%Cr supermartensitic stainless steel pipeline material through this EngD research project. The primary aim was to determine the risk of SSC at seabed temperatures (5 °C) compared to standard room temperature tests (24 °C), using simulated Produced Water and Condensed Water test environments at two partial pressures of H_2S. The secondary aim was to evaluate the suitability of the standard four-point bend

loading method by a stress and strain investigation using strain gauge measurements, finite element analysis and full-field digital image correlation.

SSC, like most environmentally assisted degradation phenomena, is a combinatorial function of many variables such as pH, chloride concentration, H_2S partial pressure, dissolved oxygen and temperature. Consequently, controlling these variables is critical to achieving accurate and reliable test results in the laboratory. Therefore, a major part of this EngD project involved developing the existing SSC test method to improve control of the test variables. This development provided Exova Corrosion Centre with a state-of-the art SSC test rig which has since been used on several commercial projects that require the qualification of CRAs for sour-service application. In addition, a new flexural bend test rig was developed and used to investigate the load and strain response of weldable 13%Cr supermartensitic stainless steel test specimens loaded in four-point bending at 24 °C and 130 °C. This development was driven by a commercial project requiring flexural bend tests to be performed at 196 °C with stable temperature control.

At the time of writing, there was no standard test procedure for using the four-point bend method as a means to evaluate SSC and SCC resistance of materials. However, NACE international – The Corrosion Society, set up Task Group TG494 to develop a standard four-point bend method for use with carbon steels, low alloy steels and CRAs. The work presented in the second half of this thesis aims to contribute to this process.

CHAPTER 2: LITERATURE REVIEW

2.1 Sour Service Corrosion

In petroleum production and drilling, the primary agents that cause corrosion are oxygen (O_2), carbon dioxide (CO_2), hydrogen sulphide (H_2S) and chlorides (Cl^-) [5]. Oil and gas fields that contain CO_2 are referred to as *sweet* while those that also contain H_2S are referred to as *sour*. Both CO_2 and H_2S are classified as acid gasses that when dissolved in water, increases the corrosion rate of steels.

CO_2 is present in crude oil reservoirs and natural gas wells and forms carbonic acid (H_2CO_3) when dissolved in water. Corrosion in CO_2-containing environments leads to the formation of iron carbonate ($FeCO_3$) which is insoluble in water. If corrosion is uniform and the scale covers the entire surface of the steel, then iron carbonate provides a protective barrier against further corrosion. During secondary recovery operations, sweet reservoirs are flooded with seawater to maintain reservoir pressure and production rate. The mixture of seawater and reservoir water (formation water) provides the right conditions for sulphate-reducing bacteria growth. These bacteria reduce the oxygen content of sulphates (SO_4^{2-}) found in seawater to produce H_2S, hence this process is called *reservoir souring*.

H_2S is a highly toxic, colourless gas that promotes embrittlement through the absorption of atomic hydrogen. Atomic hydrogen can be generated from a number of sources such as general and localised corrosion reactions, cathodic protection and welding

processes. When hydrogen absorbs into steel it causes premature failure by environmentally-assisted cracking mechanisms such as Hydrogen Induced Cracking (HIC), Stress Oriented Hydrogen Induced Cracking (SOHIC) and SSC. In addition to reservoir souring, H_2S can be found naturally in oil, gas, formation waters or any area where there is decaying matter and stagnant water. Oil and gas exploration is accessing new and deeper reserves to meet an ever increasing world demand for energy and the number of sour-service oil and gas fields encountered is also increasing: nearly 40% of the world's gas reserves contain levels of CO_2 and H_2S that pose obstacles to their development [6]. These sour gas fields are found throughout the world in Europe, Africa, North and South America, the Far East, Middle East and Central Asia. Qualification of materials for fit-for-purpose use in sour service environments is done by simulating two commonly encountered service environments:

1) Produced Water simulates formation water or injected seawater extracted from oil wells. Produced waters are rich in chlorides and are naturally buffered with sodium bicarbonate ($NaHCO_3$). EFC17 [7] defines standard Produced Water for laboratory testing that consists of 100,000 mg/L of chloride ions (165 g/L NaCl) at pH 4.5.

2) Condensed Water simulates water condensation on the inner surface of gas pipelines as pressure and temperature decreases. In contrast to the Produced Water environment, Condensed Water is typically low in chlorides and buffering ions but is also more acidic. EFC17 [7] defines standard Condensed Water as 1000 mg/L of chloride ions (1.65 g/L NaCl) and pH 3.5 with no bicarbonate. The problem with simulating this environment is that buffers are required to achieve a stable pH when testing. NACE MR0175/ISO 15156 [4]

recommends that artificial acetate buffers are used but these are not found in real service conditions. There is also disagreement on how these buffers influence the SSC resistance of 13%Cr stainless steels which is addressed in Section 2.2.6.5.

2.1.1 Generalised Corrosion Processes

Corrosion is an electrochemical process that requires two reactions to occur in order to maintain charge balance. These are anodic oxidation (metal dissolution) and cathodic reduction. Taking corrosion of iron as an example, positively charged metal ions (cations) are released into solution at the *anode*, leaving behind two liberated electrons in the metal [8]:

$$Fe \rightarrow Fe^{2+} + 2e^{-} \quad (2.1)$$

This reaction results in a separation of electrical charge at the metal-solution interface: cations form a positively charged layer on the solution side and electrons form a negatively charged layer in the metal. If undisturbed this electrical double layer opposes further dissolution because the positively charged Fe^{2+} ions are retained by the negative charge in the metal and repelled by the positive layer of cations in solution [9]. In practice, electrons produced at the anode are consumed at the *cathode* and this disrupts the balance of the electrical double layer. In acidic solutions, the two main cathodic reactions are reduction of hydrogen (2.2) and reduction of oxygen (2.3) [8]:

$$2H^{+} + 2e^{-} \rightarrow H_2 \quad (2.2)$$

$$O_2 + 4H^{+} + 4e^{-} \rightarrow 2H_2O \quad (2.3)$$

Hydrogen ions and dissolved oxygen fuels the cathodic reaction which in turn fuels the anodic reaction. Therefore, the presence of oxygen in an acidic solution will increase the

likelihood of corrosion in steels. Since dissolved H_2S is a source of hydrogen ions, this also increases corrosion rates in steels. In sour environments, H_2S and HS^- ions dissociate to form H^+ ions [10]:

$$H_2S \rightarrow H^+ + HS^- \quad (2.4)$$

$$HS^- \rightarrow H^+ + S^{2-} \quad (2.5)$$

The net corrosion reaction of steel in sour service involves the production of iron sulphide and atomic hydrogen:

$$Fe + H_2S \rightarrow FeS + 2H^o \quad (2.6)$$

As with Iron carbonate in CO_2 corrosion, iron sulphide is insoluble in water and forms a protective barrier against further corrosion. Unless there is total coverage on the steel surface, localised corrosion can occur in unprotected areas. Iron sulphide can also form as FeS_2, Fe_7S_8 or Fe_9S_8 depending on factors such as pH and H_2S partial pressure [10].

2.1.2 Localised Corrosion Processes

Pitting is one of the most frequently encountered forms of localised corrosion in oil and gas production and is particularly dangerous as it can often go undetected until failure occurs. Pitting is localised anodic dissolution of steel which is accelerated by low pH and high chloride environments. Stainless steels are susceptible to pitting when there is a break or flaw in the protective passive layer. This can be caused by mechanical damage or where there is an irregular surface feature such as an inclusion, which in some cases would develop its own non-protective oxide layer locally. When a pit forms, the base of the pit is quickly

depleted of oxygen and becomes anodic relative to the cathodic external surface of the steel. At the anode, hydrolysis of metal cations generates hydrogen ions [8]:

$$Fe^{2+} + H_2O \rightarrow FeOH^{+} + H^{+} \quad (2.7)$$

The production of these hydrogen ions causes the pH at the base of the pit to fall and negatively charged chloride ions (Cl^-) migrate to the pit for charge balance (Figure 2.1). The result is a highly corrosive acidified metal-chloride solution that prevents the passive layer reforming and promotes further dissolution and pit growth [8].

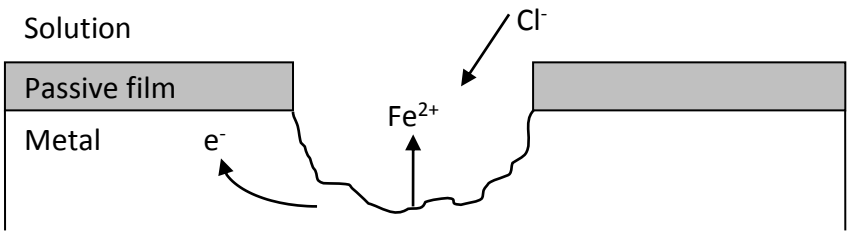

Figure 2.1 Schematic of pitting corrosion adapted from [8]: metal ions are released into solution and chloride ions are drawn in to the pit for charge balance

In combination with the aggressive local solution chemistry, the irregular shape of a corrosion pit can provide regions of high stress concentration from which cracking can initiate (Figure 2.2). Even though the pit base may have the most aggressive local solution chemistry, Horner *et al*. [11] showed that that pit-to-crack transitions can develop predominantly at the pit wall close to the pit mouth due to localised plastic strain in this region[1]. Once the cracks nucleate on the pit walls, the cracks grow around the pit at a rate faster than the rate of pit growth, to coalesce and form a complete through-crack.

[1] This work used 3D X-ray microtomography and finite element analysis to observe pit-to-crack transition and subsequent crack evolution in a 3 NiCrMoV steam turbine disc steel.

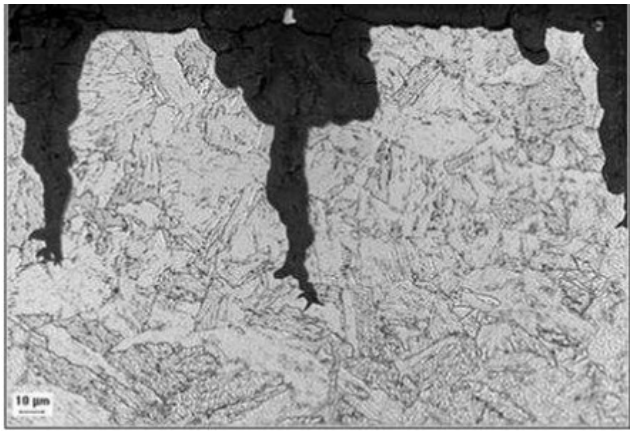

Figure 2.2 Pitting and SSC in a supermartensitic stainless steel. 110 ksi (758 MPa), 13-5-2 grade tested at 200°C in a pH 4, 25 bar CO_2, 100000 mg/l Cl environment [12].

Polarisation curves are used to characterise the electrochemical nature of pitting corrosion by applying a potential sweep in an electrolyte and measuring the resultant current. A typical polarisation curve for a stainless steel is shown in Figure 2.3 [8]

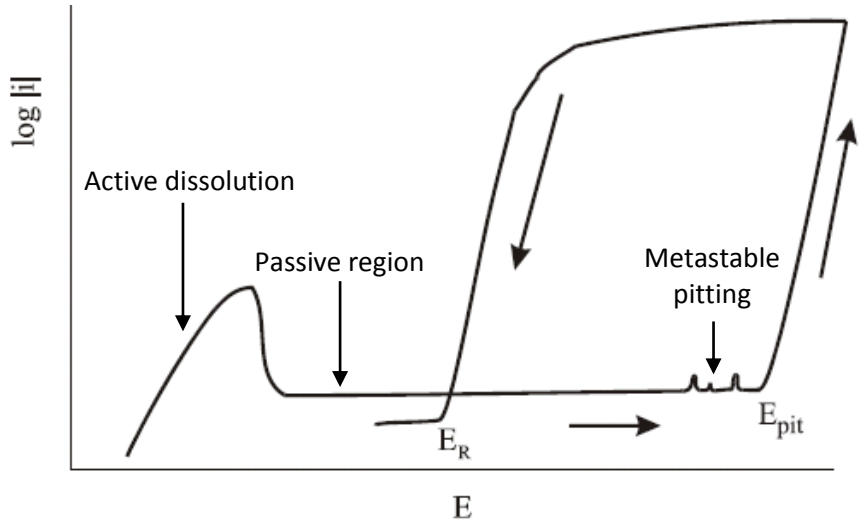

Figure 2.3 Typical polarisation curve showing transition from active dissolution to passive behaviour and pit growth at the pitting potential (E_{pit}) as potential is increased. On the reverse sweep, pits remain stable until the repassivation potential (E_R) is reached when the pit dies [8]

At low potentials there is active dissolution. As potential increases, the metal passivates and current flow from the surface is very low. Increasing the potential further results in metastable pit growth and can be seen on the polarisation curve as small peaks of current flow (metastable pitting refers to the initiation of small pits that die when the

passive film repassivates and cations diffuse away from the pit). The pitting potential (E_{pit}) is a measure of a material's resistance to pitting corrosion: the higher the pitting potential the more resistant the material is to localised corrosion attack. When the pitting potential is exceeded, there is local film breakdown and an increase in current density that signifies pit growth. When the potential is reversed, the pits remain stable and the current density remains high. The point on the reverse sweep where pits die is termed the repassivation potential (E_R).

Increasing the chromium content of stainless steel provides greater passivity and also raises the pitting potential [13]. It should be noted that in a fully passive state, CRAs are most susceptible to pitting corrosion at elevated temperatures since increasing temperature accelerates chemical reactions, the transport of species involved in the corrosion reactions, and electrochemical reactions at the metal surface. In H_2S-containing environments, where chlorides directly break down the passive film, adsorbed sulphur species act to retard passive film growth and enhance dissolution. This results in the stabilisation of pits that would otherwise be metastable in environments without H_2S. Consequently, pitting corrosion will occur at lower potentials in environments containing H_2S [14].

2.1.3 Hydrogen Charging Mechanisms

Hydrogen is formed on metals as a result of impressed current cathodic protection or corrosive cathodic reduction of aqueous protons [15]. Atomic hydrogen liberated at the cathode can either combine to form molecular hydrogen or absorb into the metal substrate where it diffuses to regions of high stress concentration such as grain boundaries, inclusions

or dislocations which can also act as hydrogen trapping sites [10, 16, 17]. Hydrogen charging is promoted by the presence of H_2S and can lead to environmentally-assisted cracking mechanisms such as SSC, HIC and SOHIC [10]. The influence of H_2S on hydrogen uptake in steels can be described by three popular theories:

1. Classical Theory

The classical theory states that hydrogen ions in solution combine with electrons released during anodic reactions to form adsorbed hydrogen on the surface of the metal. In environments free of H_2S, atomic hydrogen predominantly combines to form molecular hydrogen which harmlessly bubbles away [10,15,18]:

$$H^+_{sol} + e^- \rightarrow H_{ads} \quad (2.8)$$

$$H_{ads} + H_{ads} \rightarrow H_2 \quad (2.9)$$

This theory states that H_2S 'poisons' the hydrogen degassing reaction (2.9) so adsorbed atomic hydrogen (H_{ads}) absorbs directly into solid solution in the metal (H_{abs}) [10,19,20,29]:

$$H_{ads} \rightarrow H_{abs} \quad (2.10)$$

2. Direct Proton Transfer

A second theory, proposed by Crolet & Bonis [21] suggests that charging is by direct transfer of hydrogen ions (H^+) from the electrolyte into the metal. Even though this theory agrees with the classical idea that adsorbed hydrogen atoms recombine to form hydrogen gas (equations 2.8 & 2.9), it states that the same reaction is not inhibited by H_2S and there is no 'poisoning' effect. Instead, charging and degassing coexist and sulphides adsorb on the surface to directly promote proton transfer into the metal.

$$H^+_{sol} + HS^-_{ads} \rightarrow H_2S_{ads}$$
$$H_2S_{ads} \rightarrow HS^-_{ads} + H^+_{abs} \quad (2.11)$$

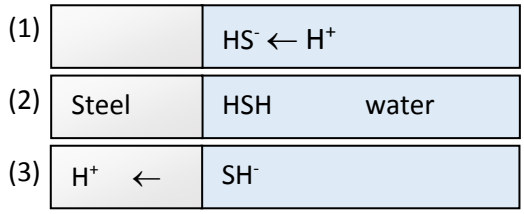

Figure 2.4 Illustration of direct proton transfer [21]. Adsorbed HS^- acts as a catalyst for direct proton transfer rather than a 'poison' to molecular hydrogen recombination. Charging and degassing coexist

3. Hydrogen Promotion through a Transition State Complex

In a third alternative theory, Dean [15] suggests that H_2S adsorbs on the steel surface and catalytically promotes hydrogen entry through a transition state complex $[HSH]_{ads}$:

$$H^+_{ads} + SH_{ads} \rightarrow [HSH]_{ads}$$
$$[HSH]_{ads} \rightarrow HS_{ads} + H_{abs} \quad (2.12)$$

This process is shown schematically in Figure 2.5. Sulphur acts as a gateway for atomic hydrogen to enter the steel. Hydrogen entering the steel is originally attached to the promoter hydride (SH_{ads}), not to the surface of the steel. When the hydrogen atom enters the steel, it is replaced by another hydrogen atom that is adsorbed on the steel surface.

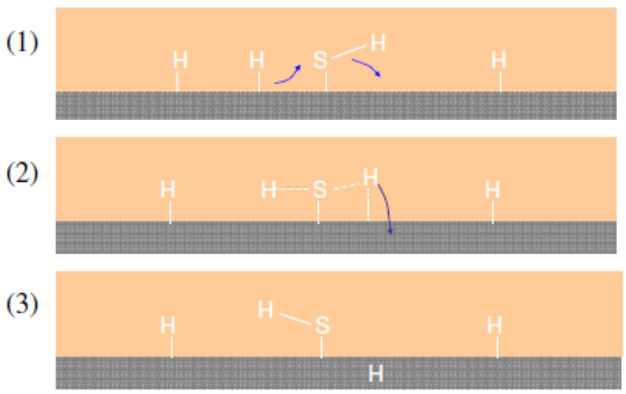

Figure 2.5 The promoter mechanism on steel [15]. Atomic hydrogen attached to the promoter hydride (SH_{ads}) adsorbed on the surface of the steel in (2) enters the metal in (3).

2.1.4 Sulphide Stress Cracking

Sulphide Stress Cracking has been a recognised failure mechanism in oilfield environments since 1952. It can occur in steels subjected to a tensile stress (residual or applied) when exposed to wet H_2S containing environments. SSC is a form of hydrogen embrittlement which means hydrogen absorption reduces the ductility of steel. Once in solid solution, atomic hydrogen will readily diffuse to sites of high internal stress such as grain boundaries, inclusions and regions of triaxial stress at notches [10]. SSC occurs when a critical concentration of atomic hydrogen diffuses into the metal and a threshold stress is exceeded [18], which can be well below the yield strength of the material [22].

SSC initiates at the surface of the metal then propagates in a direction perpendicular to the tensile stress. SSC is commonly reported to be intergranular in nature and this could be linked to the propensity for hydrogen to diffuse to grain boundaries resulting in local embrittlement at these sites. Furthermore, grain boundaries may also promote the formation of carbides and result in the depletion of elements beneficial to corrosion resistance, leading to localised dissolution and further embrittlement at the grain boundaries. SSC resistance can be improved by grain size refinement, homogeneous grain structure and reduced segregation of impurity elements along grain boundaries [23].

The SSC resistance of carbon steels, stainless steels and nickel based alloys is directly related to strength or hardness level [18] where SSC is more likely as strength increases. Maximising SSC resistance in high strength steels for oilfield casing and tubing applications is achieved by quenching and tempering processes [10]. Quenching (rapid cooling) transforms

austenite to fresh martensite which is responsible for the very high strength levels in these steels. Fresh martensite is very brittle which makes the material more susceptible to SSC but this brittleness can be removed at the expense of some hardness when the steel is tempered.

If only a fraction of the austenite transforms to martensite during the quench, then the microstructure will contain retained austenite. This can be problematic for SSC resistance since austenite can be mechanically transformed to fresh brittle martensite by plastic strain [24]. Therefore steels which exhibit a high percentage of martensite transformation during quenching have maximum resistance to SSC following tempering.

Low-alloy and carbon steels are generally more susceptible to SSC as pH reduces and H_2S concentration increases [10]. This is due to the increased amount of hydrogen ions available in the aqueous media. For martensitic stainless steels, SSC is influenced by pH, chlorides and H_2S, with pH being the most limiting factor followed by chloride content [25]. Other parameters such as temperature, the presence of elemental sulphur and dissolved oxygen in the test solution have also been identified as influential on corrosion and SSC performance [7,26] but the interaction between the different parameters is not fully understood [26].

It is generally accepted that carbon steels are most susceptible to SSC at room temperature and less susceptible as temperature increases [10,18,22,27]. This is shown in Figure 2.6 and is due to the mobility of hydrogen in steel: room temperature is optimal for

hydrogen to effectively reach the crack site causing further embrittlement. At elevated temperatures hydrogen escapes the metal and at sub-ambient temperatures hydrogen mobility is reduced. At temperatures greater than 49 °C Stress Corrosion Cracking (SCC) becomes a concern, particularly in high chloride containing environments [18]. SCC is driven by anodic dissolution in contrast to the hydrogen embrittlement-driven SSC mechanism.

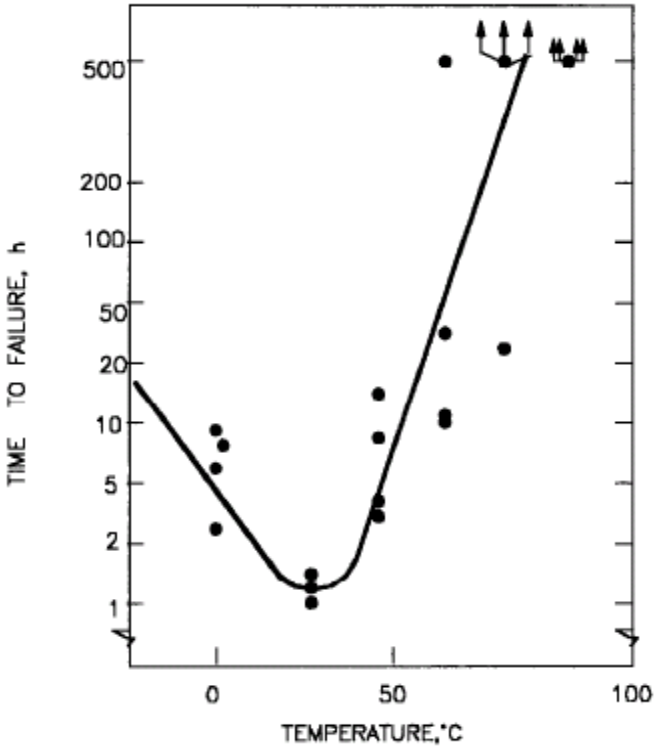

Figure 2.6 Influence of temperature on the SSC resistance of carbon steels. Carbon steels are most susceptible to SSC near room temperature [10]

For corrosion resistant alloys, the risk of SSC is generally greatest at temperatures higher than room temperature [28]. Although 13%Cr stainless steels are classified as corrosion resistant alloys, the risk of SSC has been reported to be greatest at room temperature like carbon steels [26,28]. In the case of 13%Cr stainless steels, SSC resistance is linked to passive film stability [26] since SSC is almost always preceded by some form of localised attack [29]. Active dissolution of the passive film is facilitated by high H_2S content,

low pH and high chloride levels. Dissolved oxygen in the water phase fuels the cathodic reaction and can lead to an increase in pitting corrosion, hence increasing the likelihood of SSC [30]. This will be exacerbated at low temperatures since oxygen solubility increases as water temperature decreases [31] (Oxygen dissolution is exothermic process, so cooling induces a shift in the equilibrium that favours dissolution).

2.1.5 Hydrogen Induced Cracking

HIC is generally observed in lower-strength carbon steels (<700 MPa yield strength) used in plate and pipe products in sour service [10]. Absorbed atomic hydrogen collects at microscopic imperfections[2] inside the steel and recombines to form hydrogen gas that becomes trapped within the metal. Pockets of hydrogen gas increase in pressure until a critical level is reached that initiates internal cracking. A highly strained region surrounds the cracks causing the cracks to link with other HIC sites on parallel planes in a stepwise formation through the thickness of the steel, reducing the load bearing cross-section of the component until failure occurs. On a larger scale, as more hydrogen enters the steel the internal pressure deforms the surrounding steel causing blisters at the surface.

Like SSC, HIC increases as pH decreases and H_2S levels increase. Unlike SSC, HIC does not require a tensile stress to initiate. HIC susceptibility increases with temperature up to about 50 °C then decreases as temperature exceeds 50 °C [10]. HIC susceptibility can be reduced by reducing the sulphur content of the steel as this reduces the number and size of

[2] Hydrogen gas is typically trapped at laminations (metal defects with separation aligned parallel to the worked surface) or elongated non-metallic inclusions such as MnS

MnS inclusions from which HIC can initiate. Elongated MnS inclusions generate high stresses which can promote crack initiation and propagation [5].

2.1.6 Stress-Oriented Hydrogen Induced Cracking

SOHIC is a form of hydrogen damage that can occur in low strength pipe and pressure vessel carbon steels operating in sour service environments. SOHIC can be thought of as a two stage mechanism starting with the formation of HIC and followed by SSC that links the HIC cracks in a through thickness direction (Figure 2.7). In SOHIC, shear stresses imposed by an externally applied (in-plane) stress oppose the stresses due to hydrogen pressure inside the HIC crack. This shifts the location of maximum shear stress in a way that inhibits the stepwise linking associated with HIC and favours a stacked array unique to SOHIC [32].

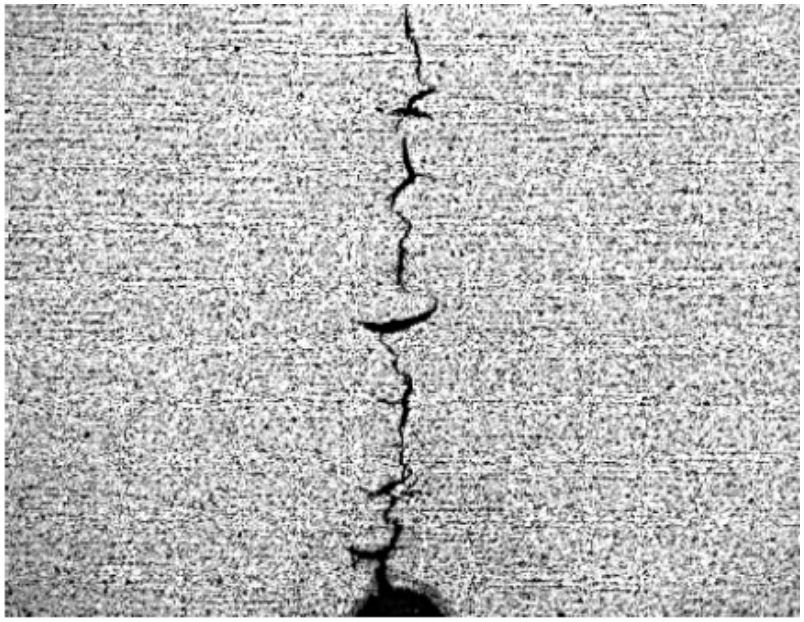

Figure 2.7 Example of SOHIC in 'HIC-resistant' A516-70 steel [33]. Short in-plane blister cracks generated ahead of a notch which link up in the through-thickness direction. The notch was produced by electro discharge machining (EDM)

2.2 13%Cr Stainless Steels for Oil & Gas Applications

Corrosion resistant alloys were developed to provide enhanced CO_2 corrosion resistance at elevated temperatures to exceed the capabilities of carbon steels used with inhibitors. Amongst the range of commercially available corrosion resistant alloys, the ferritic/austenitic duplex stainless steels offer the highest corrosion resistance in CO_2 and H_2S environments (Figure 2.8). However, these alloys are also the most expensive due to the high chromium and nickel content.

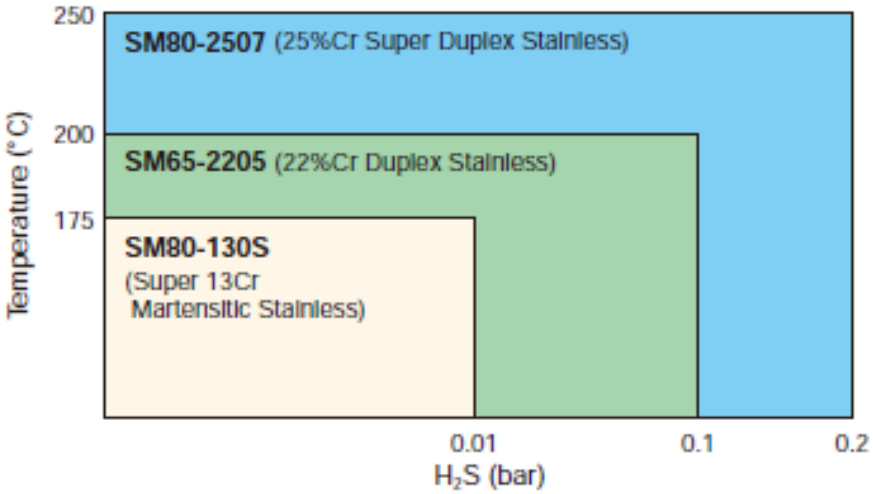

Figure 2.8 Operating limits of commercially available corrosion resistant alloys in H_2S containing environments [34]

The family of 13%Cr martensitic stainless steels provide a cost-effective alternative to 22%Cr duplex and 25%Cr super-duplex stainless steels and have been widely used where the corrosion resistance of these duplex grades is not required [23,28]. Conventional 13%Cr stainless steels have poor weldability so are not generally used for line pipe applications. To address this, the supermartensitic 13%Cr stainless steels were developed to provide improved corrosion resistance and weldability by virtue of their low carbon content [35].

13%Cr martensitic stainless steels have been used in the oil and gas industry for down-hole tubular products, or so called *Oil Country Tubular Goods* (OCTG) since the 1980s [5,36,37]. More recently, these steels were developed to provide improved resistance to general corrosion, pitting corrosion and SSC, as well as improved welding properties [23]. The newer 13%Cr steels have been inconsistently described as *modified*, *alloyed* and *supermartensitic* within the published literature depending upon the amount of carbon, nickel and molybdenum alloying additions. Terms such as *lean* (1.0-2.5%Ni, <1.0%Mo), *medium* (2.5-4.5%Ni, 1.0-2.0%Mo) and *fat* (4.5-6.5%Ni, >2.0%Mo) have also been used to distinguish the different grades [38] along with '*13-4-1*' (13%Cr, 4%Ni, 1%Mo) to categorise *medium* grades and '*13-5-2*' (13%Cr, 5%Ni, 2 %Mo) for *fat* grades [39].

Typical strength grades include 80 ksi (552 MPa), 95 ksi (655 MPa) and 110 ksi (758 MPa), depending on the applied heat treatment. Highly alloyed high-strength grades are desirable for down-hole tubular applications, particularly in deep sour-gas fields where both high strength and high corrosion resistance is required [40]. Line pipe applications require good weldability so the ultra-low carbon *weldable* supermartensitic stainless steels were developed. These steels are lower strength (80 ksi / 552 MPa) due to their low carbon content.

Table 2.1 specifies the chemical composition and environmental limits for some 13%Cr martensitic stainless steels along with their Unified (alloy) Numbering System (UNS) reference and are described in more detail in the following sections.

Table 2.1 Chemical compositions of standard martensitic stainless steels as listed in Table D6 of NACE MR0175/ISO 15156-3 [4]

UNS		C max. [a] w_C %	Cr max. [a] w_{Cr} %	Ni max. [a] w_{Ni} %	Mo max. [a] w_{Mo} %	Si max. [a] w_{Si} %	P max. [a] w_P %	S max. [a] w_S %	Mn max. [a] w_{Mn} %	N w_N %	Other max. [a] w %
S41000		0,15	11,5 to 13,5			1	0,04	0,03	1		
S41425		0,05	12 to 15	4 to 7	1,5 to 2	0,5	0,02	0,005	0,5 to 1,0	0,06 to 0,12	Cu 0,3
S41426		0,03	11,5 to 13,5	4,5 to 6,5	1,5 to 3	0,5	0,02	0,005	0,5		Ti 0,01 to 0,5; V 0,5
S41427		0,03	11,5 to 13,5	4,5 to 6,0	1,5 to 2,5	0,50	0,02	0,005	1,0		Ti 0,01; V 0,01 to 0,50
S42000		0,15 min[a]	12 to 14			1	0,04	0,03	1		
S42400		0,06	11,5 to 14	3,5 to 4,5	0,3 to 0,7	1	0,03	0,03	0,5 to 1		
S42500		0,08 to 0,2	14 to 16	1 to 2	0,3 to 0,7	1	0,02	0,01	1	0,2	
J91150		0,15	11,5 to 14	1	0,5	1,5	0,04	0,04	1		
J91151		0,15	11,5 to 14	1	0,15 to 1	1	0,04	0,04	1		
J91540		0,06	11,5 to 14	3,5 to 4,5	0,4 to 1	1	0,04	0,03	1		
		0,15 to 0,22	12 to14	0,5		1	0,02	0,01	0,25 to 1		Cu 0,25
K90941		0,15	8 to 10		0,9 to 1,1	0,5 to 1	0,03	0,03	0,3 to 0,6		
		0,15 to 0,22	12 to 14	0,5		1	0,02	0,01	0,25 to 1		Cu 0,25

[a] Min. indicates minimum mass fraction. Where a range is shown, it indicates min. to max. mass fractions.

NACE MR0175/ISO 15156 [4] specifies environmental limits of conventional (UNS S42000), modified (UNS S42400) and super (UNS S41425 and S41426) grades as 100 mbar H_2S at pH ≥3.5 for any combination of temperature and chloride concentration occurring in production environments. Maximum hardness levels are also outlined in this standard.

2.2.1 Conventional 13%Cr stainless Steels

In the early 1980s, the 'conventional' 13%Cr martensitic stainless steels were developed for OCTG with typical strength grades ranging from 80 - 95 ksi (552 – 655 MPa) [29]. These AISI 420 or UNS S42000 grades contain between 0.15-0.22% carbon and 11.5–14% chromium [39] and offer good CO_2 corrosion resistance up to 125 °C with limited SSC and SCC resistance in the presence of H_2S [38]. Conventional 13 %Cr stainless steels have been regarded as non-weldable for line pipe applications [23,41,42,43] because of the

relatively high carbon content for this type of steel.[3] The heat generated during welding will transform some parts of the martensitic microstructure to austenite, which then transforms to fresh martensite as the steel cools. Fresh martensite has low toughness and makes the material more susceptible to SSC. Toughness can be improved after welding through the application of post-weld heat treatment (PWHT), but in the case of conventional 13%Cr stainless steels, this can take several hours in order to achieve acceptable hardness and toughness in the heat-affected-zone (HAZ) [41]. PWHT allows some of the trapped carbon to diffuse out of the martensite, relieving strain in the crystal structure and promoting the formation of very small carbides. The resultant microstructure with improved toughness is called *tempered martensite* and this is described in more detail in Section 2.2.5.

2.2.2 Modified 13%Cr Stainless Steels

The terms 'modified' and 'super' have been used synonymously in the literature but modified tends to refer to lower alloyed grades such as '*13-4-1*' or UNS S42400 with 3.5-4.5% nickel and 0.3-0.7% molybdenum and as such provide higher resistance to local and general corrosion in CO_2 environments than conventional 13%Cr grades at elevated temperatures. SSC resistance typically decreases with increasing strength of martensitic stainless steels since toughness also decreases with increasing strength. One benefit of the modified 13%Cr stainless steel grades is that higher strengths can be achieved up to 95 ksi (655 MPa) that have the same SSC resistance as conventional lower strength grades rated at 80 ksi (552 MPa) [44].

[3] Typically low-carbon steels contain less than 0.25% C, medium-carbon steels contain 0.25-0.55% C and high-carbon steels contain 0.55-1.0% C.

2.2.3 Supermartensitic Stainless Steels

The 13%Cr 'supermartensitic' grades were developed in the 1990s as a cost effective alternative to the duplex and super-duplex stainless steels with higher nickel (4-7%) and molybdenum (1.5-3%) additions than the conventional grades [4]. Two examples are UNS S41425 and UNS S41426 although these steels are sometimes also referred to as 'modified' or '13-5-2' in the literature. The metallurgy of these steels is explained in later sections but essentially the low carbon and high nickel content improves toughness so higher strengths are achievable compared to conventional martensitic stainless steels [45,46]. In fact the main advantage of these steels is the ability to increase strength grades up to 110 ksi (758 MPa) while maintaining SSC resistance equivalent to conventional 80 ksi (552 MPa) grade stainless steels [39,47]. The high molybdenum content gives improved resistance to pitting corrosion compared to conventional grades, typically offering CO_2 corrosion resistance at temperatures up to 160 °C [48].

The 110 ksi (758 MPa) grade supermartensitic stainless steels are some of the most widely used corrosion resistant alloys in oil and gas projects [25] and are generally used for down-hole tubular applications. Since this exceeds the 105 ksi (723 MPa) limit given in NACE MR0175/ISO 15156 [4], these materials must be qualified for service on a fit-for-purpose basis.

2.2.4 Weldable 13%Cr Supermartensitic Stainless Steels

The chemistry of supermartensitic stainless steels was modified with an ultra-low carbon content <0.01% allowing them to be welded with limited use of PWHT [41]. The ultra-low carbon content improves SSC resistance because it lowers the maximum hardness in the HAZ following welding [49] and reduces precipitation of chromium and molybdenum based carbides during the tempering process, thereby improving CO_2 corrosion resistance. Weldable grades were developed with additions of 1.5%Ni for sweet CO_2 environments and with 5%Ni and 2%Mo for mildly sour environments [43]. Nickel is added to stabilise the austenite field when the content of carbon is reduced. Molybdenum improves SSC resistance, but as a ferrite stabiliser necessitates further additions of nickel to maintain the austenite field. Prior to the development of weldable 13%Cr supermartensitic stainless steels, conventional duplex (22%Cr) and super-duplex (25%Cr) stainless steels were generally used for flow line applications because of their good corrosion resistance in mildly sour environments and good weldability without the need for PWHT [23,42].

Weldable 13%Cr supermartensitic stainless steels are not currently included in NACE MR0175/ISO 15156 so are normally tested on a fit-for-purpose basis. These steels have been successfully tested for SSC resistance at 40 mbar H_2S environments up to 140 °C [26] but service related failures have been observed by IGSCC at the fusion line of welded pipelines. Such failures have been mitigated by the application of a short PWHT (typically 650 °C for 5 minutes) to temper any fresh martensite and de-sensitise any chromium carbides that may have formed during the welding process [36,50,51,52,53].

2.2.5 Metallurgy of 13%Cr Martensitic Stainless Steels

2.2.5.1 The Iron-Carbon Phase Diagram

The iron-carbon phase diagram in Figure 2.9 shows the temperature-composition map of austenite, ferrite and cementite in steel at equilibrium. Pure iron melts at 1540 °C and can readily accommodate dissolved carbon. Below 1540 °C, iron solidifies to a solid solution with the carbon atoms positioned in interstitial sites between iron atoms. At temperatures between 1540 °C and 1395 °C, iron exists as delta ferrite (δ-Fe) and has a body-centered cubic (BCC) crystal structure. Between 1395 °C and 912 °C iron exists as austenite (γ-Fe) with a face-centered cubic (FCC) crystal structure. Austenite has a much higher solubility for carbon than ferrite because the interstitial spacing is greater in the FFC structure compared to the BCC structure. Austenite transforms to BCC ferrite (α-Fe) at 912 °C or the A_3 temperature. The iron-carbon phase diagram shows that adding carbon to iron lowers the A_3 temperature until the *eutectoid* point is reached.[4]

At room temperature, the solubility of carbon in α-ferrite is very low, so carbon reacts with iron to form cementite (Fe_3C). At temperatures below the A_1 temperature (727 °C), austenite grains in low-carbon hypoeutectoid steels will transform to *pearlite*, a two phase region of alternating plates of ferrite and cementite. Pearlite may nucleate at a grain boundary and it is generally agreed that the rate of growth is governed by the diffusion of carbon atoms, hence the crystallographic change occurs as readily as the redistribution of carbon allows [54].

[4] The eutectoid point in the iron-carbon system has a composition of 0.77 %C at the A_1 temperature (727 °C) whereby austenite transforms directly into pearlite (ferrite + cementite)

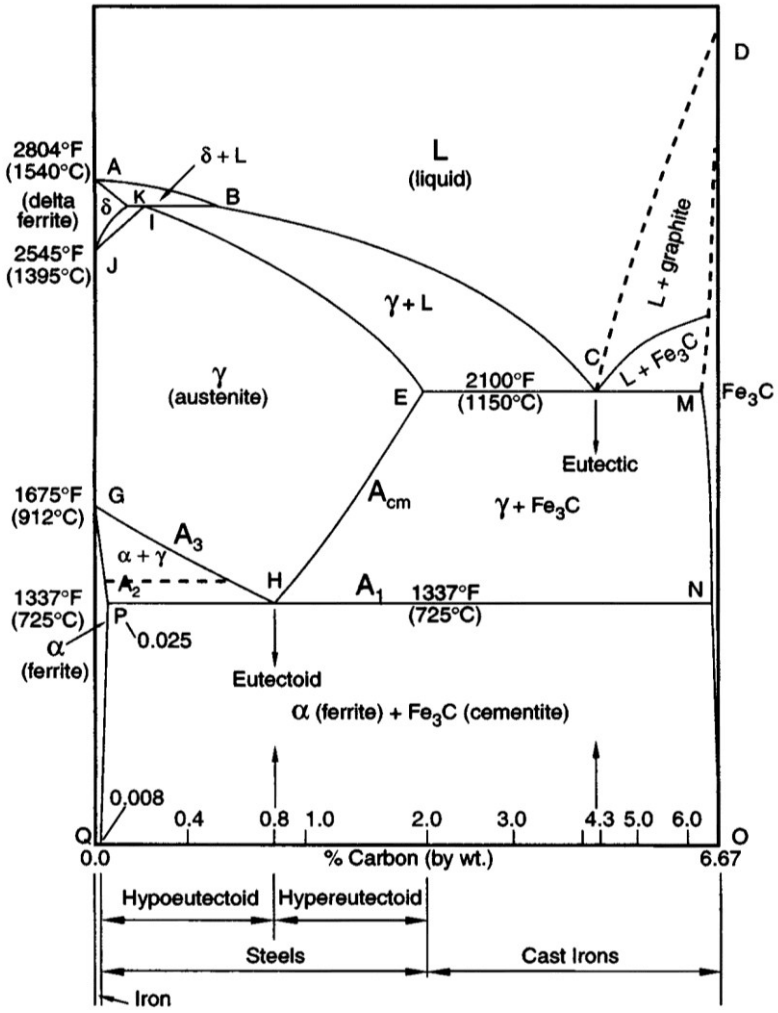

Figure 2.9 Iron-carbon equilibrium phase diagram [55]

2.2.5.2 Formation of Martensite

When steels are heated to the austenite (γ-Fe) field and then rapidly cooled (quenched) to room temperature, dissolved carbon atoms do not have time to diffuse out of the FCC austenite structure to form pearlite as shown on the iron-carbon phase diagram. Instead, a rapid transformation occurs at approximately the speed of sound [56] which traps carbon atoms in the BCC ferrite structure and produces a distorted body-centered tetragonal (BCT) crystal structure called *martensite.* The trapped carbon atoms and lattice distortion impede the motion of dislocations which makes martensite extremely hard, strong and brittle.

In contrast to the austenite to pearlite transformation, martensitic transformation does not involve diffusion, nucleation or growth, hence martensite forms without any chemical compositional change from the austenite phase [56,57,58]. The change in crystal structure from FCC austenite to BCT martensite is driven by homogeneous shearing of the parent phase and the amount of martensite formed depends *only* on temperature, not on the amount of time at a given temperature. For this reason, martensitic transformation is described as *athermal* [59]. Martensite starts to form at the M_s temperature and finishes at the M_f temperature. Both M_s and M_f strongly depend on carbon content (Figure 2.10) as well as other alloying elements in the metal. For richly alloyed supermartensitic stainless steels, M_s is approximately 200 °C [60]. Any austenite that remains untransformed at room temperature is called *retained austenite*.

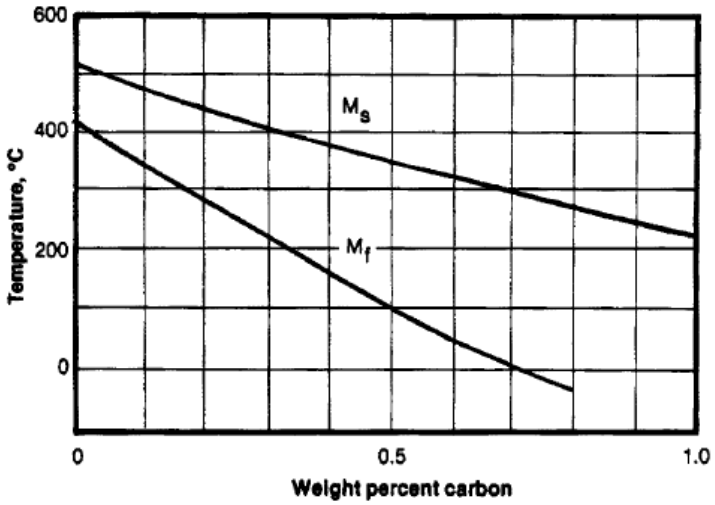

Figure 2.10 Influence of carbon on the transformation temperature of austenite to martensite [61]

To minimise elastic strain energy during transformation, martensite forms as thin plate or lath shapes on crystallographic planes called habit planes, constrained within the prior austenite grain boundaries [57,59]. In alloys containing less than approximately 0.6wt% C, the morphology is lath-like where the laths are very long and about 0.5 µm

wide [59]. The laths are aligned parallel to each other and grouped into larger structures called blocks and packets. In alloys containing more than approximately 1.0wt% C, martensite forms as lenticular or plate martensite and grows across the entire prior austenite grain (Figure 2.11). Between approximately 0.6wt% C and 1.0wt% C, martensite is a mixture of lath and plate morphologies [57]. Conventional 13%Cr martensitic stainless steels have a maximum carbon content of around 0.22wt% [39], so martensite in these steels will be of lath morphology.

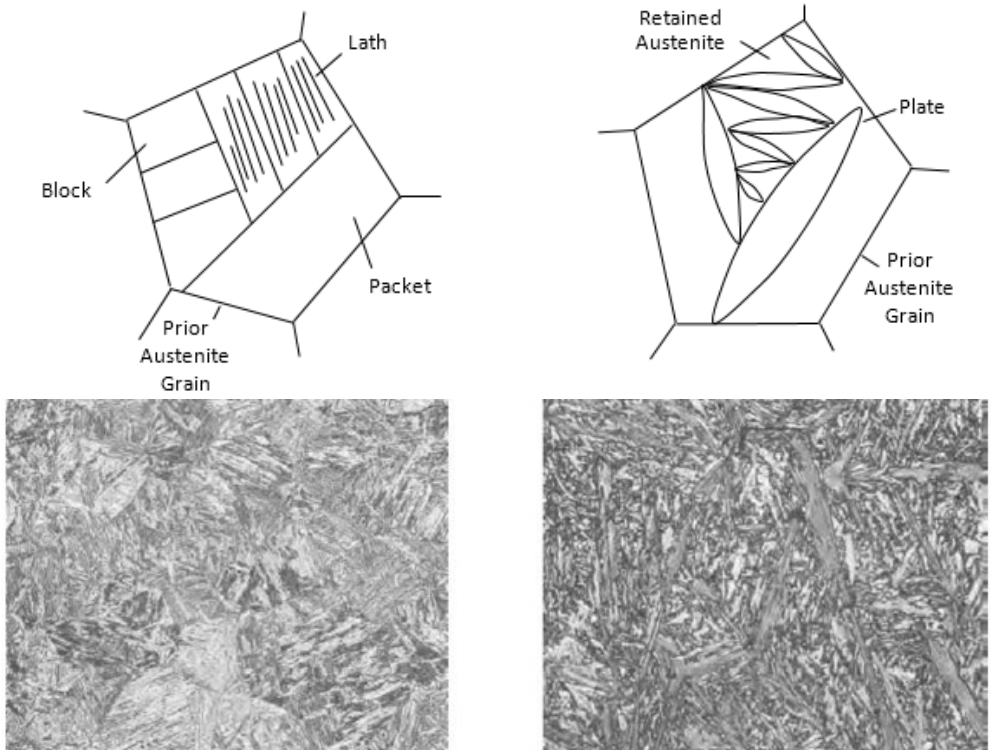

Figure 2.11 Lath and plate martensite microstructures. Matensite (left) associated with <0.6wt% carbon and plate martensite (right) associated with >1.0wt% carbon [57]

The strain needed to transform the FCC lattice of austenite into the BCT lattice of martensite is known as *Bain Strain*. Bain Strain describes homogeneous deformation of the parent lattice and implies orientation relationships between the parent and product phase which is inconsistent with observed orientation relationships, so Bain Strain alone is not the complete deformation process. The observed shape deformation associated with martensitic

transformation is an invariant-plane strain (IPS), leaving a coherent boundary between the parent austenite lattice and the product martensite lattice (the habit plane). Figure 2.12 outlines the transformation process:

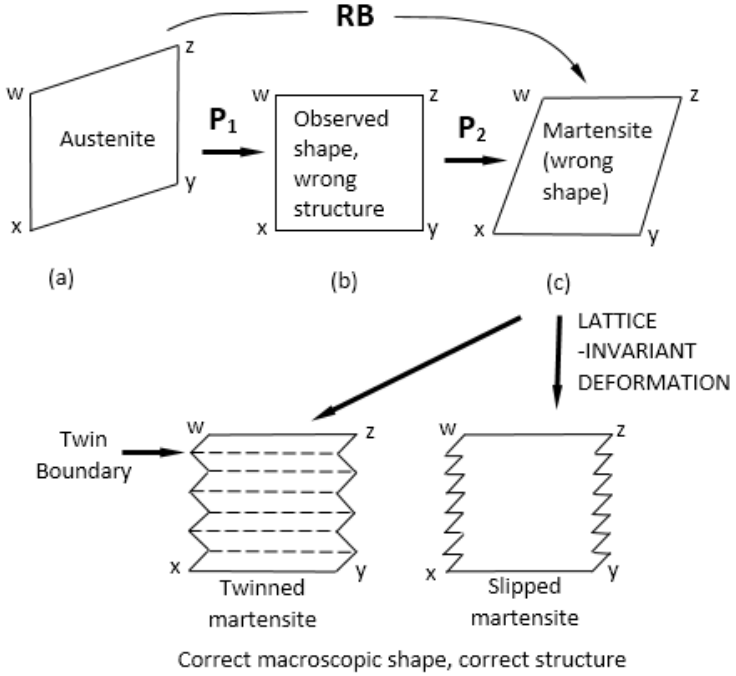

Figure 2.12 Combined effect of rigid body rotation 'R', Bain strain 'B' and lattice-invariant deformation to describe the transformation of austenite to martensite. P1 and P2 describe individual homogenous shear strains [59]

It is clear that a single homogeneous strain applied to the parent austenite phase cannot satisfy the observed shape and structure of the resultant martensite phase. A single invariant plane strain (IPS) provides the observed shape of martensite (P_1 in Figure 2.12) but gives the wrong crystal structure. Combining a second homogeneous shear (P_2) with P_1 provides the correct structure but the wrong shape. Similarly, the combined effect of Bain Strain (B) and rigid body rotation (R) is an invariant line strain (ILS), not the required IPS. Therefore an additional strain is needed in the form of an inhomogeneous lattice-invariant deformation to cancel the macroscopic shape changing effect and preserve the observed habit.

The lattice-invariant deformation produces a substructure of martensite plates in the form of slip or twin steps as shown schematically in Figure 2.13. The type of lattice deformation depends on the composition and the cooling rate. Slip occurs in low carbon containing martensite resulting in thin lathes aligned parallel to each other with a high density of dislocations. Twinning occurs where carbon contents are between 0.2% and 0.5% so each martensite plate is made up of parallel twin plates of 2-50 nm in thickness [54].

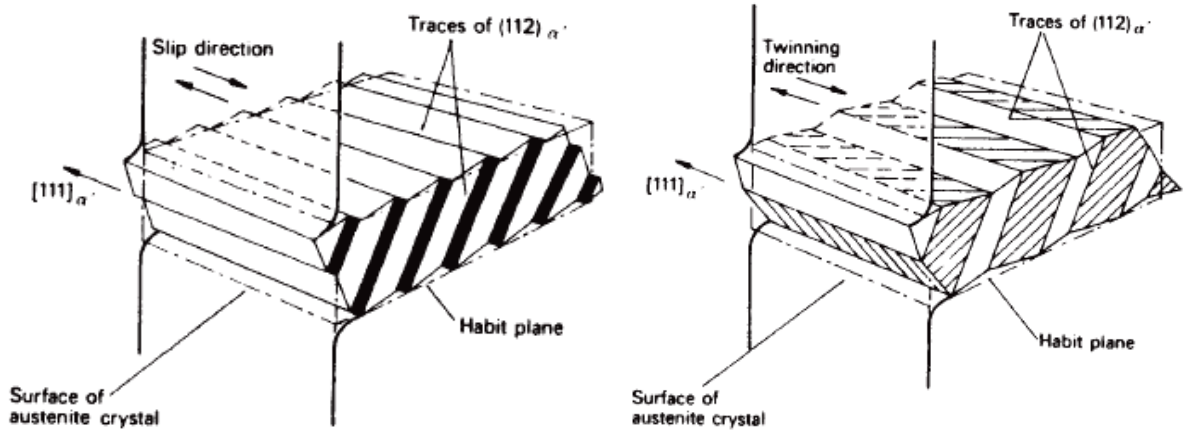

Figure 2.13 Slip and Twinning in martensite plates [59]

The expansion of martensite constrains any retained austenite in the microstructure from all sides, preventing it from expanding and hence transforming to martensite. Therefore, any in-service elastic deformation associated with external loads results in a volume expansion allowing retained austenite to transform into fresh martensite [57]. Fresh martensite is very hard and brittle and will make the material more susceptible to hydrogen embrittlement unless some ductility is re-introduced by a tempering process.

2.2.5.3 Tempered Martensite

The hardness, strength and brittleness of martensite depends on the amount of carbon and other alloying elements dissolved in the prior austenite phase: the higher the carbon content the higher the hardness and strength. Contributions to strength arise from the carbon in solution, carbides precipitated during the quench, dislocations introduced during transformation and grain size [54]. Tempering allows dislocations to move through tempered martensite more easily than fresh martensite, giving tempered martensite improved toughness at the expense of hardness and strength, improving resistance to hydrogen embrittlement. The tempering process involves heating of martensite to an intermediate temperature of about 350 °C to 500 °C for about an hour [61] and the resulting hardness depends on the tempering temperature and the time held at this temperature (Figure 2.14).

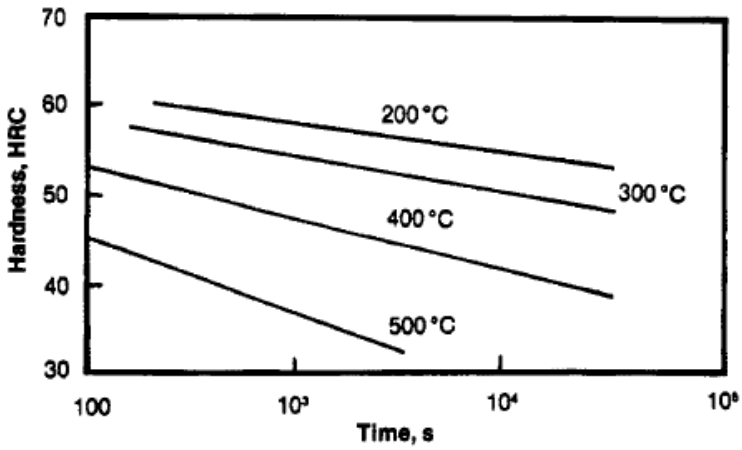

Figure 2.14 Hardness of tempered martensite as a function of time and temperature [61]

Tempering relieves residual quenching stresses introduced by the martensitic transformation process and allows some of the locked-in carbon to precipitate out into finely dispersed carbides. Structural changes associated with tempering occur in three stages.

During the first stage, fine particles of ε-carbide[5] precipitate with the corresponding formation of low-carbon martensite. This low-carbon martensite grows at the expense of the high-carbon martensite until the structure consists of retained austenite, ε-carbide and martensite with reduced tetragonality [54]. In the second stage any retained austenite decomposes into carbides and ferrite. In low carbon steels containing less than 0.3wt% C and tempered above 200 °C, these carbides add more sites for microvoid initiation which leads to a drop in toughness by a mechanism called tempered-martensite embrittlement [62]. In the third stage, cementite precipitation occurs with the dissolution of ε-carbides so that the martensite loses its BCT structure to become BCC ferrite. At this point the hardness has been significantly reduced. Tempering above the Ac_1[6] transformation temperature promotes the precipitation of finely distributed austenite along the martensite interlath boundaries and prior austenite grain boundaries [24,42,63]. Tempering above the A_{c3} temperature will grow austenite grains which might result in the formation of untempered martensite on cooling back to room temperature [62].

2.2.5.4 Retained Austenite & Toughness

When FCC steel is quenched to room temperature, the austenite to martensite transformation continues until the martensite finish temperature (M_f) is reached. If M_f is below the final quench temperature, then only a fraction of austenite will transform to martensite. The remaining austenite is termed *retained austenite* and can improve toughness because it is a softer phase than martensite. This can also be beneficial in terms

[5] In hypoeutectoid steels, carbide precipitated during tempering is called ε-carbide of composition $Fe_{2,4}C$. These are small particles in contrast to the Fe_3C platelets formed in pearlite.
[6] The subscript 'c' in A_{c1} refers to the actual temperature of the transformation on heating

of SSC resistance and hydrogen trapping as explained in the following sections. The amount of retained austenite can be influenced by alloying elements that lower M_s and annealing treatments above the temperature whereby austenite forms during heating (Ac_1). Both M_s and M_f drop as carbon content increases, hence high-carbon steels can contain more retained austenite than lower-carbon steels.

A problem with retained austenite is that it can be converted to brittle fresh martensite when cold worked. Therefore toughness can be improved with low levels of retained austenite through grain-size refinement. Refining the prior-austenite grain size provides both high strength and improved toughness [64]. Since martensitic transformation is constrained to prior austenite grain boundaries, a small austenite grain will result in a fine martensitic structure. This improves toughness because of the increased number of grain boundaries in the microstructure. Grain boundaries impede dislocation motion to increase strength and impede the propagation of brittle cleavage cracks to improve toughness. Each individual grain is oriented differently and this creates cleavage steps, localised deformation and tearing near the grain boundary [54]. The additional work done required to change the direction of a propagating crack increases the toughness of the steel.

2.2.5.5 Alloying Elements

In pure iron, the change from ferrite (α-Fe) to austenite (γ-Fe) occurs at a single temperature. Alloying with additional elements changes the temperature range over which α-Fe and γ-Fe can co-exist in equilibrium. In terms of the binary iron-carbon phase diagram in Figure 2.9, alloying elements can influence equilibrium in two ways [59]:

1. By expanding the γ-field and encouraging the formation of austenite over wider compositional limits. These elements are called γ-stabilisers and include carbon, nitrogen, manganese, nickel, copper and zinc.

2. By contracting the γ-field and encouraging the formation of ferrite over wider compositional limits. These elements are called α-stabilisers and include titanium, phosphorous, vanadium, niobium, tungsten, molybdenum, aluminium, silicon and chromium.

Chromium, molybdenum, manganese and nickel are the four major alloying elements added to steels. Segregation of these elements to grain boundaries can produce a grain boundary drag effect called *solute drag* which can reduce the rate of austenite grain growth to maintain strength and toughness in the steel. Both chromium and molybdenum will segregate to cementite (Fe_3C) constituents of steel to form carbides such as $Cr_{23}C_6$ and Mo_2C. Nickel, a non-carbide forming element, prefers to segregate to ferrite. Manganese tends to be in between these groups and can be used as a cheaper substitute for the more expensive nickel. Titanium, vanadium, niobium and tungsten form very stable carbides that pin austenite grain boundaries and reduce the rate of grain growth [65]. As the size of carbides increase, the contribution to strength decreases.

Chromium and molybdenum carbides (e.g. $Cr_{23}C_6$ and Mo_2C) are harder than cementite (Fe_3C). When tempered, chromium and molybdenum cannot diffuse as fast as carbon hence $Cr_{23}C_6$ and Mo_2C remain smaller for longer giving the alloyed steel higher strength compared to plain carbon steels. The formation of $Cr_{23}C_6$ at grain boundaries can lead to intergranular corrosion by depleting nearby regions of Cr in a process called

sensitisation. This can be mitigated by the addition of molybdenum to Cr/Ni stainless steels which slows the formation of $Cr_{23}C_6$, by reducing carbon content or by alloying with niobium and titanium which form carbides more stable than $Cr_{23}C_6$, so they preferentially combine with the available carbon and lessen the opportunity for $Cr_{23}C_6$ to nucleate [59].

Most alloying elements (with the exception of cobalt and aluminium) which enter into solid solution in austenite lower M_s which can increase the amount of retained austenite in martensitic stainless steel [59]. For 13%Cr martensitic stainless steels, it has been reported that this effect is strongest with chromium and nickel [66]. Chromium is a fundamental element as it gives steel its 'stainless' property by means of a thin chromium-oxide film on the surface that protects against corrosion. As a ferrite stabiliser, chromium additions must be balanced with austenite stabilisers to maintain the γ-field required to obtain a martensitic microstructure upon quenching. For a simple Fe-Cr low-carbon martensitic stainless steel, a single austenitic phase is achievable when chromium additions are kept below approximately 12 wt% as shown in figure 2.15 [60]. When chromium is added above approximately 14 wt%, δ-ferrite forms at the solution temperature and will remain in the microstructure on cooling. Steels designed with a small volume fraction of δ-ferrite facilitate the nucleation of $M_{23}C_6$ carbides at δ/γ interfaces. This is beneficial when M_f is below room temperature because precipitation of $M_{23}C_6$ at grain boundaries reduces the carbon content of the matrix and raises M_s so that on subsequent cooling to room temperature, more austenite will transform to martensite [59]. However, since δ-ferrite is softer than martensite, excessive quantities in the final microstructure will reduce strength and excessive formation of $Cr_{23}C_6$ at grain boundaries can lead to sensitisation.

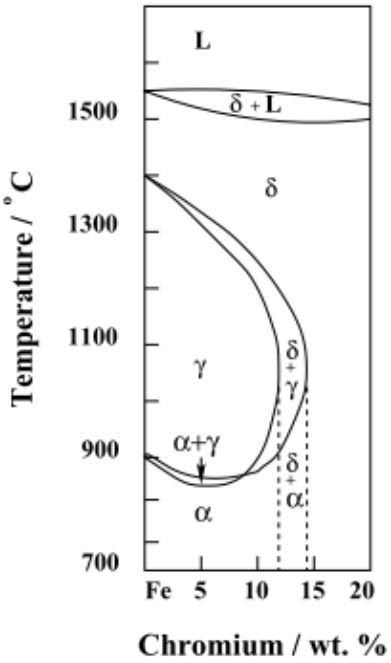

Figure 2.15 Part of a constitution diagram showing the liquid, austenite and ferrite (α & δ) phases in a Fe-Cr steel with carbon content below 0.01 wt.% [60].

Additions of molybdenum increase hardness by the formation of Mo_2C carbides and increases the Ac_1 temperature which reduces the susceptibility to retained austenite formation during tempering. Enrichment of molybdenum in the outer layers of the passive film is thought to stabilise the underlying chromium oxide passive layer by the formation of a protective molybdenum-sulphide (MoS) layer in the presence of H_2S [49]. This prevents H_2S accessing the underlying chromium-oxide layer [44]. In 13%Cr martensitic stainless steels, molybdenum concentrations are limited to a maximum of 3% because when this is exceeded, molybdenum starts to precipitate with iron to form intermetallic phases such as Fe_2Mo [41], reducing the corrosion resistance of the alloy. Mo_2C carbides are also considered to act as hydrogen trapping sites which improves resistance to hydrogen embrittlement [67].

Small additions of titanium (about 0.15%) form stable Ti (C, N) inclusions in preference to the precipitation of chromium carbides [68]. The solubility of Ti (C, N) inclusions is low even near the melting point of the metal and this has a pinning effect that restricts grain growth in weld heat affected zones [23]. This is beneficial as a refined grain size improves strength, toughness and SSC resistance. However, as-welded Ti-alloyed steels are susceptible to intergranular stress corrosion cracking by phosphorus segregation, so PWHT is necessary to form molybdenum precipitates along the grain boundary which captures detrimental phosphorus [68,69].

Niobium additions also form very stable carbides. The effect of lowering nitrogen to 0.01% and adding 0.1% niobium to 13%Cr supermartensitic stainless steel is shown to decrease the amount of chromium and molybdenum rich precipitates through the formation of nano-scale niobium carbonitridies (Figure 2.16). Here, niobium preferentially combines with residual carbon and nitrogen to supress the formation of Cr_2N and $M_{23}C_6$, where M is a combination of chromium and molybdenum [70].

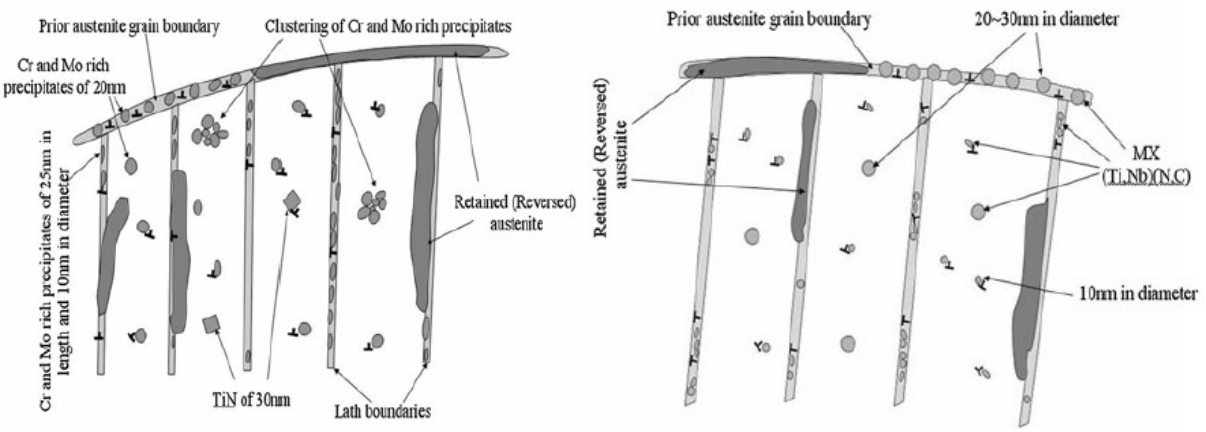

Figure 2.16 Precipitation behaviour of 13-5-2 steel (0.01 N) without Nb (left) and with 0.1Nb (right). Nb addition to low N steel suppresses Cr and Mo rich precipitates.[70]

Niobium additions have been used to develop low-carbon 13%Cr supermartensitic stainless steels with strengths exceeding 110 ksi (758 MPa). Hashizume *et al*. [46] showed that a minimum of 0.02%Nb and 0.02%C was required to obtain stable mechanical properties in a 125 ksi grade (862 MPa) 13%Cr supermartensitic stainless steel with improved SSC resistance over niobium free steels of lower strength. In addition, this work showed that there was no significant difference in M_s for niobium additions up to 0.09% compared to niobium-free steels. Kimura *et al*. [71] also showed that niobium precipitation prevents grain growth and improves low temperature toughness in 13%Cr OCTG containing 0.02-0.04% Nb.

2.2.6 The SSC Resistance of 13%Cr Martensitic Stainless Steels

SSC in 13%Cr martensitic stainless steels is a combinatorial function of pH, chlorides and H_2S, with pH being the most limiting factor followed by chloride content [25]. Other parameters such as temperature, dissolved oxygen, alloy composition, microstructure, strength and passive film stability also influence corrosion and SSC performance. However, the interaction between these parameters is not fully understood and there is no consensus on the sour-service application limits for 13%Cr stainless steels. This is partly due to inconsistencies throughout the published test data: variations exist in the test method used (e.g. tensile, four-point bend or C-ring loading), applied stress (e.g. 90% AYS or 100% AYS determined from uniaxial tensile test data, 0.2% plastic strain determined from flexural bend tests), chloride levels, pH levels, H_2S partial pressure, buffering system, de-aeration procedures and test temperatures. The following sections review the literature to

benchmark current understanding on how these variables influence the SSC resistance of 13%Cr martensitic stainless steels.

2.2.6.1 Temperature

For carbon steels the risk of SSC is greatest at room temperature and for corrosion resistant alloys the risk is generally greater at elevated temperatures [28]. Although 13%Cr martensitic stainless steels are classified as corrosion resistant alloys, it is commonly reported that the risk of SSC is also greatest at room temperature [10,28,72], despite any conclusive data to confirm this trend. At elevated temperatures (>50 °C) Sakamoto *et al*. [73] and Olsen *et al*. [14] reported an improvement in pitting and SSC resistance due to an increase in the stability of the passive film. Enerhaug *et al*. [26] reported that room temperature is the most critical temperature for SSC due to a 'weakness' of the passive film. However this comparison was only made against elevated temperature (140 °C) tests and there is insufficient data in the literature to confirm if this statement holds when temperature is reduced below 20 °C.

In addition to passive film stability, SSC resistance at elevated temperature may also be linked to hydrogen permeation. Hinds *et al*. [74] showed that the diffusivity of hydrogen in a 13%Cr supermartensitic stainless steel was controlled by reversible trapping at martensite-austenite grain boundaries; this is in contrast to conventional (Type 410) 13%Cr where trapping is predominantly irreversible and associated with carbides. Permeation tests on 13%Cr supermartensitic stainless steel showed that trap occupancy decreases with temperature (at a constant lattice concentration) reflecting an increase in hydrogen mobility

and degassing with temperature. It should be noted that this work represents bulk charging conditions typical of active dissolution of the oxide film. When the oxide film is stable (passive) it acts as a barrier to hydrogen uptake, so it is not clear if the same effect would be seen where charging occurs due to local film rupture such as pitting corrosion.

In 2005, Bodycote tested a weldable 13%Cr supermartensitic stainless steel at 7 °C, 25 °C and 115 °C and showed that cracking was most severe at 7 °C [3]. In contrast, Chambers *et al.* concluded that 5 °C was no more severe than room temperature following SSC tests on a conventional 13%Cr grade and two 13%Cr supermartensitic grades [75]. These opposing results are typical in the literature and reflect the discontinuity between the test methods used: Such differences include loading (Chambers used tensile test specimens stressed to 90% AYS whereas Bodycote used the four-point bend method at 100% AYS) and test environment (Chambers tested in 100,000 mg/l Cl^-, pH 4.5 at 38 mbar H_2S, compared to 30,000 mg/l Cl^-, pH 5 at 69 mbar H_2S used by Bodycote). Additionally, neither could rule out the possibility of oxygen contamination during the test as in-situ oxygen monitoring was not performed.

2.2.6.2 Oxygen Contamination

Oxygen contamination in the electrolyte can lead to premature failures in martensitic stainless steels. Oxygen fuels the cathodic reaction which increases the likelihood of pitting and SSC in sour environments. It has been reported that oxygen contamination increases the rest potential of modified 13%Cr stainless steels [76] and it has been suggested that oxygen levels as low as 50 ppb can greatly accelerate corrosion [77]. Electrochemical tests on a

15%Cr martensitic stainless steel [78] showed that an injection of 50 ppb O_2 increases the open-circuit potential by 50 mV, therefore increasing susceptibility to pitting and cracking in sour conditions (Figure 2.17).

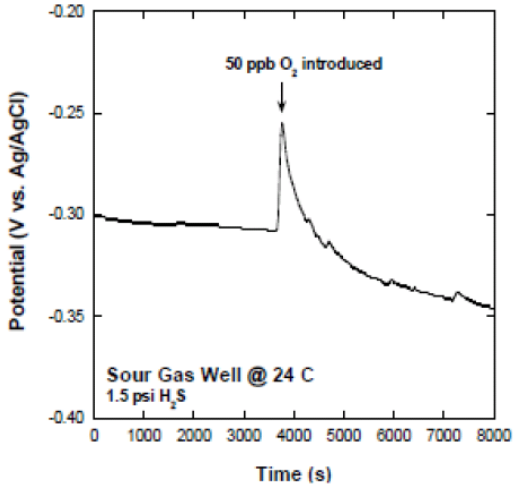

Figure 2.17 Influence of 50 ppb oxygen contamination on the open circuit potential of a 15%Cr martensitic stainless steel [78]

EFC17 guidelines [7] recommend that oxygen levels are kept below 10 ppb in the electrolyte as a safeguard when testing corrosion resistant alloys. Craig [5] states a reasonable threshold below which attack does not occur is 20 ppb. When H_2S is added to an aerated solution, a colloid may be formed with elemental sulphur. Sulphur deposits on the test surface can become sites for crevice corrosion and crack initiation. In laboratory tests, oxygen contamination can come from the gas source, poor de-aeration prior to testing, discontinuous purging of H_2S or improper sealing of the test cell. An investigation by Omura *et al*. [30] showed that placing an SSC test cell inside a nitrogen chamber was effective in minimising (but not eliminating) oxygen contamination in the test solution during the de-aeration nitrogen purge. Figure 2.18 shows that dissolved oxygen can rise to 25 ppb even when a nitrogen chamber is used, although this is dependent on the nitrogen bubbling rate used.

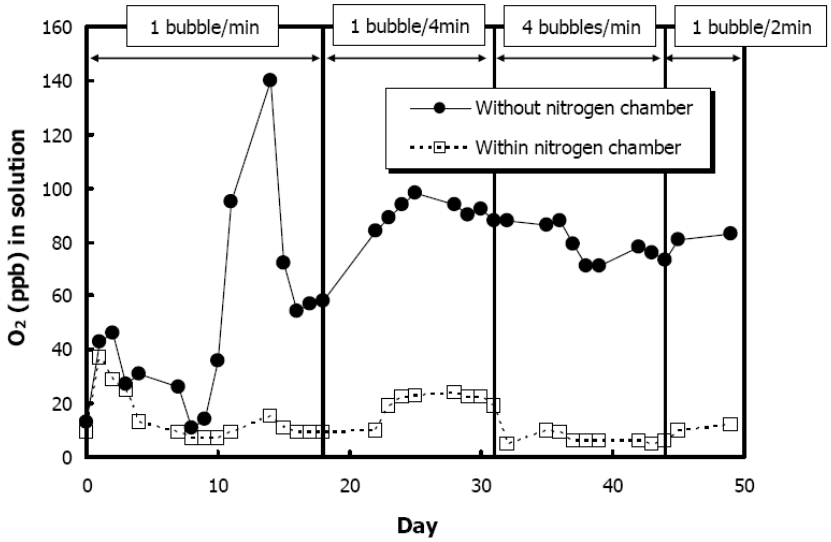

Figure 2.18 Dissolved oxygen in mildly-sour test solutions purged with nitrogen gas [30]. The use of a nitrogen chamber reduces oxygen contamination and nitrogen purge rate is also influential.

2.2.6.3 Passive Film Stability

13%Cr stainless steels are inherently protected from corrosion by a chromium-rich passive film with thickness of approximately 20 nm [79]. The passive film is formed by an oxidation-reduction reaction in which the chromium and iron are oxidised and the passivating agent is reduced [80]. The chromium oxide (Cr_2O_3) component of the passive film is less soluble than the iron oxide (Fe_2O_3) component in acidic solutions, so the passive film becomes enriched with chromium and dissolves at a lower rate.

Sidorin *et al*. [79] reported that the passive film on a conventional 13%Cr stainless steel exposed to 3% NaCl/CO_2 can provide an effective barrier to anodic dissolution while supporting hydrogen evolution at the cathode. In H_2S containing environments, passive film stability is compromised and dissolution is controlled by H_2S partial pressure, solution pH and chloride levels. Passive film dissolution allows atomic hydrogen to diffuse into the steel, promoting hydrogen embrittlement.

The benefit of alloying 13%Cr martensitic stainless steels with molybdenum to protect the chromium oxide layer has already been discussed. The SSC resistance of a low carbon 13%Cr martensitic stainless steel was quantified by Hashizume *et al*. [81] in terms of how molybdenum influences the depassivation pH (pH_d)[7]. They report that pH_d falls with increasing additions of molybdenum. Hara and Asahi [82] report the same effect but do not present the supporting data. The data presented by Hashizume *et al*. shows the apparent decrease in pH_d is less than 0.1 over the four specimens tested (Figure 2.19). It could therefore be argued that the data presented lies within normal experimental error so there is no real affect here. The improved SSC resistance may be better explained by the formation of a protective molybdenum sulphide layer, the presence of molybdenum sulphides which reduce the number of active sulphides on the metal surface (e.g. MnS), or the growth of Mo_2C carbides acting as hydrogen trapping sites as discussed previously.

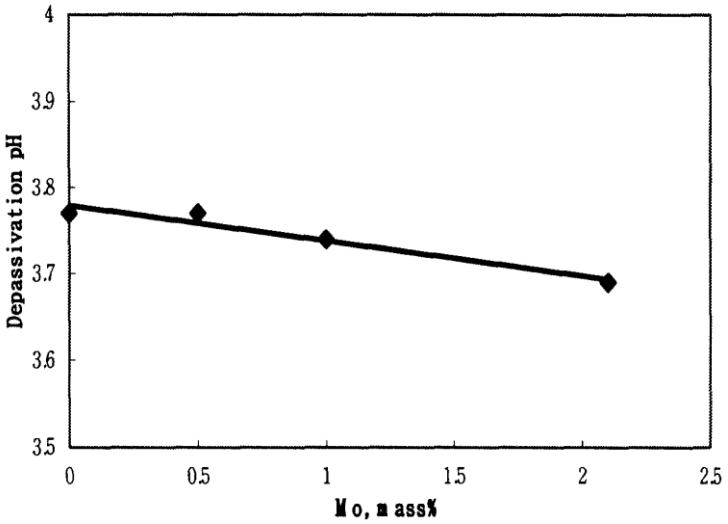

Figure 2.19 Effect of Mo on depassivation pH in 13%Cr martensitic stainless steels [81]. When the solution pH falls below the depassivation pH, passive film dissolution occurs.

[7] Passive film dissolution occurs when the solution pH falls below the depassivation pH. Conversely, the passive film is stable when the solution pH is above the depassivation pH.

2.2.6.4 Chloride Levels

It is well known that chlorides directly attack the passive film [73,83,84,85] which leads to localised pitting, resultant hydrogen uptake and finally SSC. In addition, the influence of chlorides becomes more severe as pH reduces and/or H_2S partial pressure increases [39,86]. Takabe *et al*. [87] showed that the depassivation pH of a supermartensitic (UNS S41426) stainless steel increased with chloride concentration in 10 mbar H_2S+CO_2 environments: At 24 °C, the depassivation pH was 3.0 to 3.5 at 100,000 mg/l Cl^-, but increased to 4.4 at 181,000 mg/l Cl^-.

2.2.6.5 Solution pH & Buffering Systems

When qualifying materials for sour-service applications, it is important to simulate field conditions as closely as possible within a laboratory environment. Solution pH is of particular importance since this will determine whether the material is operating in the active state, resulting in general corrosion, or the passive state where local passive film breakdown results in pitting and SSC. In real service conditions, production flow replenishes the electrolyte at the metal/solution interface to maintain a stable pH. In contrast, laboratory tests are often performed under stagnant flow conditions and this can result in local drifts in pH (more acidic at anodes and more alkaline at cathodes). The reason for this is hydrolysis of metal cations (equation 2.7) at the anode is less efficient than the reduction of hydrogen ions (equation 2.2) at the cathode and the net effect is an overall increase in solution pH [38]. For this reason, buffers are used to stabilise pH in laboratory tests whereas bicarbonate and CO_2 partial pressure controls pH in real systems.

Sodium bicarbonate ($NaHCO_3$) is a natural buffer found in formation waters and is added to simulated Produced Water solutions under continuous CO_2 purging to achieve a pH of 4.5. Condensed Water environments (pH 3.5) are nominally un-buffered in real service conditions, so replicating this environment in a laboratory while maintaining a stable pH during a sour-corrosion test requires the use of artificial buffering with weak acids. EFC17 [7] recommends the use of sodium acetate (CH_3COONa) acidified with hydrochloric acid (HCl) to pH 3.5. In practice, hydrochloric acid is often replaced by acetic acid (CH_3COOH) because of fears that HCl increases the amount of Cl^- ions in the test solution, even though the few millimoles of HCl required for pH adjustment is immediately transformed into acetic acid, CO_2 and a few millimoles of chloride [88].

Ueda and Takabe [89] reported additions of 0.5% acetic acid to a 5% $NaCl/CO_2$ environment increased the corrosion rate of 13%Cr steel, however there was no acetate or bicarbonate present and pH was around 4. Sidorin *et al*. [79] & Pletcher [90] reported that the corrosion rate of conventional 13%Cr stainless steel in 3% $NaCl/CO_2$ environments is independent of acetic acid concentration because the passive film can inhibit electron transfer reactions leading to metal dissolution while being able to support the cathodic evolution of hydrogen and reduction of acetic acid.

There is currently no consensus on how the use of artificial acetate buffers influences pH stability, passive film stability, pitting susceptibility and ultimately SSC susceptibility of 13%Cr martensitic stainless steels. The first edition of EFC17 recommended that 4 g/l sodium acetate buffer was used for all corrosion resistant alloys, but this was deemed too severe for

supermartensitic stainless steels as it resulted in active corrosion and cracking at room temperature in Condensed Water tests [26]. The second edition of EFC17 was subsequently revised to a weaker concentration of 0.4 g/l for use with 13%Cr supermartensitic stainless steels. Amaya and Ueda [91] reported that 4 g/l CH_3COONa buffer directly causes passive film breakdown of 13%Cr supermartensitic stainless steels when compared to 0.4 g/l CH_3COONa, yet Turnbull [38] disagrees suggesting there is little difference unless the material is anodically polarised. Amaya and Ueda [91] explained that even though the buffering capacity is greater in 4 g/l CH_3COONa/CH_3COOH solutions, pH stability is worse because of increased general corrosion rates.

Both Augustin *et al*. [92] and Omura *et al.* [30] reported considerable pH drift (from pH 3.5 to 4.0) when performing SSC tests at 30 mbar H_2S using 50 g/l NaCl Condensed Water solutions buffered with 4 g/l CH_3COONa/HCl, but reported good pH stability when solutions were acidified with CH_3COOH. In contrast, SSC tests (35 mbar H_2S, 1.65 g/l NaCl, pH 3.5) performed by Chambers *et al*. [75] using 0.4 g/l CH_3COONa/HCl showed very stable pH values (3.5 initial, 3.6 final).

Drugli *et al*. [93] concluded that the risk of active corrosion of 'alloyed' 13%Cr steel (0.01%C, 6%Ni, 2%Mo) increases in acetate-buffered Condensed Water solutions compared to un-buffered solutions at the same pH. However there are two problems that stand out from this work: first the tests were not directly comparable as the H_2S partial pressure was higher in the buffered solution compared to the un-buffered solution. Secondly the de-aeration procedure was not done in an airtight vessel; the test samples were lowered

through an opening in the vessel during a pure CO_2 purge which is likely to contaminate the test solution with oxygen.

Craig [5] states that in highly buffered acetate solutions, acetate ions can migrate into a corrosion pit and prevent the build-up of chloride ions, preventing pit growth and giving non-conservative results. To compliment this, Meng *et al*. [94] showed that the pitting potential of a 15%Cr steel was higher in an acetate-buffered Produced Water solution compared to the same solution buffered with bicarbonate (Figure 2.20). This may explain reports that bicarbonate is more aggressive than acetate with regards to SSC and pitting resistance of 13%Cr alloys [75,76].

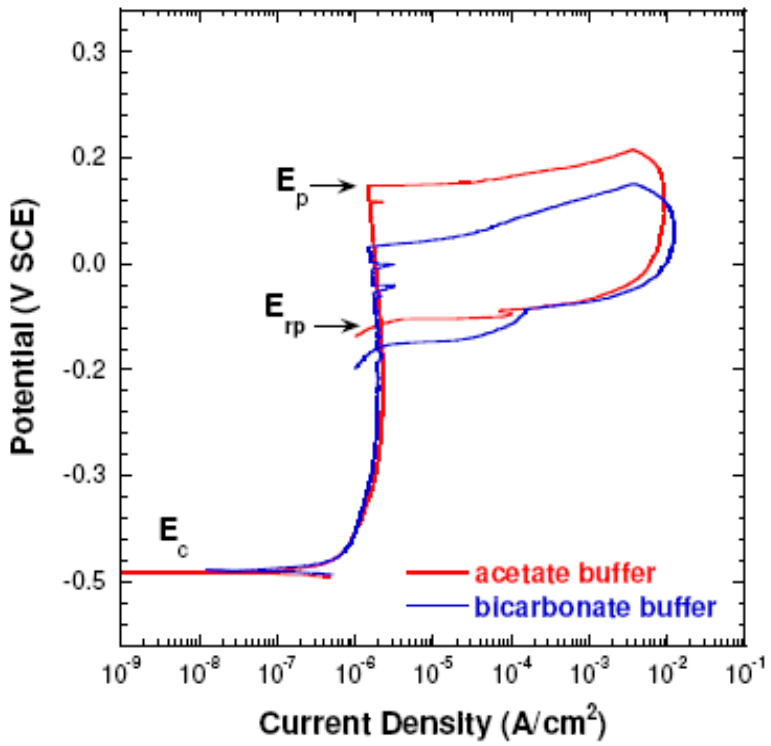

Figure 2.20 Cyclic polarization curves for 15%Cr steel in 100,000 mg/l chloride solutions containing either acetate or bicarbonate buffer at pH 4.5 and 25 °C [94]. Higher pitting potential (E_p) in acetate buffered solution indicates less likelihood of pitting compared to the bicarbonate buffered solution.

2.2.6.6 Strength

In general, 13%Cr martensitic stainless steels become more susceptible to SSC as strength is increased primarily due to the reduced material toughness. Furthermore, the hydrogen diffusion coefficient[8] decreases with an increase in strength implying an increased susceptibility to hydrogen embrittlement [40]. Vitale [95] showed that a 99 ksi (682 MPa), low-carbon modified 13%Cr stainless steel had 'superior' SSC resistance when compared to the same steel with a higher strength (123 ksi / 848 MPa). Similarly, Hashizume *et al.* [96] showed that SSC resistance decreased as strength increased for conventional 13%Cr OCTG exposed to 10% NaCl (pH 4.0 & 4.5) environments. However, this work also showed that strength did not influence the SSC resistance of 13%Cr supermartensitic stainless steels tested at pH 4.5, probably because the passive film is stable at this pH and hydrogen uptake is limited to local pit sites, hence SSC resistance depends on pitting resistance not strength at pH 4.5 as demonstrated by Kimura *et al*. [40]. The additional alloying elements in 13%Cr supermartensitic stainless steels allows strength levels of 110 ksi (758 MPa) with equivalent SSC resistance to conventional 13%Cr stainless steels with lower strength levels of 80 ksi (552 MPa). In addition, the SSC performance of supermartensitic stainless steels such as UNS S41425 is improved when strength is lowered to 80 ksi (552 MPa) [47]. In response to demands for higher strength corrosion resistant alloys, supermartensitic stainless steels were developed with small additions of niobium (0.02%) to achieve strengths up to 125 ksi (862 MPa) with improved SSC resistance over equivalent strength grades without niobium additions [46].

[8] Steel with a high ability to accumulate hydrogen shows a small hydrogen diffusion coefficient.

2.2.6.7 Retained Austenite

Potentiodynamic measurements on '13CrNiMo' plate metal (12.74%Cr, 3.71%Ni, 0.53%Mo) performed by Bilmes *et al.* [97] showed that the presence of retained austenite in the microstructure benefits the pitting corrosion resistance of both weld and parent metal. Other reports state that retained austenite is not harmful to the corrosion resistance of 13%Cr stainless steels since chromium and molybdenum do not concentrate in the austenite phase, which would otherwise lead to localised corrosion [23,98,99,100]. A study by Kimura *et al*. [99] showed that the rest potential and the pitting potential were independent of retained austenite content, while a later study by Bilmes *et al.* [101] showed that pitting and repassivation potentials shift towards the noble direction as retained austenite content increases, thus improving pitting resistance. Kimura *et al*. [99] suggested that the increase in pitting potential is due to a decrease in precipitated chromium and molybdenum[9] in the martensitic matrix. Since these elements do not concentrate in the austenite phase, the amount of chromium and molybdenum in the matrix increases with the amount of retained austenite.

Tests[10] have shown that retained austenite improves the SSC resistance of 13%Cr martensitic stainless steels. Nose and Asahi [98] showed that a weldable grade with more than 10% retained austenite had better SSC resistance than the same steel with lower levels

[9] Precipitation of chromium carbides deplete the matrix of chromium and weaken the passive chromium oxide film, increasing pitting susceptibility. Molybdenum slows the formation and growth of these detrimental chromium carbides

[10] The tests described were performed using NACE TM0177 method A tensile specimens loaded to 90 % AYS at 25 °C, pH 4.0 and 100 mbar H_2S.

of retained austenite under the same test conditions: even a large amount of fresh martensite was not harmful to SSC in the steels containing 10% or more retained austenite. The test samples were normalised at 950 °C for 30 minutes, air cooled then heat treated (300 °C to 720 °C) for 30 minutes to give levels of retained austenite ranging from 0% to 18%. The best SSC resistance was achieved by the samples containing the highest levels of retained austenite (13% & 18%). Kimura *et al*. [99] did similar tests on modified 13%Cr specimens and showed that steels containing 37.3% retained austenite were resistant to SSC whereas steels containing 4.8% and 17.8% retained austenite were not.

The link between improved SSC resistance and retained austenite could simply be explained by a reduction in material strength. This would apply to low pH environments when the material is in the active state [96]. Furthermore, Figures 2.21 to 2.23 show that hydrogen trapping in the softer austenite phase reduces the hydrogen content in the martensitic matrix [99,100] hence reducing the likelihood of SSC when the passive film is destabilised. However, Nose *et al*. [98] stated that retained austenite may only be effective in preventing SSC when hydrogen entry is intermittent (e.g. by pit re-passivation), not when hydrogen entry is continuous as with active corrosion. This is presumably because the austenite phase will saturate under continuous charging and hydrogen will simply build up in the martensite phase which will lead to embrittlement and failure by SSC.

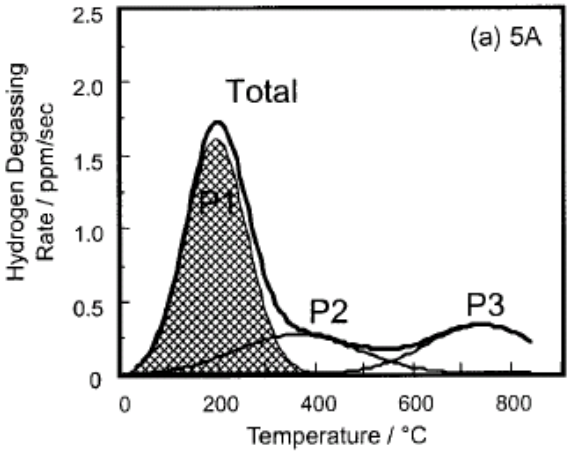

Figure 2.21 0% retained austenite: P1 is hydrogen in martensite; P2 & P3 are non-diffusible hydrogen [100]

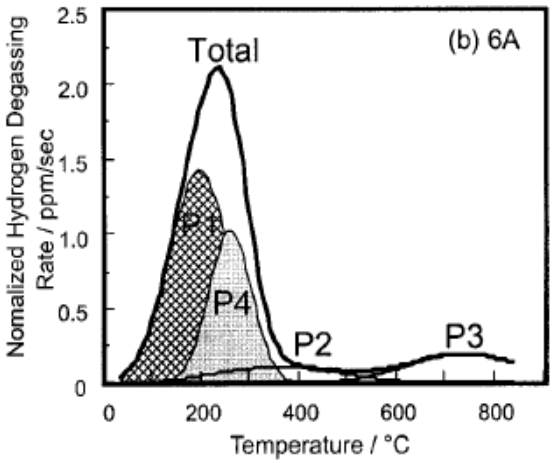

Figure 2.22 4.9% retained austenite: P1 is hydrogen in martensite; P4 is hydrogen in retained austenite [100]

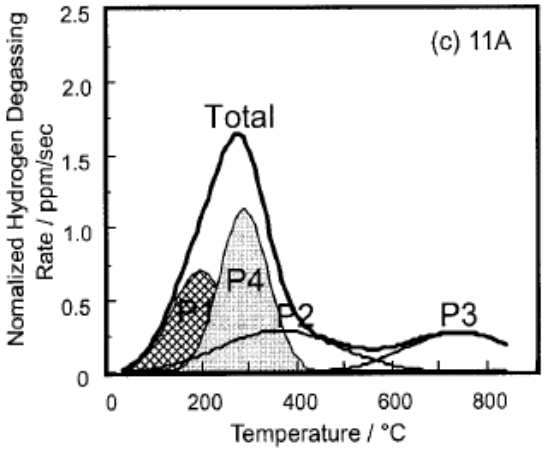

Figure 2.23 13.4% retained austenite: P1 is hydrogen in martensite; P4 is hydrogen in retained austenite [100]. More hydrogen trapped in retained austenite compared to the martensite phase.

2.2.6.8 Delta Ferrite

The effect of δ-ferrite on the SSC resistance of a low carbon (0.02%) 13%Cr stainless steel was investigated by Hara and Asahi [82]. SSC occurred in the steel with 10% δ-ferrite because the corrosion potential was lowered to the active region (Figure 2.24). The reason for the difference in corrosion potential is that δ/γ interfaces provide very effective nucleating sites for $Cr_{23}C_6$ which can lead to a chromium depleted zone and increase the

chance of pitting corrosion. Kane *et al.* [78] reported that small amounts of δ-ferrite (up to 5%) should not influence cracking and would probably have a minimal effect on pitting.

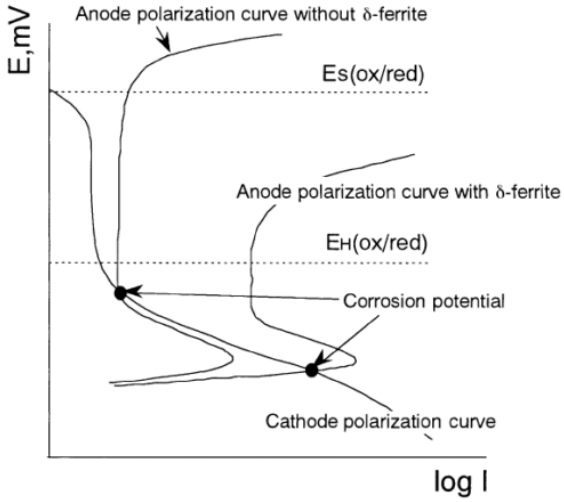

Figure 2.24 Effect of δ-ferrite on the corrosion potential of 13%Cr martensitic stainless steels [82]. The presence of δ-ferrite positions the corrosion potential in the active region.

2.2.6.9 Applied Stress

Laboratory SSC test specimens are typically loaded to 90% or 100% of actual yield stress (AYS) depending on the test method used (tensile or bending). Hashizume *et al.* [102] investigated the electrochemical behaviour of low carbon 13%Cr weld joints by using a solution flow type micro-droplet cell[11]. Application of stress (0.2% strain) resulted in a shift in the rest potential to a more negative value due to the breaking of welding scale, indicating that stress is a significant factor in the SCC behaviour of low carbon 13%Cr welded joints. Another consideration is that plastic strain can reduce levels of retained austenite by transforming austenite into fresh brittle martensite [103]. Plastic strain may also rupture the passive chromium oxide film, increasing susceptibility to pitting corrosion and eventually SSC in 13%Cr stainless steels [38].

[11] Tests carried out in aerated 0.1 kmol/m^3 Cl ions (NaCl+HCl pH=4.0) at room temperature

2.2.7 Application Limits

The following sections define SSC limits for different grades of 13%Cr martensitic stainless steel based on published laboratory test data. Documented field experience has shown that 13%Cr steels have higher H_2S partial pressure limits than indicated by laboratory test results [104]. Possible reasons for this behaviour include: higher or more consistent pH in the aqueous phase, including buffering effects; oil wetting of the metallic surface, inhibiting corrosion; elevated service temperatures or more complete anaerobic conditions in production environments.

2.2.7.1 Conventional Grades

The H_2S serviceability limits for conventional (UNS S24000) martensitic stainless steels is set at 100 mbar H_2S (pH ≥3.5) in NACE MR0175/ISO15156 [4]. Domain diagrams published by Marchebois *et al.* [83] show that the risk of SSC increases with chloride content (Figure 2.25) and suggest that the serviceability limits defined in the ISO standard may only apply for low chloride concentrations. Interestingly, the domain diagrams show general corrosion occurred at pH 3.5 which indicates active dissolution of the chromium oxide film.

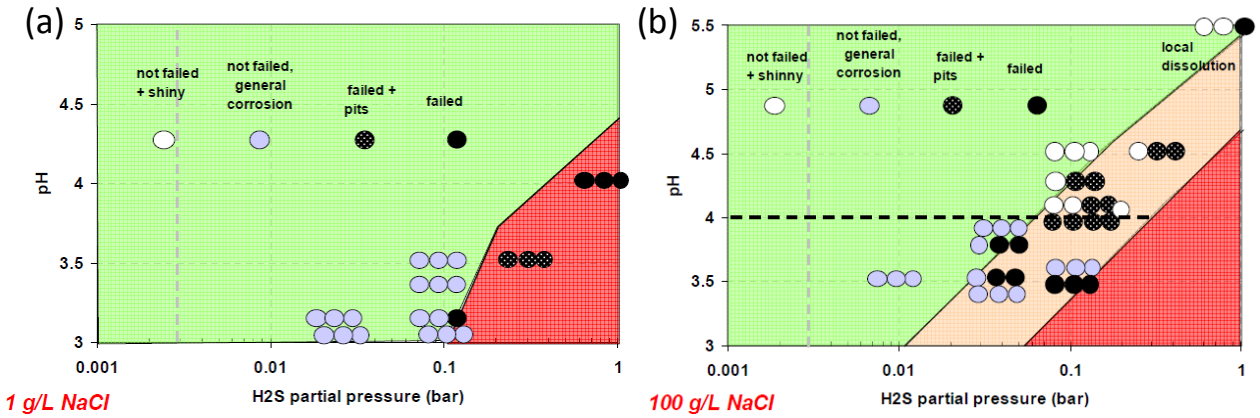

Figure 2.25 Domain diagrams for conventional L80-13Cr steels in (a) 1 g/L NaCl and (b) 100 g/L NaCl. Data from tensile test specimens loaded to 90% AYS [83]

2.2.7.2 Modified 13%Cr Grades

Cayard and Kane [29] reviewed the literature in 1998 and plotted a pH-H_2S domain diagram that included both conventional (80-95 ksi / 552-655 MPa) and modified (80-110 ksi / 552-758 MPa) grades (Figure 2.26). The data was based on specimens tested at 25 °C, stressed from 80-100% specified minimum yield strength (SMYS) in brine solutions containing 30,000 to 60,000 mg/l Cl^-. The results are plotted with the defined regions of SSC severity outlined in NACE MR0175/ISO 15156 [4]. Safe threshold values for modified grades can be taken as:

- 10 mbar H_2S at pH 3.5
- 100 mbar H_2S at pH 4.0
- 1 bar H_2S at pH 6.0

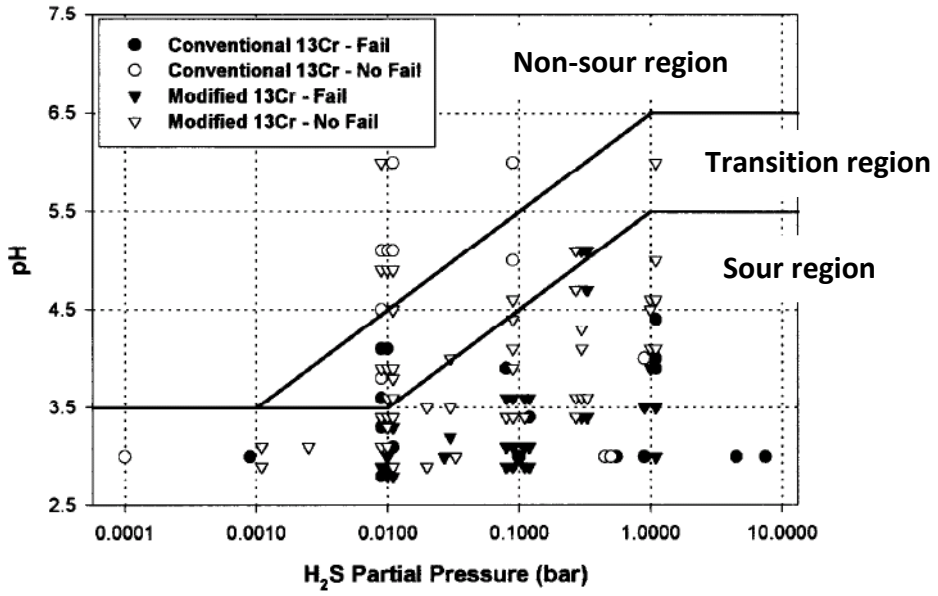

Figure 2.26 Domain diagram for conventional (552-655 MPa) and modified (552-758 MPa) 13%Cr grades. All tests performed at 25°C, stressed from 80-100% SMYS in chloride solutions ranging from 30,000 to 60,000 mg/l [29].

2.2.7.3 Supermartensitic Grades

The SSC domain diagrams in Figure 2.27 show that the 95 ksi (655 MPa) and 110 ksi (758 MPa) grades have approximately the same susceptibility to SSC in both high and low chloride environments. The authors observed that the SSC resistance transition is well defined for the 758 MPa grade (clear limit between failure and no failure) but not with the 655 MPa grade (pits and secondary cracks but no failure) which suggests that the higher strength steel provides improved pitting resistance over the lower strength steel. Furthermore, no general corrosion was reported which indicates that the oxide film remains in a passive / semi-passive state at pH 3.0.

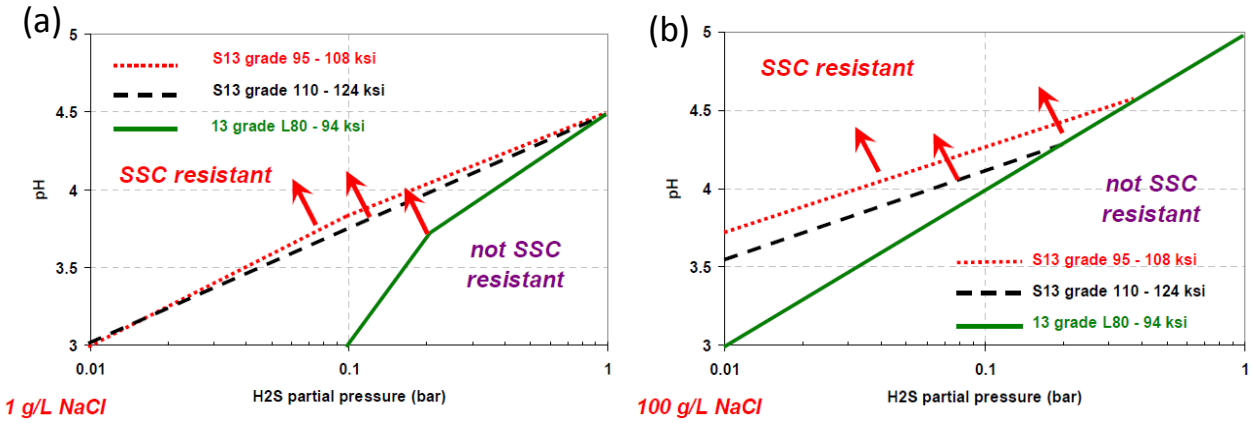

Figure 2.27 SSC domains for Super 13%Cr (655-854 MPa) and conventional 13%Cr (552-648 MPa) in (a) 1 g/L NaCl (a) and (b) 100 g/L NaCl [83]

Figure 2.28 shows two domain diagrams for 110 ksi grade (758 MPa) 13%Cr supermartensitic stainless steels compiled from various sources [39,75,86,105]. All the test data was from tensile test specimens loaded to 90% AYS with H_2S partial pressures ranging from 1 - 100 mbar and solution pH ranging from 2.8 - 5.5. Material grades were defined as UNS S41426 [75,86], 'Super' 13Cr [39] and 13-5-2 [105]. The low chloride tests were conducted in 1000 mg/l chloride and the high chloride tests were conducted in 100,000 mg/l

chloride [39,75], 140,000 mg/l chloride [86,105] and 181,000 mg/l chloride environments [105].

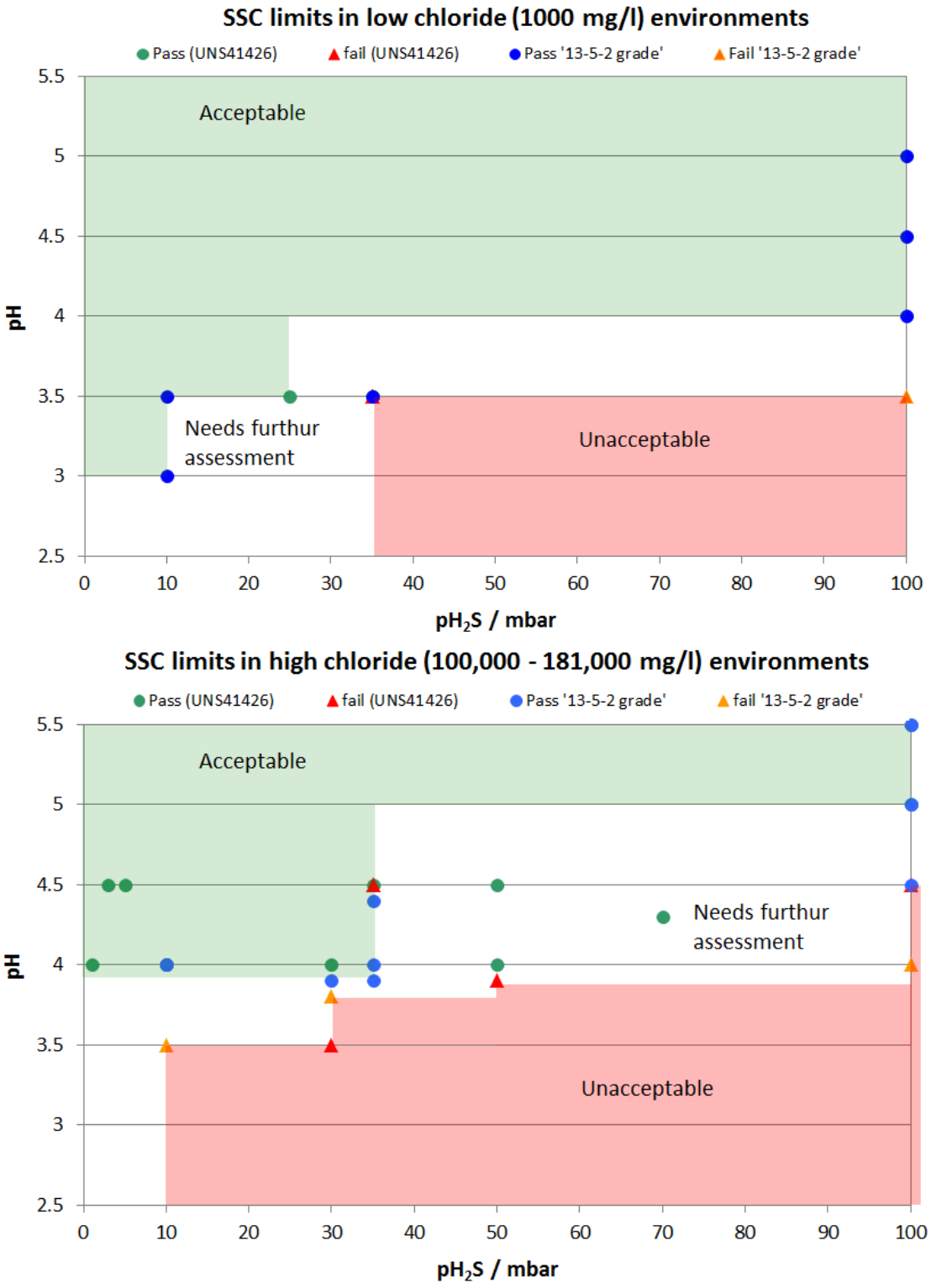

Figure 2.28 SSC resistance domain diagram for high and low chloride environments. Figure created from various published SSC test data [39,75,86,105]

In terms of pH, the domain diagrams in Figure 2.28 suggest that pH 4.5 is the borderline safe limit for SSC resistance in high chloride environments and between pH 3.5-4.0 for lower chloride environments. The areas labelled 'needs further assessment' contain either conflicting pass/fail results or highlight absence of test data. For example, in the high chloride test environment, a UNS S41426 grade failed at pH 4.5 and 35 mbar H_2S in 100,000 mg/l chloride solution buffered with $NaHCO_3$ [75] but passed in what would be expected to be a more severe test environment: pH 4.5 and 50 mbar H_2S in 140,000 mg/l chloride solution buffered with $NaHCO_3$ [86].

The main inconsistency identified by the literature review was the type of buffering system used, as detailed in Table 2.2. Grouping the results by buffering system would not have provided enough data to compile the domain diagrams. However, it should be noted that there was no clear evidence that the results were influenced by any particular buffering system.

Table 2.2 Buffering systems used in the SSC test results presented in Figure 2.28

Reference	High chloride buffer	Low chloride buffer
Hashizume *et al.*[105]	140,000 mg/l Cl: 0.41 g/l CH_3COONa + HCl 181,000 mg/l Cl: 0.5% CH_3COOH + NaOH	0.5% CH_3COOH + NaOH
Marchebois *et al.* [39]	4 g/l CH_3COONa + HCl	4 g/l CH_3COONa + HCl
Chambers *et al.* [75]	0.4 g/l CH_3COONa + HCl	$NaHCO_3$ 0.4 g/l CH_3COONa + HCl
Takabe *et al.* [86]	$NaHCO_3$ 0.41 g/l CH_3COONa + CH_3COOH 0.82 g/l CH_3COONa + CH_3COOH	$NaHCO_3$ 0.41 g/l CH_3COONa + HCl

2.2.7.4 Weldable Supermartensitic Grades

The majority of published SSC test data is based on 110 ksi (758 MPa) down-hole tubular grades as reviewed in the previous section. At the time of writing there were no pH-H_2S domain diagrams presented in the literature for weldable line-pipe grades. Table 2.3 summarises the SSC limits published by various authors on a range of weldable 13%Cr martensitic materials for line-pipe applications. The test data comes from a combination of tensile test specimens loaded to 90% AYS and four-point bend test specimens loaded to 100% AYS.

Table 2.3 SSC limits of weldable 13 %Cr supermartensitic stainless steels (room temperature)

Reference	13%Cr grade	Chloride level	pH	H_2S limits	Test method
Rogne *et al*.[106]	4-6Ni, 0.7-1.5Mo 4-6Ni, 2-2.5Mo	Not specified	3.0-3.5	10 mbar	Not specified
			4.5-5.0	30 mbar	
Miyata *et al*.[43]	0.01C, 5Ni, 2Mo	65,200 mg/l (10% NaCl)	4.0	>20 mbar	Tensile
Ueda *et al*.[49]	0.007C, 6.2Ni, 2.5Mo	31,400 mg/l (5% NaCl)	3.17	>10 mbar	Four-point bend
Enerhaug *et al*. [26]	6.5Ni, 2.5Mo	68,000 mg/l	4.0	>40 mbar	Four-point bend
Miyata *et al*. [107]	5.1Ni, 2Mo	31,400 mg/l (5% NaCl)	4.0	>10 mbar	Tensile

Although the results of the weldable 13%Cr supermartensitic stainless steels cannot be directly compared to those of the higher strength UNS S41426 grades, the H_2S limits given in Table 2.3 fall within the domains outlined for the low chloride environment in Figure 2.28 suggesting that the room temperature H_2S limits of UNS S41426 can be used as a guide for the expected H_2S limits of the weldable grades.

2.3 Material Qualification for Sour Service

For most sour-service qualification projects, materials are tested in accordance with NACE MR0175/ISO 15156 [4]. This standard originated in 1975 and has evolved into the current (2003) ISO standard that gives guidance on material selection and laboratory test methods for the petroleum and natural gas industries.

In 1975, the National Association of Corrosion Engineers (now known as NACE International) published NACE standard MR0175 "*Sulphide Stress Cracking Resistant Metallic Materials for Oilfield Equipment*" to provide guidelines for the selection of materials that are resistant to sulphide stress cracking in sour oilfield environments. The standard applies when H_2S partial pressure is equal to or greater than 0.05 psi (3.4 mbar) and was made a legal requirement in the USA and Canada. However, this standard only addressed SSC and no other cracking mechanisms.

During the late 1980s, the European Federation of Corrosion (EFC) set up working party 13 to consider the qualification of materials for sour service not covered by NACE MR0175. In the mid-1990s two guidelines were published; EFC16 (for carbon and low alloy steels) and EFC17 (for corrosion resistant alloys) on how to test and qualify these materials for sour gas production. These guidelines include more cracking mechanisms such as; HIC; SOHIC; SCC and SSC. The EFC documents defined sour service domains which considered in-situ pH, leading to the concept of materials being qualified for use in mildly sour environments rather than the more rigid approach defined in NACE MR0175 (Figure 2.29).

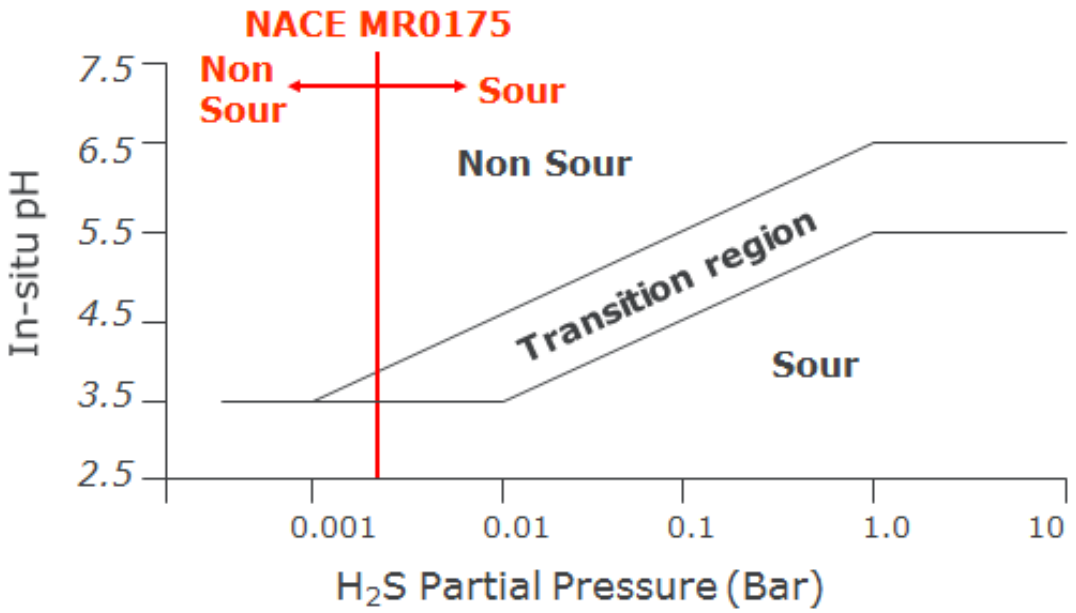

Figure 2.29 The concept of in-situ pH and NACE MR0175 definitions of a sour environment [108]: NACE MR0175 defines a rigid definition of sour service (above 3.4 mbar) whereas EFC 16 defines sour environments into regions of severity (non-sour, transition, sour) based on H_2S partial pressure and solution pH.

The three documents were eventually combined to form international standard NACE MR0175/ISO15156: "*Petroleum, petrochemical and natural gas industries – Materials for use in H_2S – containing environments in oil and gas production*". NACE MR0175/ISO 15156 consists of 3 parts that enable the selection and qualification of metallic materials for resistance to H_2S related cracking in oil and gas production.

Part 1 outlines the general principles for the selection of cracking-resistant materials and addresses *all* the mechanisms of cracking that can be caused by H_2S. This part gives guidance on evaluating service conditions for selecting pre-qualified SSC/SCC resistant materials; qualification and selection based on documented field experience; defining laboratory test requirements to qualify a material for H_2S service and re-assessing existing alloys when service conditions change.

Part 2 gives requirements and recommendations for the selection and qualification of carbon and low alloy steel. This includes factors (such as H_2S partial pressure, chlorides pH etc.) that affect the behaviour of these materials in H_2S containing environments; SSC regions of environmental severity; hardness requirements in parent and welded material; laboratory testing requirements and informative reference for calculating H_2S partial pressures and determining in situ pH.

Part 3 gives requirements and recommendations for the selection and qualification of corrosion resistance alloys (CRAs), addressing the resistance of these materials to damage caused by SSC and other mechanisms. As with part 2, Part 3 identifies the factors that affect cracking resistance of CRAs in H_2S containing environments. This part refers to EFC17 [7] and NACE TM0177 [109] for qualification of CRAs by laboratory testing. However, a key point in this standard is that it stipulates that SSC testing of CRAs is carried out at ambient temperature (24 °C $\pm$3 °C) and the maximum design temperature (for SCC) for 30 days. Sub-ambient SSC testing is not a requirement of NACE MR0175/ISO 15156 as it is assumed that ambient temperature is the more severe environment for SSC susceptibility.

2.3.1 Standard Test Methods

NACE MR0175/ISO 15156 refers to EFC17 [7] and NACE TM0177 [109] for SSC test method requirements. The primary methods used to load specimens are classified as *constant load*, *sustained load*, *constant total strain*, and *continuously increasing strain*.

The only way to truly achieve a *constant load* for the duration of a test is by hanging a dead weight on the end of the specimen. Alternatively, spring loaded devices and proof rings can be used to apply a *sustained load* to the specimen. A proof ring is a calibrated ring of material that when deflected by a given distance, applies a known load to the test specimen under uniaxial tension. *Constant strain* is achieved by deflecting the specimen to a given load and then fixing this displacement for the duration of the test. The problem with this is that a truly constant strain is difficult to achieve because of stress relaxation in the loading frame. *Continuously increasing strain* is achieved simply by loading the specimen at a constant rate until failure.

NACE TM0177 "*Laboratory Testing of Metals for Resistance to Specific Forms of Environmental Cracking in H_2S Environments*" [109] originally issued in 1977 with the latest revision in 2005, covers the testing of metals subjected to a tensile stress for cracking resistance in H_2S containing environments. This standard contains methods for testing metals using tensile, bent-beam, C-ring, and double-cantilever-beam (DCB) test specimens. The Slow Strain Rate Test (SSRT) method is covered in NACE standard TM0198 [110].

2.3.1.1 Method A: NACE Standard Tensile Test

This method is a crack initiation test using smooth uniaxial tensile loading. The test is performed under constant-load (dead-weight) or sustained load (proof ring) in either NACE Solution A or NACE Solution B environments[12]. The test is performed at 24 °C (±3 °C) under 1 bar H_2S for 30 days. The standard does not specify a loading stress level and the acceptance criteria is no cracking at ten times magnification. On initial loading, the tensile stress is uniformly distributed across the thickness of the test area, so cracking can result in complete fracture of the test piece as shown in Figure 2.30.

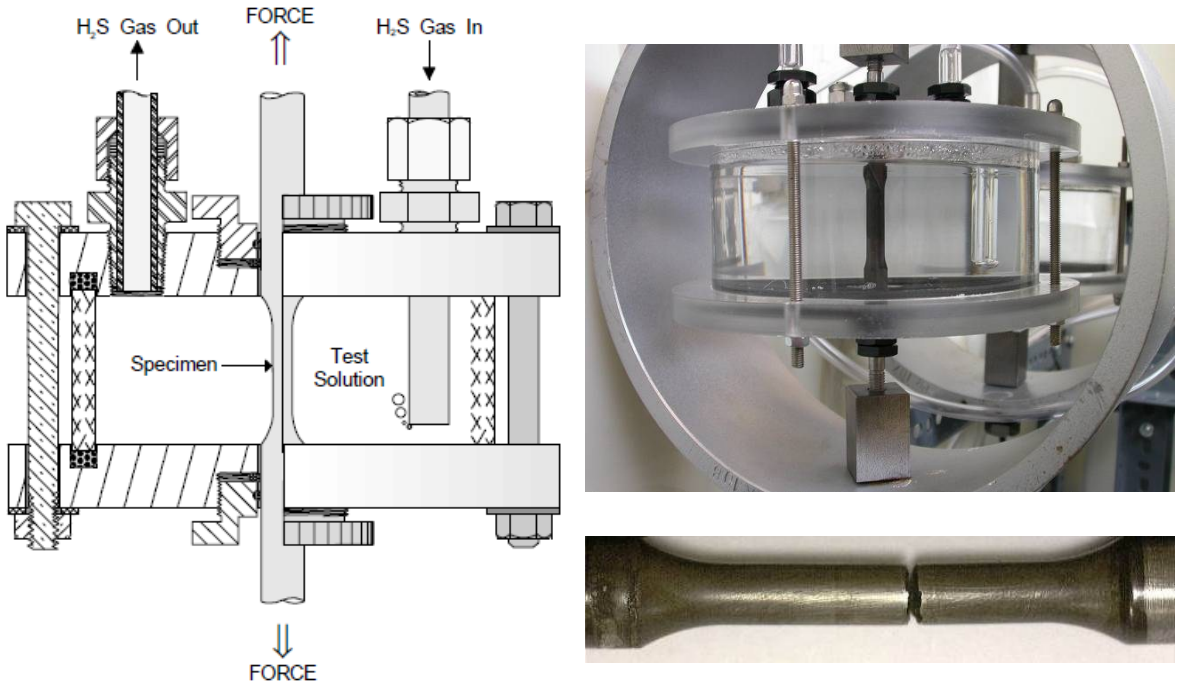

Figure 2.30 NACE Standard Tensile Test: Schematic (left) [109], tensile test specimen loaded by a 'proof-ring' (upper-right) and a carbon steel specimen fractured in two halves (lower-right) [108].

[12] NACE Solution A consists of 5.0% NaCl with 0.5% glacial acetic acid (CH_3COOH) to achieve a pH of 2.7. NACE Solution B consists of 5.0% NaCl with 0.4% sodium acetate (CH_3COONa) and 0.23% CH_3COOH to achieve a pH of 3.5.

2.3.1.2 Method B: NACE Standard Bent-Beam Test

This method is a crack initiation test using three-point loading (Figure 2.31). The test is performed under constant-strain by loading the beam to a particular deflection. The beam contains two 0.71 mm diameter holes at the mid length to assess SSC susceptibility in the presence of a stress concentration. The test solution consists of 0.5% glacial acetic acid (CH_3COOH) and no sodium chloride (NaCl). Testing is performed at 24 °C (±3 °C) under 1 bar H_2S for 30 days. The standard does not specify a loading stress level and the acceptance criteria is no cracking at ten times magnification.

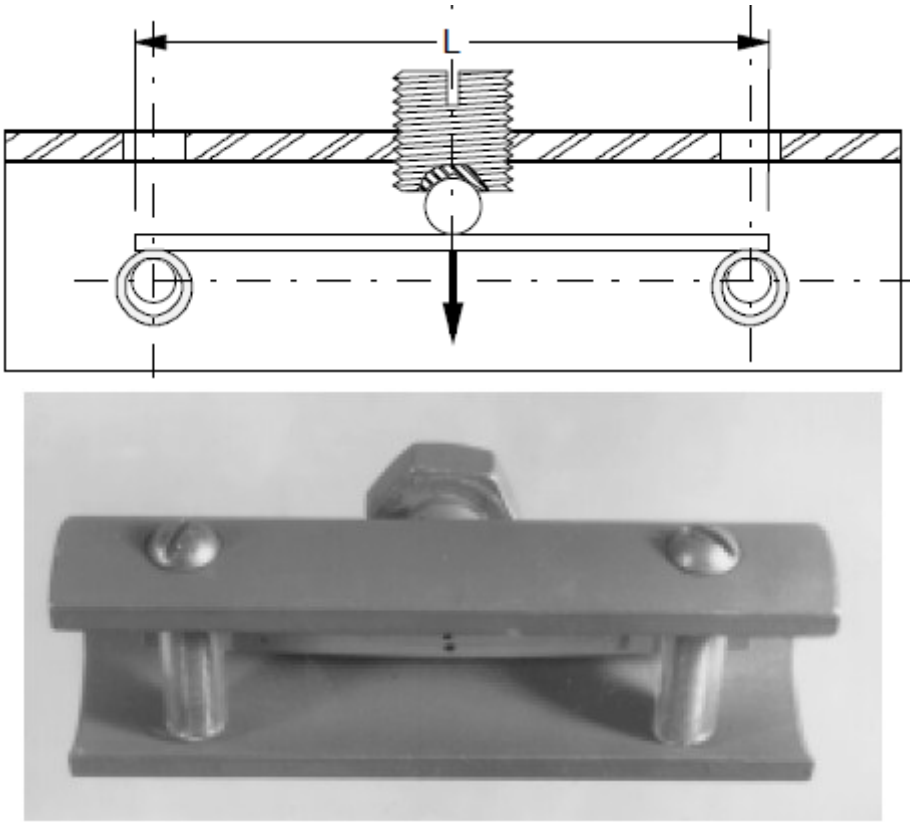

Figure 2.31 NACE Standard Bent-Beam Test: Schematic (top) showing specimen loaded in 3-point bending, photograph (bottom) showing 2x0.77 mm holes drilled at the mid-length to generate a stress concentration [109].

2.3.1.3 Method C: NACE Standard C-Ring Test

Method C provides a crack initiation test for metals under circumferential loading (hoop stress) using an un-notched C-ring test specimen (Figure 2.32) and is ideally suited for testing transverse sections of tubing and bar. The C-ring is loaded through bolting fixtures that deflect the specimen to the required stress on either the inner or outer surfaces. To avoid galvanic effects, the loading bolts must be of the same material as the test specimen or electrically isolated using PTFE and PEEK insulation. TM0177 specifies that the test surface of the specimen should be polished to a 0.81 µm or less [109].

As with Method A, the C-ring test is performed at 24 °C (±3 °C) under 1 bar H_2S for 30 days with either NACE Solution A or Solution B environments. No loading stress is specified and the acceptance criterion is no cracking at ten times magnification.

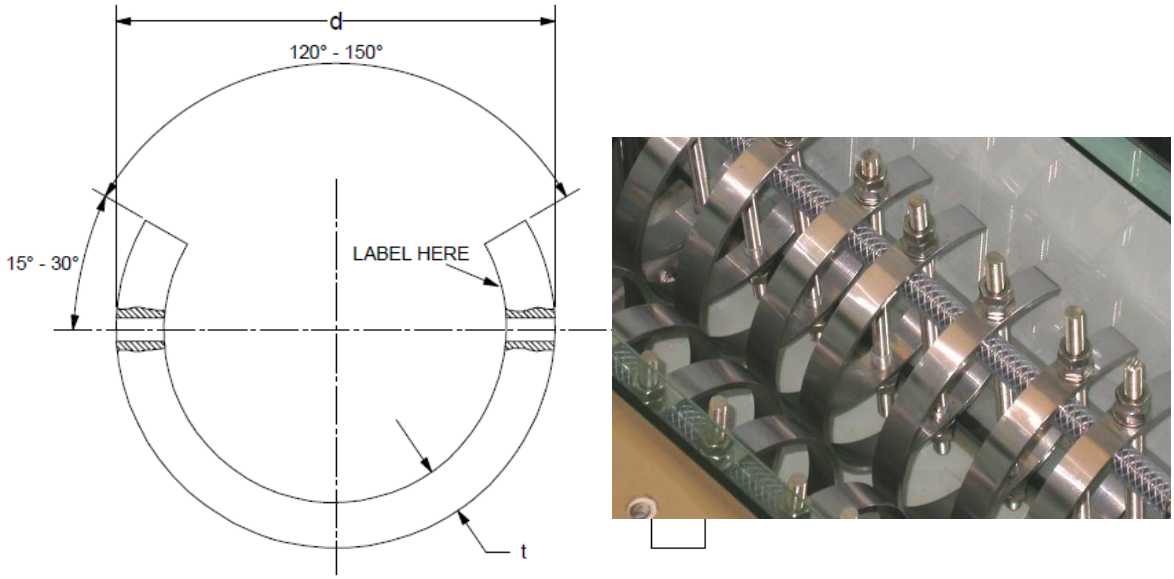

Figure 2.32 NACE Standard C-Ring Test: Schematic of test specimen (left) [109] and photograph of loaded c-rings in test solution (right) [108].

2.3.1.4 Method D: NACE Standard DCB Test

Method D provides a measure of resistance to crack propagation in terms of a critical stress intensity factor K_{1SSC} (for SSC) using a Double-Cantilever-Beam (Figure 2.33). The benefit of this method is that it does not depend on the uncertainty of pitting or crack initiation (a crack will always initiate in a valid test) and does not depend on evaluation of failure/no failure results. The specimen is loaded using a double-tapered wedge made of the same material as the test specimen and the test method gives a direct numerical rating of crack propagation resistance for the material. At 14 days, this is a shorter test than those described previously and is carried out at 24 °C (±3 °C) at 1 bar H_2S in either NACE Solution A or Solution B environments.

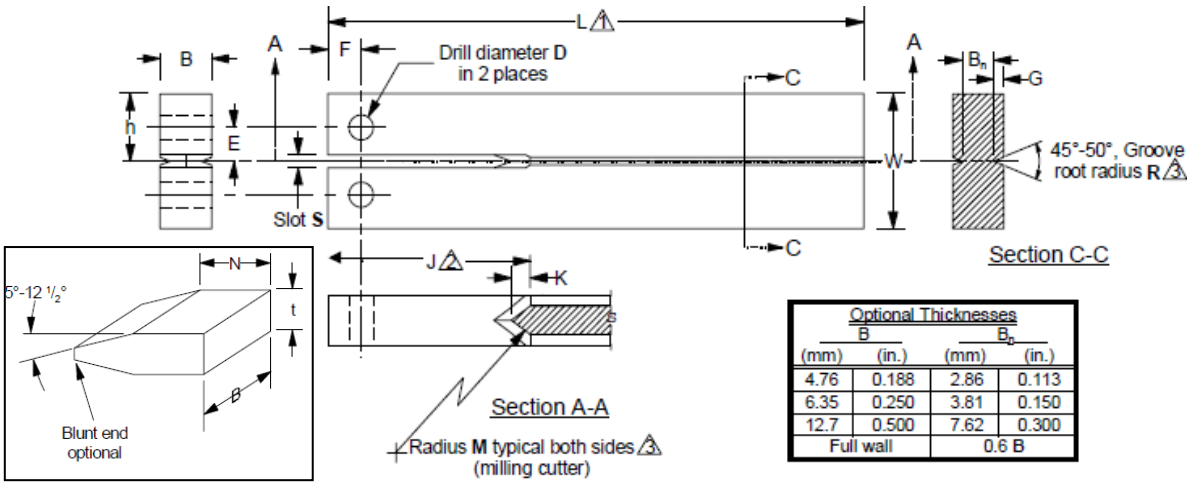

Figure 2.33 NACE Standard Double-Cantilever-Beam Test: Schematic of test specimen and double-tapered wedge used for loading (insert) [109].

2.3.1.5 Slow Strain Rate Test (SSRT)

The SSRT is a *continuously increasing strain* method described in NACE standard TM0198 [110] and provides a rapid screening and ranking test for corrosion resistant alloys. Tensile type specimens are pulled to failure at a strain rate of $4x10^{-6}$ s^{-1} within an autoclave. The autoclave allows tests to be carried out from 0.03 to 34.5 bar H_2S at 25 °C to 205 °C, in 5 to 25% NaCl environments. A calibration 'in air' test is conducted first then the environmental tests are carried out and compared to this test to determine SSC resistance (Figure 2.34). Specimens are evaluated based on type of failure (ductile or brittle), any secondary cracking, % elongation ratio and % reduction of area ratio.

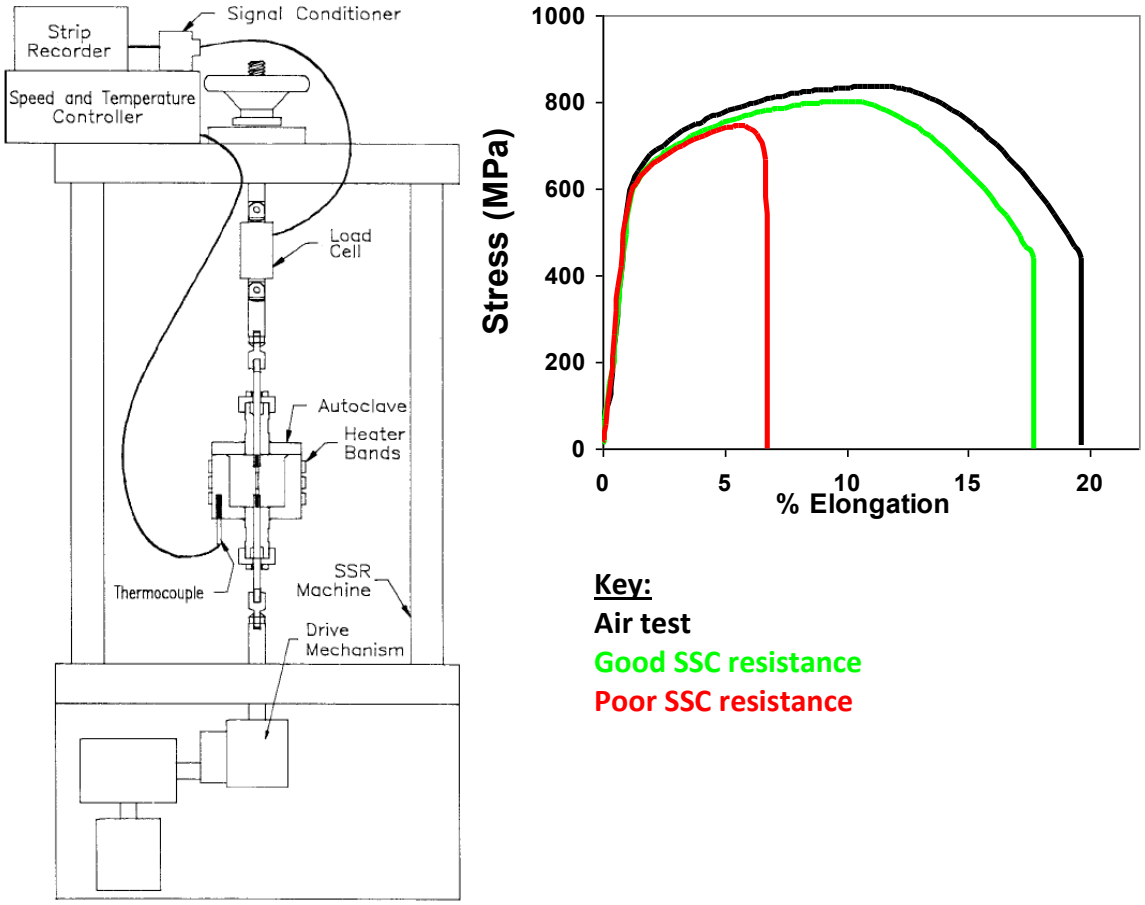

Figure 2.34 NACE TM0198 Slow Strain Rate Test. Schematic of test setup (right) and typical Slow-Strain-Rate Test results (left) [108].

2.3.1.6 Full Ring Test

Health and Safety Executive report OTI 95 635 [111], describes a Full Ring test method which utilises a full circumferential ring of line-pipe that is mechanically loaded and filled with a sour environment. This method can be applied to ring sections in excess of 18" diameter to detect SSC, HIC and SOHIC. The benefit of this method over small scale tests is that the sample can contain a full circumferential weld. This retains the residual stresses produced during manufacture and welding, provided that the length of the sample is equal to or greater than its diameter. Figure 2.35 shows a typical setup; load distribution blocks compress the outer surface and the ring is contained with a clear gas-tight lid. After purging with nitrogen gas, the pipe is filled with a test solution and saturated with H_2S. The test typically lasts 30 days, after which the pipe is examined for cracking by a non-destructive test method.

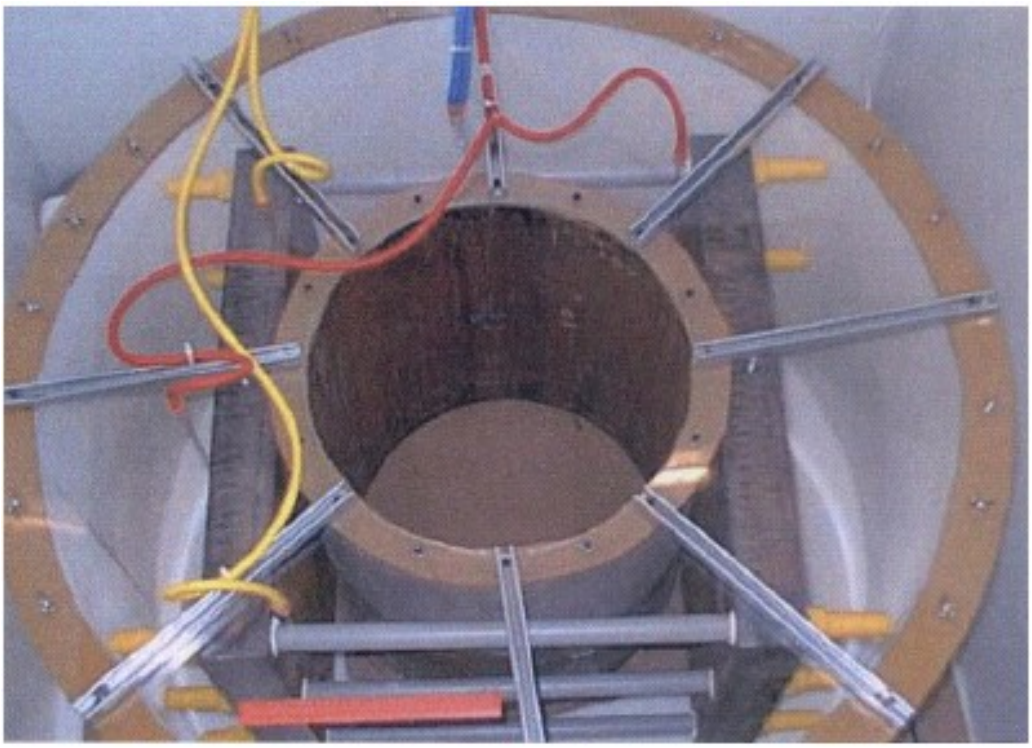

Figure 2.35 Full Ring Test: Sample loaded and encapsulated [112]

2.3.1.7 Four-Point Bend Test

The four-point bend test is a simple, low-tech method of applying stress to a relatively large surface area of a test piece and is particularly suited for testing root-intact welded specimens. Loading is achieved by turning a bolt to displace two inner loading rollers that deflect a beam sitting on two outer support rollers (Figure 2.36). This is a *constant strain* loading method recommended in NACE MR0175/ISO15156-3 [4] and EFC17 [7] for SSC testing of corrosion resistant alloys in sour environments. If loading is carried out within the elastic limits of the material, standards such as ASTM G39 [113] and ISO 7539-2 [114] can be used to calculate the stress on the tensile test surface using elastic bending theory by measuring beam deflection (see Section 2.4). However, loading becomes more complex for corrosion resistant alloys as they are loaded to 100% of Actual Yield Strength (AYS), as stipulated in the NACE and EFC guidelines. Under this level of load, the stress/strain response of the material moves into the plastic regime and the linear elastic equations given in ASTM and ISO standards are no longer valid to use. The solution is to use a strain gauge bonded to the test face to directly measure loading strain.

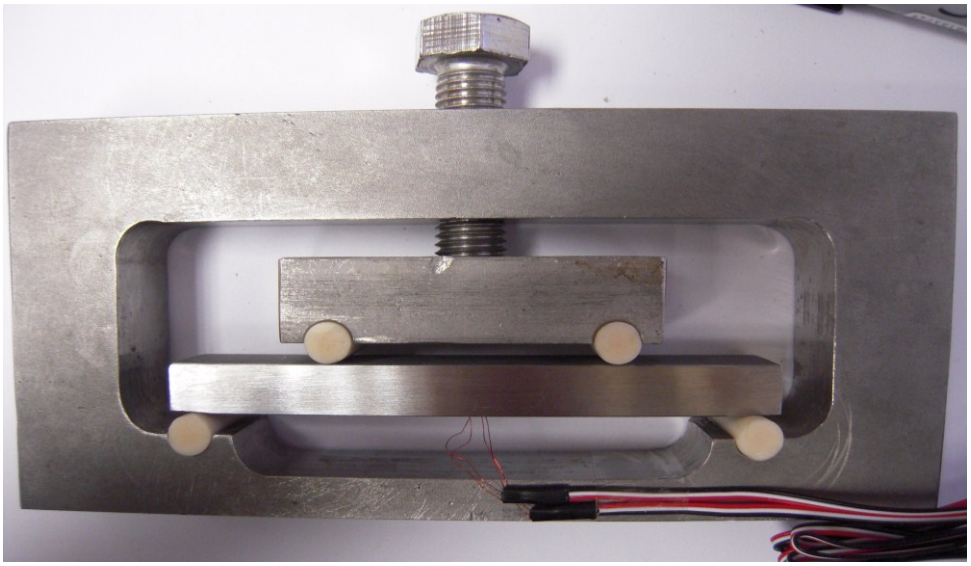

Figure 2.36 SSC specimen loaded in four-point bending

When strain gauges are used, the operator needs to know the loading strain required to achieve 100% AYS on the test surface of the specimen. NACE MR0175/ISO 15156-3 [4] specifies that this is determined from tensile stress-strain curves. However, it has been questioned as to whether this is the correct way to determine the loading strain for a four-point bend test [115]. The rationale being that stress is uniformly distributed through the thickness of a tensile test specimen whereas a stress gradient exists through the thickness of a four-point bend specimen; i.e. stress changes from compression on the back face to tension on the test face. Therefore, the two methods are not comparable and the influence of the stress-gradient needs to be taken into account when setting the loading strain in bending.

Turnbull & Nimmo [116] reported that a 13%Cr supermartensitic stainless steel loaded from tensile stress-strain data would be strained approximately 18% lower than if it were loaded using flexural bend test data (A flexural bend test is a four-point bend test whereby load and strain is recorded while the test piece is deflected at a constant rate. The resultant load/strain curve is then used to determine the value of strain at 0.2% plastic strain for loading four-point bend SSC test specimens prior to exposure).

2.4 Stress & Strain Distribution in Four-Point Bending

2.4.1 Elastic Bending Theory

When a beam is subjected to pure bending, one side of the beam will extend in tension and the opposite side will shorten in compression. This generates a linear gradient of bending stresses through the thickness of the beam (Figure 2.37). Provided that all deformations are elastic, and assuming the material is both homogeneous and isotropic, the longitudinal stresses through the thickness of the beam change from tension on one face to compression on the opposing face, with a surface between the two where both stress and strain is zero. This surface is called the *neutral plane*, and its intersection with the cross-section of the beam is called the *neutral* axis. The neutral axis passes through the *centroid of area* of the beam cross-section; for a beam with double-symmetric (rectangular) cross-section, the neutral axis is located at the mid-point of the cross-section [117].

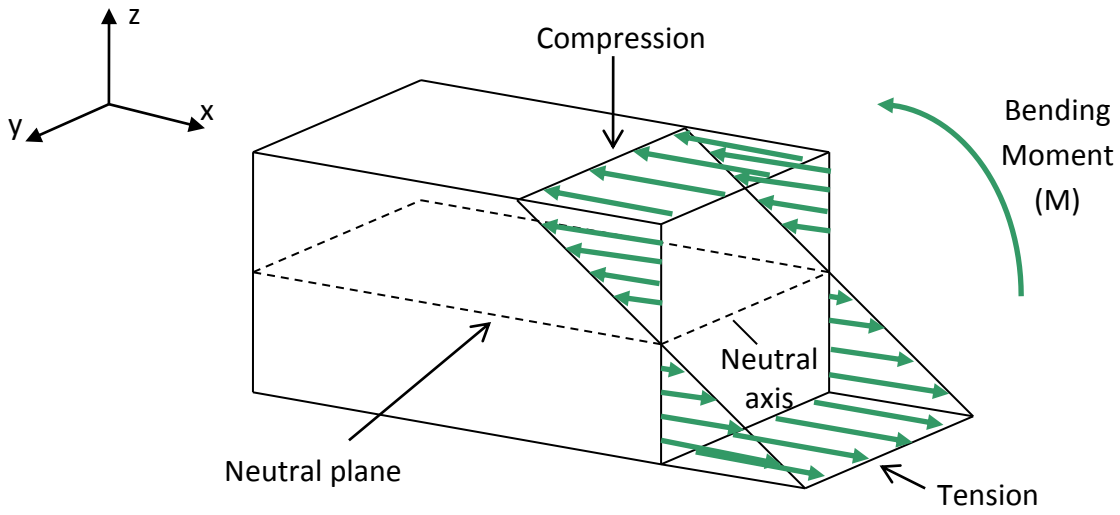

Figure 2.37 Stress distribution within a rectangular section beam subjected to pure bending [118]

Hooke's law states that strain for small elastic deformation is a linear function of stress [119]. Therefore, in pure elastic-bending, a linear gradient of strain will also exist from compression to tension through the thickness of the beam. This linear model also assumes equal compressive and tensile responses, so the strain at the tensile surface is equal in magnitude but opposite in sign to the strain at the compressive surface.

Resistance to bending is determined by the *second moment of area/inertia* (*I*) and is a function of the beam's cross-sectional shape and area. The second moment of area is calculated for any shape using the formula [119]:

$$I = \int_A y^2 \, dA \tag{2.13}$$

Where:
A = cross-sectional area of the beam (m^2)
y = distance from neutral axis (m)

For a beam with rectangular cross-section, such as that in Figure 2.37, this gives [120]:

$$I = \frac{bh^3}{12} \tag{2.14}$$

Where:
I = second moment of area (m^4)
b = width of beam (m)
h = height of beam (m)

Stiffness increases with the second moment of area, so beams with more material away from the neutral axis have greater resistance to bending, since *I* depends on h^3.

In four-point bending, the beam rests on two outer support rollers and is loaded through two inner rollers spaced symmetrically about the central point of the beam. The inner loading rollers produce shear loads which induces shear stresses in the cross section of the beam. These shear stresses are greatest at the neutral axis. However, since the cross sectional dimensions of beams are characteristically small in relation to their length, shear stresses are comparatively low in value so the assumption of plane sections remaining plane after bending may be used with reasonable accuracy [117]. Figure 2.38 shows the bending moment and shear stress distributions along the length of a beam when loaded elastically in four-point bending. In a four-point bend test, the tensile surface between the two inner rollers is used as the test surface, providing a relatively large test surface of uniform tensile stress where the bending moment is at its maximum value.

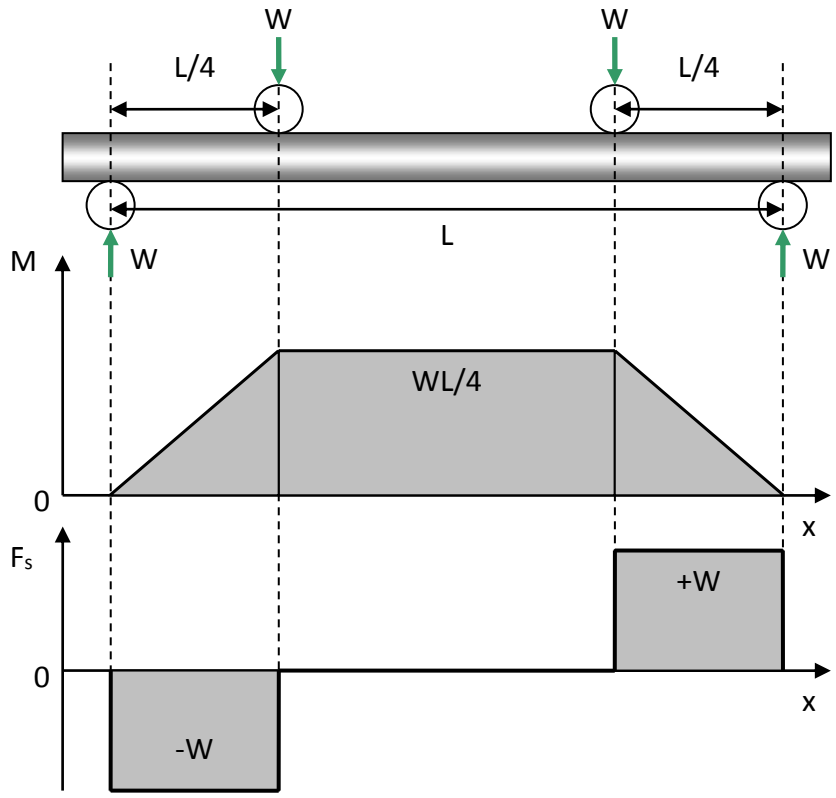

Figure 2.38 Bending moment (M) and shear-force (F_s) distributions along the surface of a beam subjected to load (W) in four-point bending. Figure adapted from [118].

2.4.1.1 Bending Modulus

Young's modulus (E) is a constant that relates tensile stress to linear strain and is determined by dividing stress by strain in the elastic region of a stress-strain curve from a uniaxial tensile test. To determine Young's modulus in four-point bending, the *engineer's bending equation* can be used [118]:

$$\frac{M}{I} = \frac{\sigma}{y} \tag{2.15}$$

Where:
M = Bending moment (Nm) σ = Bending stress (Nm^{-2})
I = Second moment of area (m^4) y = distance from the neutral axis (m)

Since $\sigma = E\varepsilon$ [119], equation 2.15 can be used to determine the elastic modulus in bending, using strain which can be measured directly from electrical resistance strain gauges:

$$E = \frac{M.y}{\varepsilon.I} \tag{2.16}$$

2.4.1.2 Poisson's Ratio

Poisson's ratio (v) is an elastic material parameter that defines the ratio of transverse to longitudinal strain ($\varepsilon_2/\varepsilon_1$). In uniaxial tension, the Poisson's ratio of steels will increase during plastic deformation to a maximum value of 0.5, where there is no further volume change [117]. Figure 2.39 shows the measured strain ratio in four-point bending on a 13%Cr steel covering the elastic and plastic regions [115]. This work suggests that Poisson's ratio remains practically constant (around 0.25) from 1000 με in the elastic regime to 10000 με in the plastic regime.

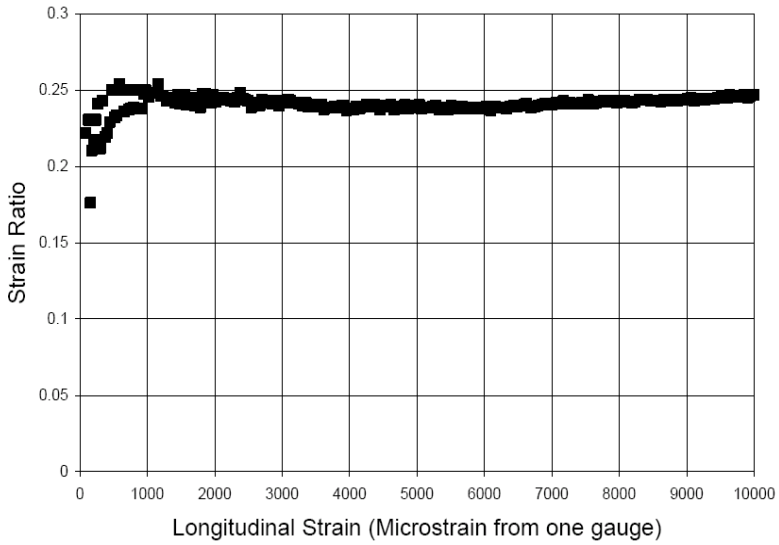

Figure 2.39 Effective Poisson's ratio in four-point bending for 13%Cr steel [115]

When a beam with a rectangular cross section is subjected to a bending moment, the through-thickness stress distribution varies linearly from compression to tension through the thickness as described previously. However, the Poisson effect causes the cross-section of the beam to distort from its unstressed rectangular shape by a process known as *anticlastic bending* [117]. Anticlastic bending describes how longitudinal stresses cause lateral expansion at the compressive surface and lateral contraction at the tensile surface. The resultant effect is that the tensile surface distorts to a concave shape and the compressive surface distorts to a convex shape as shown in Figure 2.40.

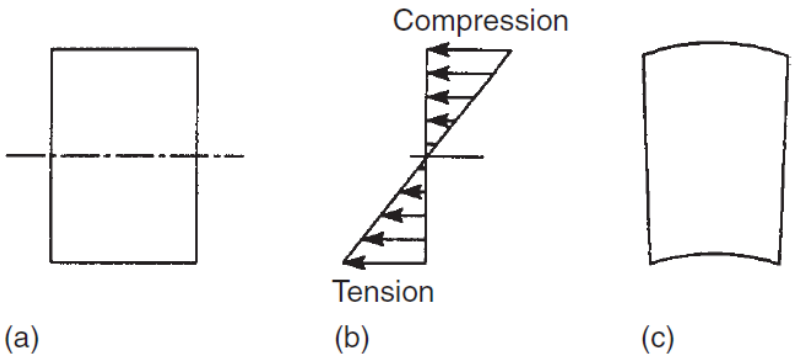

Figure 2.40 Anticlastic bending of a beam section: (a) rectangular beam section prior to bending, (b) through-thickness stress distribution due to positive bending moment in vertical plane, (c) Anticlastic bending due to the Poisson effect causes the section to distort as shown [117]

2.4.2 Elastic-Plastic Bending of beams

When the stresses within a beam exceed the elastic limit or yield stress of the material, plastic deformation will occur and this can dramatically change the flexural behaviour of the beam. The outer fibres farthest from the neutral axis are the most highly stressed fibres in a beam, and therefore they are the first to deform plastically when subjected to a sufficiently high bending moment. When the outer fibres yield and other fibres in the cross-section remain elastic, the cross-section is said to be *partially-plastic*. As the bending moment is increased and the plastic zones fully penetrate the entire cross section, the section is *fully-plastic* or in a state of plastic collapse [121]. Figure 2.41 shows the stress distribution through the thickness of a beam with a rectangular cross section subjected to elastic, partially-plastic and fully-plastic bending moments, assuming a perfectly plastic response (i.e. no work hardening of the material).

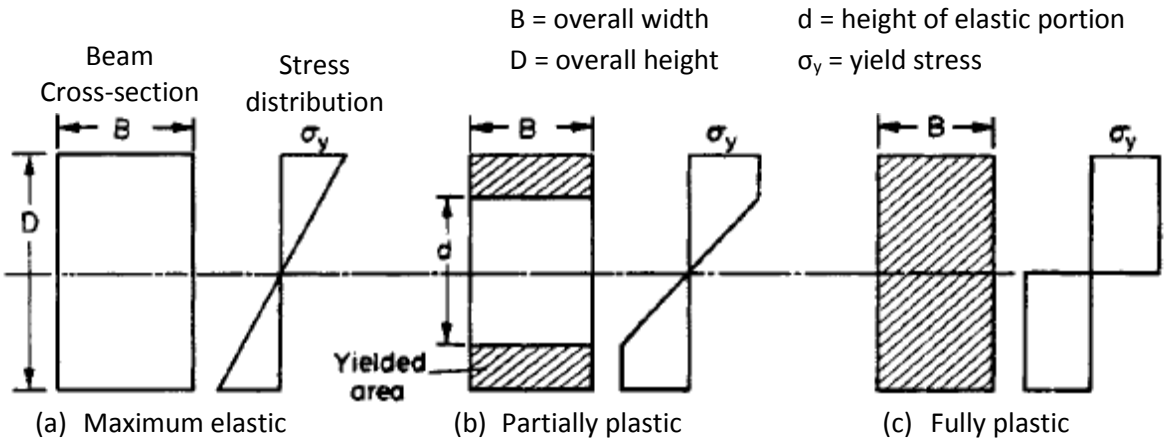

Figure 2.41 Stress distributions through the thickness of a rectangular section beam when subjected to (a) an elastic moment where the yield stress has just been reached in the outer fibres, (b) a partially-plastic moment where the plastic zone penetrates from the top and bottom surfaces, (c) a fully plastic moment where the plastic zone fully penetrates the entire cross-section [121]

2.4.2.1 Residual Bending Stresses and Strains

When an elastic-plastic beam is fully unloaded from the applied bending moment, a state of residual stress will remain in the cross-section following the recovery of elastic bending stresses [122]. The plastically deformed areas at the top and bottom surfaces constrain the underlying elastic material from returning to its unstrained state. This generates a self-balancing residual stress field that 'pushes' the top surface into residual compression and 'pulls' the bottom surface into residual tension leaving a residual curvature in the beam (Figure 2.42). The maximum residual stress in a partially-plastic beam may occur at the outside or at the inner boundary of the yielded portion depending on the depth of plastic penetration. There is no residual stress at the neutral plane of the beam [121].

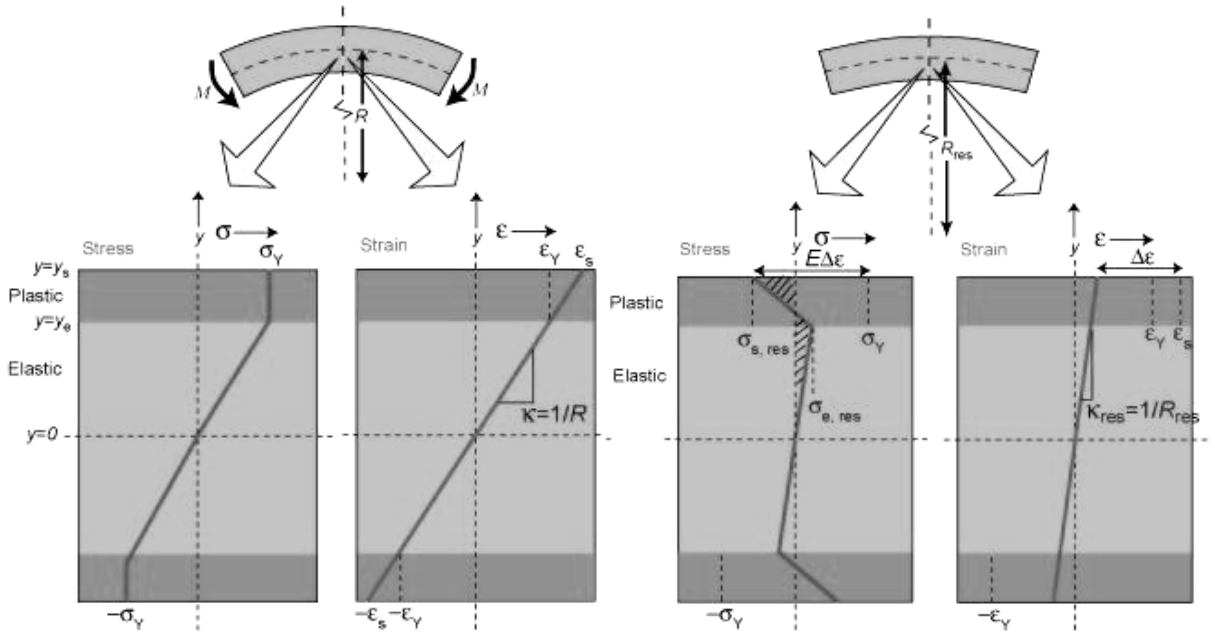

Figure 2.42 Residual stress and strain distribution through the thickness of a rectangular-section beam loaded to a partially-plastic state. Left: Initial loading condition, Right: residual stress and strain after unloading [123]

The residual stress distribution in a strain-hardening material is shown in Figure 2.43 and is non-linear due to work hardening in the plastic zones. The loading stress is represented by lines 'oab' and 'ocd'. The bending stresses superimposed during the

unloading process are given by the line 'eof' and are assumed to be elastic. The remaining residual stress produced after unloading is represented by the distribution given in (c).

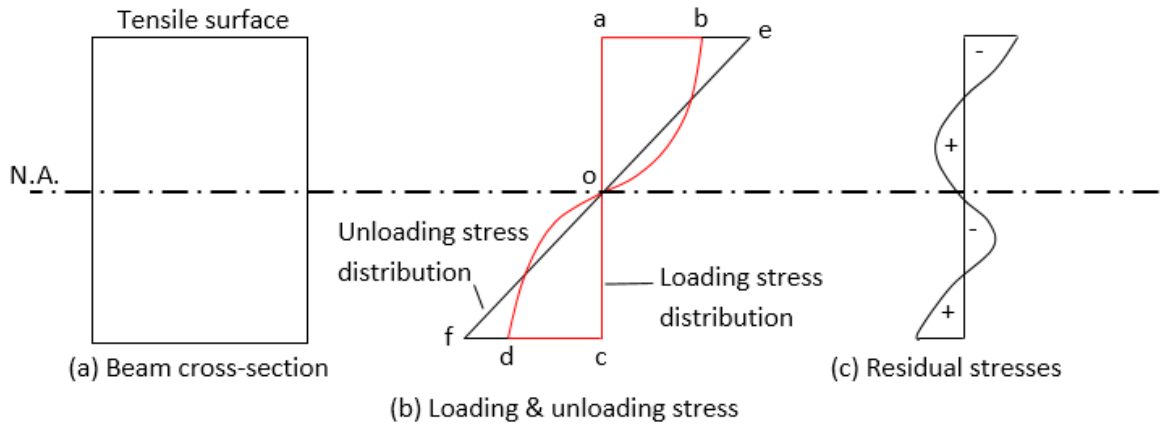

Figure 2.43 Residual stress produced after unloading a rectangular-section beam constructed from strain-hardening material loaded to a partially plastic state. The remaining residual stress produced after unloading is given in (c). Figure adapted from [121]

2.5 Strain Measurement

Linear strain (ε) is a measure of deformation in a material and is expressed as a ratio of extension (ΔL) against initial length (L) [119]:

$$\varepsilon = \Delta L/L \tag{2.17}$$

In the elastic regime, strains generated in four-point bending can be accurately predicted using elastic bending theory as described previously. In the plastic regime, the response is non-linear, and equations based on linear elasticity are no longer valid. To overcome this, strain can be determined by direct measurement, typically using electrical resistance strain gauges, or with computer modelling techniques such as finite element modelling (FEM). Since electrical resistance strain gauges are limited to measuring local strains at the point of application, alternative techniques such as Digital Image Correlation (DIC) can be employed to determine a *full-field* strain distribution over the entire surface of the test specimen. Strain measurement using full-field technology gives a more complete

picture of surface strain distribution than can be practically achieved with strain gauges alone. Electrical resistance strain gauges, DIC and FEM will now be described in the context of strain measurement in four-point bending.

2.5.1 Electrical Resistance Strain Gauges

Strain gauges work on the principal that the resistance of a metal changes when it is stretched or compressed [119]. General purpose strain gauges are typically made from copper-nickel or nickel-chrome alloy wire, arranged in a grid pattern on the surface of an electrically insulating base (Figure 2.44).

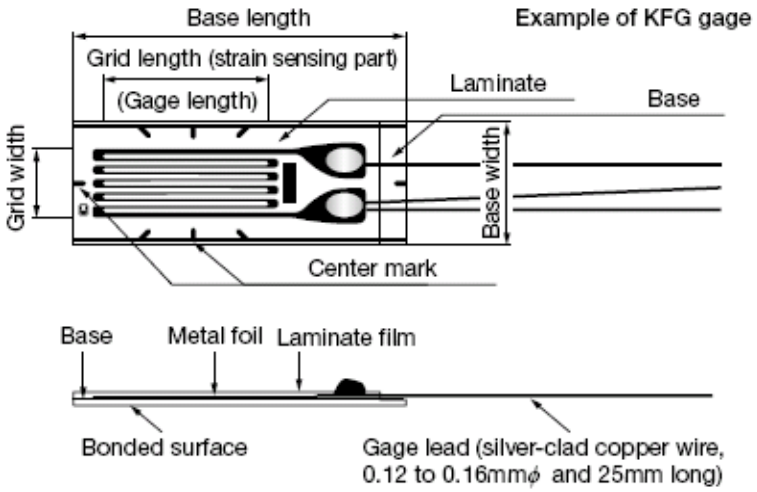

Figure 2.44 Structure of a typical electrical resistance strain gauge [124]

The strain gauge is bonded to the surface of the test specimen with a specially designed adhesive such as cyanoacrylate. When a force is applied to the test specimen, expansion and contraction is transferred directly to the gauge through the adhesive and the insulating base. When the gauge wire stretches, its resistance increases, and when the wire contracts, its resistance decreases. The resistance change is measured through a bridge circuit to give a voltage that is directly proportional to strain.

2.5.1.1 Gauge Misalignment Errors

Strain gauges are used to set the loading strain of four-point bend SSC test specimens by measuring the strain along the principal axis on the tensile test surface. Since the strain gauges are manually attached to the specimens, it is important to understand the errors associated with gauge misalignment. For a single strain gauge in a biaxial strain field (e.g. only subjected to a longitudinal strain and a transverse strain due to Poisson's effect), the magnitude of misalignment error depends upon the gauge misalignment angle (β), the ratio between the maximum and minimum principal strains, and the angle between the maximum principal strain axis and the aligned strain gauge direction (ϕ) [125,126]. The corresponding error in strain indication due to angular misalignment is defined as:

$$n = \frac{\varepsilon_1 - \varepsilon_2}{2}\left[\cos 2(\phi \pm \beta) - \cos 2\phi\right] \quad (2.18)$$

Where:

n = misalignment error
ε_1 = maximum principal strain
ε_2 = minimum principal strain
ϕ = gauge angle measured from principal axis
β = misalignment angle

The polar strain diagram in Figure 2.45 shows a biaxial strain field superimposed on the axis of a biaxial strain gauge rosette misaligned by angle β. The distance to the boundary along any radial line is proportional to the normal stain along the same line. Since the boundary of the polar strain diagram is relatively flat near the axis of maximum and minimum principal strains, there is little difference in strain for small angular misalignments (β) compared to the strain on the principal axis. Hence misalignment errors only become significant at angles around 45° to the principal axis where the slope of the polar strain diagram is very steep.

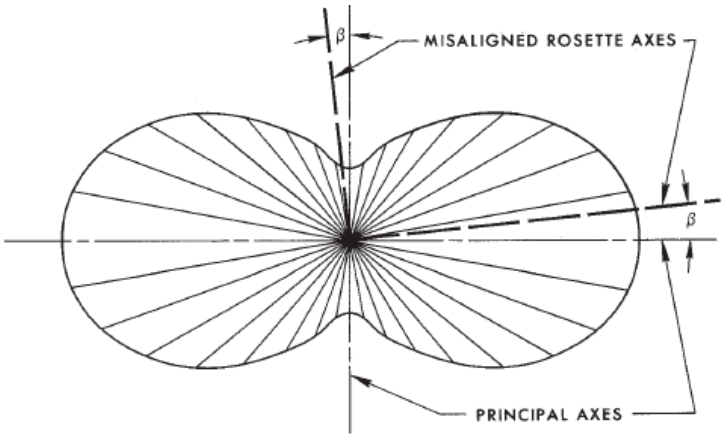

Figure 2.45 Biaxial strain field with rosette axes misaligned by angle β from the principal axis [125]

2.5.2 Digital Image Correlation

Digital Image Correlation (DIC) was first developed in the 1980s [127] and is now a well-established and effective non-contact technique used extensively in experimental mechanics in a range of applications such as characterising material behaviour, measuring the evolution and uniformity of strain, mapping strain fields around features and defects, crack tip and crack propagation studies, dynamic vibrational analysis, high temperature measurement and FE validation [128]. DIC has been used to obtain stress-strain curves from uniaxial tensile tests as an alternative to using an extensometer with proven accuracy and reliability with the additional benefit of being able to measure local necking strain which cannot be determined from the traditional method [129, 130]. The technique is capable of measuring strains in excess of 500% [127].

DIC is an optical technique that works by comparing images of a test piece at different stages of deformation and tracking blocks of pixels to measure surface displacement, which is used to build 2D or 3D full-field deformation and strain maps.

Figure 2.46 shows an example of DIC used to map the strain distribution in a weld loaded in four-point bending.

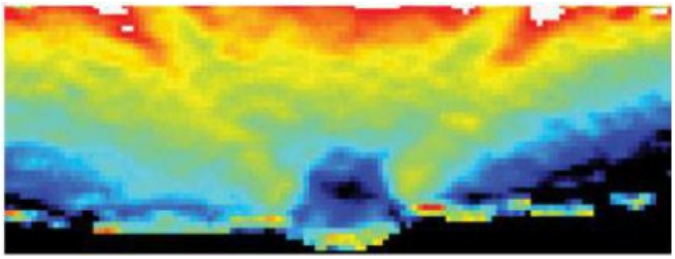

Figure 2.46 DIC used to map the strain distribution in a weld loaded in four-point bending [128]. Red indicates regions of high strain and blue indicates regions of low strain

Strain and displacements are measured by tracking the movement of a random speckle pattern applied to the surface of a test piece from digital images acquired during loading. The analysis itself is performed by a sub-pixel registration algorithm and the most commonly used algorithms include: the correlation coefficient curve-fitting method, the Newton-Raphson iteration method and the gradient-based methods, having resolutions ranging from 0.5 to 0.01 pixels [128]. The Newton-Raphson method is reported to be the most accurate algorithm but is much slower than the other approaches [131].

The sub-pixel registration algorithms track the greyscale intensity pattern in a small area called a subset (Figure 2.47) before and after deformation. A cross-correlation term (c) is used to measure the similarity between the reference image and the deformed image [129].

$$c(\Delta x, \Delta y) = \sum_{x=-n}^{n} \sum_{y=-n}^{n} I_1(x, y) I_2(x + \Delta x, y + \Delta y) \tag{2.19}$$

Where:
c = cross-correlation term
$I_1(x, y)$ = the pixel intensity in the subset before deformation
$I_2(x + \Delta x, y + \Delta y)$ = the pixel intensity in the subset after deformation

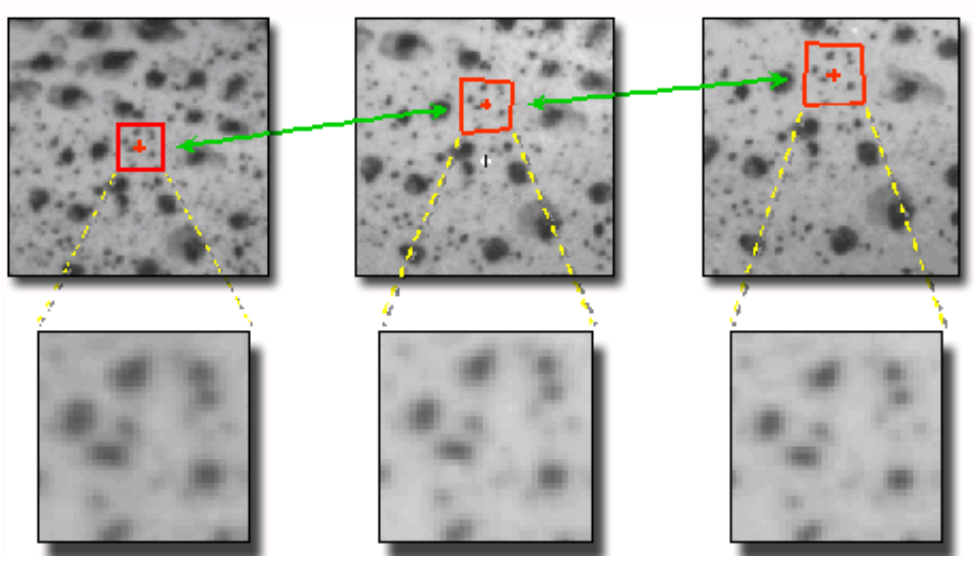

Figure 2.47 Movement of pixels in subset (red box) during deformation [132]

The normalised correlation term (Equation 2.20) defines the maximum correlation coefficient $c'(\Delta x, \Delta y)$ which is equal to or close to one [129]. When $c'(\Delta x, \Delta y) = 1$, the greyscale distribution of the two subsets are identical. DIC uses the maximum correlation coefficient to track a point during deformation. This process is repeated for a large number of subsets to obtain a full-field data map of displacement and deformation.

$$c'(\Delta x,\ \Delta y) = \frac{\sum_x \sum_y I_1(x, y) I_2(x + \Delta x, y + \Delta y)}{\sqrt{\sum_x \sum_y I^2_1(x, y) I^2_2(x + \Delta x, y + \Delta y)}} \tag{2.20}$$

The DIC system can be used to measure 2D or 3D displacements and strain. Two-dimensional analysis uses a single digital camera to provide an x-y map of axial and transverse displacements and strain on a planar surface. Sutton *et al*. [133] showed that the 2D-DIC imaging system is sensitive to out-of-plane motion with in-plane strain errors; however, 3D-DIC stereovision systems can simultaneously measure all three components of displacement without introducing in-plane displacement errors. For 3D analysis, a

stereoscopic camera pair is used to acquire images of the test sample from two different viewing angles (Figure 2.48). In addition to displacement and strain, measurements of shape (contour) can be made by calculating the position of all the subsets in the speckle pattern within the camera coordinates, when fitted to an arbitrary plane in the specimen.

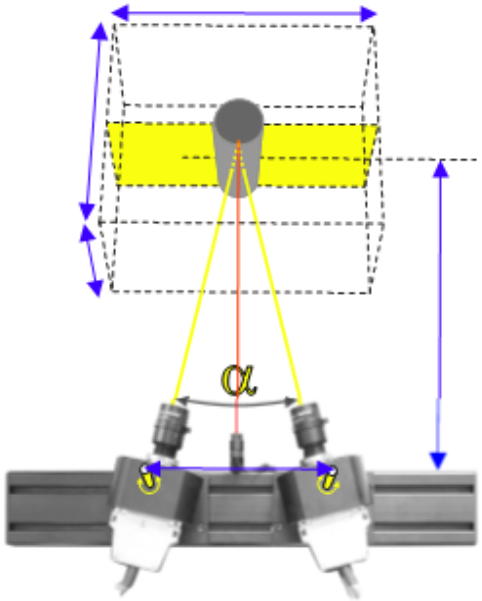

Figure 2.48 Stereoscopic camera pair setup used for 3D DIC measurements [134]

Factors associated with experimental setups, such as the quality of lighting, camera noise, lens distortion, the scale and type of pattern or coating on the test piece, will degrade the images and affect the accuracy of the DIC calculations [128]. The absolute strain resolution depends on the digital image resolution (number of pixels in the image), specimen surface area, the distance between the camera and the specimen, the focal length of the lens and the average spacing of the speckle applied to the surface of the specimen. Image resolution and specimen surface area can be related to the area that a single pixel occupies in an image (ζ_wx ζ_h). Pixel size (ζ) decreases as resolution increases, and increases as specimen dimensions increase [135].

$$\varsigma_w = \frac{w}{c} \qquad \varsigma_h = \frac{h}{r} \tag{2.22}$$

Where:

ς_w = pixel width (mm/pixel) — ς_h = pixel height (mm/pixel)

w = specimen width (mm) — h = specimen height (mm)

c = number of pixel columns in the image — r = number of pixel rows in the image

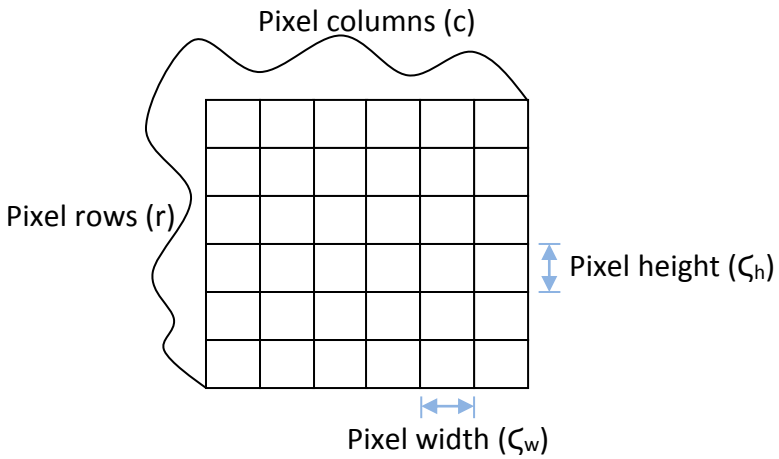

Figure 2.49 Definition of pixel height & width in a digital image. Figure adapted from Cintron *et al*. [135]

The distance between the camera and the specimen depends on the specimen dimensions; a larger specimen area will require a longer distance between the camera and the specimen. The focal length is the distance between the optical centre of the lens and the focal point on the surface of the charge-coupled device (CCD) when the specimen is in focus. The effectiveness of the speckle pattern is related to the quantity of pixels per black speckle, and a good speckle pattern must be random with a considerable quantity of black speckles of different shape and size [135].

2.6 Finite Element Modelling

Many practical engineering problems can be described in terms of partial differential equations whereby the function involved depends on two or more independent variables. Typically, these problems cannot be solved by classical analytical methods so the finite element method was developed as a numerical technique that can be used to approximate solutions to the partial differential equations with a high degree of accuracy [136]. In the finite element method, the component under investigation is modelled and divided into a finite number of smaller elements, with simple and regular shapes, interconnected at common points called nodes. The accuracy of the finite element solution depends on the number of elements. As more elements are used, the accuracy of the solution approaches that of the differential equation.

2.6.1 Elastic Stiffness Matrix

For stress analysis problems, the *stiffness* or *displacement* method is generally used. This method assumes that nodal displacements are the unknown variables which are related to nodal forces by a stiffness matrix in its formulation.[13] The basic equation for the entire model can be expressed by a *global stiffness equation* [137]:

$$\{F\} = [K]\{U\} \tag{2.23}$$

Where:
{F} = column vector of global nodal forces
[K] = Global stiffness matrix, determined by geometry, material and elemental properties
{U} = Column vector of nodal displacements

[13] Alternatively, the *force* method can be used to find the nodal displacements from an assumed stress distribution.

The modelling process can be generalised into five steps, which are summarised below in terms of a 3D stress-analysis using the stiffness/displacement method [137].

2.6.1.1 Discretization and Element Selection

Discretization describes the meshing process, which is aided by automatic mesh generators in the Computer Aided Engineering (CAE) package. In three-dimensional analysis, the basic solid elements used are hexahedral (8 nodes), tetrahedral (4 nodes) and wedge elements (6 nodes), as shown in Figure 2.50 [138]. The solid elements in ABAQUS[14] can be used for linear analysis and complex non-linear analyses involving contact, plasticity and large deformations [139]. There is often a trade-off between elements being small enough to attain accurate results, yet large enough to reduce computational cost. Hexahedral elements are generally used for stress analysis and are the most cost effective in terms of computing power; nonetheless, complex geometries can be easily meshed using tetrahedral elements or a combination of element types. Finite elements are offered with first-order (linear) and second-order (quadratic) interpolation.

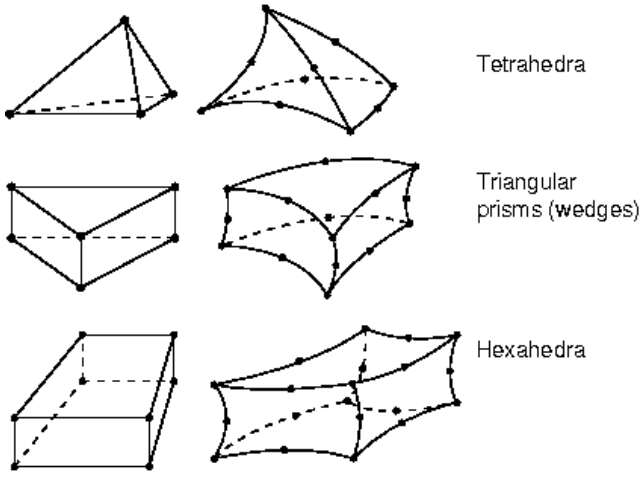

Figure 2.50 First-order linear (left) & second-order quadratic (right) elements used in ABAQUS [138]

[14] ABAQUS is a commercial finite element software package

Fully integrated *first-order* elements are poor at representing the linear through-thickness stress variation in bending because the Poisson effect causes shearing at the integration points, which locks the elements and results in an overly-stiff response (i.e. Shear locking). *Second-order* elements capture stress concentrations more effectively than first order elements and are also effective in bending dominated problems; the additional nodes capture stress gradients which would otherwise require a very fine mesh of first-order elements. However, second-order elements are computationally more expensive than first-order elements.

Reduced integration first-order elements help reduce running time (i.e. it's more cost effective) and can make certain analyses, with complex stress fields, more stable. However, since first order, reduced integration elements only have one integration point, it is possible that they distort in such a way that the calculated strains are all zero, resulting in uncontrollable distortion of the mesh, with unstable and inaccurate solutions. This is termed *hourglassing* and is prevented by adding artificial stiffness to the element using *enhanced hourglass control*. While enhanced hourglass control offers good bending behaviour in linear elastic materials, it may give overly stiff responses to problems displaying plasticity in bending [138].

First-order tetrahedral elements are generally avoided for stress analysis problems as they tend to be overly stiff and exhibit slow convergence with mesh refinement [138]. For practical reasons, it is sometimes necessary to use tetrahedral and wedge elements to fill

arbitrarily shaped regions of a hexahedral mesh, but this may require a finer mesh (at higher computational cost) to obtain accurate results.

2.6.1.2 Displacement Function Selection

Each element is defined by a discrete number of nodes situated on the boundary of the element. The displacement function describes the three Gaussian displacement components, in a Cartesian coordinate system, at each node of the element. The shape (or interpolation) functions map the geometry of each element to the global co-ordinate system. For example, the displacement function for a linear hexahedral element, with eight corner nodes (Figure 2.51), is given by equations 2.24 and 2.25 [137].

$$\begin{Bmatrix} u \\ v \\ w \end{Bmatrix} = \sum_{i=1}^{8} \left(\begin{bmatrix} N_i & 0 & 0 \\ 0 & N_i & 0 \\ 0 & 0 & N_i \end{bmatrix} \begin{Bmatrix} u_i \\ v_i \\ w_i \end{Bmatrix} \right) \tag{2.24}$$

Where N_i defines the shape functions and u_i, v_i and w_i are nodal displacements [137]:

$$N_i = \frac{(1+ss_i)(1+tt_i)(1+z'z'_i)}{8} \tag{2.25}$$

Equations 2.24 and 2.25 define the unknown Gaussian displacements (*u*-*v*-*w*) when parallel to the global (*x*-y-z) coordinate system. The shape functions map the local (*s*-*t*-*z'*) coordinates of any node on the element to the global (*x*-*y*-*z*) coordinate system and have the property that N_i is equal to 1 at node *i* and 0 at all other nodes (i.e. $-1 \leq (s,t,z') \leq 1$).

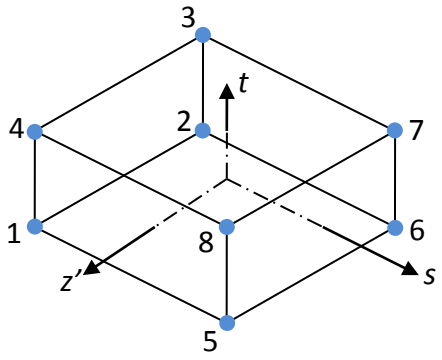

Figure 2.51 Linear hexahedral element with local *s-t-z'* coordinates attached. Adapted from [137]

2.6.1.3 Defining the Strain/Displacement & Stress/Strain Relationships

These relationships are required for deriving the element stiffness matrix in the proceeding step. The element strains and the stress-strain relationship for a three-dimensional, infinitesimal element are given by equations 2.26 and 2.27 [137].

$$\{\varepsilon\} = \begin{Bmatrix} \varepsilon_x \\ \varepsilon_y \\ \varepsilon_z \\ \gamma_{xy} \\ \gamma_{yz} \\ \gamma_{zx} \end{Bmatrix} = [B]\{d\} \qquad \& \qquad \{\sigma\} = \begin{Bmatrix} \sigma_x \\ \sigma_y \\ \sigma_z \\ \tau_{xy} \\ \tau_{yz} \\ \tau_{zx} \end{Bmatrix} = [D]\{\varepsilon\} \tag{2.26}$$

Where [B] is the strain/displacement matrix, expressed as a function of s-t-z' coordinates, {*d*} is a column matrix of all unknown nodal displacements for the element and [D] is a matrix describing linear elastic constitutive equations based on Hooke's law [137].

$$[D] = \frac{E}{(1+\nu)(1-2\nu)} \begin{bmatrix} 1-\nu & \nu & \nu & 0 & 0 & 0 \\ & 1-\nu & \nu & 0 & 0 & 0 \\ & & 1-\nu & 0 & 0 & 0 \\ & & & 1-2\nu/2 & 0 & 0 \\ & & & & 1-2\nu/2 & 0 \\ \text{symmetry} & & & & & 1-2\nu/2 \end{bmatrix} \tag{2.27}$$

2.6.1.4 Deriving the Element Stiffness Matrix [k]

The stiffness matrix equations are developed using the *principle of virtual work*. The principle of virtual work states that the work done by a set of forces in equilibrium moving through a set of small, compatible displacements is zero. For deformable bodies, the total virtual work (δW) consists of the sum of external virtual work (δW_{ext}) and internal virtual work (δW_{int}) [140]:

$$\delta W = \delta W_{int} + \delta W_{ext} \tag{2.28}$$

Equation 2.28 must hold for any virtual displacements and corresponding virtual strains that satisfy the displacement boundary conditions and is fundamental in the finite element method for giving approximate solutions for displacement, stress and strain. The behaviour of individual elements is described by the element stiffness equation:

$$\{f\} = [k]\ \{u\} \tag{2.29}$$

Where:
$\{f\}$ = column vector of elemental nodal forces
$[k]$ = Element stiffness matrix, determined by geometry, material and elemental properties
$\{u\}$ = Column vector of unknown element nodal displacements

2.6.1.5 Element Equation Assembly to Obtain Global Equations

This step adds all the individual element equations (2.29) together to obtain the global stiffness equation described by Equation 2.23. The global stiffness matrix [K] in the global stiffness equation is a singular matrix because its determinant is equal to zero. To remove this singularity, boundary conditions are imposed on the model to hold it in place and avoid it moving as a rigid body [137]. Following this step, the final stage of the analysis

consists of solving the equations to obtain the unknown variables at each node (i.e. displacement). Secondary variables such as stress and strain can be determined as they can be directly expressed in terms of displacement.

2.6.2 Elastic-Plastic Analysis

Plasticity models are written as *rate-independent* models, where the response does not depend on the rate of deformation (typical of metals at temperatures well below their melting temperature and at low strain rate), or as *rate-dependent* models, where the response does depend on the rate at which the material is strained (e.g. simple metal creep models). Even during plastic deformation, an elastic component of strain continues to accompany the plastic strain [122]. The basic assumption of elastic-plastic models is that the total deformation can be divided into an elastic part and a plastic part [138]. Plasticity occurs when stress (σ) exceeds the yield stress (σ_y):

$$\sigma - \sigma_y > 0 \tag{2.31}$$

The increment of equivalent plastic strain ($\Delta\varepsilon_{eq}^{pl}$) is obtained explicitly through [141]

$$\Delta\varepsilon_{eq}^{pl} = \frac{\sigma - \sigma_y}{3G + H} \tag{2.32}$$

Where $H = \delta\sigma_y / \delta\varepsilon_{eq}^{pl}$ is the plastic hardening at the beginning of the increment and $G = E/2(1+\nu)$ is the shear modulus. The equivalent plastic strain at time $t + \Delta t$, after defining the incremental plastic strain from equation 2.32, is updated by:

$$\Delta\varepsilon_{eq}^{pl}new = \varepsilon_{eq}^{pl}old + \Delta\varepsilon_{eq}^{pl} \tag{2.33}$$

2.6.3 Modelling the Four-Point Bend Test

The finite element method has been used to study the stress distribution on specimens loaded in four-point bending. The following sections describe where finite element modelling has been used to represent beams loaded in four-point bending. Both parent and welded specimens are considered.

2.6.3.1 Parent Specimens

Huurman and Pronk [142] describe the four-point bend test for determining the stiffness moduli of pavement (asphalt concrete) materials. A 3D FE model of a beam measuring 450x50x50 mm, using quadratic 20-node brick elements is presented. In the 3D simulation, four-point loading is applied directly to the upper and lower surfaces by displacing the nodes 0.1 mm in the vertical direction at the inner loading points and constraining the nodes at the outer support points. This method introduces larger stresses at the locations where the beam is displaced and constrained (Figure 2.52).

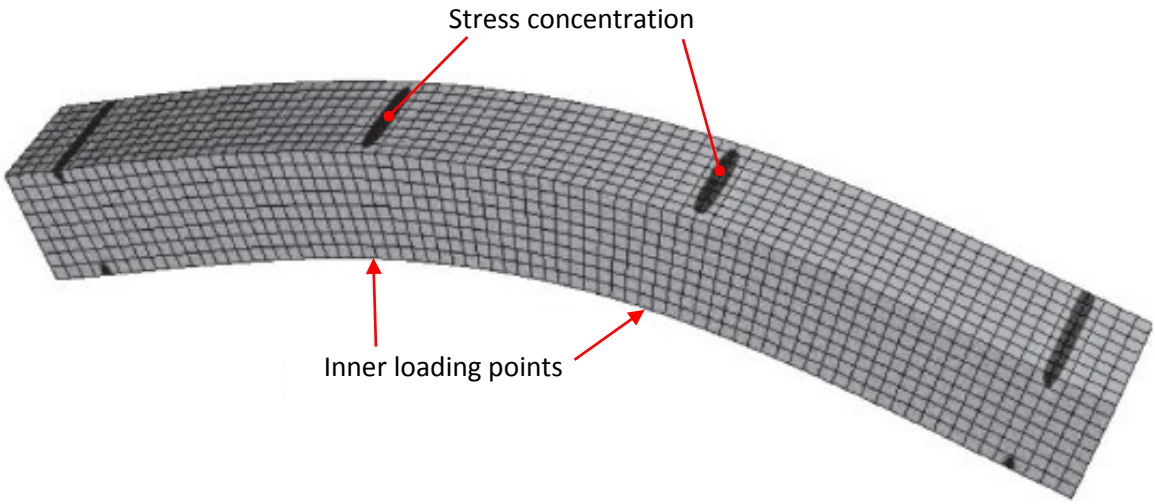

Figure 2.52 Stress concentration at the loading points on the surface of a 3D beam. Loading by displacement of nodes at the inner loading points (130 mm centres) and constraining nodes at the outer support points (400 mm centres) [142]

Figure 2.52 indicates that the vertical stress introduced at the outer supports is uniform over the width of the beam. At the location of the inner loading points, the distribution is not uniform, with significantly smaller stresses introduced at the edges of the beam (Figure 2.53). This phenomenon can be explained by the anticlastic bending effect described previously [117].

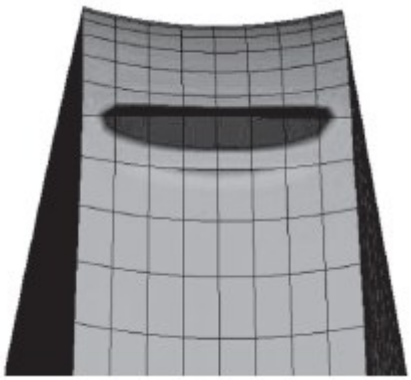

Figure 2.53 Non-uniform stress distribution over the width of the tensile surface at the inner loading point where nodes have been displaced by 0.1 mm. Stresses introduced at the edges of the beam are lower due to the change in cross-sectional shape. Deformations are exaggerated by a factor of 4000 [142]

Zhai *et al.* [143] modelled the stress distribution on the tensile surface of a flat four-point bend specimen with homogeneous material properties (no welded joint) and investigated the influence of inner-roller spacing (t), outer-roller spacing (L) and specimen thickness (h). The FE models (Figure 2.54) showed that a t/h ratio between 1.2 and 1.5 provided a region of uniform stress between the inner rollers with small peak stresses at the roller positions. A t/h ratio of 3 shifts the maximum stress to the inner rollers, whereas a t/h ratio between 0.5 and 1 gives a large stress gradient from the inner rollers to the mid-point of the beam. In terms of roller spacing, when the L/t ratio is less than 3, peak stresses are generated at the roller positions.

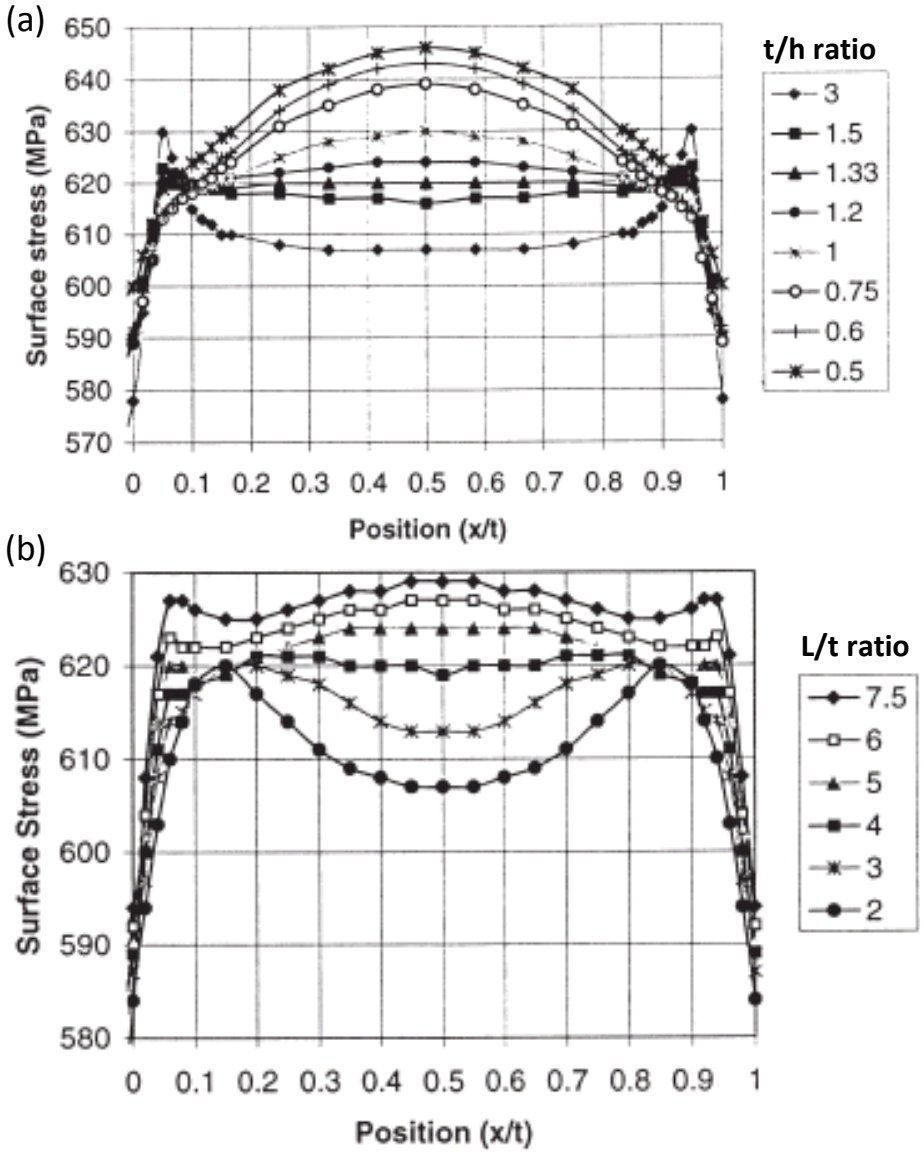

Figure 2.54 Stress distributions corresponding to different ratios of (a) inner roller spacing 't' to specimen thickness 'h' and (b) outer-roller spacing 'L' to inner roller spacing 't'. Depending upon the ratio, peak stresses can be generated on the tensile surface at the inner-roller positions [143]

Lube *et al*. [144] identified the peak stresses on the tensile surface at the inner roller positions as *wedging stresses* caused by friction at the loading points between the roller and the specimen. These wedging stresses can give rise to out-of-plane moments and additional axial forces acting on the beam, which lead to additional tensile stresses on the tensile surface as shown in Figure 2.55.

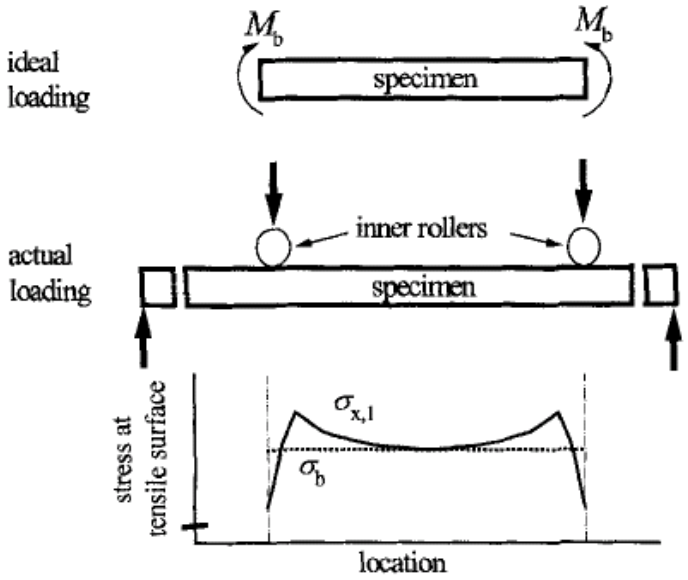

Figure 2.55 Wedging stresses generated on the tensile surface of a beam: solid curve ($\sigma_{x,1}$) represents actual loading stresses whereas the dotted curve (σ_b) represents simple beam theory and pure bending [144]

2.6.3.2 Welded Specimens

The introduction of a weld into the beam can have a significant effect on the load-displacement response, particularly if the yield strength of the weld metal is lower than that of the parent material; i.e. the weld metal is under-matched [115]. Amaya *et al*. [145] showed that high stress concentrations are generated in the heat-affected zone (HAZ) near the fusion line when a 13%Cr stainless steel specimen welded with under-matched (22%Cr duplex stainless steel) consumable was loaded in four-point bending. The finite element model in this work was based on a specimen machined with a rectangular cross-sectional area.

Nimmo *et al.* [115] modelled the strain distribution on the surface of a 13%Cr four-point bend specimen with matching weld filler. Two models were analysed: one with both surfaces machined flat and one with only the compressive surface (weld cap) machined flat

to keep the weld root intact. The work highlighted that the weld-root profile influenced the strain distribution on the tensile surface, particularly in the transverse direction. Pipes are often misaligned during welding and this can potentially influence the stress distribution on the surface of root-intact welded four-point bend specimens [116,146]. Turnbull & Nimmo [116] observed that pipe misalignment becomes problematic when root-intact welded specimens are machined on the compressive face as this leads to a step change in thickness and depending on the magnitude of the step, can result in non-uniform straining with the thinner section more heavily deformed.

Bosch *et al*. [147] investigated the stress distribution in full-thickness four-point bend specimens containing a longitudinal weld. The 2D finite element simulation (Figure 2.56) demonstrated that stress concentrations up to 28% occurred in the HAZ. This was validated with strain gauge measurements and showed that the surface stress distribution in full-thickness four-point bend specimens is comparable to the stress distribution in a pipe under pressure, in field operation as well as in a full-scale test. Two dimensional simulations can be plane strain or plane stress analysis; the latter was employed in the reported example.

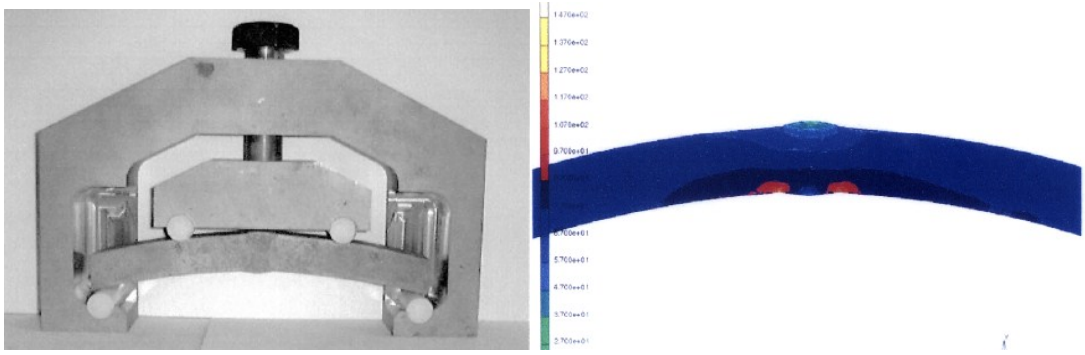

Figure 2.56 FEA of full-thickness four-point bend specimen containing a longitudinal weld. The FE simulation showed that stress concentrations of up to 28% occurred in the HAZ. Strain gauge measurements recorded stress concentrations of up to 23% in the same area [147]

CHAPTER 3: SCOPE OF WORK

The primary aim of this EngD project was to validate the results of a scoping investigation made by Bodycote Corrosion Centre in 2005 which suggested that a girth-welded 13%Cr supermartensitic stainless steel pipe was more susceptible to SSC when exposed to seabed temperatures below 24 °C. This EngD project compares the SSC resistance of a weldable 13%Cr supermartensitic stainless steel pipeline material at 5 °C and 24 °C using the four-point bend loading method. The existing test method was developed to control critical test parameters such as dissolved oxygen and solution pH to ensure that the SSC tests could be accurately performed to the requirements of EFC17 [7]. All SSC test work presented in this thesis was carried out at Exova Corrosion Centre. Part of this work has been published in NACE 2013 conference paper 2589.

A secondary aim of this project was to investigate the suitability of the four-point bend loading method for assessing the SSC resistance of corrosion resistant alloys. This aim was accomplished utilising strain-gauged flexural bend test specimens, full-field digital image correlation and finite element modelling. It should be noted that complexities such as specimen geometry (fully-machined and as-received), specimen thickness, roller friction and edge preparation (chamfers and fillet radii) were considered in this investigation. The results of this research project are presented in the following chapters:

- Chapter 5: Test Material Characterisation
- Chapter 6: Sulphide Stress Cracking Investigation
- Chapter 7: Stress & Strain Investigation of the Four-Point Bend Test

3.1 Test Material Characterisation

Nippon Steel & Sumitomo Metal Corporation supplied the weldable 13%Cr supermartensitic stainless steel pipeline material used in this investigation. Chapter 5 presents the results of the material characterisation tests performed on the parent material and includes microstructural analysis, retained austenite measurements, tensile properties (at 5 °C, 24 ° C and 130 °C), impact toughness, surface roughness and hardness measurements. This work was used to identify material-related factors that could influence SSC resistance at seabed temperatures.

3.2 Sulphide Stress Cracking Investigation

The Sulphide Stress Cracking Investigation in Chapter 6 interrogates the test method used to perform SSC tests on corrosion resistant alloys and improves this method by control of critical test parameters such as dissolved oxygen and solution pH. Published test results (See domain diagrams in Figure 2.28) were used to define the room temperature SSC limits for UNS S41426 13%Cr supermartensitic stainless steel. These high strength 110 ksi (758 MPa) grades are commonly used for down-hole tubular applications and represent the majority of SSC tests described in the literature. Since UNS S41426 is chemically similar to the weldable 13%Cr grade used in this EngD project, these domain diagrams were used to set the test parameters for the SSC tests using the region marked as *Needs Further Assessment*:

- 70 mbar H_2S at pH 4.5 in simulated Produced Water environments.
- 35 mbar H_2S at pH 4.5 in simulated Produced Water environments.
- 70 mbar H_2S at pH 3.5 in simulated Condensed Water environments.

All SSC tests were performed at 5 °C and 24 °C using the four-point bend loading method on as-received (retaining the inner bore pipe surface as the test face) and fully-machined (rectangular cross-section and ground to a 600 grit finish) specimens. Figure 3.1 shows a typical test setup:

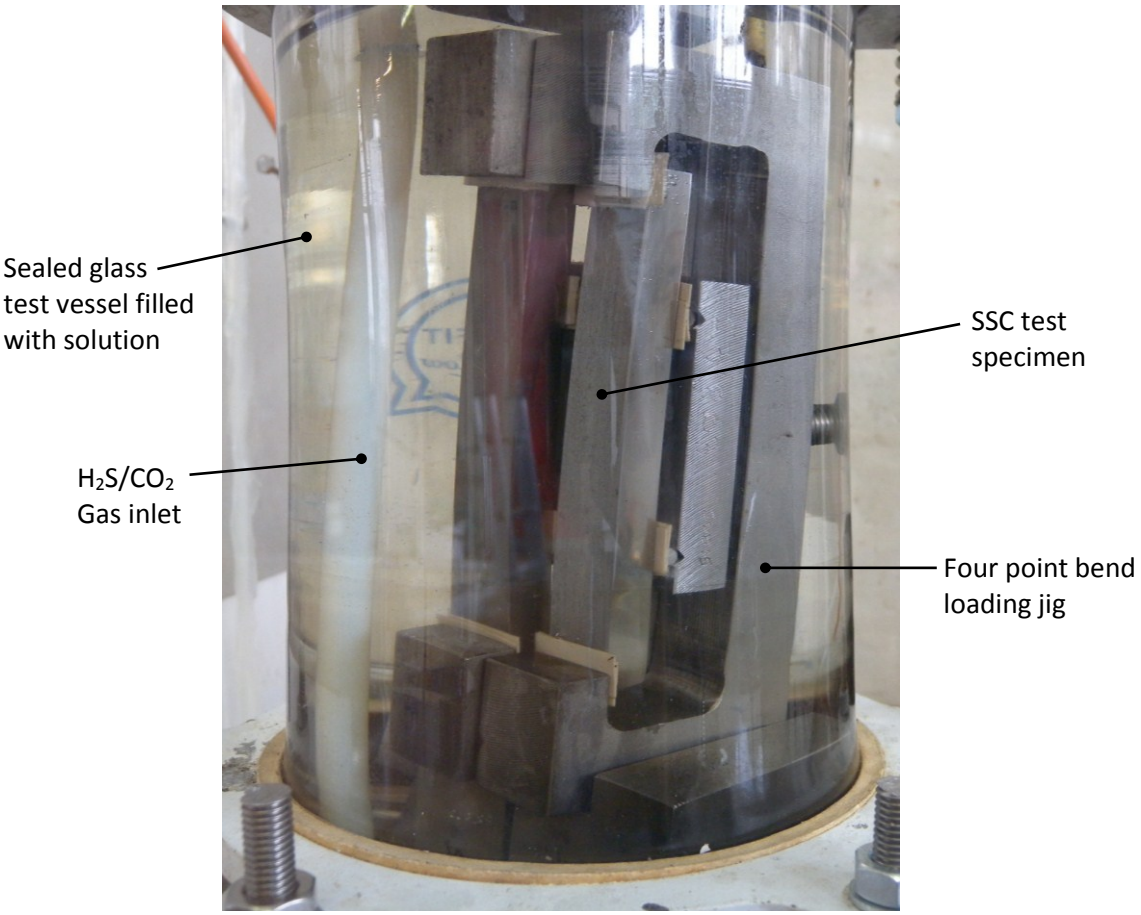

Figure 3.1 Four-point bend SSC test specimens inside a test vessel

The results and discussion for the Sulphide Stress Cracking Investigation presented in Chapter 6 is divided into three main sections:

- Verification of the Scoping SSC Tests.
- SSC Test Protocol Development & Modification.
- Seabed Temperature SSC Investigation.

3.2.1 Verification of the Scoping SSC Tests

Verification tests were performed in the first year of this EngD project to explore the existing SSC test method used by Bodycote Corrosion Centre for testing corrosion resistant alloys. The SSC tests were performed to verify the preferential low temperature cracking observed by Bodycote in 2005 [3]. Table 3.1 details the number of tests conducted during this investigation.

Table 3.1 Scoping SSC test matrix

Specimen	QTY	Test temperature (°C)	Test Environment	pH	H_2S partial pressure (mbar)
As-received	3	24	Produced Water (165 g/l NaCl, bicarbonate buffer)	4.5	70
Fully machined	2				
As-received	3	5			
Fully machined	2				
As-received	3	24			38
Fully machined	2				
As-received	3	5			
Fully machined	2				
As-received	3	24	Condensed Water (1.65 g/l NaCl, 400mg/l acetate, HCl)	3.5	70
Fully machined	2				
As-received	3	5			
Fully machined	2				

3.2.2 SSC Test Protocol Development & Modification

EFC17 [7] recommends that oxygen levels must remain below 10 ppb in the test solution and that pH must remain within a ±0.1 tolerance throughout the SSC test. Based on the observations made during the verification SSC tests performed in the first year, it was necessary to develop the existing test method to provide accurate control of these variables. Figure 3.2 shows the steps taken in the development phase:

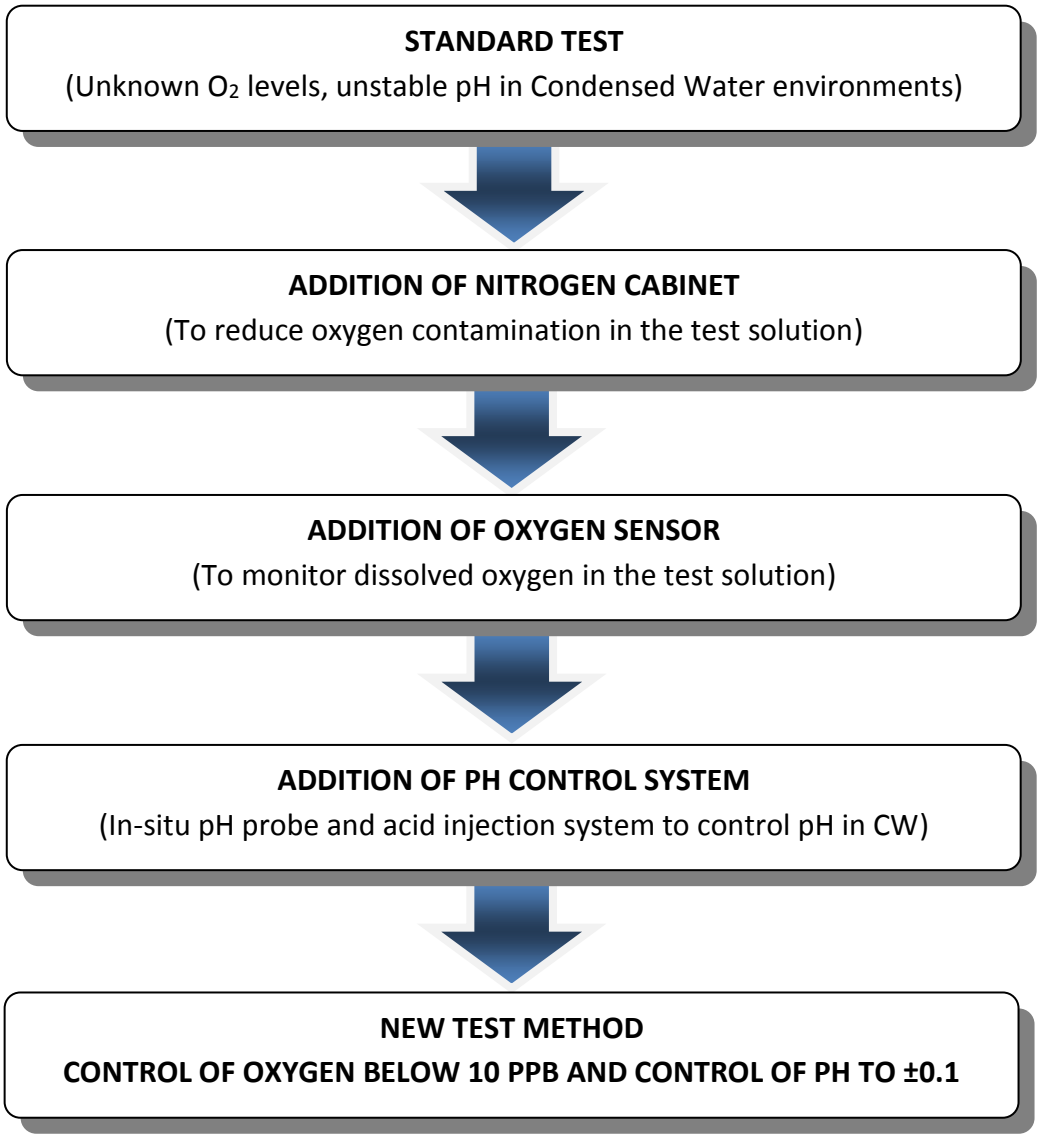

Figure 3.2 Steps taken during the SSC test protocol development and modifications phase

Omura *et al*. [30] showed that placing the test vessel inside a nitrogen chamber is an effective safeguard for minimising oxygen contamination of the test solution. This idea was used for the test rig development and was improved by adding an H_2S-resistant oxygen probe to the test cell for in-situ oxygen monitoring during the SSC test. Furthermore, a pH probe was also added to monitor solution pH during the test. The problem of pH drift in simulated Condensed Water solutions was overcome by designing an acid injection system

capable of adjusting pH during the SSC test without introducing oxygen into the system. Additional development work included re-designing the existing four-point bend SSC loading jig to improve strain stability over the 30 day test period and investigating the solubility of H_2S in simulated produced and Condensed Water environments at temperatures in the range of 5 °C to 25 °C.

3.2.3 Seabed Temperature SSC Investigation

The contracted work for Nippon Steel & Sumitomo Metal Corporation is presented in the Seabed Temperature SSC Investigation. With the controls in place from the Improved SSC test protocol development and modification phase, further SSC tests were performed to investigate the SSC resistance of the weldable 13%Cr supermartensitic stainless steel pipe material. The test programme is outlined in Table 3.2. In addition to the SSC tests, corrosion coupons were included in the test solution to assess the material's susceptibility to pitting corrosion without an applied stress.

Table 3.2 Seabed Temperature SSC Investigation test matrix

Specimen	QTY	Test temperature (°C)	Test Environment	pH	H_2S partial pressure (mbar)
As-received	2	24	Produced Water (165 g/l NaCl, bicarbonate buffer)	4.5	69
Fully machined	2				
As-received	2	5			
Fully machined	2				
As-received	2	24			35
Fully machined	2				
As-received	2	5			
Fully machined	2				
As-received	2	24	Condensed Water (1.65 g/l NaCl, 400 mg/l acetate, 0.5% acetic acid)	3.5	69
Fully machined	2				
As-received	2	5			
Fully machined	2				

3.3 Stress & Strain Investigation of the Four-Point Bend Test

The stress and strain distribution of parent weldable 13%Cr supermartensitic stainless steel test specimens loaded in four-point bending is presented in Chapter 7. This shows how specimen cross-section, specimen thickness, roller friction and edge preparation (chamfers and fillet radii) influences stress and strain concentrations which can potentially influence SSC results when using the four-point bend loading method. The FE work was backed up with strain measurements from flexural bend test specimens and through the use of digital image correlation. This work consists of three sections:

- Flexural Bend Tests.
- Tensile & Flexural-Bend Test Comparison.
- Full-Field stress & Strain Analysis.

3.3.1 Flexural Bend Tests

The existing flexural bend test facility at Exova Corrosion Centre was limited to test temperatures below 100 °C. Commercial projects requiring flexural bend tests at 196 °C prompted a development phase to increase Exova's testing capabilities. Therefore, as part of this EngD project, a new flexural bend test rig was designed with a custom built heat chamber capable of accurately controlling the ambient test temperature from 24-200 °C. This rig was used to perform the range of four-point flexural bend tests detailed in Table 3.4 and Table 3.5, with the exception of the 5 °C tests which were carried out at the University of Birmingham using a liquid nitrogen cooled test chamber.

Table 3.3 Flexural bend test matrix

QTY	Test Temp (°C)	Orientation from pipe	Specimen Size (mm) (L x W x D)	Rollers	
				Ø (mm)	Spacing (inner/outer)
3	130	Longitudinal	130x20x10	10	60 / 120 mm
4	5				
4	24				
4			130x20x5		
4			130x20x2.5		
3	24	Transverse	70x20x4		30 / 60 mm

Table 3.4 Flexural bend test matrix for error assessment (24 °C)

QTY	Error	Orientation from pipe	Specimen Size (mm) (L x W x D)	Rollers	
				Ø (mm)	Spacing (inner/outer)
1	Control specimen	Longitudinal	130x20x10	10	60 / 120 mm
2	Gauge misalignment (β)				
1	Specimen misalignment (θ)				

3.3.2 Tensile & Flexural-Bend Test Comparison

This section uses finite element analysis to explain why the 0.2% offset strain determined from a tensile test is lower than the 0.2% offset strain determined from a four-point flexural bend test. EFC17 [7] stipulates that corrosion resistant alloys are loaded to 100% of the actual yield stress (AYS) for SSC testing so that specimens are loaded to a nominal value of 0.2% plastic strain in tension. If tensile SSC test specimens are used, then this strain can be set directly from the 0.2% offset strain determined from a uniaxial tensile stress-strain curve on the same material. If four-point bend specimens are used for the SSC tests, then there are two options: use the same 0.2% offset strain generated from a uniaxial

tensile stress-strain curve or use the 0.2% offset strain determined from a flexural bend load-strain curve. To date there is controversy within the industry over which offset strain to use for SSC specimens loaded in four-point bending.

NACE MR0175 / ISO 15156-3 [4] specifies the use of tensile stress-strain data to determine the value of strain at 100% AYS for use with four-point bend specimens. This approach has been questioned and actively discouraged in the literature as it reportedly leads to an underestimation of the total strain needed to achieve 0.2% plastic strain in bending [116]. For this reason, some oil and gas companies prefer to use flexural bend test data to set the loading strain for four-point bend SSC/SCC test specimens as it is a more conservative approach.[15]

3.3.3 Full-Field Stress & Strain Analysis

The final part of this project investigates the stress and strain distribution on the tensile test surfaces of fully-machined (flat surface) and as-received (concave surface) four-point bend specimens. It would be impractical and expensive to use strain gauges to create full-field maps of strain on the surfaces of the test specimens, so finite element analysis (FEA) was used to generate contour maps of stress and strain for the two geometries. FEA was also used to investigate how frictional forces at the loading rollers influences stress and strain concentrations on the test surface and how edge preparation (chamfering and fillet

[15] This is an active area of investigation for NACE task group TG494. Part of the work presented in this thesis has contributed to this topic.

radii) influences stress and strain concentrations at the edges. The models were validated with strain gauge measurements and full-field Digital image correlation (DIC) measurements.

Table 3.5 Finite element modelling test matrix

Geometry	Symmetry	Friction	Edge Geometry
Fully-machined (rectangular cross-section)	Quarter	0.7	90°
		0.5	
		0	
		0	15° x 1 mm chamfer
			45° x 1 mm chamfer
			75° x 1 mm chamfer
			0.5 mm radius
			1.0 mm radius
			2.0 mm radius
As-received (retains pipe curvature)	Quarter	0	90°
			45° x 1 mm chamfer
			0.5 mm radius
Condensed Water test specimen	Half	0	As measured from the actual test specimen

CHAPTER 4: EXPERIMENTAL PROCEDURE

4.1 Material Characterisation

Nippon Steel & Sumitomo Metal Corporation supplied a one meter section of seamless pipe for this research project (Figure 4.1). The pipe was classified as an API 5LC Grade LC80-130S weldable 13%Cr supermartensitic stainless steel with an outer diameter of 323.9 mm and wall thickness of 12.7 mm. The internal and external surfaces were alumina blasted and cleaned with a two-stage (H_2SO_4, HF/HNO_3 mix acid) pickling process. Table 4.1 shows the chemical composition of the test material, determined from Optical Emission Spectroscopy.

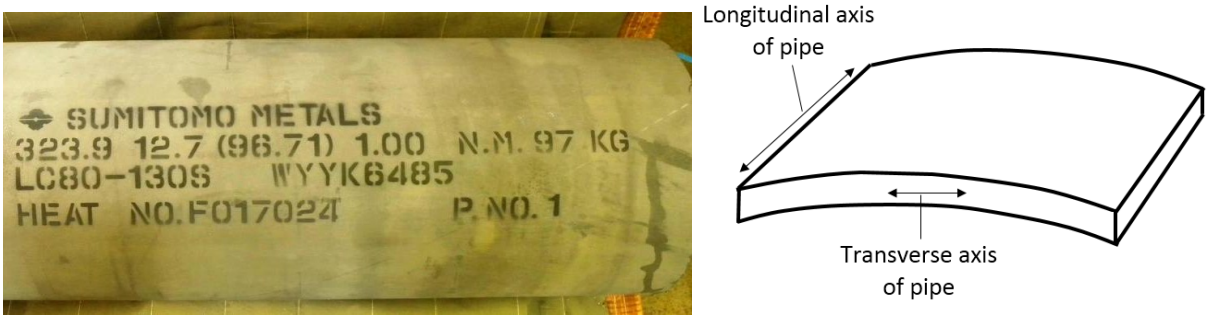

Figure 4.1 Pipe material used for test work with definition of longitudinal and transverse axes

Table 4.1 Chemical composition of LC80-130S

Element	wt.%	Element	wt.%	Element	wt.%	Element	wt.%
C	0.01	S	<0.005	Al	0.028	Ti	0.15
Si	0.23	Cr	12	B	<0.001	V	0.03
Mn	0.42	Mo	2.47	Cu	0.04	N	0.007
P	0.015	Ni	6.41	Nb	<0.01		

4.1.1 Microstructure

Specimens were cut from the supplied pipe to investigate the microstructure in the longitudinal and transverse orientations as defined in Figure 4.1. Each specimen was wet ground to a 1200 grit finish with silicon carbide paper then polished to a 1 µm diamond finish. Microstructures were revealed using the etchants listed in Table 4.2 and examined under an optical microscope.

Table 4.2 Etchants used in the investigation

Etchant	Composition	Purpose	Procedure
Vilella's	5 ml HCl 1 g Picric acid 100 ml Ethanol	Reveals martensite, less aggressive than Marbles and Acidified Ferric Chloride	Swabbed for one minute
Marbles	10 g $CuSO_4$ 50 ml HCl 50 ml H_2O	Reveals martensite but more aggressive than Vilella's	Swabbed for 2 seconds
Acidified Ferric Chloride	300 g FeCl 100 ml HCl 1000 ml H_2O	Good contrast between austenite grains. More aggressive than Vilella's	Swabbed for 2 seconds

4.1.2 Retained Austenite

Since the SSC resistance of 13%Cr stainless steels is believed to be influenced by the amount of retained austenite in the tempered martensitic microstructure [98,99], x-ray diffraction (XRD) was used to determine the volume percent of retained austenite in the test material. The tests were carried out on a Philips X'Pert diffractometer at 24 °C using Cu Kα radiation and generator settings of 40 kV and 40 mA. A scan range of $40° \leq 2\theta \leq 120°$ was employed with a 2θ step interval of 0.02°. The focal spot was 1 mm x 1 mm and the depth of x-ray penetration was estimated to be approximately 2 µm [148]. X-ray diffraction patterns and integrated intensities were determined using Philips X'Pert "Highscore" software.

Ten specimens measuring 20x10x5 mm were prepared from transverse sections of the supplied pipe then wet-ground and polished to a 6 µm diamond finish for this investigation. Each specimen was etched in Vilella's reagent and examined under a light microscope for signs of heat effects or surface deformation which could potentially transform retained austenite to martensite near the surface. Following the visual examination, the specimens were re-polished for XRD analysis.

The volume percent of retained austenite was determined by comparing the integrated Cu Kα XRD intensities of ferrite and austenite phases with theoretical integrated intensities. Since the theoretical intensities for martensite and ferrite are nearly the same, the theoretical intensities for martensite were calculated assuming a body-centred cubic cell (α-ferrite). Calculating the theoretical integrated intensity (R) of martensite and austenite requires knowledge of the lattice parameter (a_o) for each phase. Since the lattice parameter is directly proportional to the spacing (d) of any particular set of lattice planes, the Bragg angle θ was measured for each set of lattice planes to determine d:

$$d = \frac{\lambda}{2\sin\theta} \tag{4.1}$$

Where:
λ = 1.541838 Å (weighted average) for Cu Kα radiation [148]

The lattice parameter (a) for each plane was then determined using the relationship:

$$a = d\sqrt{h^2 + k^2 + l} \tag{4.2}$$

Where:
$h^2 + k^2 + l^2$ = quadratic form of Miller indices taken from standard tables [148]

The 'a' values were plotted against $\sin^2\theta$ and extrapolated to $\sin^2\theta = 1$ to give an accurate value of a_o for each phase. Assuming near random crystallographic orientation, the theoretical integrated intensities (R) for austenite and martensite was calculated using the formula [149]:

$$R^{hkl} = \frac{(/F/^2 pLPe^{-2M})}{v^2} \tag{4.3}$$

$/ F /^2$ is the *structure factor* multiplied by its complex conjugate and describes the intensity of the beam diffracted by all the atoms of the unit cell in a direction predicted by the Bragg law. The structure factor for body-centred cubic ferrite is $F = 2f$ and for face-centred cubic austenite is $F = 4f$ [148]. Atomic scattering factors ($f = f_o + \Delta f' + \Delta f''$) take into account spatial distribution of electrons in the atom and are obtained from standard tables [150]. The structure factor $/ F /^2$ for ferrite and austenite are:

$$\text{Ferrite:} \quad / F /^2 = 4[(f_{fe} + \Delta f' + \Delta f'')(f_{fe} + \Delta f' - i\Delta f'')] \tag{4.4}$$

&

$$\text{Austenite:} \quad / F /^2 = 16[(f_{fe} + \Delta f' + \Delta f'')(f_{fe} + \Delta f' - i\Delta f'')] \tag{4.5}$$

The term (p) is the *multiplicity factor* which is the number of different (hkl) planes in a form that have the same spacing. *LP* is the *Lorentz Polarization factor* which is a geometrical factor obtained from tables [148]. The temperature factor (e^{-2M}) allows for thermal vibration of the atoms and is found by the relation:

$$M = B\frac{\sin^2\theta}{\lambda^2} \tag{4.6}$$

Where:
B = 0.355 [149]

The final parameter in the theoretical integrated intensity equation is the volume of the unit cell (*v*) and is defined as the cube of the lattice parameter (a_o).

The percentage volume of retained austenite is estimated from measurements of integrated intensities (Iα & Iγ) assuming that martensite and austenite are the only phases present. In contrast to the Reference Intensity Ratio (RIR) method, which is based on measuring the intensity of one or more peaks for each phase and the added internal standard, the whole diffraction pattern was considered giving an analysis that is averaged over all of the peaks and is less susceptible to errors associated with preferred orientation.[16] The method used is outlined in detail by Dickson [151] as an extension to the direct comparison method:

$$\frac{C\gamma}{C\alpha} = \left[\frac{1}{n\gamma}\sum_{0}^{n\gamma}\frac{I\gamma}{n\gamma}\right] \div \left[\frac{1}{n\alpha}\sum_{0}^{n\alpha}\frac{I\alpha}{n\alpha}\right] \qquad (4.7)$$

Where:

γ= austenite
α = ferrite (martensite)
C = volume fraction of the particular phase
I = measured integrated intensity
n = number of measured (*hkl*) reflections
R = theoretical integrated intensity

From the calculated value of Cγ/Cα, the volume fraction of retained austenite (C_γ) was found from the relationship Cγ + Cα = 1:

$$C\gamma = \left[\frac{C\gamma}{C\alpha}\right] \div \left[1 + \frac{C\gamma}{C\alpha}\right] \qquad (4.8)$$

[16] This is necessary as the pipe making process will impart a degree of crystallographic texture to the material

4.1.3 Tensile Tests

Uniaxial tensile tests were performed to define yield strength, ultimate tensile strength and Young's Modulus using standard ASTM A370 round specimens [152]. Both longitudinal (Ø=8.75 mm, Gauge = 35 mm) and transverse (Ø=6.25 mm, Gauge = 25 mm) specimens were tested at 24 °C and 130 °C[17] using an Instron screw driven tensile tester. Only longitudinal specimens were tested at 5 °C using a DMG screw driven tensile tester fitted with a liquid-nitrogen-cooled temperature controlled enclosure (Figure 4.2).

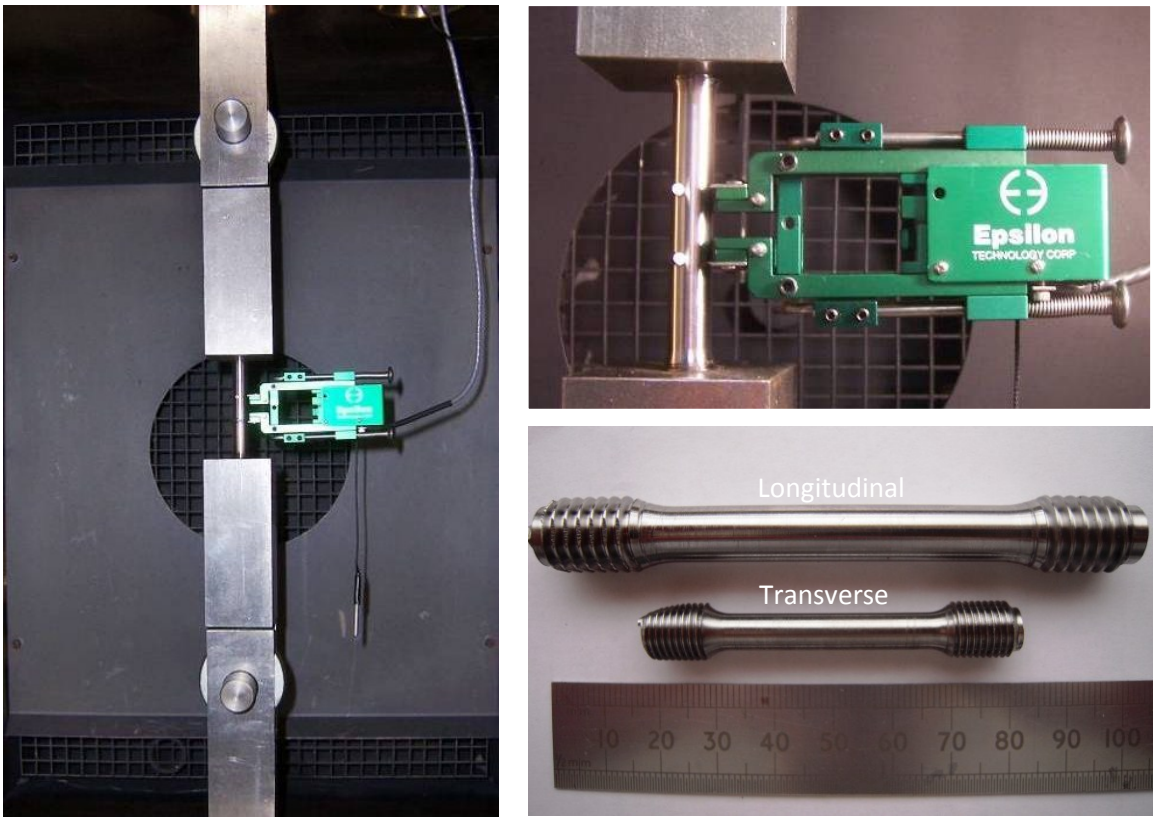

Figure 4.2 Tensile testing in a temperature controlled enclosure. Inserts show extensometer used and examples of longitudinal and transverse test specimens.

[17] 130 °C is representative of a typical in-service operating temperature for a supermartensitic pipeline [116].

4.1.4 Impact Toughness

Charpy impact tests were performed using the method described in ASTM standard E23 [153]. Thirty-three specimens measuring 55x10x10 mm were cut from a longitudinal section of the supplied pipe and wet-ground to a 600 grit finish. Tests were performed in triplicate at each temperature in the range of -196 °C to +22 °C. Plots were made of impact energy versus temperature and percentage shear versus temperature to determine the ductile-brittle transition temperature (DBTT).

4.1.5 Surface Roughness

Nine surface roughness (Ra) measurements were made across the surfaces listed below using a Surtronic 3+ surface profiler. The average value was reported:

1. **Inner Bore**: This is the alumina blasted surface which is retained on the *as-received* four-point bend SSC test specimens.
2. **Ground surface**: The inner bore surface was ground using a 120 grit automatic grinding tool in the same way the scoping SSC test specimens were prepared for strain gauge application (Section 4.2.4.1).
3. **600 grit finish**: wet-ground to represent a *fully-machined* four-point bend SSC test specimen surface.

4.1.6 Surface Imaging

A JEOL 6060 scanning electron microscope (SEM) was used to image the fracture surfaces of Charpy impact specimens and the as-received, 120 grit and 600 grit surfaces used in the surface roughness measurements. The SEM was operated at an accelerating voltage of 20 kV, in secondary electron mode at a working distance of 10 mm.

4.1.7 Microindentation Hardness Measurements

Hardness tests were made using a Mitutoyo MVK-H1 hardness testing machine with a Vickers indenter and a load of 200 grams-force (1.96 N). Vickers hardness was determined by measuring the mean diagonal length of the indentation as defined in ASTM standard E384 [154]:

$$HV = 0.0018544 \times P/d^2 \quad (4.9)$$

Where:
HV = Vickers hardness number
P = Load (N)
d = Mean diagonal length of indentation (mm)

A sample was cut from transverse section of the supplied pipe, wet ground to a 1200 grit finish with silicon carbide paper and polished to a 1 µm diamond finish. Sixty-four micro-hardness measurements were taken across the thickness of the pipe sample at 0.2 mm intervals from the outer surface to the inner bore.

4.1.8 Nanoindentation Hardness Measurements

Nanoindentation hardness measurements were made using a NanoTest system which has load and displacement resolutions of 100 nN and 0.1 nm, respectively. Indentations were made using a three-sided Berkovich indenter and measured as a mean contact pressure (H).[18] This was converted to Vickers hardness (HV) using the following equation:

$$HV = 94.495 \times H \quad (4.10)$$

[18] The mean contact pressure is the peak load (mN) divided by the projected area of contact. The projected area of contact is determined by the geometry of the indenter and the depth of contact.

Two specimens were prepared with different surface finishes: one with an as-received pipe surface and the other with a surface ground to a 120 grit finish using an automatic grinding tool. Both specimens were nickel plated, mounted in conductive Bakelite and the transverse faces were polished to a 1 µm finish. The purpose of the nickel plating was to protect the specimen from rounding at the edges during polishing, as this would influence the hardness measurements.

Forty nanoindentation hardness measurements were made on the polished face of each specimen in a 10x4 grid pattern. The four rows were spaced approximately 10 µm apart to a depth of approximately 40 µm from the surface; however the exact location of the indents relative to the surface was determined under a microscope after testing (see Figure 4.3). In addition to the near-surface measurements, five indentations were made in the substrate, approximately 5 mm from the surface, for comparison with the Vickers Microindentation hardness measurements.

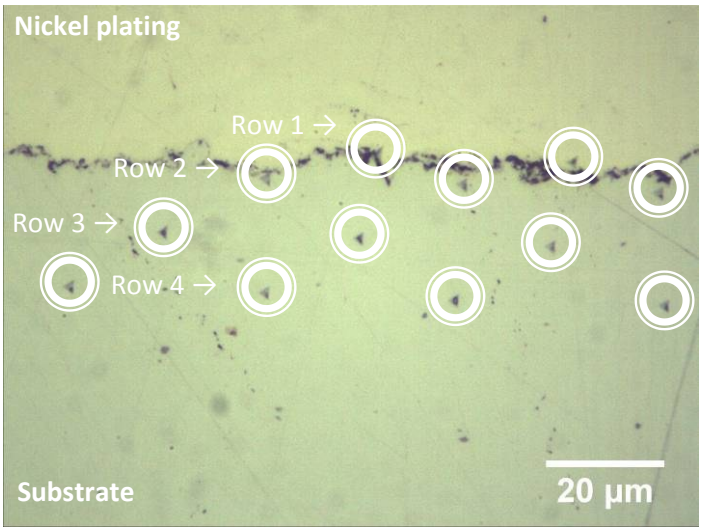

Figure 4.3 Indentations made on the cross-section of specimen with as-received surface. The specimen was nickel plated to protect the edges from rounding during the polishing procedure.

4.2 Sulphide Stress Cracking Investigation

4.2.1 SSC Test Specimen Geometry

All the four-point bend SSC specimens were prepared from the longitudinal orientation of the parent pipe and tested in the as-received or fully-machined surface condition. Figure 4.4 details the two types of specimen used: The as-received specimens measured 130x20x12.7 mm and retained the pipe curvature (full thickness of pipe) whereas the fully-machined specimens measured 130x20x10 mm with a rectangular cross-section. All machined faces and edge chamfers (approximately 45°) were wet-ground to a 600 grit finish using silicon carbide paper and left to air-passivate for a minimum of 48 hours before exposure to the test environment.

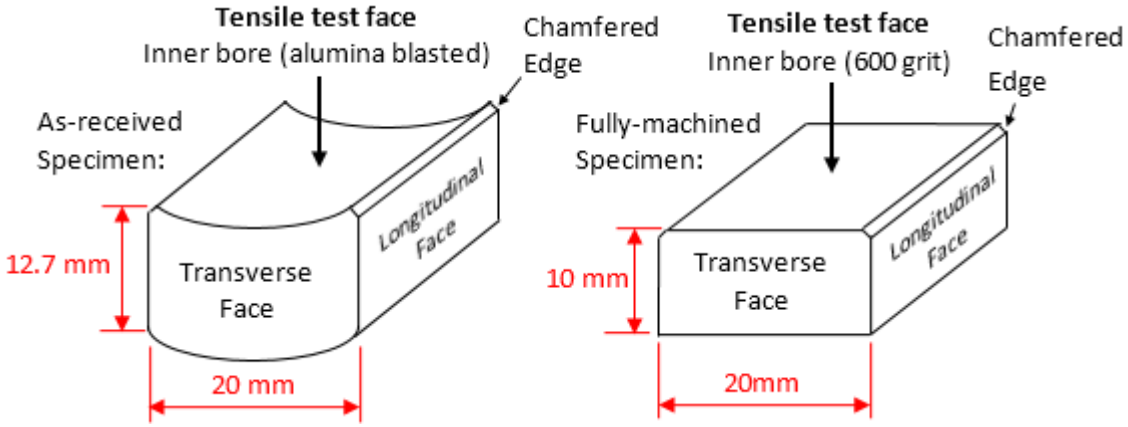

Figure 4.4 Cross-sectional geometry of as-received and fully-machined SSC test specimens

4.2.2 SSC Test Environments

The SSC tests were performed in simulated Produced Water and Condensed Water environments at 5 °C and 24 °C for 30 days with varying amounts of H_2S as described in the following sections. The Produced Water solution was prepared by dissolving 165 g/l NaCl (100,000 mg/l Cl^-) in 10 litres of de-ionised water. Following a 2 hour CO_2 gas purge, a small amount of sodium bicarbonate ($NaHCO_3$) buffer was added until the pH stabilised at 4.5. The

Condensed Water solution was prepared by dissolving 1.65 g/l NaCl (1000 mg/l Cl^-) and 400 mg/L sodium acetate (CH_3COONa) buffer.[19] Following the 2 hour CO_2 gas purge, the solution was acidified with to achieve a pH of 3.5 as described in the following sections.

Once loaded (as detailed in the following sections), the four-point bend test specimens were sealed inside the test vessel and the test solution was sealed inside a second airtight de-aeration vessel. The gas outlet from the test vessel was connected to the de-aeration vessel and the system was purged with nitrogen gas. An oxygen analyser was used to monitor the oxygen content of the test solution inside the de-aeration vessel. Once the oxygen content fell below 10 parts-per-billion (ppb), the test solution was transferred to the test vessel by creating a pressure differential between the two vessels. The test started once the H_2S/CO_2 gas mixture was added to the de-aerated solution.

4.2.3 SSC Post Test Evaluation

At the end of the test, the specimens were removed from the test vessel, flushed in de-ionised water and dried. Each specimen was examined for cracks by red dye-penetrant inspection (DPI) as detailed below:

1. The specimen is cleaned with a cloth and dedicated cleaner/remover spray
2. The red penetrant is applied by aerosol and left for 15 minutes to allow the penetrant to permeate into any cracks.
3. Excess penetrant is removed using a clean cloth, followed by a wipe with another cloth sprayed with cleaner/remover.
4. White developer is sprayed on to the specimen causing the dye to exit the crack and stain the developer, highlighting the location of cracks on the specimen.

[19] 400 mg/L sodium acetate in accordance with the second edition of EFC17

Sections were then taken through the regions containing cracks,[20] mounted in Bakelite, polished to a 1 µm finish, etched in Vilella's reagent and examined using an optical microscope at magnifications up to x1000. The quantity, length and depth of the cracks were measured and recorded using optical microscopy and "Image J" image analysis software.

4.2.4 Verification of the Scoping SSC Tests

Figure 4.5 shows the apparatus used for these tests. Note that although the solution was de-aerated with a pre-test nitrogen purge, oxygen was not monitored during the test.

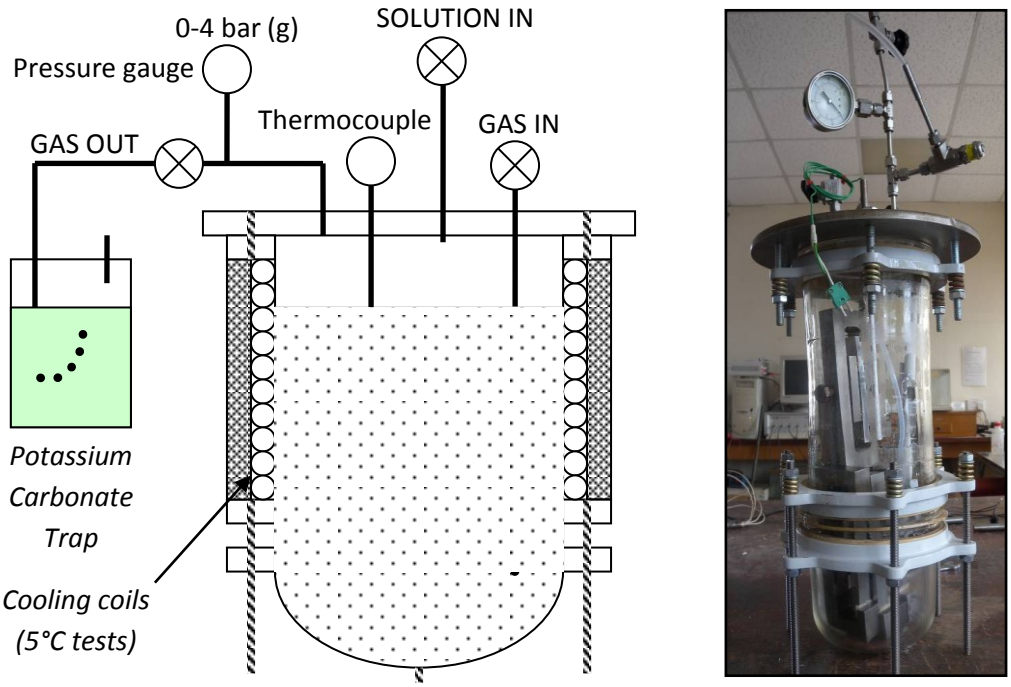

Figure 4.5 Apparatus used for the scoping SSC tests: Glass test vessel, inlet and outlet valves for solution and gas, thermocouple sensor and copper cooling coils fed from a chiller unit

These tests were performed at 70 mbar H_2S and 38 mbar H_2S using gas mixtures of 3.5% H_2S in CO_2 and 1.9% H_2S in CO_2, respectively. The test gas was continuously purged

[20] In the absence of any visible cracking, two sections were taken through the central region at the 1/3rd and 2/3rd width locations

through the solution for 30 days while maintaining a positive pressure of 1 bar (gauge) inside the test vessel. It should be noted that Hydrochloric acid (HCl) was use to acidify the Condensed Water test solution to achieve a starting pH of 3.5.

4.2.4.1 Scoping SSC Test Specimen Preparation and Loading

Each SSC test specimen was fitted with a biaxial strain gauge on the tensile face at the mid-length, mid-width position and loaded to the 0.2% offset strain determined from room temperature flexural bend tests. For the as-received specimens, a small area was ground away using an automatic grinding tool fitted with a 120 grit sanding band for stain gauge attachment. The loading jig (Figure 4.6) was made of 25%Cr duplex stainless steel (UNS S31803) for corrosion resistance in the test solution and two layers of polyether ether ketone (PEEK) were placed between the specimen and the four loading points to avoid galvanic corrosion. In this arrangement, the specimen rests on two flat edges spaced 120 mm apart and is loaded with two 5 mm diameter metallic rollers spaced 60 mm apart. The strain gauges were removed after loading by soaking in acetone.

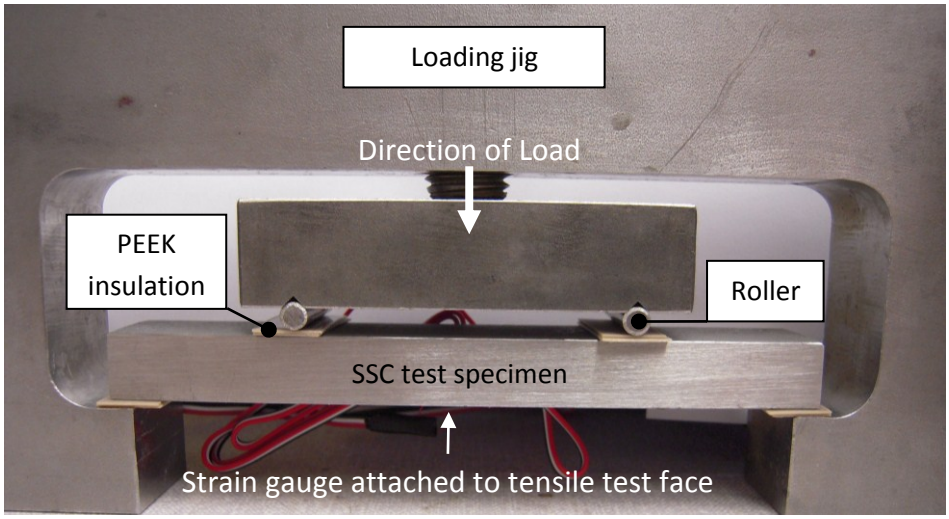

Figure 4.6 SSC test specimen in standard four-point bend loading jig, prior to loading. A biaxial strain gauge is attached to the tensile test surface of the specimen and PEEK insulation is placed between the contact points and the specimen to avoid galvanic corrosion

4.2.5 SSC Test Protocol Development & Modification

Based on the observations made during the scoping SSC tests, it was necessary to develop the existing test method to provide accurate control of dissolved oxygen and solution pH. Following this development, further SSC tests could be performed with dissolved oxygen controlled below 10 ppb in the test solution and pH controlled to a ±0.1 tolerance as defined in EFC17 [7]. Additional development work included re-designing the existing four-point bend SSC loading jig to improve strain stability over the 30 day test period and an investigation into the solubility of H_2S in simulated Produced and Condensed Water environments at temperatures in the range of 5 °C to 25 °C.

4.2.5.1 Test Rig Modifications

A new SSC test rig was designed to control and monitor dissolved oxygen and pH of the test solution. This included an Orbisphere M1100 luminescence dissolved oxygen sensor (Figure 4.7) and 410 oxygen analyser to continuously record dissolved oxygen levels for the duration of the test, a Hamilton 'ARC' pH sensor (Figure 4.8) fitted through the lid of the vessel to measure solution pH and temperature, a peristaltic pump that supplies de-aerated acetic acid to the test solution for in-situ pH control (for Condensed Water solutions), and a nitrogen chamber to house the test vessel and acetic acid reservoir.

Technical Data
Range: 0-2000 ppb
Accuracy: ±0.8 ppb or 2%, whichever is greater
Repeatability: ±0.4 ppb or 1%, whichever is greater
Limit of detection: 0.6 ppb minimum

Figure 4.7 Orbisphere M1100 luminescence dissolved oxygen sensor

Technical Data

Operating temperature range: 0-130 °C
Process pressure range: 0-6 bar
Measurement range: 0-14 pH
Measurement resolution: 0.01

Figure 4.8 Hamilton 'ARC' pH sensor

The new SSC test rig design is shown in Figure 4.9 and Figure 4.10. The idea of placing the SSC test vessel in a nitrogen chamber was developed by NPL and BP and has been shown to be effective in minimising oxygen contamination of the test solution [30]. This design also allowed the tests to be carried out at atmospheric pressure making the test easier to set up and simpler to perform. Additional design improvements included replacing all PTFE gas lines with stainless steel tubing to reduce the possibility of oxygen ingress through the material or at the seals of the fittings.

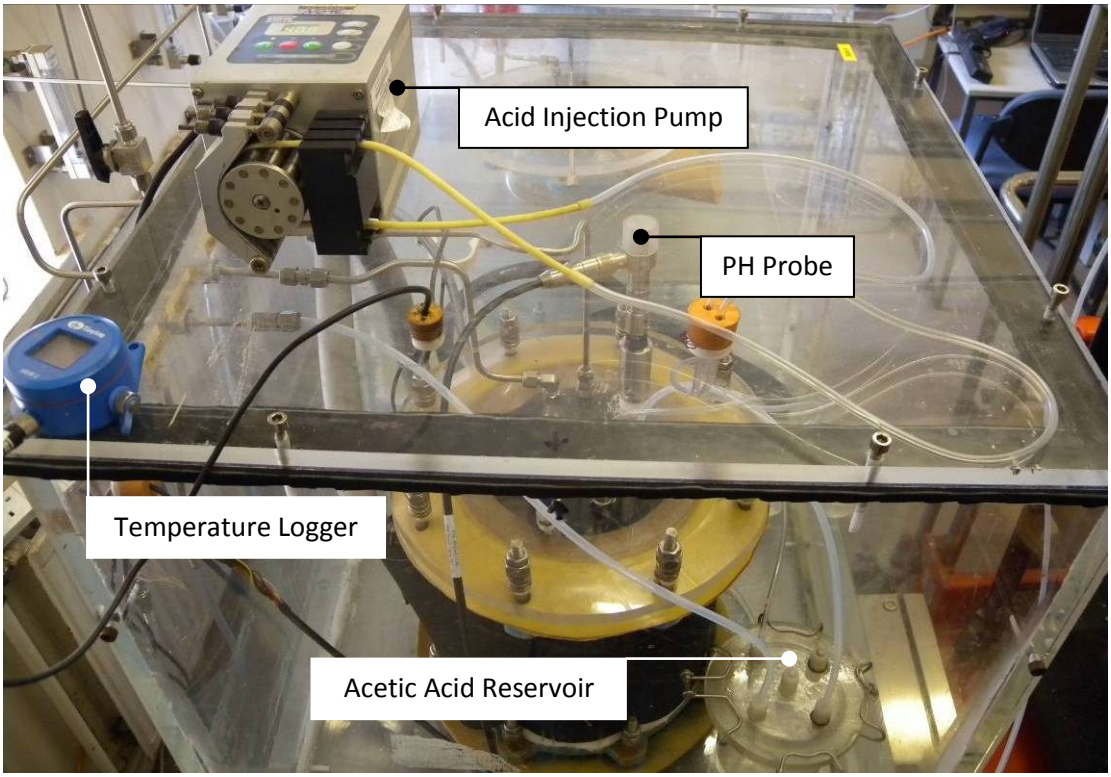

Figure 4.9 New SSC test rig incorporating a nitrogen cabinet, with O_2 and pH monitoring

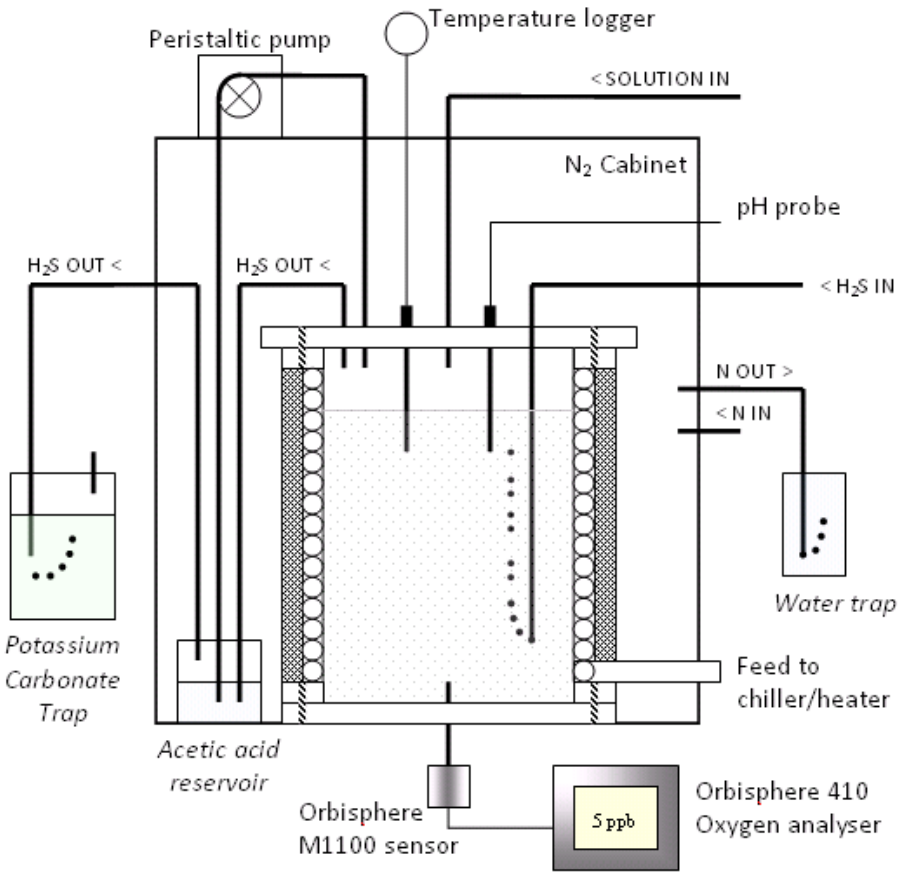

Figure 4.10 Schematic of new SSC test rig

4.2.5.2 Loading Jig Modification

The standard four-point bend loading jig used at Exova Corrosion Centre for SSC testing corrosion resistant alloys was re-designed to include four alumina rollers rather than two metallic rollers and two flat edges (Figure 4.6). The new design shown in Figure 4.11 removes the need for PEEK insulation between the rollers and the specimen and gives a more traditional four-point loading arrangement. A stiffening bar was added between the outer roller supports to reduce flexing of the rig during loading and improve strain stability. To assess the effectiveness of the new rig in maintaining constant strain on the test specimen, strain stability trials were conducted at room temperature using both new and old rigs. The trials were performed using as-received parent specimens loaded to approximately

7200 με for 30 days to mimic the length of time the test specimen would be subjected to an SSC test. Strain and temperature were recorded continuously for the duration of the trial.

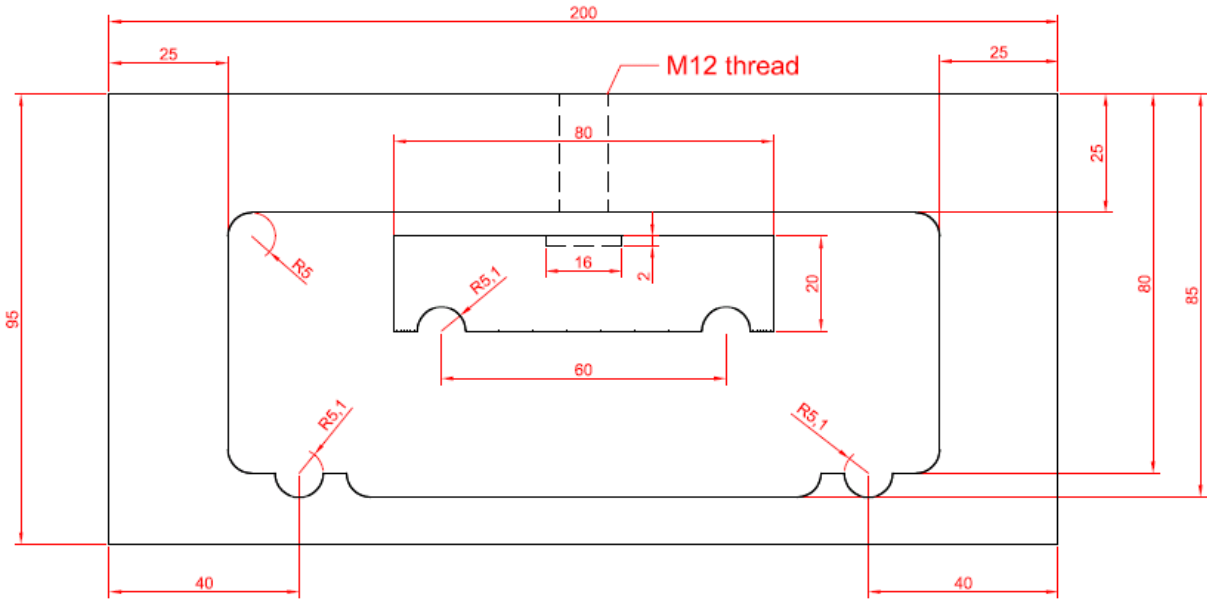

Figure 4.11 New four-point bend SSC loading jig. The jig is made from 25%Cr duplex stainless steel with four fixed points for holding alumina rollers

4.2.5.3 H_2S Solubility Measurements

Idometric titration tests were performed to measure H_2S solubility as a function of temperature and chloride concentration in Produced Water (100,000 mg/l Cl^- with $NaHCO_3$ buffer) and Condensed Water (1000 mg/l Cl^- with 400 mg/l CH_3COONa and 0.5% CH_3COOH) solutions saturated in pure H_2S at temperatures ranging from 5 °C to 25 °C. The following test method was used:

1) 10 litres of Produced Water and Condensed Water test solutions were prepared and purged with nitrogen gas in a sealed glass vessel. The solutions were chilled to the required test temperature and purged with pure H_2S gas.

2) 40 ml of 0.1 N iodine solution, 5 ml of concentrated HCl and 2 ml of starch solution was added to a conical flask and chilled to the required test temperature. 10 ml of test solution, saturated with H_2S, was extracted from the glass vessel and added to the iodine + HCl + starch solution. The mixture was titrated with 0.1 N sodium thiosulphate solution until the solution changed to a pale yellow colour. By recording the volume of sodium thiosulphate solution used, the H_2S concentration (ppm) was calculated using the following formula and the temperature of the solution was recorded after titration [155].

$$H_2S = \frac{(A - B)x17030}{C} \tag{4.11}$$

Where:
A = Normality of iodine solution x volume used (ml)
B = Normality of sodium thiosulphate solution x volume used (ml)
C = Volume of test sample (ml)

4.2.6 Seabed Temperature SSC Investigation

The SSC tests in this investigation were conducted at 69 mbar H_2S and 35 mbar H_2S at atmospheric pressure using certified gas mixtures of 6.9% H_2S in CO_2 and 3.5% H_2S in CO_2, respectively. For the Condensed Water test solutions, approximately 50 ml (0.5% wt) acetic acid (CH_3COOH) was used to achieve a starting pH of 3.5. Solution temperature, pH and dissolved oxygen levels were monitored and recorded throughout the tests.

4.2.6.1 SSC Test Specimen Preparation and Loading

In these tests, the strain gauges were applied directly to the as-received surface to avoid the damage caused by the grinding operation used in the scoping tests. The samples were loaded to 7300 με using the new loading jig (Figure 4.12) using the average 0.2% offset

strain determined from the room temperature flexural bend tests (See Section 4.3.2). Once reached, the target longitudinal strain was monitored and adjusted over a two hour period until a stable strain measurement was obtained (see strain stability test results in Chapter 6). After loading, the specimens were soaked in acetone to remove the strain gauge, degreased in an alkaline degreaser, rinsed with de-ionised water then flushed with acetone to dry.

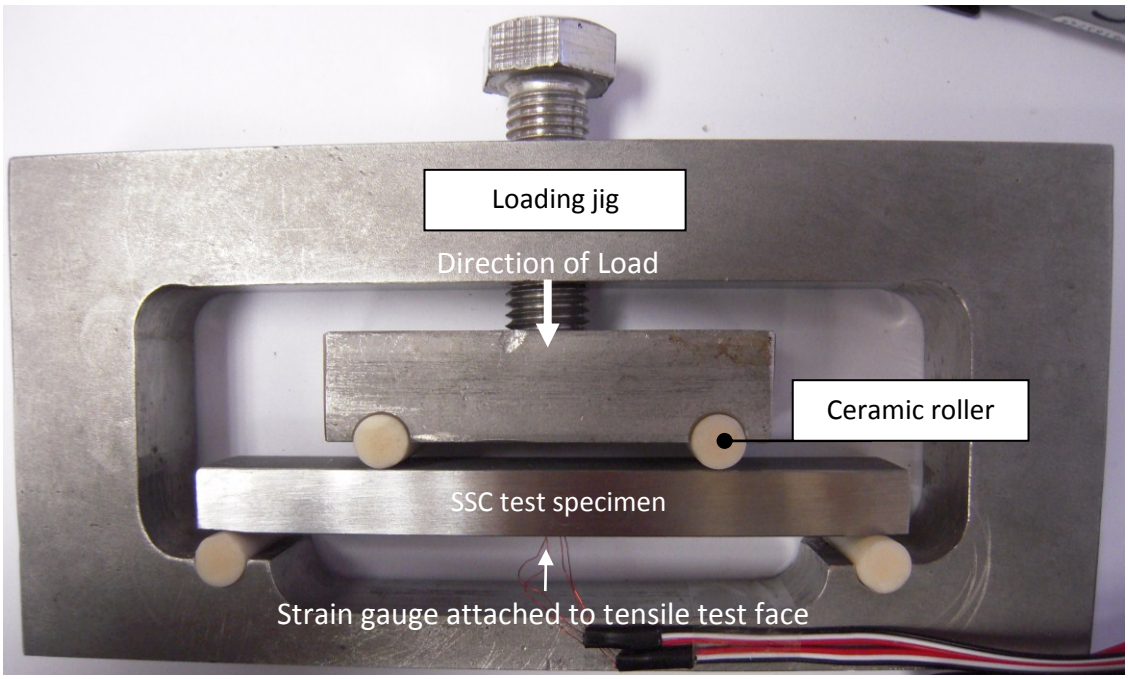

Figure 4.12 Four-point bend SSC test specimen in loading jig

Addition tests were performed in the 35 mbar H_2S environment (24 °C) whereby the specimens were left with the edges as-machined (no chamfers) in order to investigate the influence of edge preparation on SSC resistance.

4.2.6.2 SSC Test Corrosion Coupons

In addition to the SSC test specimens, two corrosion coupons were also included in the test vessels. One corrosion coupon retained the as-received pipe surface (cut edges not masked) and the other was fully-machined and wet ground to a 600 grit finish on all sides (Figure 4.13). Both coupons measured 20x20 mm and the machined faces of the as-received coupon were also wet-ground to a 600 grit finish. The coupons were cleaned with an alkaline degreaser, flushed with acetone and left to air-passivate for a minimum of 48 hours before exposure to the test environment. Each coupon was measured and weighed prior to testing.

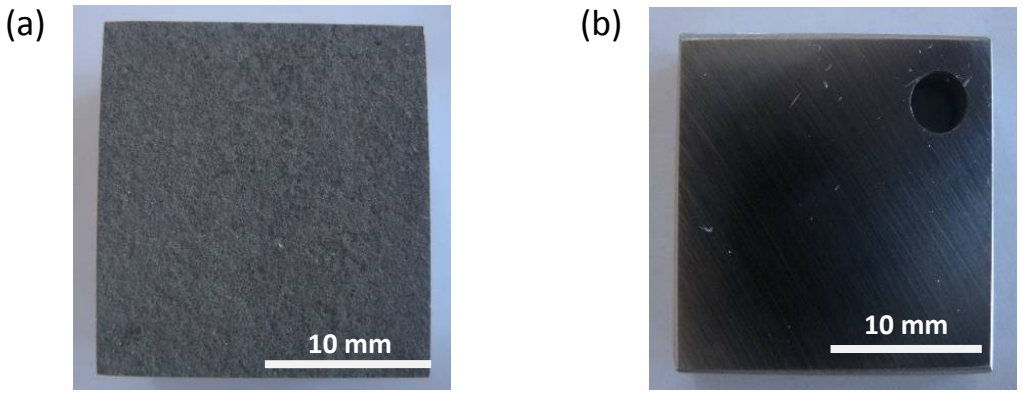

Figure 4.13 Corrosion coupons with (a) as-received pipe surface & (b) 600 grit finish

After the 30 day exposure period, the coupons were examined for evidence of pitting corrosion and weighed to determine mass loss during the test. An assessment of corrosion damage was done using the following mass equation from ASTM standard G1 [156]:

$$\text{Corrosion rate (mm/year)} = \frac{(87600 \times W)}{A \times T \times D} \tag{4.12}$$

Where:
W = Mass loss (g), A = Area (cm^2), T = Exposure time (hours), D = Density = 7.72 g/cm^3 (based on an SMI grade UNS S41426 stainless steel [157])

4.3 Stress & Strain Investigation of the Four-Point Bend Test

The SSC Investigation highlighted preferential cracking at the edges and inner loading roller positions indicating that geometry and loading configuration could be influencing the SSC test results. Consequently a stress and strain investigation was performed on weldable 13%Cr supermartensitic stainless steel material using strain-gauge measurements, digital image correlation and finite element analysis to generate full-field maps of stress and strain on parent fully-machined and as-received specimens loaded in four-point bending.

4.3.1 Flexural Bend Test Rig Development

A new flexural-bend test rig was developed at Exova Corrosion Centre to provide a temperature-controlled environment with a working range of 24 °C to 200 °C. The general design is shown in Figures 4.14 & 4.15 and consists of a 300x250x150 mm stainless steel electrical enclosure with ceramic/wool insulation, an air heater with closed-loop temperature control, and a four-point bend loading fixture.

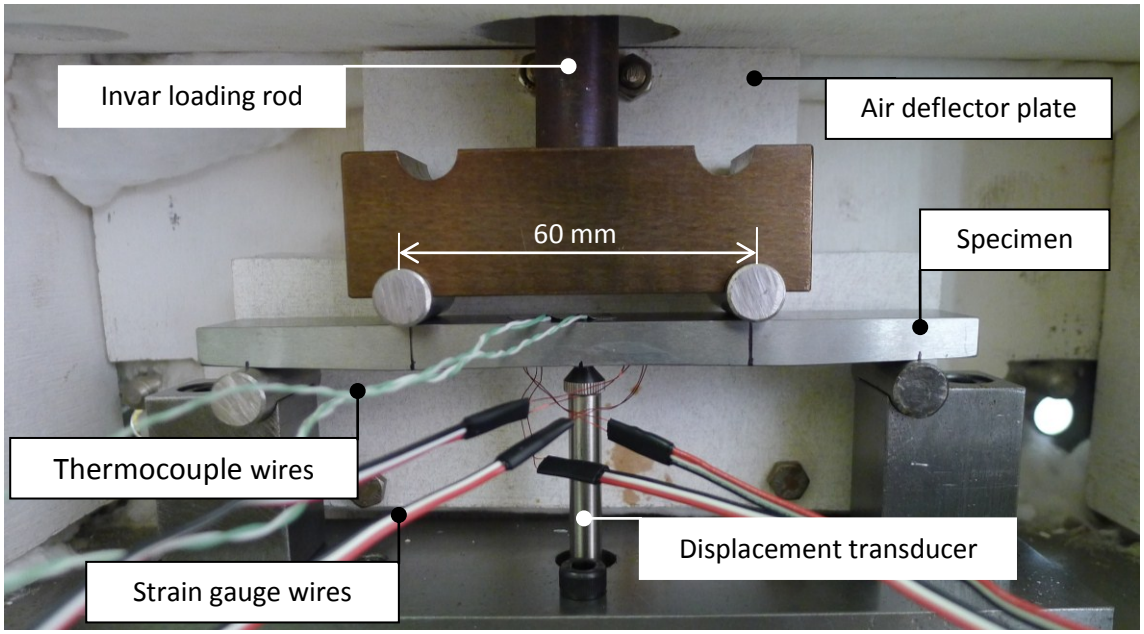

Figure 4.14 Four-point bend specimen inside the flexural bend heat chamber

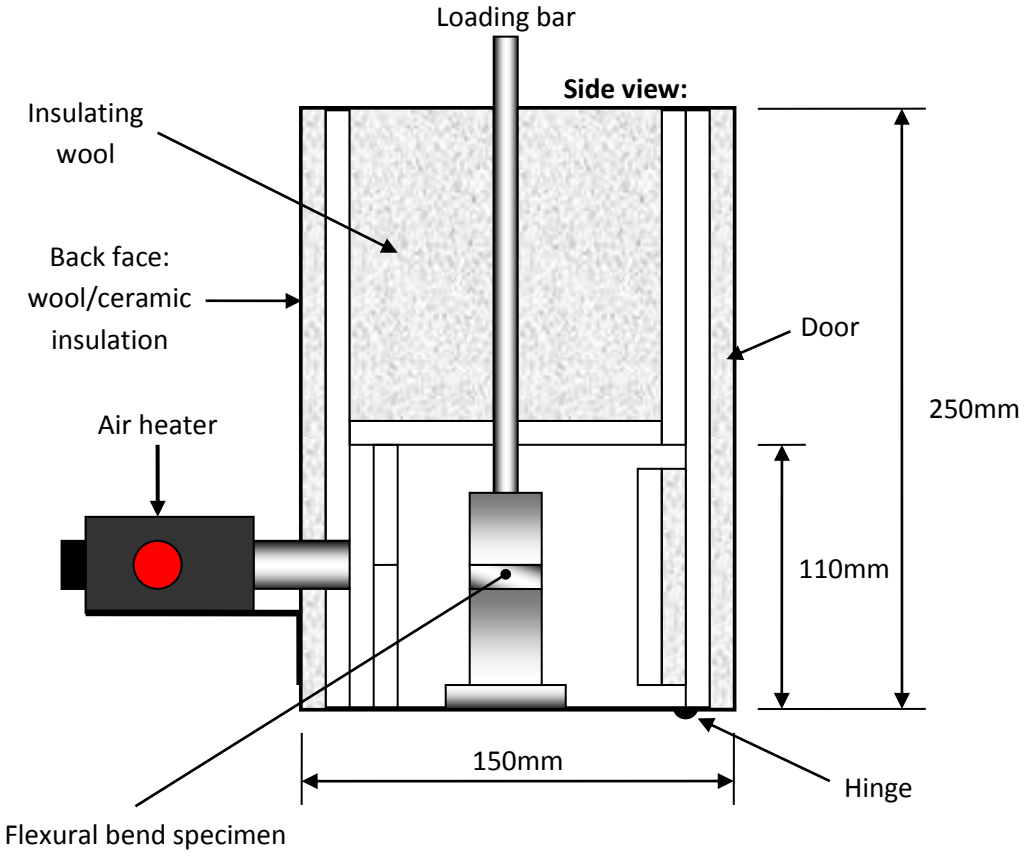

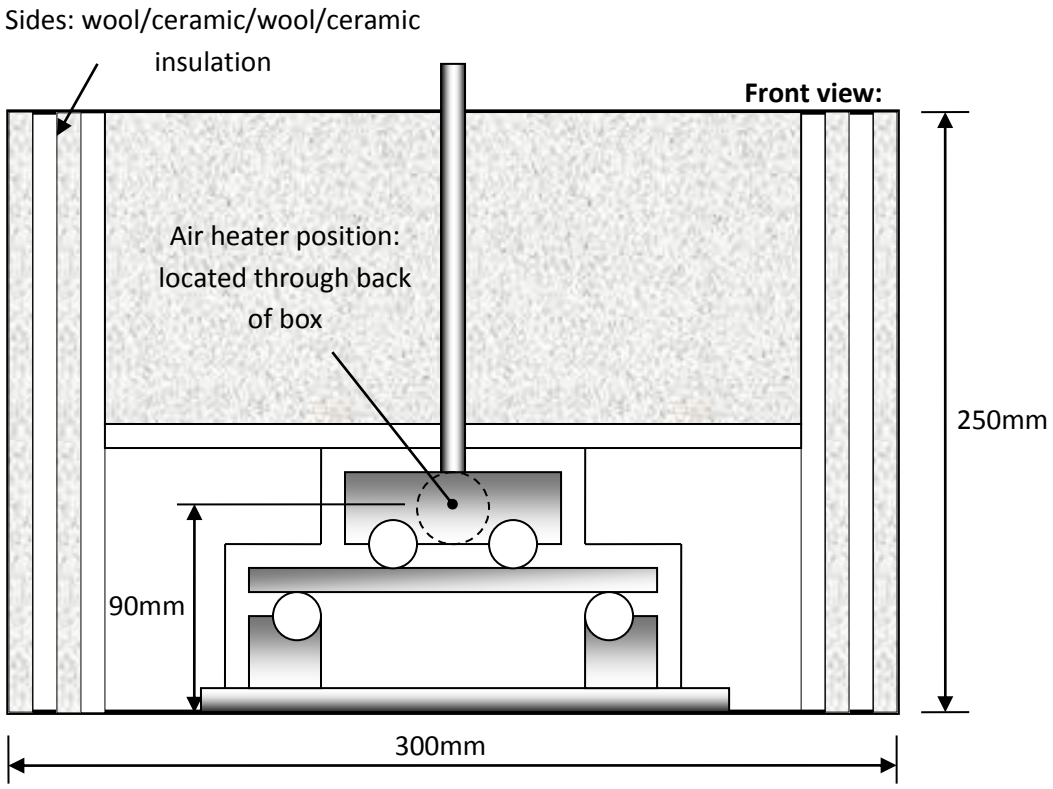

Figure 4.15 Schematic of the flexural bend heat chamber

The heat-chamber was designed to sit on the base of a standard tensile tester. Insulation was provided by two alternating layers of thermal insulating wool and 6 mm ceramic plate. The four-point bend loading fixture was manufactured from carbon steel and designed for holding 10 mm diameter rollers on 120/60 mm loading centres. The loading rod connected to the tensile testing machine via a load cell and was manufactured from Invar[21] material to minimise the effects of thermal expansion when heated.

To uniformly heat the test specimens, the air inside the heat chamber was slowly circulated at the required test temperature using a Leicester 'LHS15 system' air heater and 'CSS' controller (see Figure 4.16). The LHS15 system can heat air from a compressed air line up to a maximum temperature of 650 °C and the CSS controller provides closed-loop temperature control for accurate thermal stability.

Figure 4.16 LHS15 system air heater and CSS controller

In order to avoid direct heating of the test specimen, a deflector plate was made to divert hot air from the LHS15 air heater nozzle and circulate it around the heat chamber. Several trials showed that the shape and position of the deflector plate directly influenced the thermal gradient generated across the test specimen and the optimal design was found

[21] Invar is a 36% Nickel-iron alloy with a coefficient of thermal expansion of 1.7-2.0 x 10^{-6} K^{-1} at 20-90°C

to be an inverted 'T' shape (see Figure 4.17). The deflector plate was made of a layer of insulating wool sandwiched between two 6 mm thick ceramic plates and was bolted to the back wall of the heat chamber. The bolts secured the plate and maintained a uniform gap between the back wall and the plate to divert air evenly around the heat chamber.

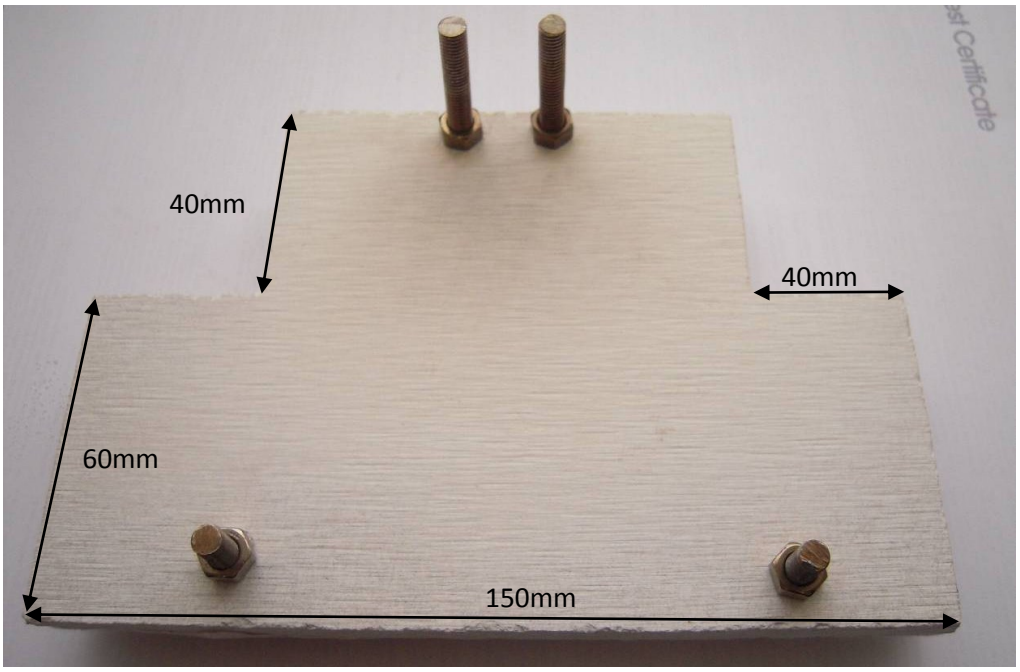

Figure 4.17 Air deflector plate used to prevent direct heating of the test specimen

A series of thermal stability trials were performed to determine the optimal controller settings (proportional, integral and derivative) and air pressure required to heat the chamber whilst minimising the thermal gradient in the test specimen. Details of these trials are presented in Appendix 1 and the final settings used in the flexural bend tests are detailed in Table 4.3 below:

Table 4.3 CSS Controller settings for elevated temperature flexural bend tests

Controller Settings					Air pressure (MPa)	Worst case set-point deviation (°C)	Worst case Thermal gradient (°C)
Set-point (°C)	P	I	D	hPH (%)			
≤50	24	0.01	0	30	0.075	49-50	± 0.5
≤100						99-101	± 1.0
≤150				80		147-151	± 2.0
≤200					0.025	196-202	± 3.0

4.3.2 Flexural Bend Tests

Flexural bend tests were performed on fully-machined specimens at room temperature and 130 °C[22] using an Instron tensile tester fitted with the heat chamber described previously. Additional tests at 5 °C were performed at the University of Birmingham using a DMG screw driven tensile tester fitted with a liquid-nitrogen-cooled temperature controlled enclosure. Each specimen was fitted with a biaxial strain gauge at the mid-width, mid-length position on the tensile surface to measure longitudinal and transverse strain components (Figure 4.18). Specimens were strained to approximately 12000 με and loaded at a constant rate of 1 mm per minute. Load, strain and deflection were recorded at a rate of one sample per second using a Vishay P3 strain recorder and used to plot graphs of load versus strain to determine the 0.2% offset strain at each temperature.

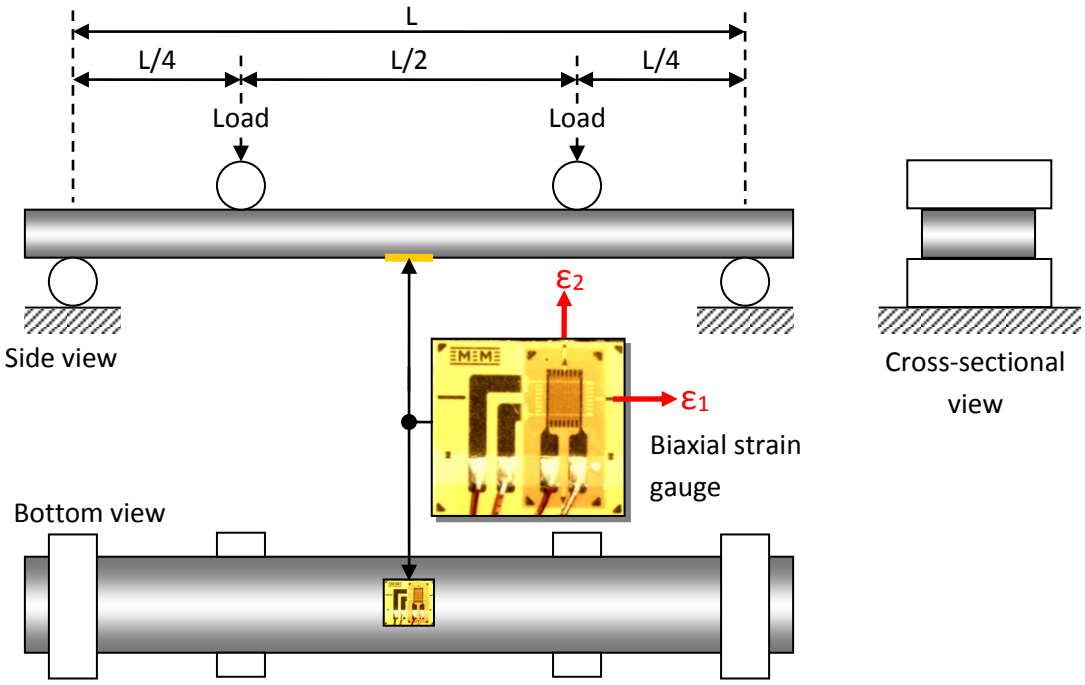

Figure 4.18 Fully-machined four-point 'flexural' bend test sample fitted with a biaxial strain gauge

[22] 130 °C is representative of a typical in-service operating temperature for a supermartensitic pipeline [116].

Following each test, a load-strain curve was plotted similar to that shown in Figure 4.19. This curve was used to determine the 0.2% offset strain by taking a line parallel to the linear elastic region of the curve from the 2000με (0.2%) point. Where this line intersected the curve, a vertical line was taken to the x-axis to give the 0.2% offset strain in four-point bending.

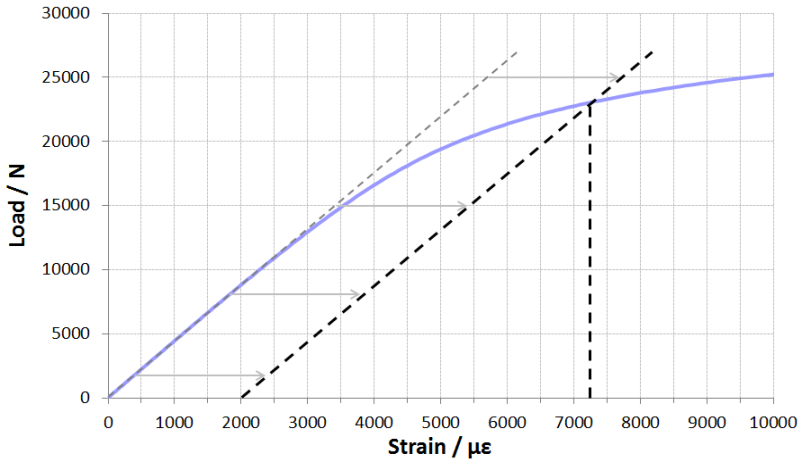

Figure 4.19 Determination of the 0.2% offset strain from a flexural bend test

The flexural bend test data was also used to determine the elastic modulus (E) and Poisson's ratio (v) using the following equations:

$$E = \frac{M.y}{\varepsilon.I} \tag{4.13}$$

$$v = \frac{\varepsilon_2}{\varepsilon_1} \tag{4.14}$$

4.3.2.1 Room Temperature Flexural Bend Tests

Ten flexural bend specimens were machined from the longitudinal orientation of the pipe for testing at room temperature (24±0.5 °C). Four of the specimens measured 130x20x10 mm, four measured 130x20x5 mm and two measured 130x20x2.5 mm. In addition, three specimens were machined from the transverse orientation of the pipe and

measured 70x20x4 mm. All the specimens were fitted with a general-purpose, three-wire biaxial strain gauge with a grid resistance of 120 ohms. The strain gauges were a 'stacked' type with the longitudinal gauge in direct contact with the specimen surface and an overlapping transverse gauge. Both longitudinal and transverse gauges were wired to the P3 strain recorder in a quarter-bridge arrangement as detailed in Figure 4.20.

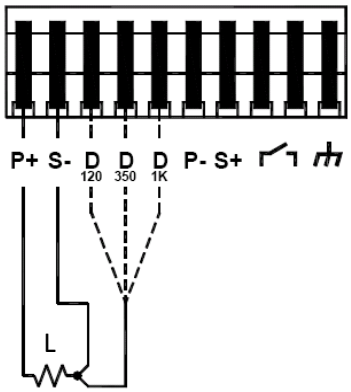

Figure 4.20 Quarter bridge wiring for room temperature strain gauge measurements

4.3.2.2 Flexural Bend Tests at 130 °C

Three flexural bend specimens, measuring 130x20x10 mm, were machined from the longitudinal orientation of the pipe and fitted with a high-temperature biaxial strain gauge rated for use up to 200 °C. The strain gauge backing and specimen surface were coated with a thin layer of M-bond 610 adhesive and left to air dry for 5 minutes. The strain gauge was then pressed down onto the specimen surface, pushing excess glue and air bubbles out of the bonding area, covered with a thin sheet of PTFE, then clamped between a layer of silicone gum and a metal backing plate. The clamped specimen was cured in an oven at 175 °C for 1 hour. Once removed cooled to room temperature, three k-type thermocouples were fitted in the positions shown in Figure 4.21 and connected to a PICO data logger to record the temperature gradient between the inner loading rollers during the test.

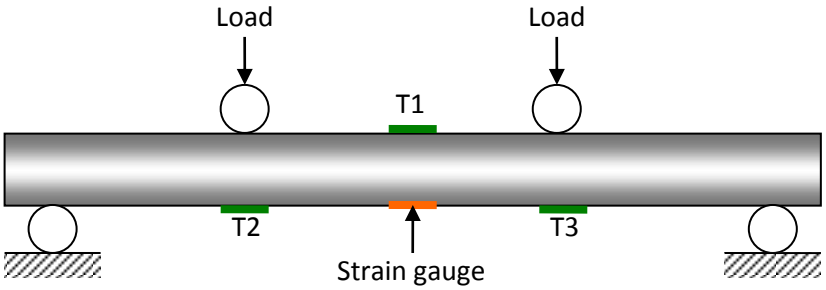

Figure 4.21 Flexural bend test sample with strain gauge & thermocouple (T) positions

The longitudinal and transverse strain gauges were wired in a half-bridge arrangement to provide temperature compensation (see Figure 4.22). With this arrangement the transverse gauge compensates for the Poisson effect on the principal strain measurement, so only the compensated longitudinal strain is measured.

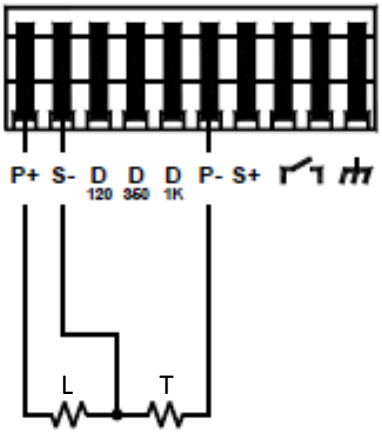

Figure 4.22 half-bridge wiring for 130 °C strain gauge measurements: L and T refer to the strain gauges fitted in the longitudinal and transverse orientations respectively.

Prior to loading, each specimen was heated to 130 °C and soaked for 30 minutes to achieve a stable temperature gradient across the test area. After the soak time, a 100 N preload was applied and the strain gauge, load cell and displacement transducer readings were zeroed. Following this procedure, the flexural bend test was performed as described previously.

4.3.2.3 Flexural Bend Tests at 5 °C and 24 °C

Four Flexural bend specimens measuring 130x20x10 mm were machined from the longitudinal orientation of the pipe and fitted with a general-purpose, biaxial strain gauge wired in a quarter bridge arrangement as described previously. Room temperature tests were repeated because different test apparatus were being used from the previous tests so it was important to ensure a valid comparison was being made between the two temperatures. Note that due to the design of the test apparatus used, beam deflection could not be measured in these tests.

4.3.2.4 Measurement Errors

Additional flexural bend tests were performed at room temperature using 130x20x10 mm specimens machined from the longitudinal orientation of the pipe. To demonstrate the errors (n) generated by strain gauge misalignment in the flexural bend test, two of the specimens were fitted with a biaxial strain gauge purposely misaligned by β=1° and β=3° to the principal axis (ϕ) and compared to a specimen with the strain gauge aligned correctly along the principal axis (β = 0). Equation 4.15 was used to calculate the corresponding error due to strain gauge misalignment:

$$n = \frac{\varepsilon_1 - \varepsilon_2}{2}\left[\cos 2(\phi \pm \beta) - \cos 2\phi\right] \tag{4.15}$$

Where:

n = misalignment error
ε_1 = maximum principal strain
ε_2 = minimum principal strain
ϕ = gauge angle measured from principal axis
β = misalignment angle

To demonstrate the errors generated by misaligning the test specimen in the loading rollers (with the strain gauge correctly aligned to the principal axis of the specimen); a single flexural bend test was performed with the specimen purposely misaligned to an angle of 2° with the principal strain axis as shown in Figure 4.23:

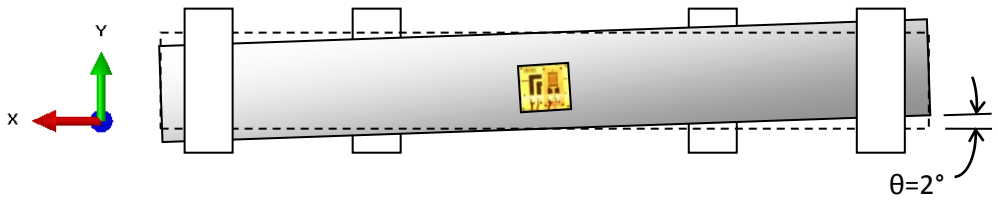

Figure 4.23 Specimen misaligned in loading jig by angle θ from the principal axis

4.3.3 Finite Element Analysis

The finite element (FE) method was used to model the four-point bend and uniaxial tensile test methods. Static, non-linear stress analysis was performed using ABAQUS 6.12 software through the University of Birmingham 'Bluebear' system. The two aims of this work were:

1. To compare the tensile and flexural-bend test methods and explain the difference observed in the 0.2% offset strain from these tests.

2. To investigate the full-field stress and strain distribution of fully-machined and as-received four-point bend tests specimens (refer to Figure 4.14), including how roller friction, specimen thickness, edge chamfers and fillet radii influences stress and strain concentration.

Modelling followed an iterative process as illustrated in Figure 4.24 below:

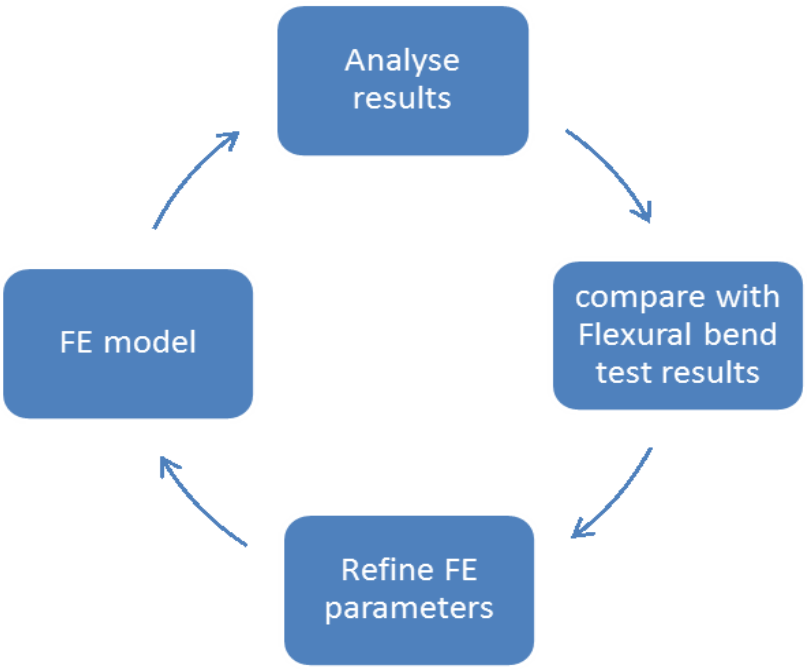

Figure 4.24 Methodology used in the finite element modelling process

4.3.3.1 Material Properties for FEA

Elastic-plastic material properties were assigned to the FE models using data points from the stress-strain curve in Figure 4.25. The stress-strain curve was generated from room-temperature uniaxial tensile tests performed on round specimens machined from the longitudinal orientation of the supplied pipe. Young's Modulus and Poisson's ratio was determined from tensile and flexural-bend tests respectively and assigned to the model, with the overarching assumption that all material properties were both homogeneous and isotropic:

- **Young's Modulus: 186,000 MPa** (determined from the elastic region of the tensile stress-strain curve using Hooke's Law: $E = \sigma/\varepsilon$)
- **Poisson's ratio: 0.30** (determined from flexural bend tests)

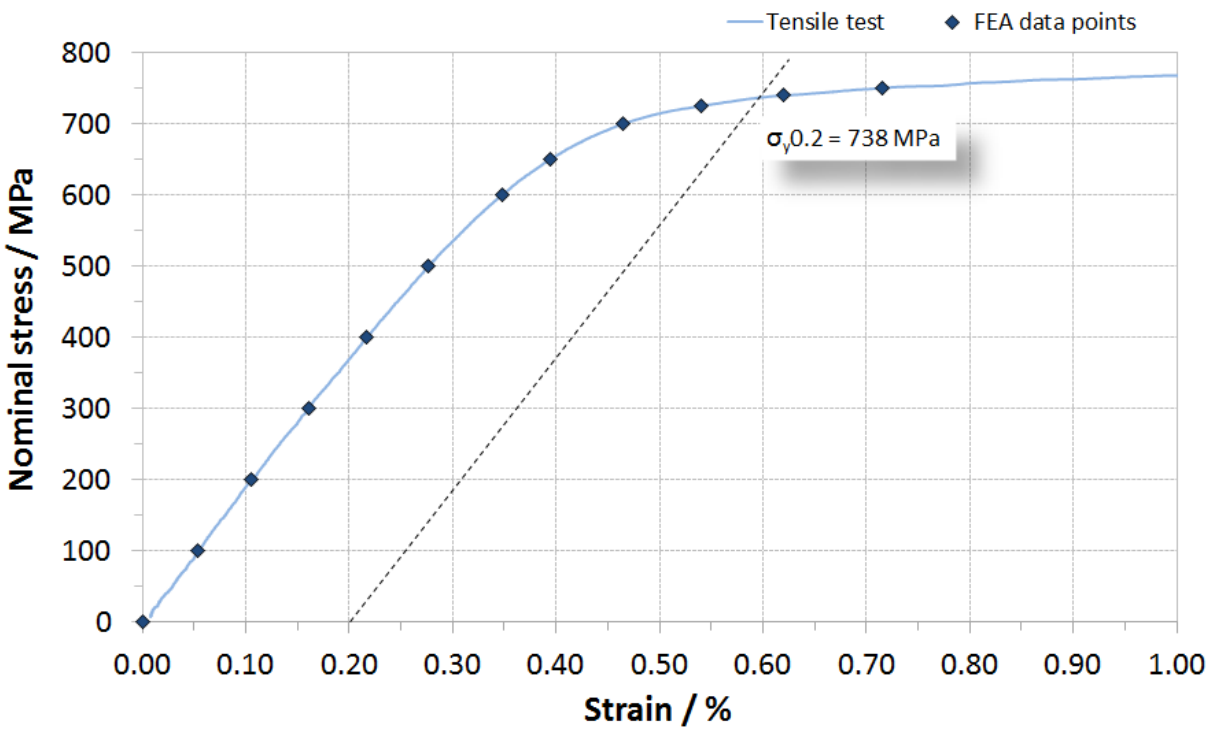

Figure 4.25 Tensile stress-strain data used for FE analysis. The markers indicate where data points were taken from the stress-strain curve and used in the FE models.

The data points taken from the stress-strain curve in the plastic regime were converted from nominal stress ($\sigma_n = F/A_o$) and nominal strain ($\varepsilon_n = \Delta l/l_o$) to true stress and true strain [138]:

$$\sigma = \sigma_n (1 + \varepsilon_n) \quad (4.14)$$

$$\varepsilon = \ln (1 + \varepsilon_n) \quad (4.15)$$

Isotropic hardening was assumed (i.e. both tensile and compressive surfaces work harden to the same degree) and the level of plastic strain was determined by decomposing the total true strain into elastic and plastic components, using equation 4.16 as shown in Table 4.4:

$$\text{Plastic Strain} = \text{True Strain} - \text{True Stress} / \text{Young's Modulus} \quad (4.16)$$

Table 4.4 Stress and strain conversions

Nominal Stress (MPa)	Nominal strain	True Stress (MPa)	True Strain	Plastic Strain
500	0.00277	501.4	0.0027662	0
600	0.00348	602.1	0.0034740	0.000237
650	0.00395	652.6	0.0039422	0.000434
700	0.00465	703.3	0.0046392	0.000858
725	0.0054	728.9	0.0053855	0.001467
740	0.0062	744.6	0.0061809	0.002178
750	0.00715	755.4	0.0071246	0.003063
800	0.014	811.2	0.0139029	0.009542

4.3.4 Tensile & Flexural-Bend Test Comparison

Two beams were modelled as 3D deformable solids with cross-sectional dimensions of 10x20 mm and extruded to a length of 130 mm (Figure 4.26) to investigate why the 0.2% offset stain in a tensile test (taken from a stress-strain curve) is different to that obtained from a flexural bend test (taken from a load-strain curve). For the tensile test model, one end of the beam was fully constrained (ENCASTRE)[23] while a load was applied to the opposite end in the form of a tensile pressure force. For the flexural-bend test model, quarter symmetry was applied to reduce the computation cost. The beam was partitioned where the loading rollers would make contact; the outermost partition was constrained to only allow rotation about the Y-axis and translation along the X-axis (U2=U3=UR1=UR3=0)[24] and the inner partition was used to apply a compressive pressure force over a small area (1 mm) to represent the contact area a 10 mm diameter roller would make with the specimen.

[23] Encastre is a boundary condition that constrains all six degrees of freedom (U1=U2=U3=UR1=UR2=UR3=0).
[24] U_n represents translation and UR_n represents rotation, where n= 1, 2 or 3 corresponding to the x, y and z axes.

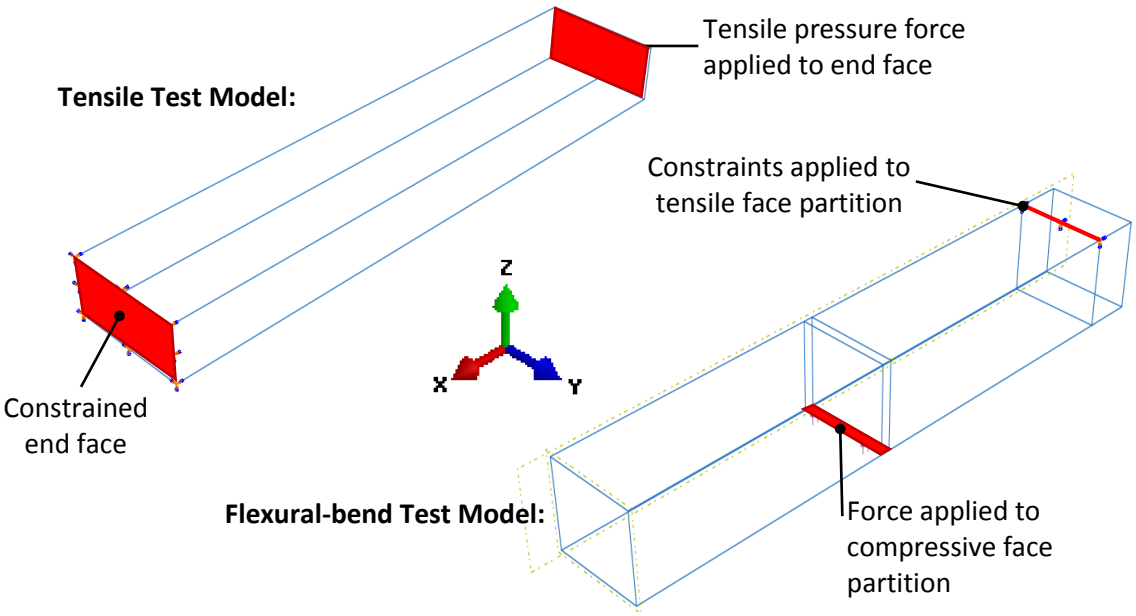

Figure 4.26 Tensile test & flexural-bend test models with locations of constraints and applied forces

Both models were meshed with C3D20R elements (20-node quadratic bricks with reduced integration) with a density of 1 mm. The surface pressure force was applied to the models over 7 loading steps: For the tensile test model, this was 20 kN, 40 kN, 80 kN, 120 kN, 140 kN, 150 kN and 160 kN applied to one end of the beam. For the flexural bend test model, this was 4 kN, 8 kN, 12 kN, 16 kN, 20 kN, 24 kN and 26 kN applied to the 1 mm contact area on the compressive surface. The use of pressure force rather than a displacement allowed load-strain, stress-strain and stress-load curves to be plotted for both test methods. The results were validated from the elastic region of the stress-load curves using the following linear-elastic equations [118]:

For the tensile model: $\sigma = F / A$ (4.17)

For the flexural bend model: $\sigma = M y / I$ (4.18)

Where:

σ = Stress (Nm^{-2})
F = Force (N)
A = Cross-sectional area (m^2)
M = Bending moment (Nm)
I = Second moment of area (m^4)
y = distance from the neutral axis (m)

4.3.5 Full Field Stress & Strain Analysis

FEA, DIC and strain gauge measurements were used to show the full-field stress and strain distribution on the tensile surface of parent four-point bend test specimens with fully-machined and as-received geometries.

4.3.5.1 FEA of the Four-Point Bend SSC Test Specimens

A four-point bend specimen was modelled as 3D deformable solid using quarter symmetry to reduce computational cost. The rollers were modelled as 3D analytical rigid bodies with a diameter of 10 mm and a non-linear analysis was performed over three steps as defined in Figure 4.27. Load was applied to the beam by displacing the inner loading roller along axis 3 to replicate the way load is applied in the real test. The following interactions were defined to model contact between the beam and the rollers:

- Surface to surface contact (standard)
- Set rollers as master surface and beam as slave surface
- Sliding formulation = finite sliding
- Descretization method = surface to surface (no adjustment)
- Contact interaction = mechanical, tangential behaviour
- Friction formulation = frictionless
- Slave adjustment = only to remove overclosures

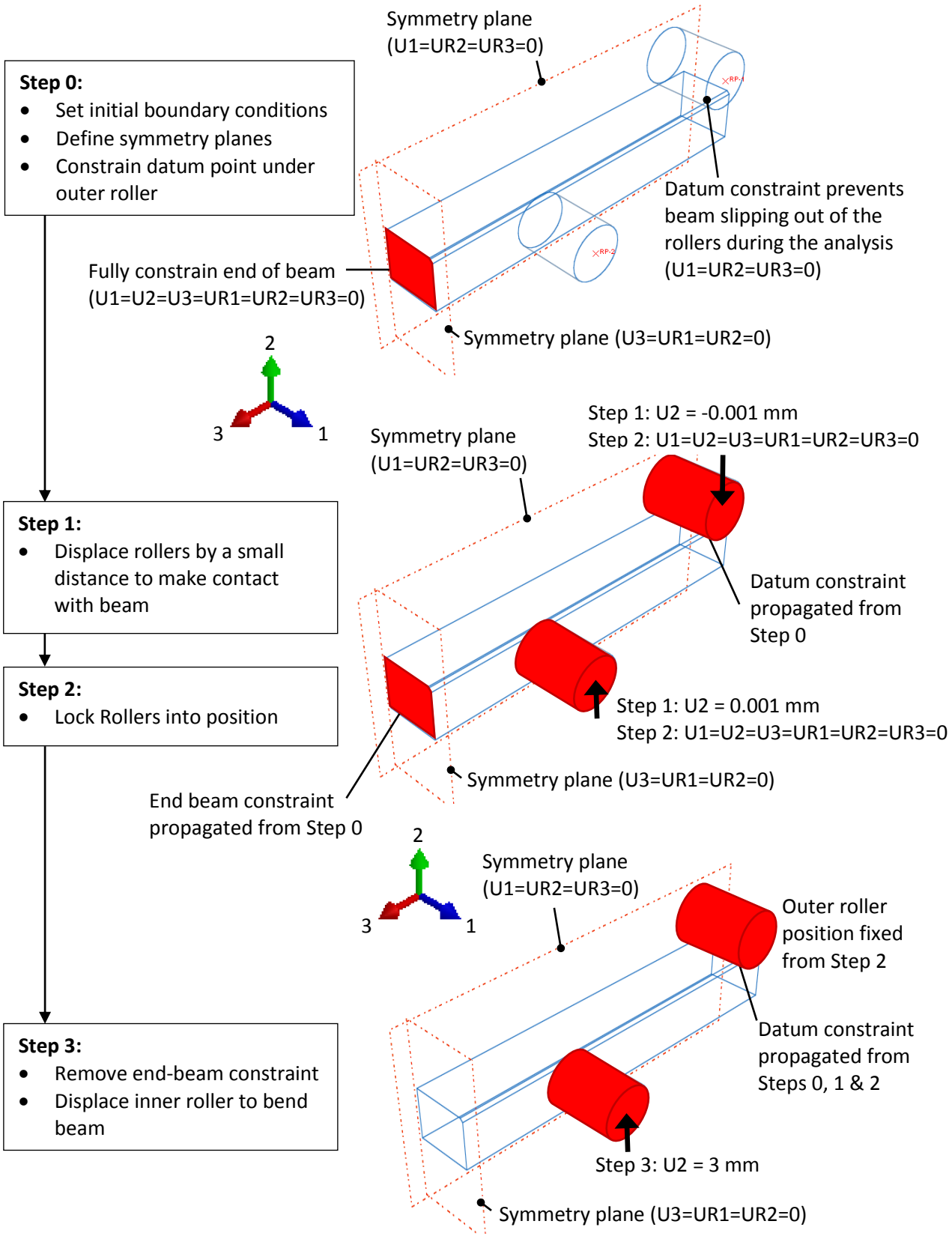

Figure 4.27 Finite Element modelling process of the four point bend test using quarter model symmetry

Mesh refinement was performed using C3D8R elements (8-node linear bricks with reduced integration) then repeated with C3D20R elements (20-node quadratic bricks with reduced integration) to determine the optimal mesh type and density to use for the four-point bend models. Longitudinal strain (LE33) and nodal displacement (U2) were obtained from a node in the centre of the tensile surface in contact with the two outer support rollers. Figure 4.28 and 4.29 show the flexural response using linear and quadratic elements compared to experimental data. The analysis showed that using linear elements requires a fine mesh (0.5 mm) to match the response of the flexural bend test data where a much coarser mesh of quadratic elements can be used without compromising accuracy. Consequently, quadratic elements were used for all the finite element models described in this section.

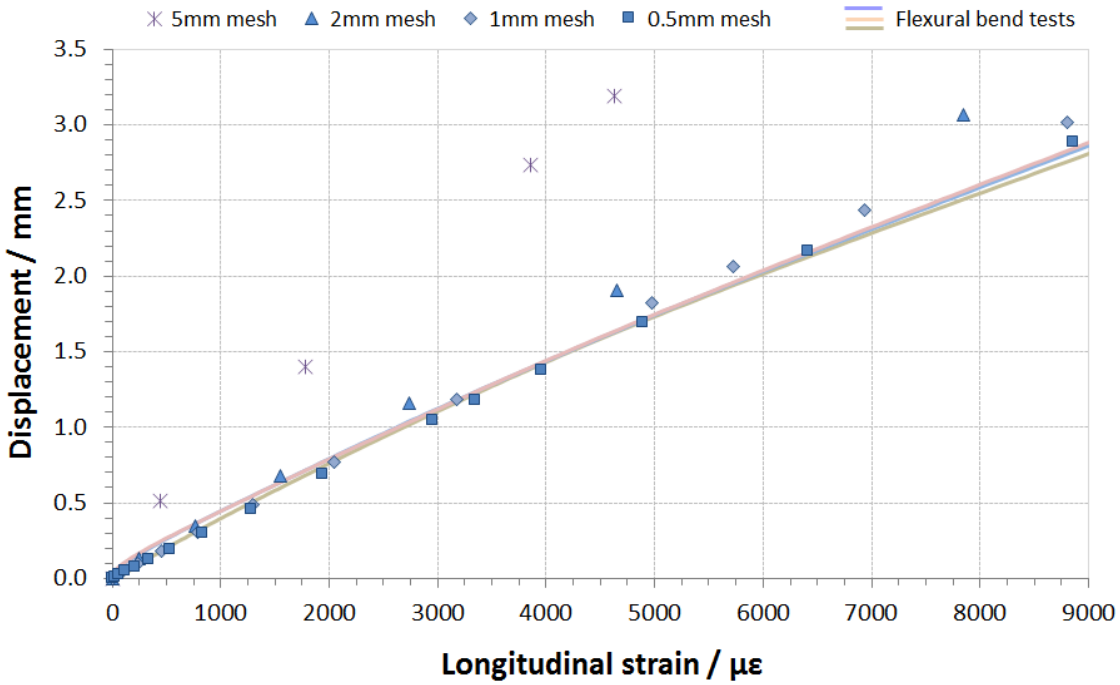

Figure 4.28 Mesh refinement using linear C3D8R elements (displacement versus strain)

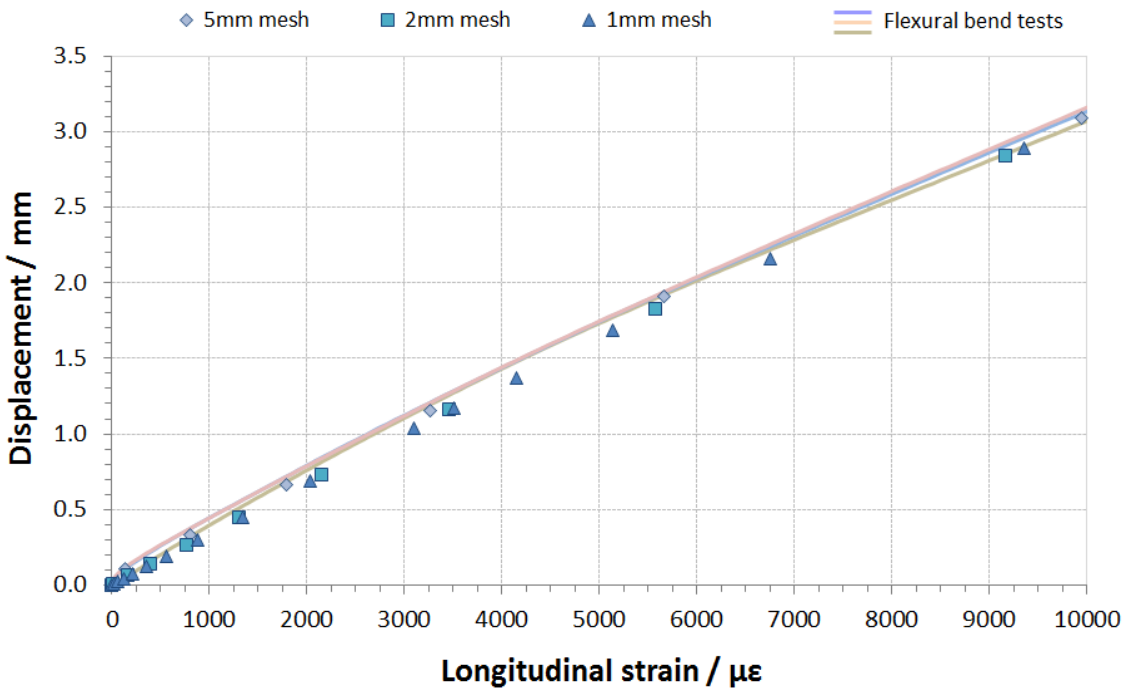

Figure 4.29 Mesh refinement using quadratic C3D20R elements (displacement versus strain)

4.3.5.2 DIC Measurements of the Four-Point Bend SSC Test Specimens

Digital Image Correlation (DIC) was used to provide full-field strain measurements of four-point bend specimens with fully-machined and as-received surface geometries to verify the results generated by the finite element models.[25] The DIC technique was chosen as it overcomes the inherent limitations of using strain gauges which can only provide localised strain measurement at the point to which they are bonded. A LIMESS digital image correlation system was used that consisted of a stereoscopic camera pair with 28 mm focal length lenses and a VIC-3D post-processor. The system was calibrated to translate the image coordinate to geometric coordinate. Both cameras were calibrated at the same time by placing a calibration plate (Figure 4.30) in front of the specimen and rotating the plate around all three axes. The software then automatically calibrated the system and

[25] DIC measurements made with the assistance of Dr Richard Greene at Strain Solutions Ltd on 26/11/12

determined the relevant intrinsic (focal length of the lenses, distortion of the lenses and the positions between the lenses and CCD image device) and extrinsic (rotation matrix and translation vector that define the geometric relation between the camera and the specimen) camera parameters.

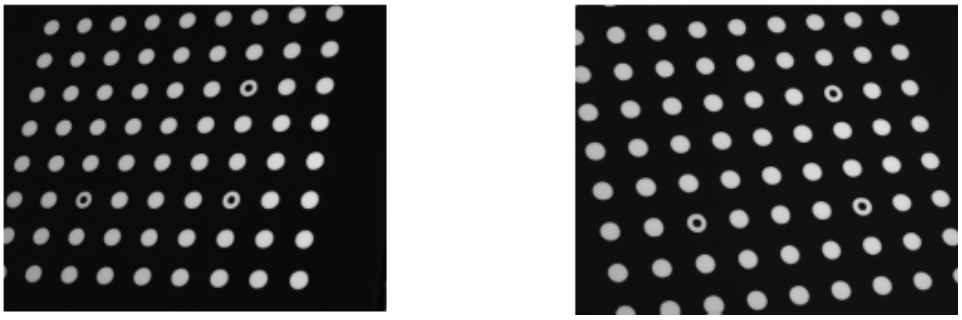

Figure 4.30 A standard calibration plate taken from the perspective of both cameras [127]

Two DIC test specimens, one with fully-machined geometry (130x20x10 mm) and one with as-received geometry (130x20x12.7 mm) were machined from the longitudinal orientation of the pipe. The surface to be tested on both specimens was cleaned, lightly abraded with 240 grit silicon carbide paper (to provide a key for the speckled paint), degreased with isopropyl alcohol, and allowed to dry. The abraded surface of the specimens was then coated with a 10-15 μm thick base coat of matt white acrylic spray paint. After drying, this base coat was over-painted with a mixture of matt-black and matt-white aerosol spray (applied at the same time) to generate a random black-grey-white surface speckle. The average spacing of the speckles was selected in order to optimise the resolution of the image correlation calculation. Each speckle, on average, occupied several pixels within the image.

A single biaxial strain gauge was fitted to the opposite (compressive) face on both test specimens for loading to the desired strain. The compressive strain required to achieve a loading strain of 7300 με on the tensile test surface was estimated from the results of a series of 'calibration tests'. The calibration tests were performed on four fully-machined specimens and four as-received specimens fitted with biaxial strain gauges at the mid-length, mid-width position on both the tensile and compressive faces. The calibration specimens were loaded to 7300 με on the tensile surface and it was determined that the corresponding strain on the compressive surface was 0.88 times lower for the fully-machined specimens and 0.92 times lower for the as-received specimens. This factor was used to estimate the tensile strain using the compressive strain gauge for the DIC experiments. The two DIC test specimens were mounted in a four-point bend test rig in front of the stereoscopic camera pair (see Figure 4.31). The specimens were preloaded (approximately -20 με) by finger-tightening the loading bolt and reference images were taken. Prior to loading, the preload strain was zeroed out of the strain gauges so the recorded loading started at zero strain.

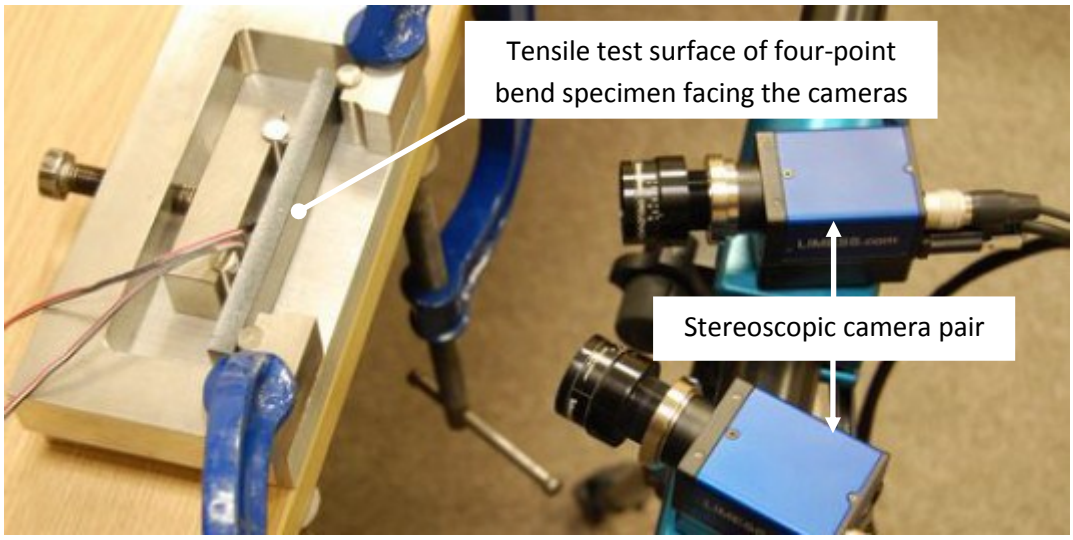

Figure 4.31 Stereoscopic camera pair used for 3D DIC measurement of a four-point bend specimen

The DIC image resolution was 1628x1236 pixels (monochrome) and a 21x21 pixel subset was used to determine displacements between loading step images. A step size of 7 pixels was selected so that every 7 pixels were analysed in the subset (i.e. 9 analysis points in each subset). The camera aspect ratio was 1.33 and the analysis area was 80x20 mm to capture the strain distribution across the surface of the test specimen including the roller positions. This meant that all the pixel columns were utilised (1628) but not all of the pixel rows were utilised in the specimen in the image (the width-to-height ratio of the analysis area needs to match the camera aspect ratio (1.33) to utilise all the pixel rows and columns. In this case the width-to-height ratio was 4). The pixel width (ζ_w) for this setup was:

$$\zeta_w = 80 / 1628 = 0.049 \text{ mm/pixel}$$

The precision of the 3D correlation was approximately 2/100 of a pixel, which translates into a strain resolution of approximately ±150 με.

The DIC specimens were loaded in four-point bending to an estimated tensile strain of 7300 με (-6424 με for the fully-machined specimen and -6716 με for the as-received specimen) and an image was taken of the deformed surface and loaded into the VIC3D post-processor for analysis. To assess the accuracy of the DIC measurements, the longitudinal strain at a given displacement was taken at the mid-length, mid-width position on the tensile surface and compared to data obtained from the finite element analysis and strain gauged specimens of the same size (Figure 4.32). The figure shows there is good agreement between all three techniques used.

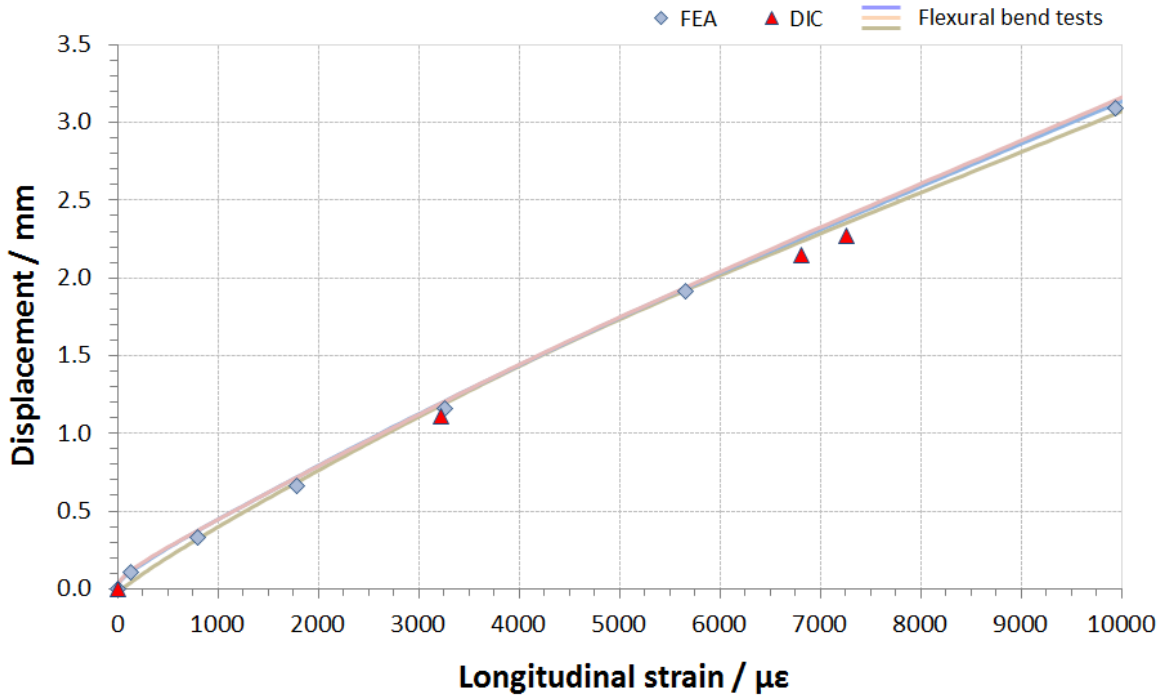

Figure 4.32 Displacement versus strain response comparing DIC, FEA and flexural bend test data

4.3.5.3 Friction at the Loading Rollers

The coefficient of static friction for steel/ceramic and steel/steel pairings is typically 0.5 [158], hence finite element models of a 10 mm thick, fully-machined four-point bend specimen were generated with penalty fiction coefficients of 0.5 to assess how friction influences the stress and strain distribution on the tensile test surface. The models were loaded to a nominal longitudinal strain of 7300 με at the mid-length, mid-width position on the tensile surface and the results were verified against data obtained from strain-gauge measurements and DIC on flexural-bend test specimens. Line plots were taken along the centre-line (x axis) of the tensile surface as shown in Figure 4.33.

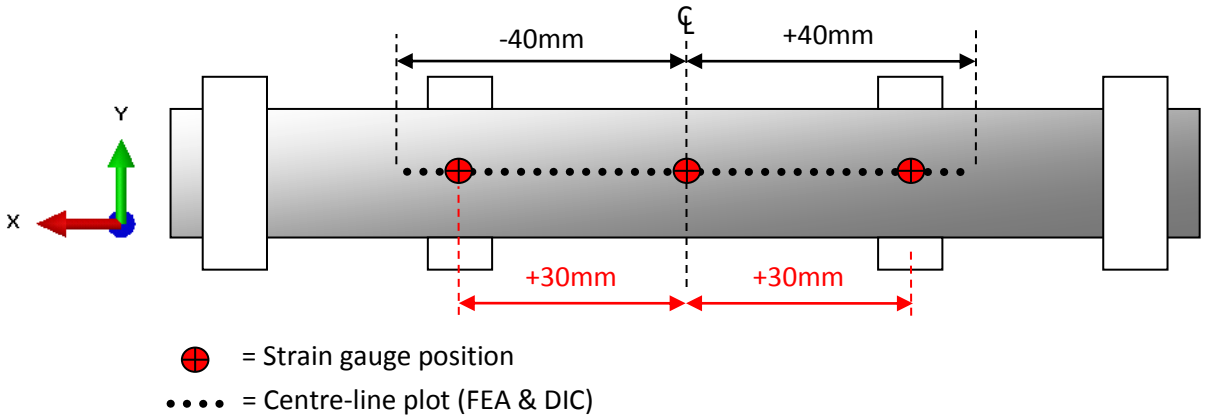

Figure 4.33 Line-plots & strain gauge positions on the tensile surface for a four-point bend specimen

4.3.5.4 Influence of Edge Preparation on Stress & Strain Concentration

FEA and DIC was used to investigate the effect of chamfer angle and fillet radius size on the stress and strain concentration when applied to the longitudinal edges on the tensile surface of four-point bend specimens. Both fully-machined and as-received specimens were considered (see Figure 4.4).

Finite element models were created to represent 130x20x10 mm fully-machined four-point bend specimens and 130x20x12.7 mm as-received four-point bend specimens with different edge preparations. The models used the same parameters defined in Section 4.3.5 (i.e. quarter model symmetry, C3D20R elements and frictionless contact between the rollers and the specimen). Figure 4.34 shows the chamfer angles and fillet radii considered. Since edge chamfers are manually applied to SSC test specimens, it cannot be guaranteed that a 45° angle will be achieved every time. Therefore chamfer angles of 15°, 45° and 75° were modelled to simulate this variability. In order to assess the effect of chamfer angle alone, all the chamfers were modelled with a length of 1 mm. The fillet radii were sized as a function of specimen thickness (t): t/5 = 2 mm, t/10 = 1 mm and t/20 = 0.5 mm.

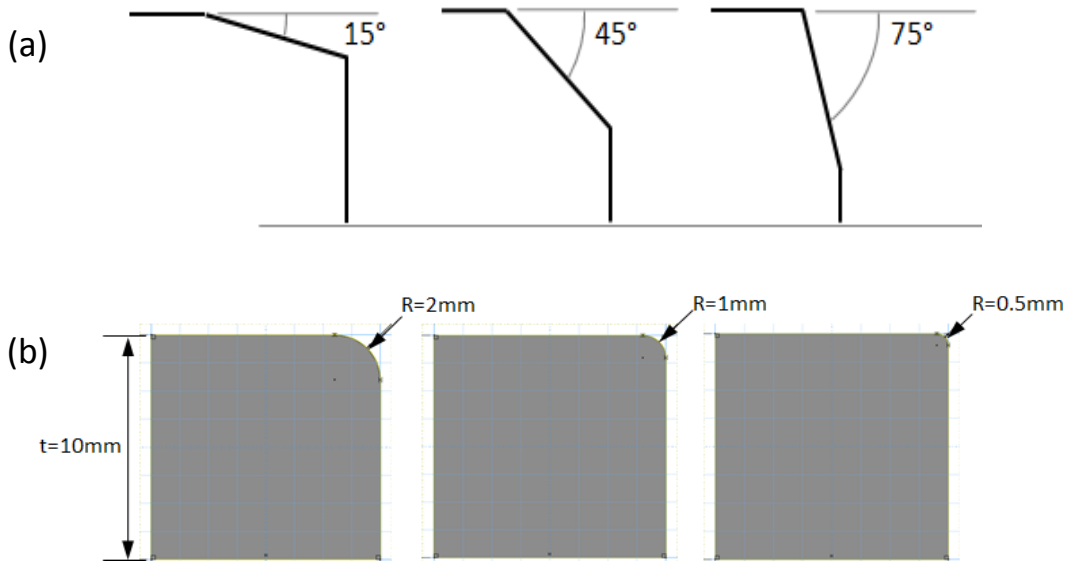

Figure 4.34 (a) Edge chamfers (15°, 45°, 75°) & (b) fillet radii (R=2 mm, R=1 mm, R=0.5 mm)

Since the focus of this analysis was the stress and strains generated at the edge of the beam, a biased mesh was used to concentrate the finest mesh density (0.5 mm) at the edges so to reduce computational cost (Figure 4.35).

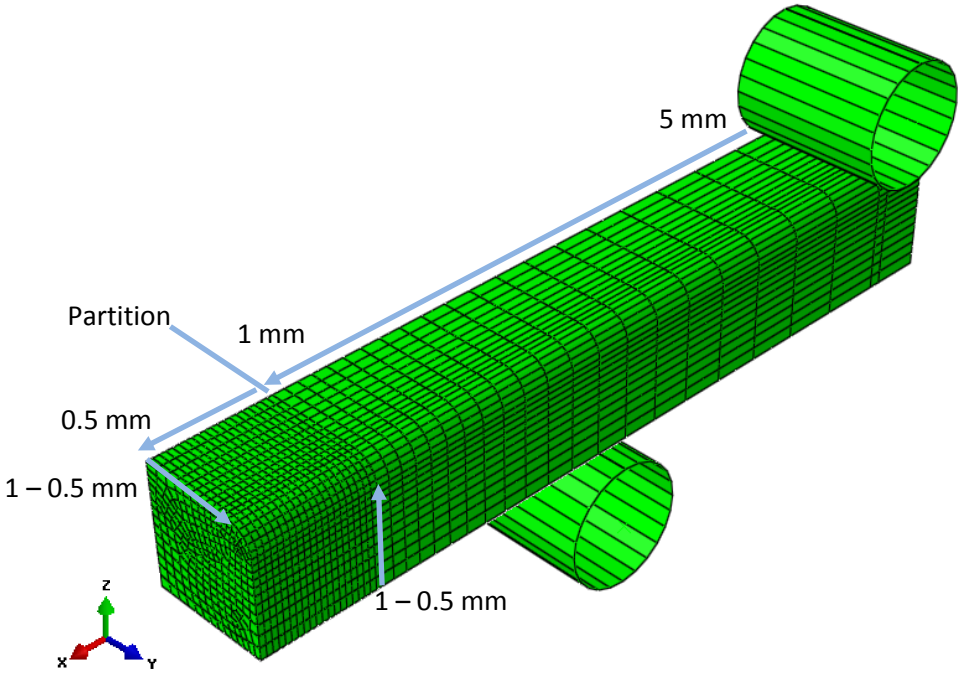

Figure 4.35 Quarter model showing partitioning and mesh bias used to refine mesh at the edge radius

Line plots were taken across the width of the tensile test surface for each FE model as detailed in Figure 4.36:

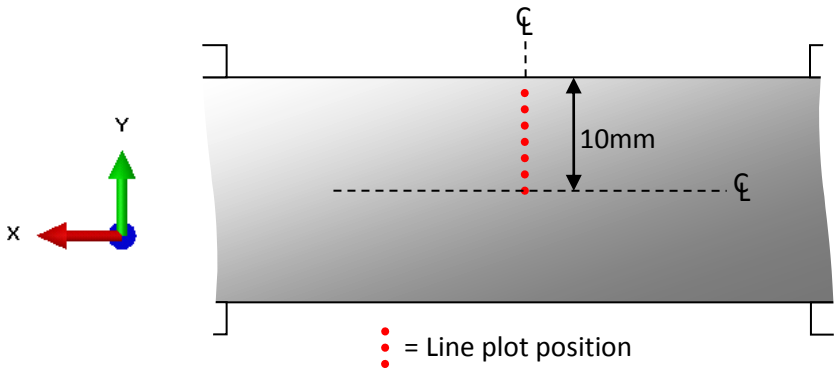

Figure 4.36 Line-plot positions across the width of the tensile surface for the four-point bend FEA models

Two DIC specimens measuring 130x20x10 mm were prepared in the same way as described in Section 4.3.5.2. For these tests, each edge on the tensile surface was prepared with a different chamfer. Three of the edges were prepared with 15°, 45° and 75° chamfers and the other edge was left unprepared (approximately 90°). Figure 4.37 shows the reference image of the preloaded specimen from the perspective of both cameras.

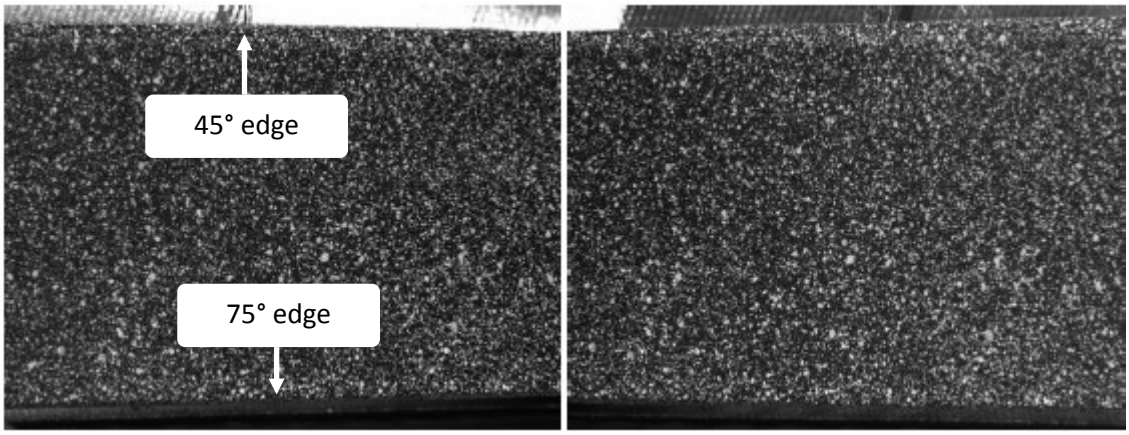

Figure 4.37 Stereo pair images of DIC specimen with one 45° chamfered edge and one with a 75° edge

The same DIC test equipment described previously was used for this test. However, in this test a 25x25 pixel subset was used with a step size of 5 and a much smaller surface area was analysed (approximately 26x20 mm). Since the width-to-height ratio of the analysis area equalled the aspect ratio of the cameras (1.33), all the pixel columns and rows could be utilised (1628x1236). The smaller analysis area for the same pixel resolution meant that each pixel represented a smaller quantity of space in the specimen image and therefore gave a higher resolution contour map of strain compared to the previous tests. For this specimen, the pixel width (ζ_w) and pixel height (ζ_h) was:

$$\zeta_w = 26 / 1628 = 0.016 \text{ mm/pixel}$$
$$\zeta_h = 20 / 1236 = 0.016 \text{ mm/pixel}$$

4.3.6 Anomalous Case of Cracking in the Condensed Water SSC Test

A Finite element model was created based on the actual geometry of as-received specimen C1 from the 69 mbar H_2S Condensed Water SSC tests in Chapter 6. Recall that this particular specimen only cracked along one edge which when measured, was 0.2 mm thicker than the edge that did not crack.

Prior to modelling, the test specimen was cut across the width to reveal the cross-sectional area where cracking occurred. A digital image was taken and imported into a CAD drawing package which was used to sketch around the outline of the image. The Sketch was scaled to the correct dimensions of the specimen and exported as a DXF file into ABAQUS. The sketch was extruded in ABAQUS to a length of 65 mm to create a 3D deformable solid,

symmetrical about the mid-length position, then meshed using Quadratic (C3D20R) elements with a mesh density of 0.8 mm. Figure 4.38 summaries the process used.

The rollers were modelled as 10 mm diameter 3D analytical rigid bodies with the assumption of frictionless contact between the rollers and the beam. Constraints were added at the edges of the beam directly under the outer support roller (U1=UR2=UR3=0) and a symmetry plane was defined at the mid-length position (U3=UR1=UR2=0). The model was loaded by displacing the inner roller until a longitudinal strain of approximately 7300 με was achieved at the mid-length, mid-width position, and full-field plots of maximum principal stress and maximum principal strain on the tensile surface of the beam were generated.

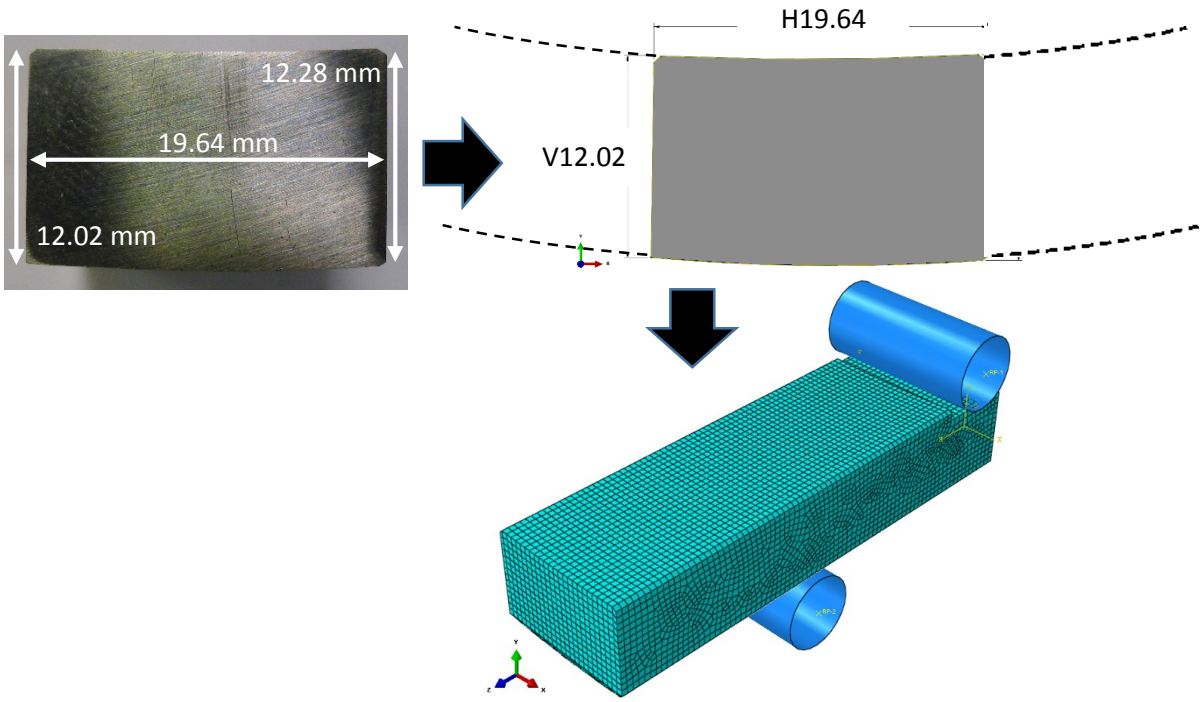

Figure 4.38 Half-model of specimen C1 based on the cross-sectional geometry where cracking was observed

CHAPTER 5: RESULTS & DISCUSSION
Test Material Characterisation

5.1 Microstructure

Figures 5.1 and 5.2 show the tempered martensitic microstructure of the parent metal when etched with Marbles reagent and acidified ferric chloride, respectively. Due to the low carbon content, martensite forms in a lath morphology constrained within prior austenite grain boundaries measuring approximately 40 µm in width. The microstructure is populated with randomly dispersed cuboidal particles ranging from 3 µm to 10 µm in length. Chemical analysis was performed on these particles using Energy Dispersive X-ray spectroscopy (EDS) analysis which shows that titanium is present in the inclusion (Figure 5.3).

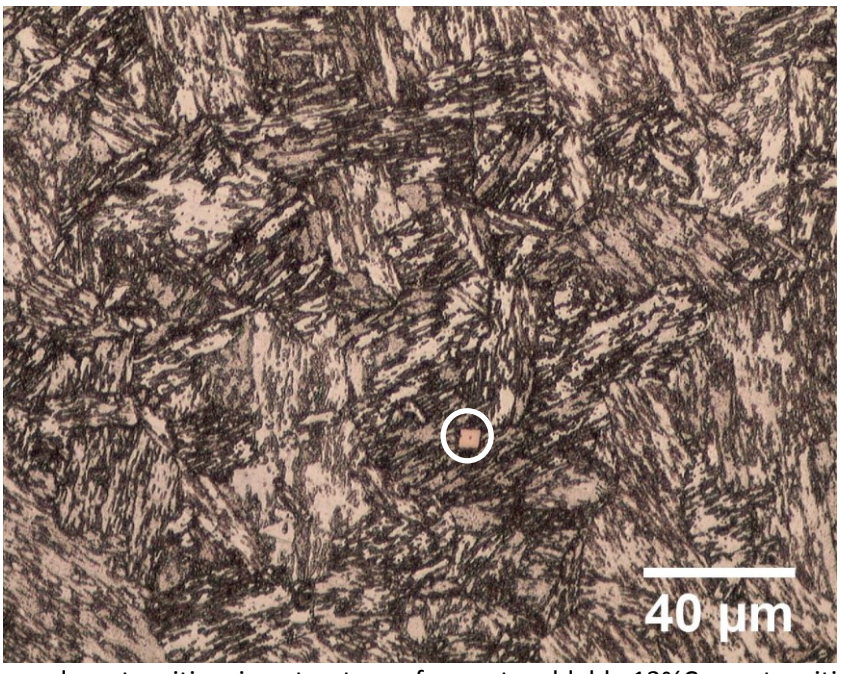

Figure 5.1 Tempered martensitic microstructure of parent weldable 13%Cr martensitic stainless steel when etched with Marbles reagent. Circle highlights a cuboidal inclusion

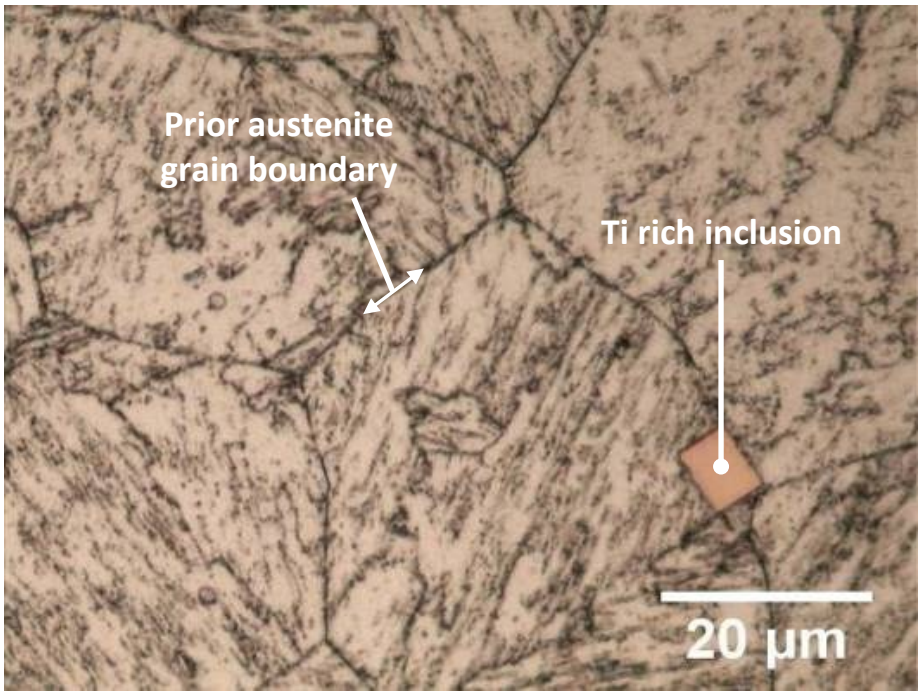

Figure 5.2 Microstructure of base material etched with acidified ferric chloride

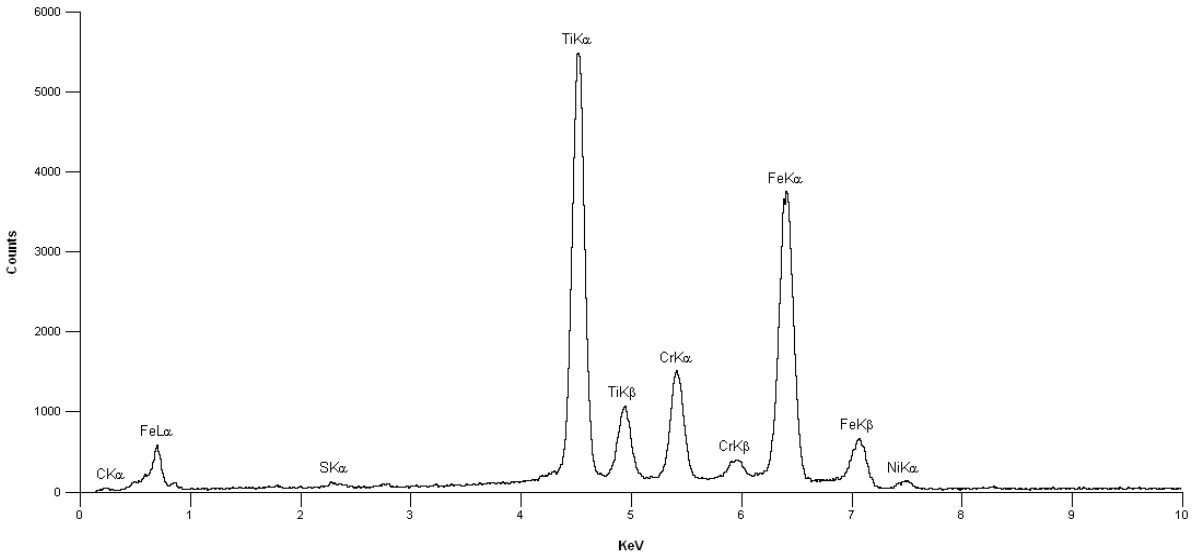

Figure 5.3 EDS analysis shows titanium is present in the inclusion

5.2 Retained Austenite

The average lattice parameters (a_o) for the ferrite and austenite phases were calculated by extrapolating to $\sin^2\theta = 1$ from 10 samples using the method described in Chapter 4. An example of the extrapolation is given in Figure 5.4 and the average lattice parameters were 2.881 ±0.002 for ferrite and 3.589 ±0.008 for austenite.

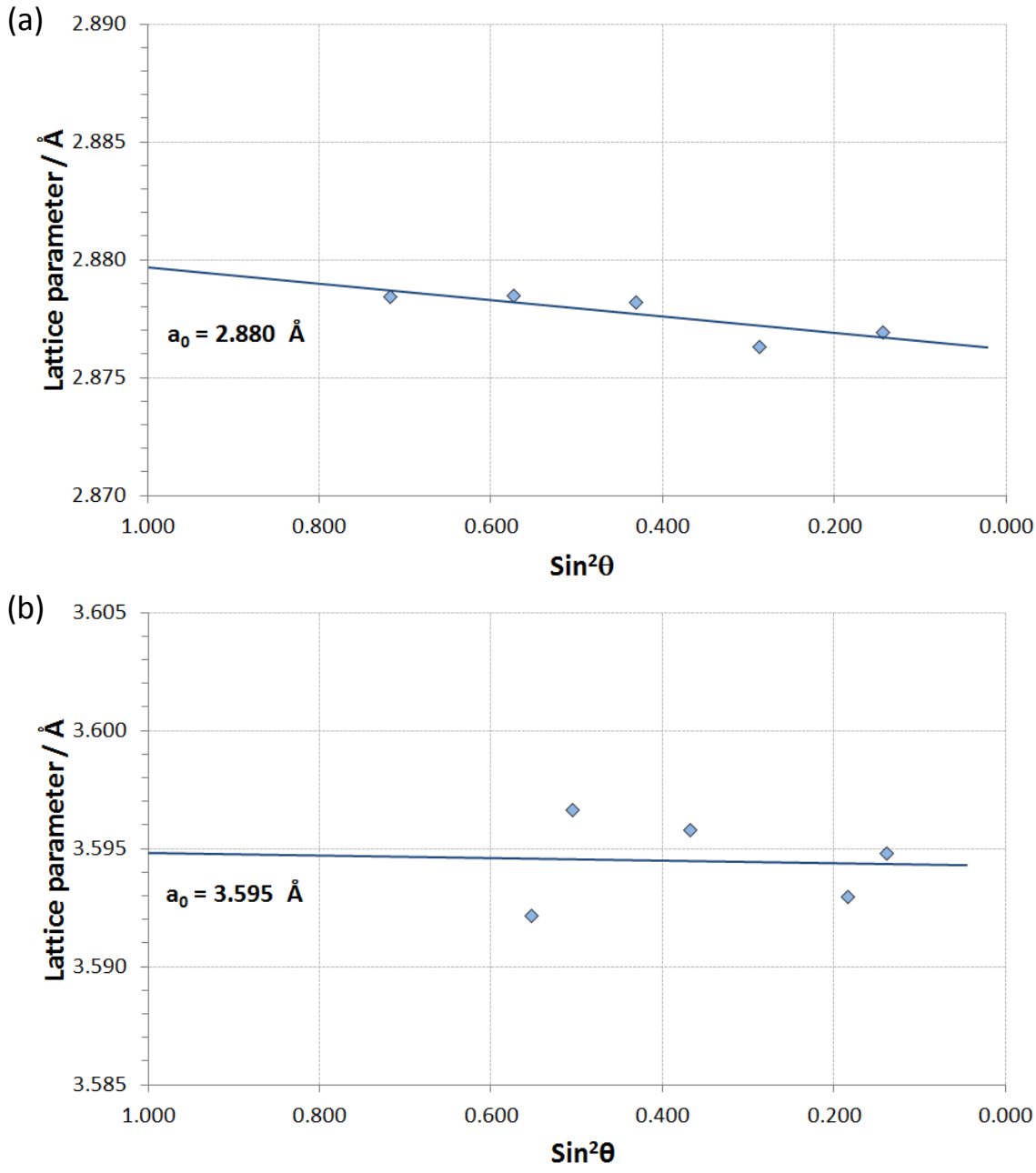

Figure 5.4 Determination of lattice parameter for (a) ferrite and (b) austenite phases

Table 5.1 details the parameters used to calculate the theoretical integrated intensity for each diffracting plane (*hkl*) as described in Chapter 4. This data was used to determine the percentage volume of retained austenite (Cγ) using the average integrated intensity of the five diffracting planes in the diffraction pattern (Figure 5.5). The volume percentage of retained austenite from ten specimens averaged 13% with a standard deviation of ±1.5%.

Table 5.1 Calculated Theoretical Intensities using Cu K_α radiation (λ = 1.541838 Å)

hkl	2θ	$/F/^2$	*p*	*LP*	e^{-2M}	*R*
(α iron, BCC, a_o = 2.88 Å, $v = a_o^3$ = 23.89)						
110	44.49	1192.7	12	11.43	0.9581	274.68
200	64.74	846.0	6	4.873	0.9180	39.79
211	81.94	714.4	24	3.138	0.8795	82.92
220	98.42	528.4	12	2.728	0.8427	25.55
310	115.7	462.2	24	3.11	0.8073	48.81
(γ iron, BCC, a_o = 3.60 Å, $v = a_o^3$ = 46.66)						
111	43.54	4957.0	8	11.91	0.9597	208.24
200	50.72	4306.6	6	8.42	0.9467	94.62
220	74.56	2968.6	12	3.665	0.8962	53.75
311	90.51	2398.3	24	2.817	0.8601	64.07
222	95.77	2253.6	8	2.737	0.8484	19.23

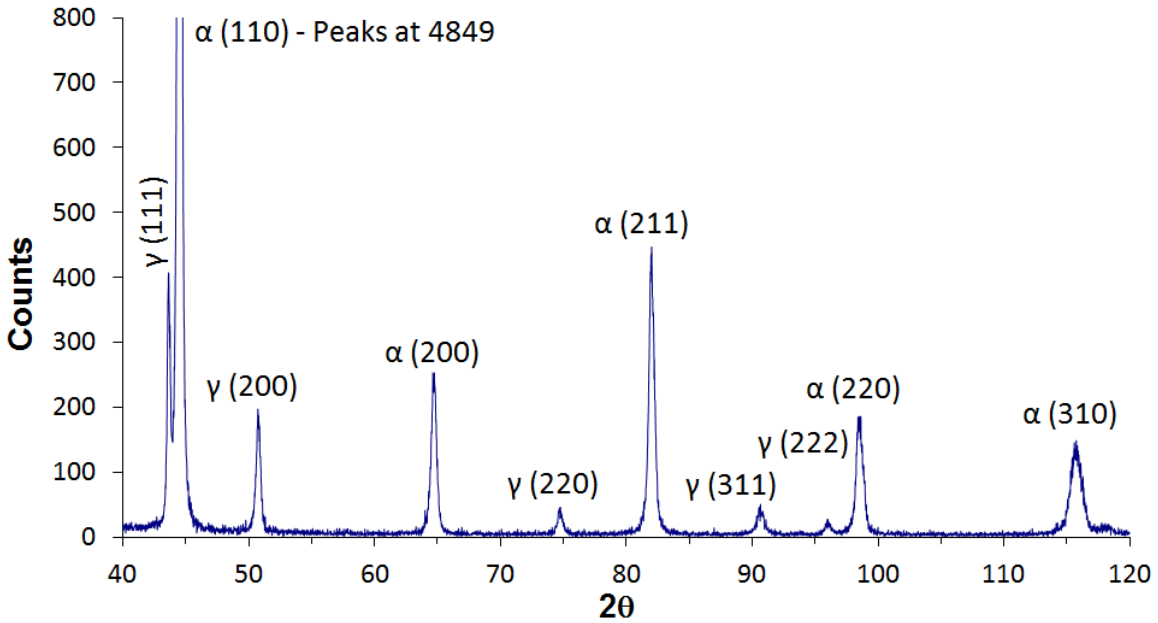

Figure 5.5 XRD pattern for the parent material containing 12% retained austenite

5.3 Tensile Tests

Figure 5.6 compares a fractured longitudinal tensile test specimen tested at 24 °C to an untested specimen (taken from the longitudinal orientation of the pipe). Following the test, elongation was 26% and reduction of area was 76%. The stress-strain curves for longitudinal and transverse specimens in Figures 5.7 and 5.8 show that yield strength decreases as temperature is increased from 24 °C to 130 °C.

Figure 5.6 Longitudinal tensile test specimens: untested specimen (top) compared to a fractured specimen tested at 24 °C (bottom). The test specimens typically elongated by 26% to fracture

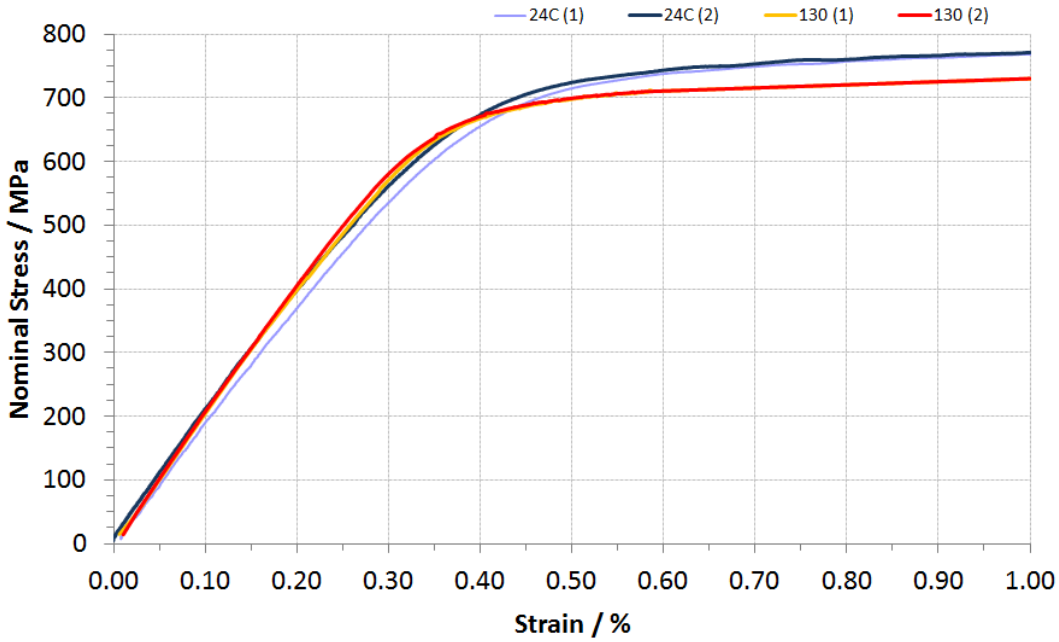

Figure 5.7 Tensile stress/strain curves: Longitudinal specimens tested at 24 °C & 130 °C. Yield strength reduces when temperature is elevated to 130 °C

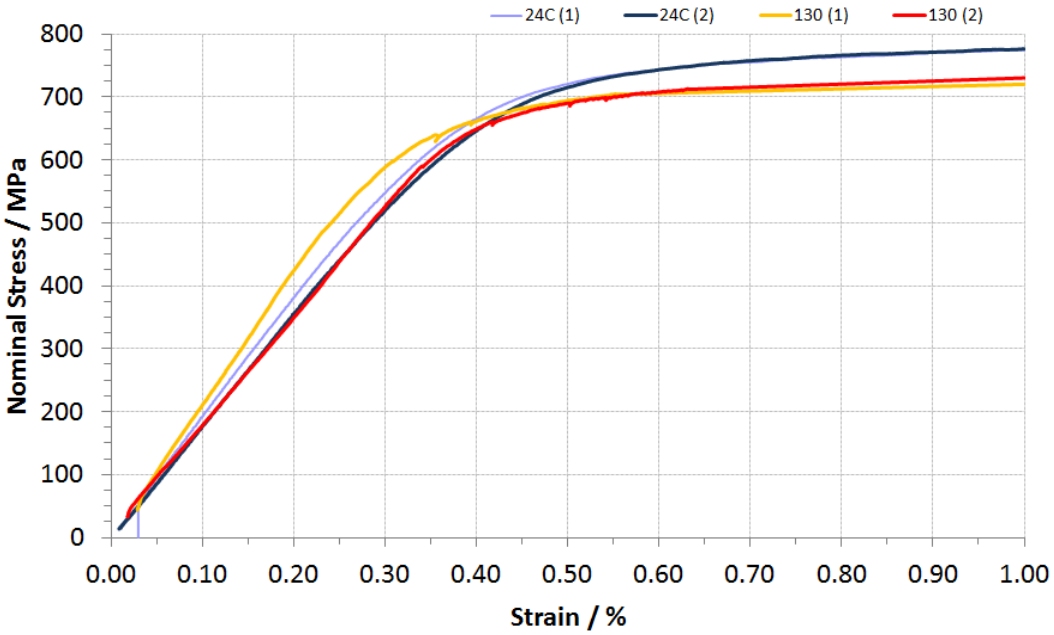

Figure 5.8 Tensile stress/strain curves: Transverse specimens tested at 24 °C & 130 °C. Transverse properties are comparable to the longitudinal properties demonstrating isotropic tensile properties in the pipe section. Yield strength reduces when temperature is elevated to 130 °C

Figure 5.9 shows the stress-strain response at 5 °C is similar to that at 24 °C. These tests were performed on a different tensile tester to the previous tests. The noise seen on the curves in Figure 5.9 was generated by the extensometer used in these tests.

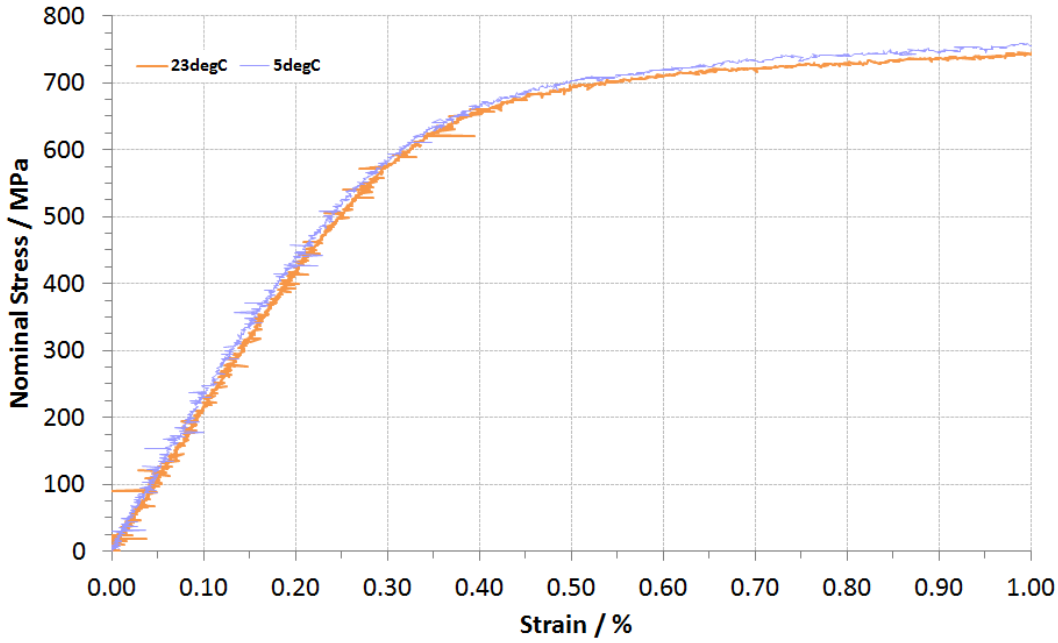

Figure 5.9 Tensile stress/strain curves: Longitudinal specimens tested at 5 °C and 24 °C. There is a slight increase in yield strength when the temperature is reduced from 24 °C to 5 °C

Tables 5.2, 5.3 and 5.4 summarise the tensile test results from the stress-strain curves given in Figures 5.9, 5.10 and 5.11. The 0.2% yield strength measured at 24 °C in Table 5.2 and 5.3 is 5% higher than the 0.2% yield strength measured at 24 °C in Table 5.4 due to the latter tests being performed on different tensile test machine. Young's Modulus is consistent within ±10% throughout the tests and yield strength decreases as temperature increases. The longitudinal and transverse test results are comparable and show that the pipe has isotropic properties in these orientations.

Table 5.2 Tensile test results: Longitudinal specimens at 24 °C & 130 °C

Temp (°C)	$\sigma_{0.2}$ (MPa)	$\sigma_{0.5}$ (MPa)	σ_{UTS} (MPa)	$\varepsilon_{0.2}$ (με)	$E_{average}$ (GPa)
24	738	714	885	6030	189
24	740	721	885	5910	
130	706	698	800	5656	204
130	706	699	805	5522	

Table 5.3 Tensile test results: Transverse specimens 24 °C & 130 °C

Temp (°C)	$\sigma_{0.2}$ (MPa)	$\sigma_{0.5}$ (MPa)	σ_{UTS} (MPa)	$\varepsilon_{0.2}$ (με)	$E_{average}$ (GPa)
24	742	720	890	5950	184
24	746	718	890	6190	
130	700	694	805	5364	194
130	709	689	810	6095	

Table 5.4 Tensile test results: Longitudinal specimens at 5 °C & 24 °C

Temp (°C)	$\sigma_{0.2}$ (MPa)	$\sigma_{0.5}$ (MPa)	σ_{UTS} (MPa)	$\varepsilon_{0.2}$ (με)	$E_{average}$ (GPa)
5	711	702	900	5492	221
5	713	696	900	5621	
24	704	693	870	5540	227
24	704	697	875	5369	

5.4 Impact Toughness

Charpy impact tests were performed to evaluate the toughness behaviour of the parent material at temperatures used for the SSC test (i.e. 5°C and 24°). The results, for both impact energy and ductile shear fracture surface, show that the ductile-to-brittle transition temperature (DBTT) is approximately -100 °C indicating that the material operates on the upper shelf during the SSC tests (Figure 5.10).

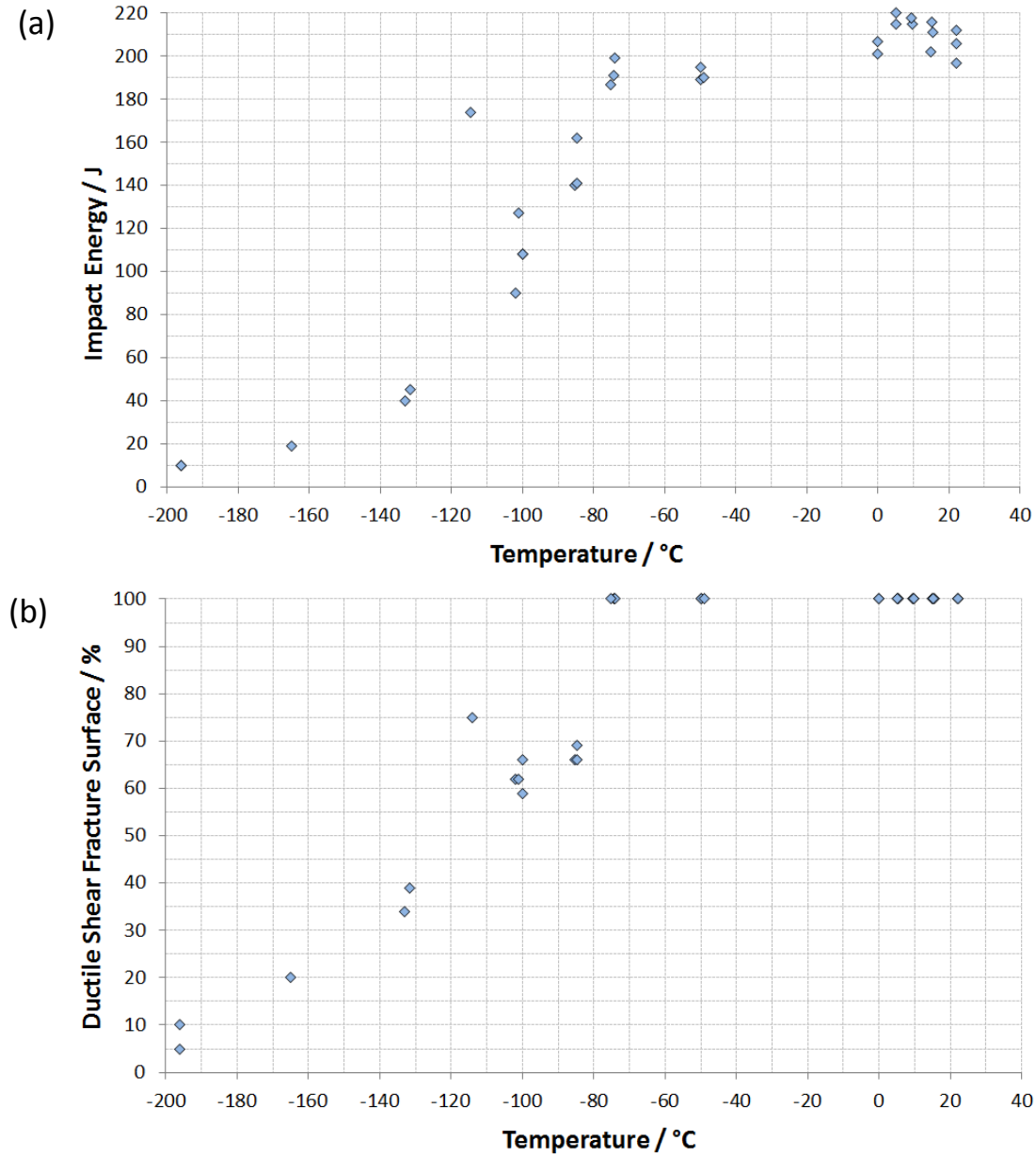

Figure 5.10 Charpy test results: (a) impact energy vs. temperature (b) ductile shear vs. temperature

Examples of fracture surfaces from the Charpy tests are shown in Figure 5.11. Specimens tested at 22 °C and -74 °C have a dimpled surface characteristic of ductile fracture. Indeed microvoids can be observed at the root of the dimples in the high magnification images. Specimens tested at -196 °C show a mixed cleavage/ductile fracture surface with areas of limited plastic deformation separating the cleavage facets. Note the fractured inclusion which appears to have initiated cleavage with some ductility on the surrounding ridges.

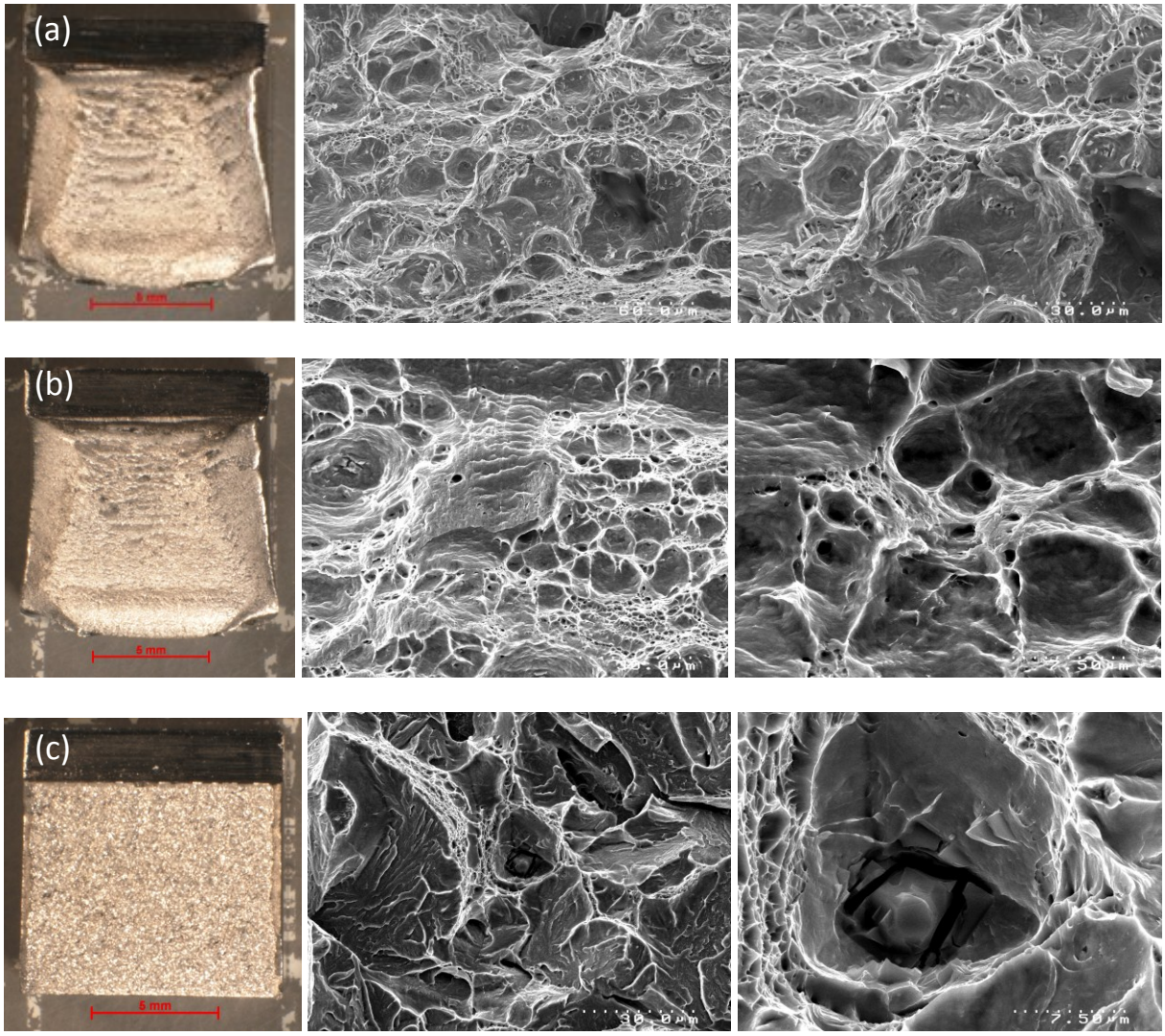

Figure 5.11 SEM images of Charpy fracture surfaces from (a) the upper-shelf at 22°C, (b) the transition region at -74°C and (c) the lower shelf at-196°C showing a fractured inclusion

5.5 Surface Roughness

Surface roughness measurements were made on three four-point bend specimens representative of the specimens used in the SSC investigation in Chapter 6. These include the alumina blasted inner bore (as-received) pipe surface, a ground surface (120 grit) representing strain gauge preparation and a fully-machined surface (600 grit). Typically rougher surfaces facilitate pitting corrosion which is a precursor to SSC, hence these roughness results are discussed in the context of the SSC test results in Section 6.4. The average surface roughness measurements in Figure 5.12 show the as-received pipe surface is the roughest (4.2 µm), followed by the ground surface (1.7 µm) and finally the fully-machined surface (0.1 µm). This order of roughness can be seen visually in the SEM images in Figures 5.13 to 5.15.

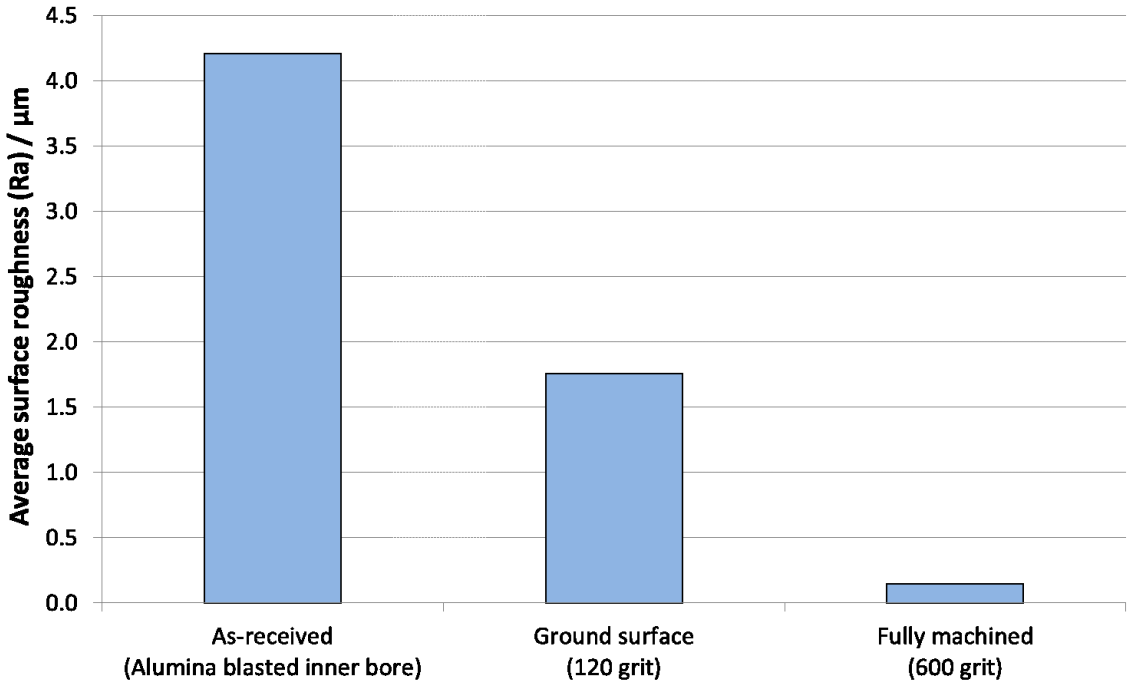

Figure 5.12 Surface roughness measurements for as-received, ground and fully-machined surfaces

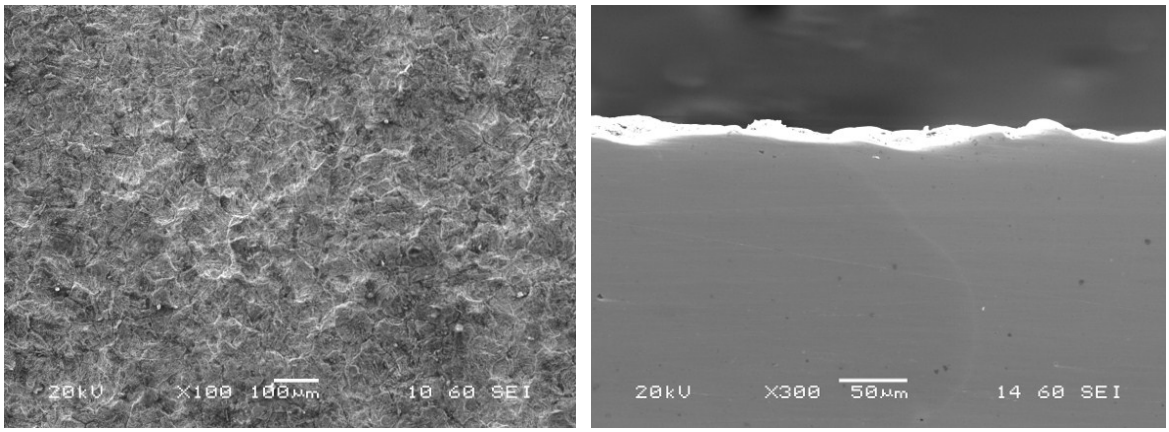

Figure 5.13 SEM image of as-received pipe surface: plan (left) cross-section (right)

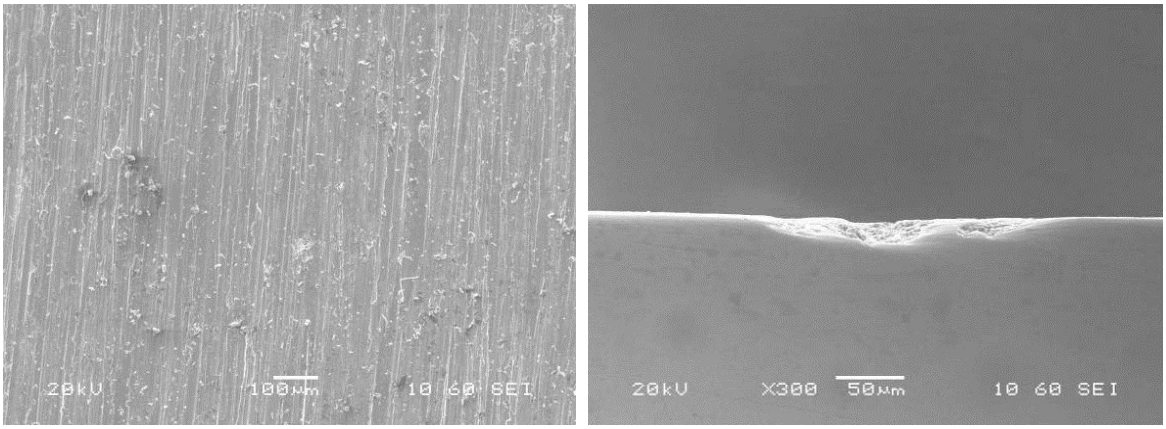

Figure 5.14 SEM image of the ground surface representing the strain-gauge application area: plan (left) cross-section (right)

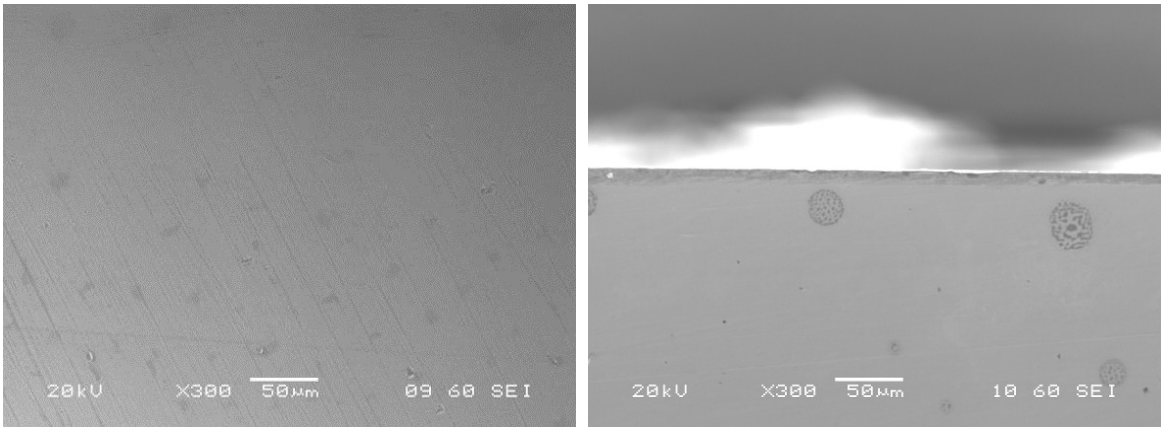

Figure 5.15 SEM image of the fully-machined surface condition: plan (left) cross-section (right)

5.6 Microindentation Hardness Measurements

The SSC resistance of steel is directly related to its strength or hardness level [18], hence hardness measurements were made through the thickness of a transverse section of parent pipe to assess the material against recommended limits given in NACE MR0175/ISO 15156-3 [4] for SSC resistance. The mean hardness was 301 HV (30 HRC) with a standard deviation of 6 HV (±2 %). Figure 5.17 shows a typical 35 µm Vickers indentation made by the 1.96 N load:

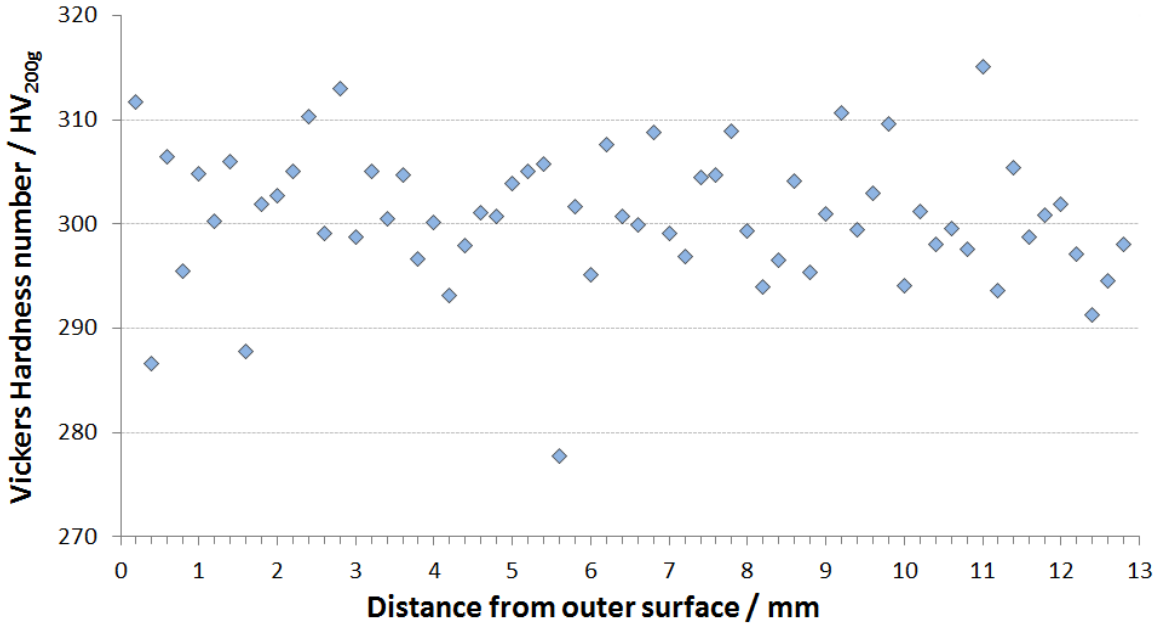

Figure 5.16 Hardness measurements (1.96 N load) taken at 0.2 mm intervals through the thickness of a transverse section of parent pipe, starting at the outer diameter

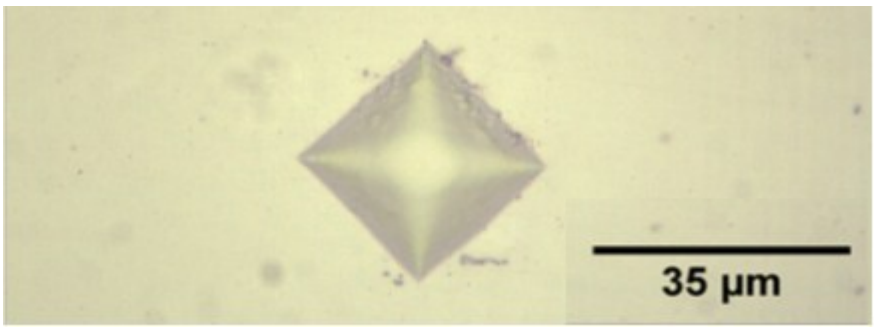

Figure 5.17 Typical Vickers indentation made in parent material from 1.96 N load

5.7 Nanoindentation Hardness Measurements

Grinding operations for strain gauge application alters the surface condition of the test sample which is subsequently exposed to a corrosive SSC test environment. Nanoindentation hardness measurements were performed to determine if such operations influences the hardness of the substrate immediately below the ground area as this could influence SSC susceptibility. Hardness measurements were made on the cross-section of two parent pipe specimens using a nanoindentation hardness tester. One specimen was left with the alumina-blasted inner-bore surface intact (as-received) and the other specimen was ground using a 120-grit automatic grinding tool as done in the scoping SSC tests to prepare the surface for strain gauge application.

The mean hardness measured mid-thickness of the pipe was 392 HV (4.15 GPa) with a standard deviation of 18 HV (0.19 GPa) or ±5 %. Figure 5.18 shows the hardness profile from the inner-bore surface for both the test specimens. The measurements were taken as close to the surface as possible to a depth of approximately 40 µm and expressed as the mean contact pressure (GPa). The results indicate that the alumina-blasted as-received surface has a higher hardness (5-7 GPa) than the ground (120 grit) surface (4-5 GPa). This confirms that the grinding operation does not locally increase hardness at the surface exposed to the SSC test environment. The hardness profile for the ground surface shows a small local increase in hardness at approximately 10 µm from the surface. This possibly shows that the grinding process has simply removed the higher hardness material associated with the as-received surface condition.

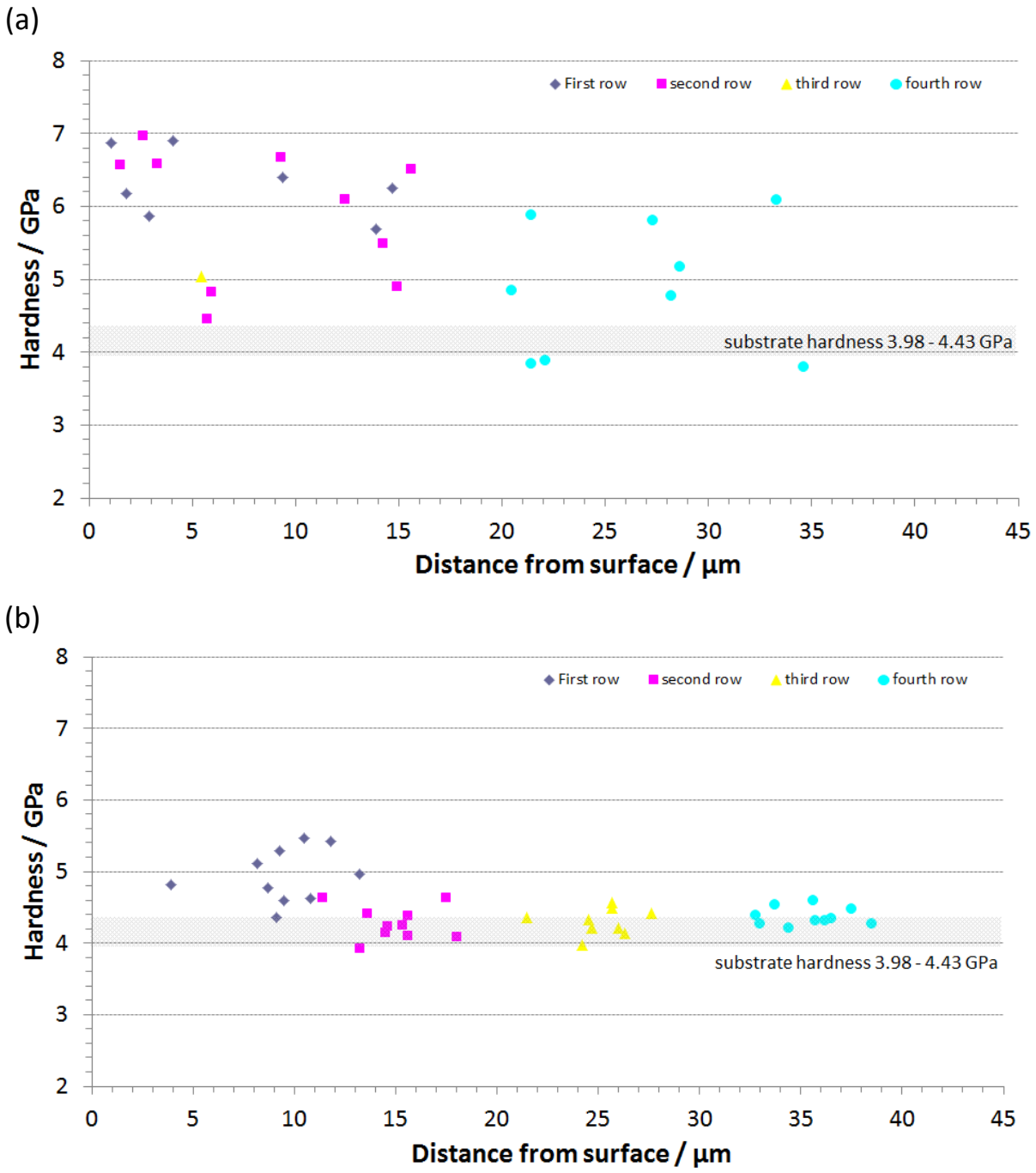

Figure 5.18 Near-surface hardness measurements for (a) alumina blasted and (b) ground surfaces. The ground surface represents strain gauge surface preparation used in the scoping SSC test specimens

5.8 Discussion

5.8.1 Microstructure

The weldable 13%Cr stainless steel pipe supplied by Nippon steel & Sumitomo Metal Corporation has a tempered martensitic microstructure populated with randomly dispersed titanium-rich inclusions. Titanium carbides typically appear grey in colour with an irregular shape under optical microscopy, yet the cuboidal shape and yellow-gold colour of the inclusions observed in this work are indicative of Ti (C, N) as reported in the literature [60]. Note that the EDS system was unable to detect nitrogen so the exact composition was not determined. Amaya *et al*. [35] showed that titanium reduces sensitisation caused by chromium carbides because the carbon atom forms stable titanium-carbide (TiC) inclusions in preference to chromium carbides. However, Enerhaug *et al*. [52] reported that titanium-alloyed supermartensitic stainless steels can be susceptible to intergranular stress corrosion cracking (IGSCC) in the as-welded condition, so titanium alone will not eliminate the risk of cracking in the HAZ of welded pipe. IGSCC in titanium-alloyed steel has been linked to phosphorus segregation at prior-austenite grain boundaries near the high-temperature fusion line in the HAZ [68,69]. Furthermore, the segregation of phosphorous atoms to grain boundaries is known to cause temper embrittlement which deteriorates impact toughness [159]. For these reasons, phosphorus levels are kept low (typically <0.02%) in supermartensitic stainless steels and welding operations are followed by PWHT to facilitate molybdenum enrichment at grain boundaries. This enrichment captures segregated phosphorous atoms and eliminates the harmful effect on SCC propagation. It must be noted that measurements of phosphorus along grain boundaries were not performed in this work.

The presence of austenite in the martensitic microstructure benefits the performance of 13%Cr martensitic stainless steels. First, phosphorus atoms do not segregate to martensite/austenite boundaries, contributing to the low temperature impact toughness of these steels [159]. Secondly, weldable 13%Cr supermartensitic stainless steels show improved SSC resistance with 10% or more retained austenite in the microstructure [95]. This is potentially due to preferential trapping of hydrogen in the soft austenite phase instead of the hard martensite phase [99,100], reducing the likelihood of hydrogen embrittlement.

XRD measurements in Section 5.2 showed that the as-received pipe contained an average volume fraction of 13% retained austenite in its unstressed condition and these measurements were consistent with XRD measurements reported in the literature for a similar grade of weldable 13%Cr supermartensitic stainless steel [60]. Cold work can transform retained austenite into martensite [100,103] so the volume fraction of retained austenite in a stressed section of material could be well below the 10% threshold that gives improved SSC resistance.[26] This is of particular importance to 13%Cr pipeline that has been reeled and unreeled during the installation process as this procedure will impart plastic strain into the material and potentially reduce its SSC resistance.

XRD has been widely used to measure retained austenite in low-carbon martensitic stainless steels and supermartensitic stainless steels [24,60,66,98-100,159,160] even though

[26] An attempt was made to quantify the effect of cold work on retained austenite content using tensile test specimens. However, the results were inconclusive so this investigation is a recommendation for future work.

the technique is influenced by stress at the sample surface, texture, grain size, instrumental limitations and a penetration depth limited to several microns [161]. These limitations could account for the relatively large scatter seen in the XRD test results for the as-received material (6% to 17%). Furthermore, the use of Cu K_α radiation increases the level of background noise and can obscure the shape of the peaks because Iron in steel fluoresces under this radiation source [149]. Magnetic techniques such as saturation magnetisation measurements have been used to overcome the shortcomings of XRD as they are more accurate and probe the bulk of the material [162].

5.8.2 Mechanical Properties

Room temperature tensile tests were performed to generate the necessary stress-strain data required for the finite element modelling work presented in Chapter 7. The material showed isotropic tensile properties in the longitudinal and transverse orientations. It is well known that yield strength decreases as temperature increases [157], and this was verified in the tensile tests performed at 24 °C and 130 °C. There was negligible difference in the measured yield stress between 24 °C to 5 °C. The Charpy impact results show that the ductile-to-brittle transition temperature is around -100 °C to -110 °C which means that the material is safely operating on its upper shelf at 5 °C and 24 °C during the SSC tests. However, fracture toughness may be reduced at 5 °C compared to 24 °C as it is seen for low alloy steels in conventional fracture mechanics testing [75,163].

The mean hardness of the as-received pipe was measured as 301 HV (30 HRC) from the microindentation tests. This value exceeds the 27 HRC limit given in Table A.19 in NACE

MR0175/ISO 15156-3 [4] for a similar grade (UNS S41426) supermartensitic stainless steel when used for downhole tubular and other subsurface equipment. The substrate hardness measurements made by the nanoindentation technique were higher than those made by the microindentation technique (392 HV compared to 301 HV). In the nanoindentation technique, hardness is measured as a *mean contact pressure* (GPa) and is determined by dividing the peak load (mN) by the projected area of contact.[27] The mean contact pressure measures the resistance of the material to combined elastic and plastic deformation whereas conventional Vickers hardness is calculated from the indenter load and a direct measurement of the residual hardness impression. When measuring the residual hardness impression, a portion of the contact area under load may not be plastically deformed, and as a result, the contact area may be less than that at peak load [164]. Vickers hardness is typically lower than the mean contact pressure by approximately 7% [165].

The nanoindentation hardness measurements showed that local grinding operations on the alumina-blasted inner bore pipe surface does not increase hardness of the underlying material close to the surface. Furthermore, the material close to the alumina-blasted surface is harder than the substrate away from the inner and outer bore. Grit blasting and shot peening are cold working processes that locally work hardens the surface and introduces near-surface residual compressive stress to the material which generally improves fatigue resistance. In addition, Tosha *et al.* reported that these processes can cause strain-induced transformation of austenite [166]. Although not investigated in this thesis, the implications

[27] The depth of penetration at peak load and the geometry of the indenter are used to estimate the size of the contact area

for this material would be the conversion of retained austenite to fresh martensite which could degrade the SSC resistance, particularly if the grinding operation exposes fresh martensite to the H_2S containing environment. However, residual compressive stresses imparted by the alumina blasting process may be beneficial to SSC resistance by slowing the rate of hydrogen diffusion in steels; Wandell [167] reports that shot peening retards the time taken for hydrogen to migrate through a metal surface and more significantly lowers the steady state permeation rate of hydrogen by as much as 24%.

When four-point-bend specimens are prepared for SSC testing with the as-received pipe surface intact, a small area of the pipe surface is removed at the mid-length, mid-width position using an automatic grinding tool fitted with a 120 grit sanding band. Although the grinding process removes the hardest layer of material (see nanoindentation test results), this does not coincide with an improved resistance to SSC (as shown in next Chapter) because the grinding operation is also removing the beneficial residual compressive stresses imparted by the grit blasting process as described above. Furthermore, grinding processes can create areas of localised damage as shown in Figure 5.14, which could act as localised stress concentrator sites and/or increased surface roughness that increases susceptibility to pitting corrosion. Hinds *et al.* [168] showed that pitting occurred preferentially at physical defects introduced during machining and grinding process rather than at inclusions in a 316L austenitic stainless steel. However, further investigation is needed to determine if weldable 13%Cr martensitic stainless steel responds in the same way.

CHAPTER 6: RESULTS & DISCUSSION
Sulphide Stress Cracking Investigation

The aim of the work presented in this chapter is to determine if a weldable 13%Cr supermartensitic stainless steel pipeline material is more susceptible to SSC at seabed temperatures (5 °C) compared to standard room temperature tests (24 °C). The SSC tests are performed in simulated Produced Water and Condensed Water environments at 70 mbar and 38 mbar H_2S partial pressures using the four-point bend test method with specimens prepared in the as-received and fully-machined condition. Recall the as-received condition retains the inner bore of the pipe and the fully-machined condition is wet-ground to a 600-grit finish with a rectangular cross-section (Figure 4.4). Note that all the SSC test results in this chapter are presented in terms of total number of cracks on the test surface, the location of cracking on the test surface and the maximum crack depth penetration through the thickness of the specimen.

6.1 Verification of the Scoping SSC Tests

These initial SSC tests were performed using the same apparatus as the SSC tests performed by Bodycote Corrosion Centre in 2005 which indicated that 7 °C was a more severe test environment than 24 °C for a weldable 13%Cr supermartensitic stainless steel. The scoping SSC test results show that SSC was more severe at 5 °C when compared to tests performed at room temperature. This work also highlighted issues with specimen preparation as cracking occurred preferentially at the chamfered edges and where the as-

received pipe surface had been removed for strain gauge application. The solution pH was unstable in the Condensed Water tests so a valid comparison of SSC resistance at 5 °C and 24 °C could not be made. Furthermore, the test setup used did not have provisions for monitoring dissolved oxygen levels in the test solution so it was not known if oxygen contamination influenced the results.

6.1.1 Scoping SSC Tests: Produced Water Results

SSC tests were performed in simulated Produced Water at 5 °C and 24 °C. The test solution pH remained stable within a ±0.1 tolerance and temperature was controlled to ±3 °C. Figure 6.1 presents the results of the as-received and fully-machine test specimens exposed to 70 mbar H_2S and 38 mbar H_2S (5 °C and 24 °C) in terms of the total number of cracks by location on the tensile test surface. The results clearly show that all the cracking on the as-received specimens occurred where the original pipe surface was abraded for either strain gauge application or where the edges had been chamfered (See Figure 6.2 and Figure 6.3). No SSC was observed where the as-received surface remained intact, indicating that the as-received surface condition is resistant to SSC at 70 mbar H_2S and 38 mbar H_2S.

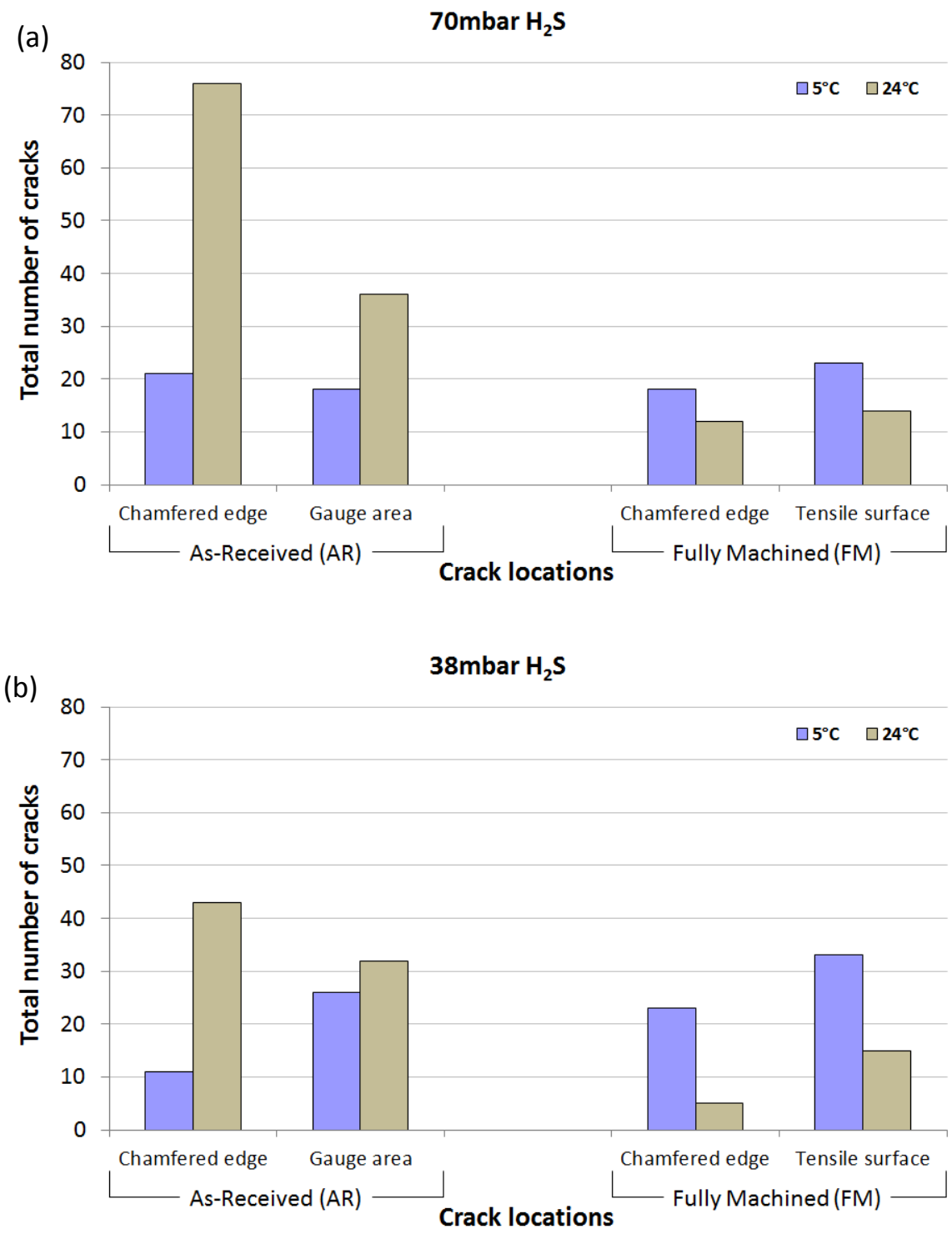

Figure 6.1 Total number of cracks by location on the tensile test surface in as-received and fully-machined specimens tested at 5 °C and 24 °C in Produced Water when exposed to (a) 70 mbar H_2S and (b) 38 mbar H_2S partial pressures. All cracking on the as-received specimens was located at the chamfered edges or the strain gauge area where the original pipe surface had been removed. No cracking was observed where the original pipe surface remained intact

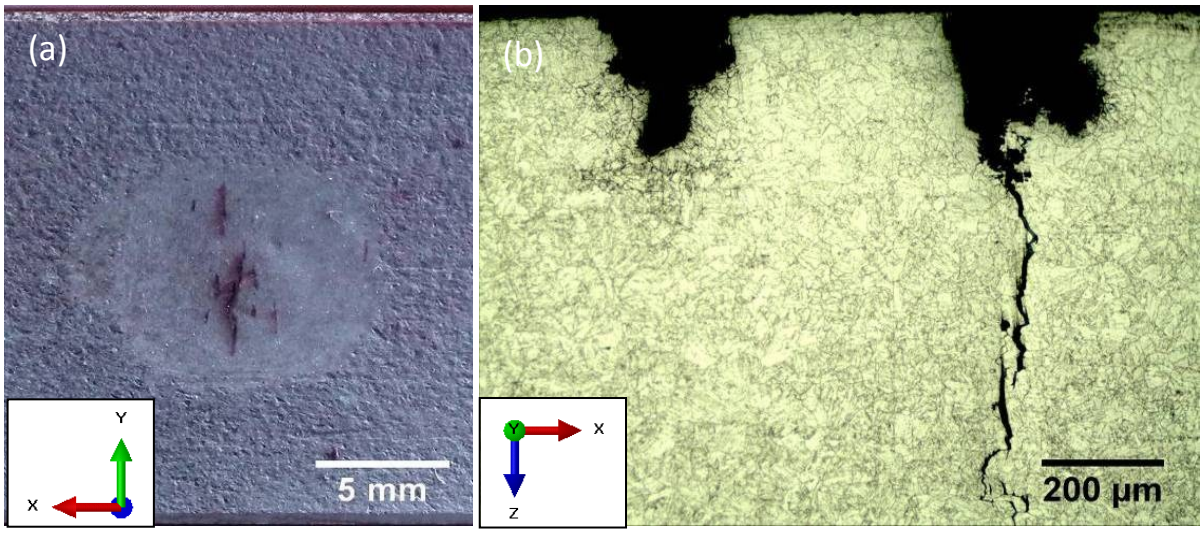

Figure 6.2 SSC concentrated on the test face of an as-received specimen where the original pipe surface has been removed for strain-gauge application. (a) Plan view on tensile test surface and (b) micrograph showing surface corrosion pit with crack propagation through the thickness of the specimen. Section etched with Vilella's reagent. Specimen exposed to 38 mbar H_2S in simulated Produced Water at 5 °C

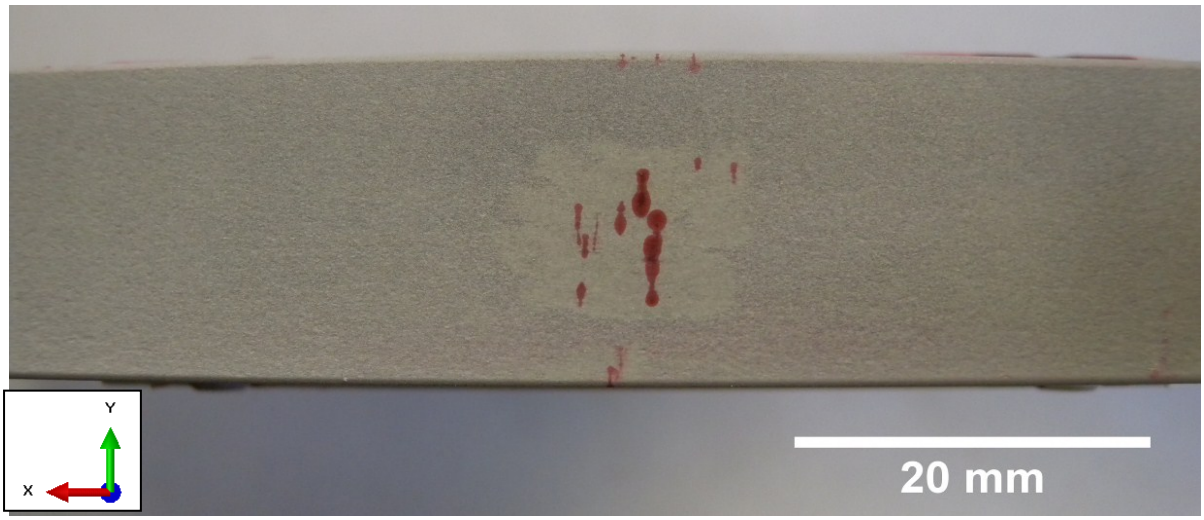

Figure 6.3 SSC concentrated on the test face of an as-received specimen where the original pipe surface has been removed for strain-gauge application and along chamfered edges. Specimen exposed to 70 mbar H_2S in simulated Produced Water at 5 °C

Since the as-received surface is entirely removed on the fully-machined specimens, cracking is more evenly distributed across the tensile surface. However there is still a tendency for cracking to occur along the chamfered edges (Figure 6.4).

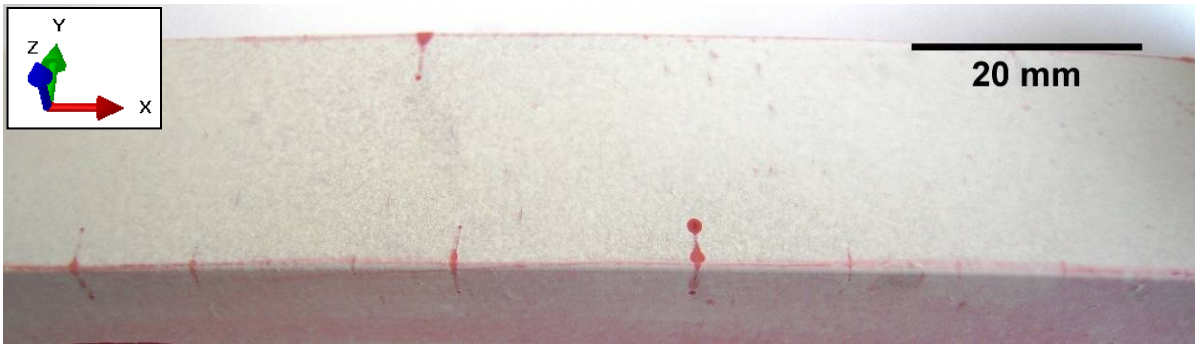

Figure 6.4 SSC concentrated along the edges of a fully-machined test specimen exposed to 70 mbar H_2S in simulated Produced Water at 5 °C

Figure 6.5 shows a section taken in the longitudinal orientation (x-axis) through the thickness of a fully-machined specimen exposed to 70 mbar H_2S in simulated Produced Water at 5 °C. Metallographic examination showed that SSC propagation was intergranular with areas of metal dissolution at the surface exposed to the test environment.

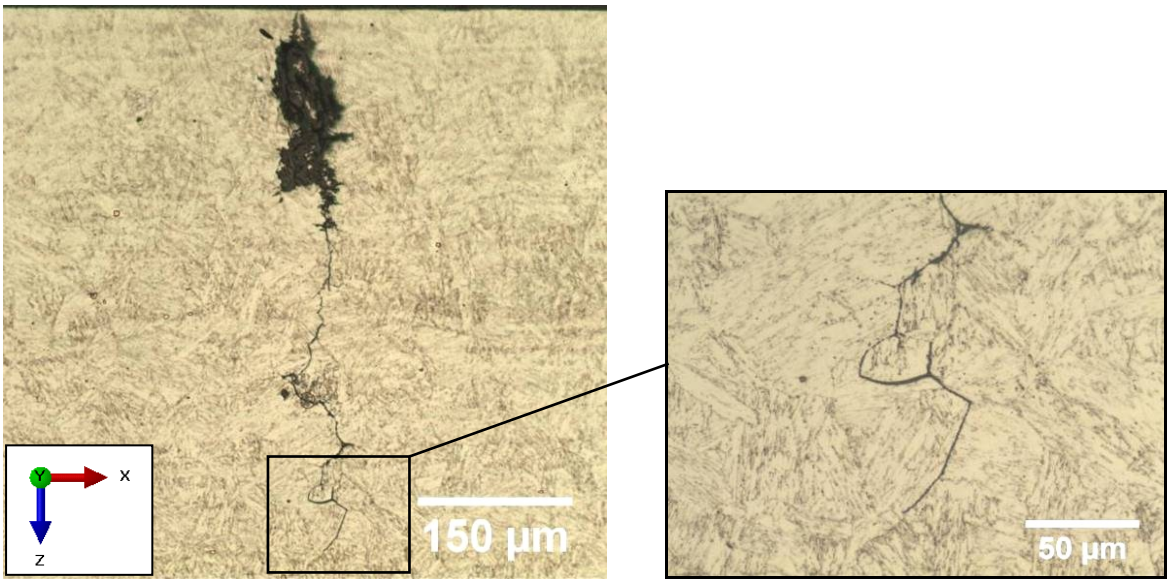

Figure 6.5 Micrograph showing intergranular SSC in a fully-machined specimen tested at 70 mbar H_2S in simulated Produced Water at 5 °C. Transverse section etched with vilella's reagent

The SSC test results are presented in terms of maximum crack depth in Figure 6.6 and show that the deepest cracks were present in the as-received and fully-machined specimens

when tested at 5 °C. The same trend was also observed with specimens exposed to 70 mbar H_2S and 38 mbar H_2S partial pressures.

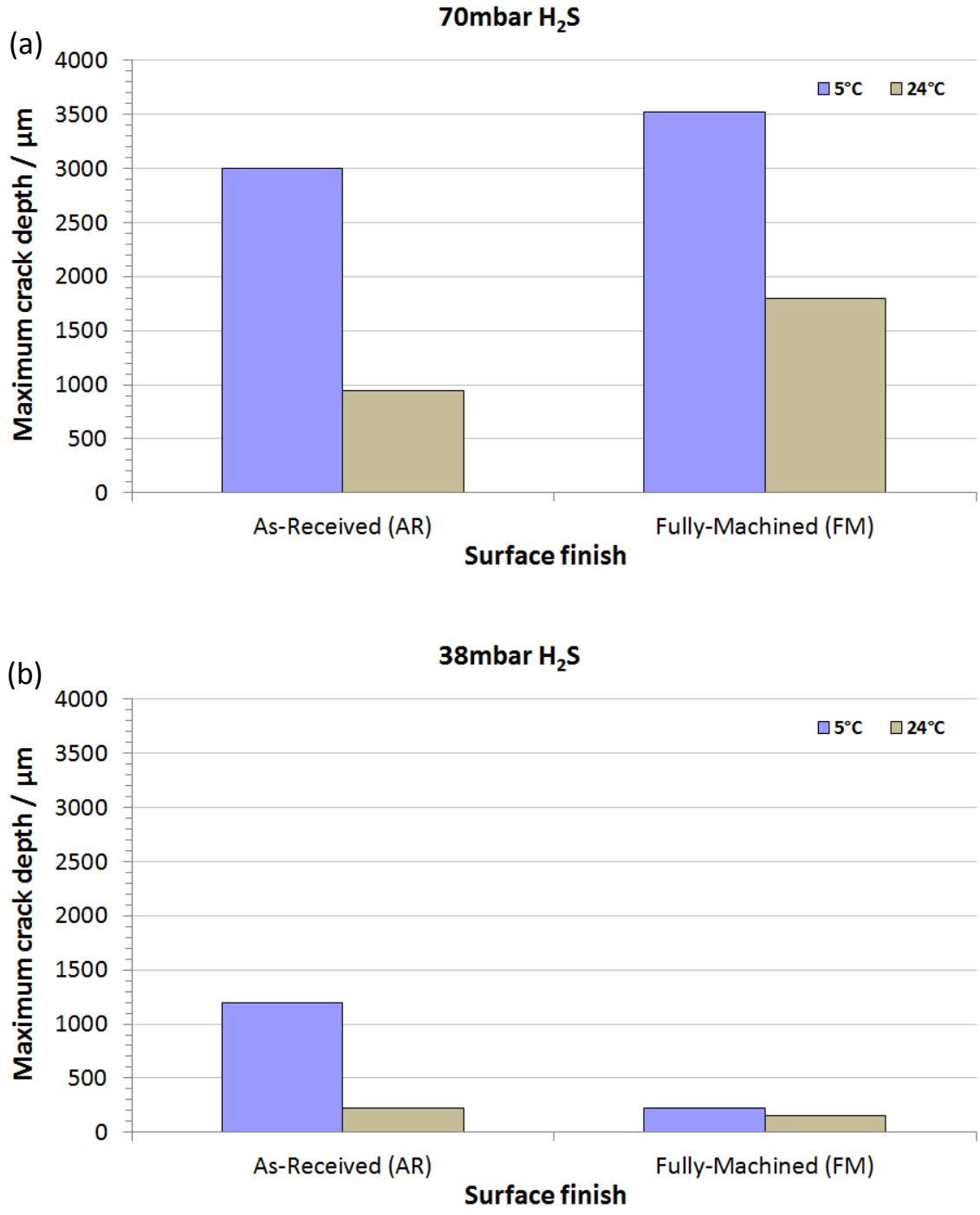

Figure 6.6 Maximum crack depth penetration though the thickness of as-received and fully-machined SSC specimens tested at 5 °C and 24 °C in Produced Water when exposed to (a) 70 mbar H_2S and (b) 38 mbar H_2S partial pressures. The deepest cracks were present in the specimens tested at 5 °C

6.1.2 Scoping SSC Tests: Condensed Water Results

Figure 6.7 shows that SSC only occurred at the chamfered edges on the as-received specimens exposed to 70 mbar H_2S when tested at 5 °C. None of the fully-machined test specimens cracked and none of the test specimens cracked at 24 °C. This is likely to be due to the unstable solution pH which drifted above the 3.5±0.1 tolerance specified in EFC17 [7]. The specimens tested at 5 °C had a final pH of 3.94 and the specimens tested at 24 °C had a final pH of 4.49 so a valid comparison between the SSC resistance at 5 °C and 24 °C could not be made from these results. For this reason, repeat tests at 38 mbar H_2S were not performed.

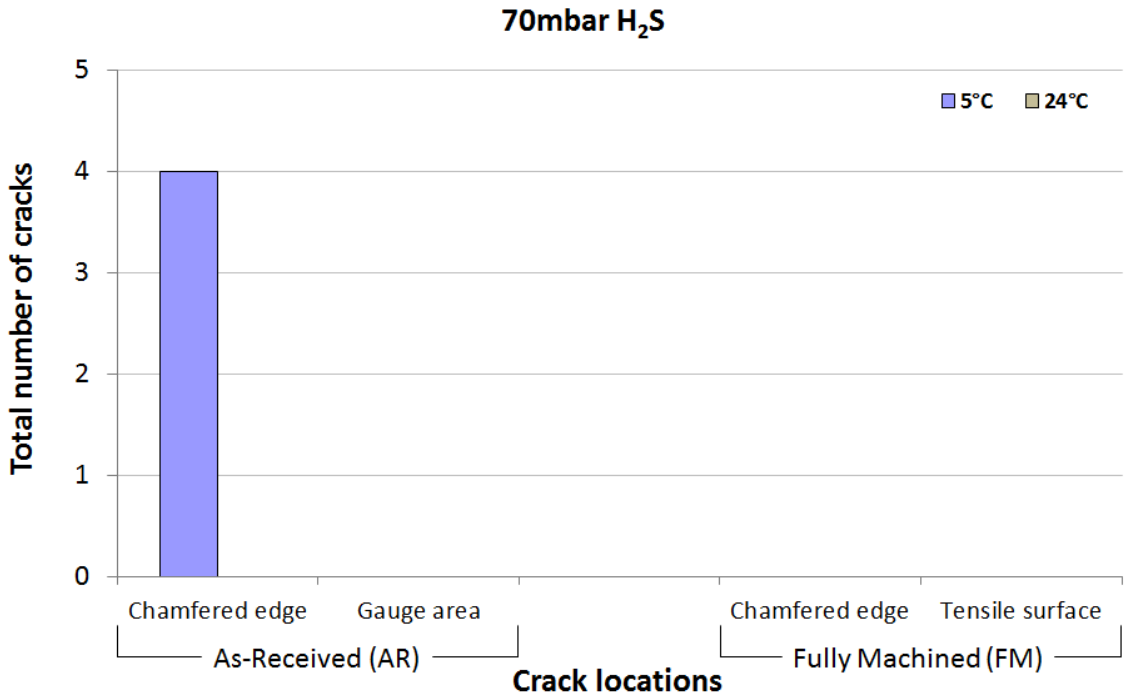

Figure 6.7 Total number of cracks by location on the tensile test surface in as-received and fully-machined specimens tested at 5 °C and 24 °C in Condensed Water when exposed to 70 mbar H_2S. Cracking only occurred on the chamfered edges of the as-received specimens tested at 5 °C

The absence of cracking on the fully-machined surfaces indicates that the material is resistant to SSC in low chloride solutions at 70 mbar H_2S for pH values of 3.94-4.49.

6.1.3 Summary of the Scoping SSC Tests

The scoping SSC test results are summarised in Figure 6.8 which shows that the deepest cracks occurred in the specimens tested at 5°C.

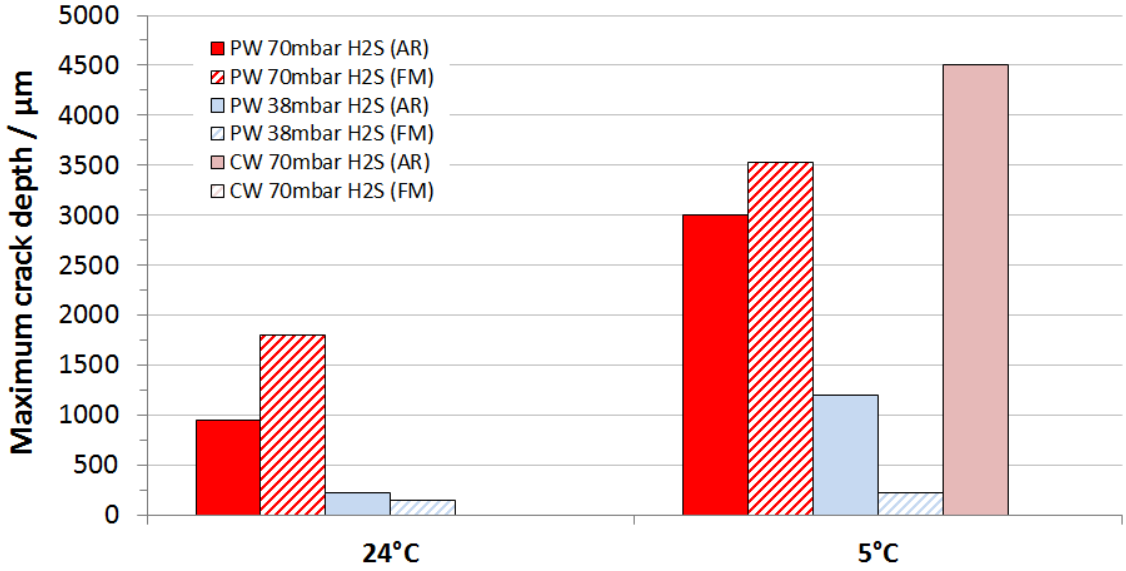

Figure 6.8 Summary of scoping SSC test results (maximum crack depth vs temperature)

Other key observations include:

1. The as-received pipe surface provides better SSC resistance than the fully-machined surface. Grinding the as-received pipe surface for application of strain gauges or at the chamfered edges increases the likelihood of SSC.

2. Solution pH in the Condensed Water environment was unstable so a valid comparison of SSC resistance at 5 °C and 24 °C could not be made.

3. The test setup used had no provisions for monitoring dissolved oxygen in the test solution, so the potential for dissolved oxygen contamination cannot be ruled out in these tests.

6.2 SSC Test Protocol Development & Modification Results

Following the observations made in the previous section, the SSC test method was developed to monitor and provide improved control of dissolved oxygen and solution pH. Strain gauges were applied directly to the as-received surface to maintain the original pipe condition and avoid preferential cracking in this area. The four-point bend loading jig was re-designed to give improved strain stability in the test specimen and idometric titrations were performed in the temperature range of 5 °C to 25 °C to assess how H_2S solubility varies with temperature in Produced and Condensed Water environments.

6.2.1 Oxygen Control

Figure 6.9 shows how oxygen varies with temperature over the duration of a 30 day SSC test in the new test rig. The graph shows that dissolved oxygen levels remain below 4 ppb for the duration of the test, well below the 10 ppb threshold stated in EFC17 [7].

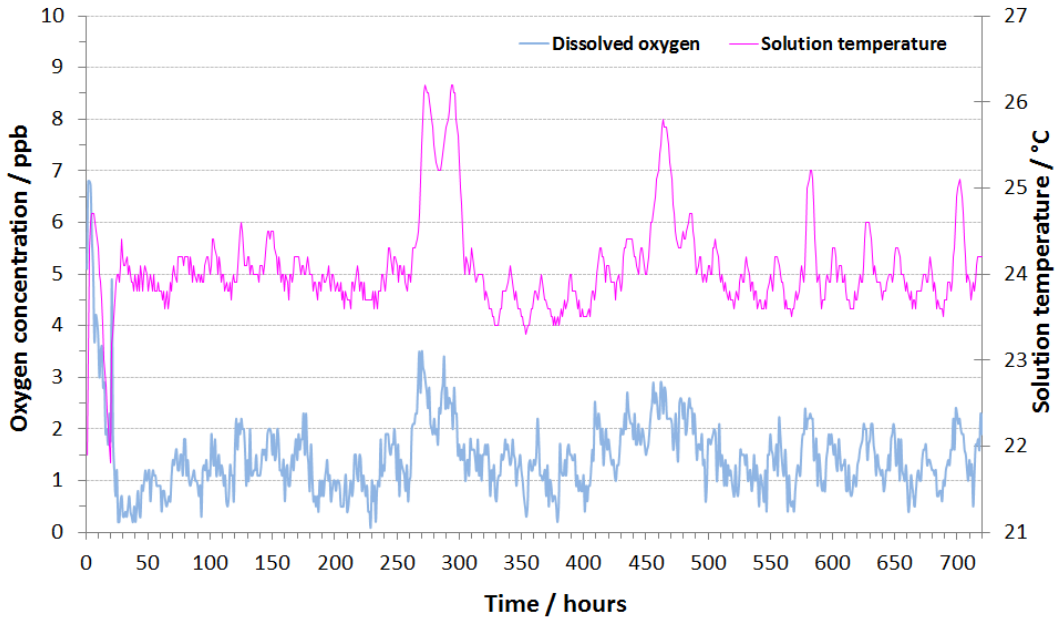

Figure 6.9 Dissolved oxygen in simulated Produced Water test solution saturated with 35 mbar H_2S @ 24 °C. O_2 remains below 4 ppb for 30 day test period. Small fluctuations due to temperature changes

Figure 6.10 shows the difference in surface appearance between a fully-machined specimen tested in the SSC scoping tests and a specimen tested in the new rig with oxygen controlled to <10 ppb throughout the test. Apart from oxygen control, both specimens were tested under the same environmental conditions (i.e., simulated Produced Water at 5 °C and 70 mbar H_2S partial pressure). More cracks and small areas of pitting can be seen on the specimen tested without oxygen control in the scoping tests compared to fewer cracks and no pitting on the specimen tested with oxygen control.

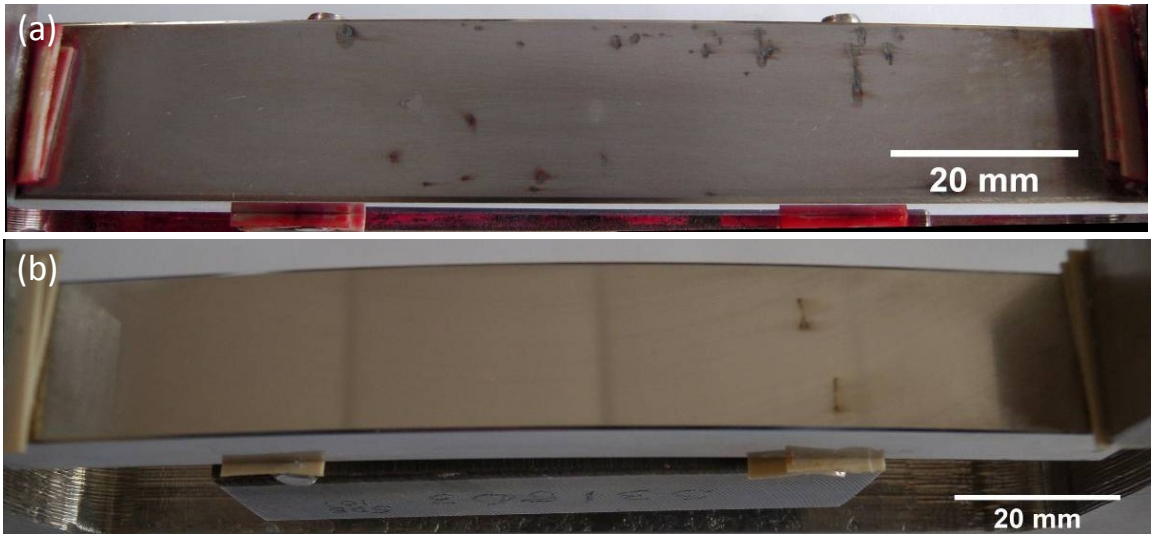

Figure 6.10 (a) SSC specimen tested in the scoping tests using original test apparatus (O_2 level unknown) & (b) SSC specimen tested in new rig with O_2 controlled to <10 ppb.

6.2.2 Loading Strain Stability

Figure 6.11 shows the longitudinal strain response of two as-received specimens loaded in a constant-strain four-point bend rig for 30 days. The blue trace shows the specimen loaded in the old style rig and the pink trace shows the specimen loaded in the new rig. The initial strain relaxation is more severe in the old style SSC rig compared to the new style rig, but after this initial drop, strain remains relatively stable in both specimens for the remainder of the test.

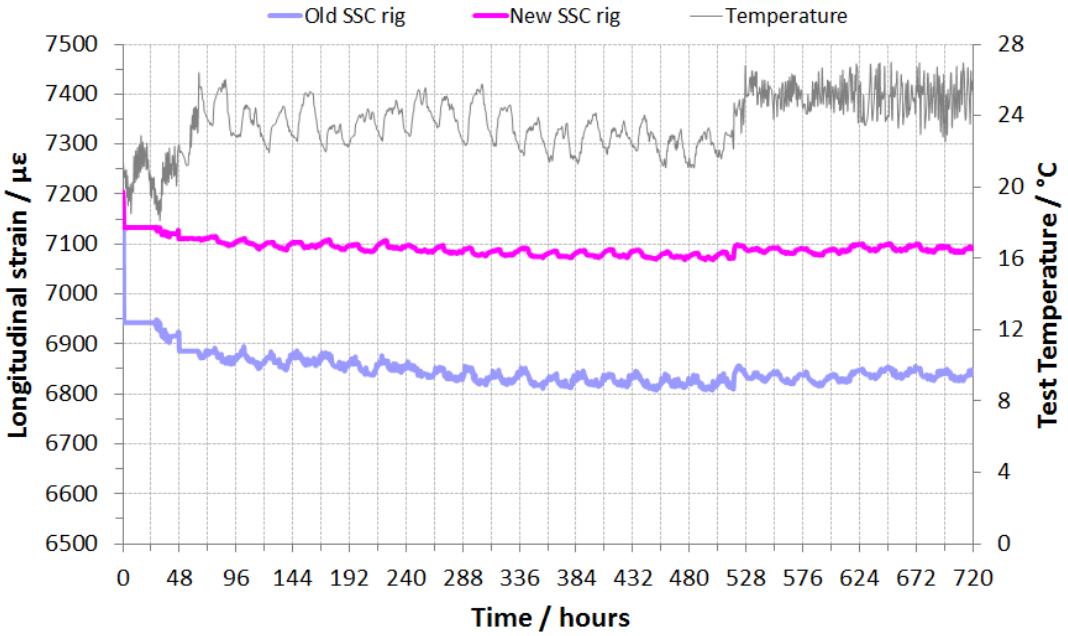

Figure 6.11 Strain response of an as-received specimen loaded in old and new style SSC rigs. Strain drops initially after loading but remains stable for the remainder of the test

The initial drop in strain occurs during the first hour after loading and is more severe with the specimen loaded in the old style rig. The reason for this can be linked to the use of PEEK insulation between the specimen and the rollers which deforms under the applied load (Figure 6.12) In both cases, strain is relatively stable after 1.5 hours (Figure 6.13), so this represents the minimum monitoring time for loading four-point bend SSC test specimens before removing the strain gauge. During this time, strain should be monitored and adjusted to the desired target strain to ensure the specimen is correctly stressed for the test.

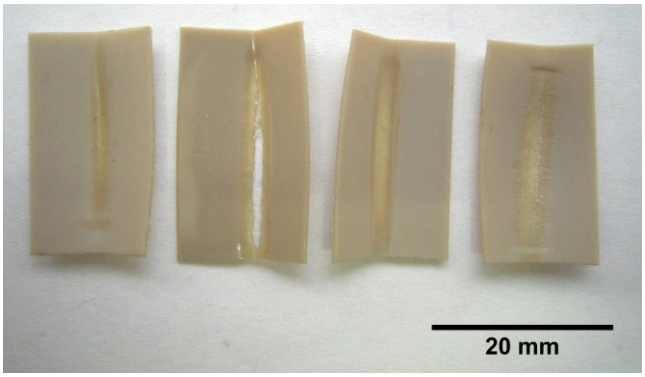

Figure 6.12 Degradation of PEEK insulation from the inner rollers of the old style rig after 30 days

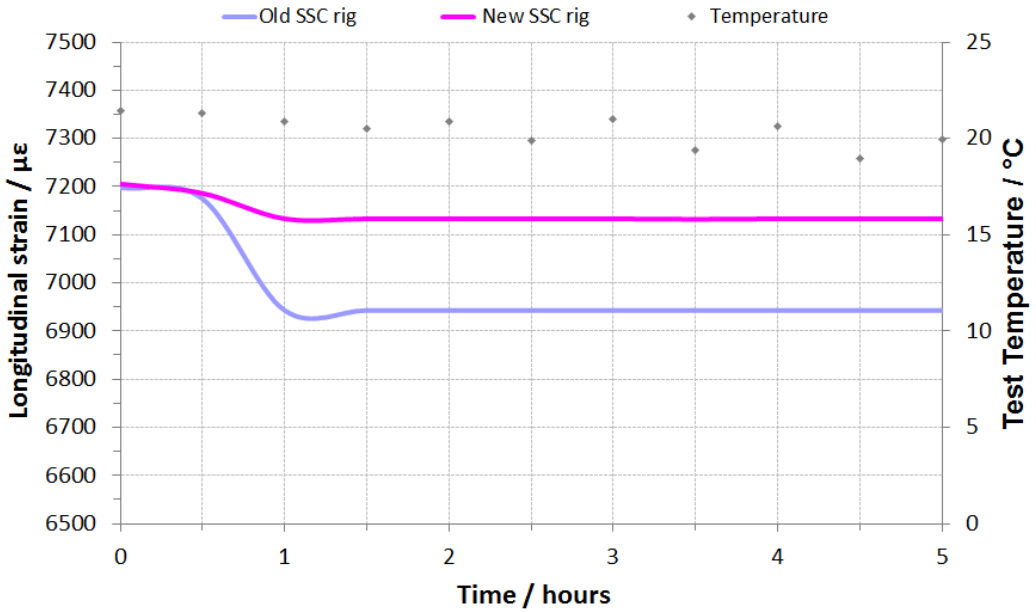

Figure 6.13 Strain response of as-received specimens loaded in old and new style SSC rigs. Initial drop in strain occurs during the first hour after loading and is more severe when using the old style rig

6.2.3 H_2S Solubility

The results in Figure 6.14 show that H_2S solubility increases with both decreasing temperature and decreasing salinity (chloride concentration). Therefore H_2S solubility is greatest in low temperature Condensed Water environments.

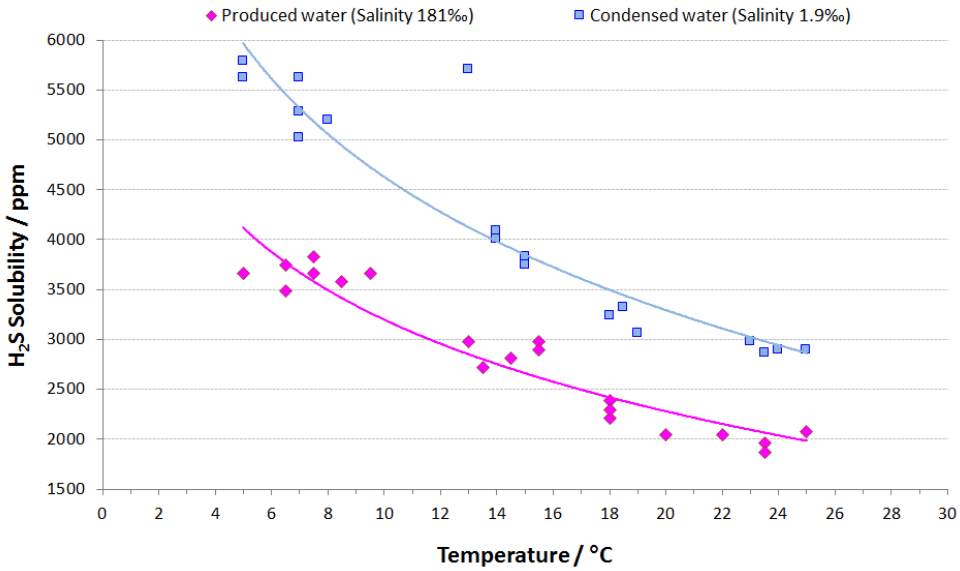

Figure 6.14 Influence of temperature and chloride concentration (salinity) on H_2S solubility. Solubility increases as temperature and salinity decreases

These results are comparable to data published by Douabul and Riley [169] where H_2S solubility (mol/l)[28] was measured in acidified distilled water and seawater (both at pH 3.0) up to a salinity of 40‰[29] (22,157 mg/l Cl^-). Although the highest salinity measured was lower than the simulated Produced Water in Figure 6.14 (181‰), the general trend holds that H_2S solubility increases with decreasing temperature and salinity.

6.2.4 Summary of the SSC Test Protocol Development & Modifications

1. A new SSC test rig has been developed to monitor dissolved oxygen and maintain pH stability of the test solution, ensuring consistency of results and compliance with EFC17 guidelines whereby oxygen must be kept below 10 ppb and pH controlled to ±0.1.

2. Strain stability trials have shown that the use of ceramic rollers reduces the amount of strain relaxation experienced after initial loading and reduces the likelihood of galvanic corrosion between loading jig and test specimen.

3. When loading weldable 13%Cr supermartensitic stainless steels in four-point bending, strain should be monitored for at least 1.5 hours after initial loading and adjusted accordingly to obtain the correct loading strain prior to exposure to the test environment.

4. Idometric titrations of simulated Produced and Condensed Water solutions showed that H_2S solubility increases with decreasing temperature and decreasing salinity.

[28] Mol/l is converted to ppm by multiplying by 1000 (mmol/l) then multiplying by the molecular weight of H_2S
[29] ‰ = parts per thousand. Salinity = chlorinity x 1.80655

6.3 Seabed Temperature SSC Investigation Results

With the controls in place from the SSC test protocol development and modifications phase, SSC tests were performed at 5 °C and 24 °C using fully-machined (rectangular cross-section and ground to a 600 grit finish) and as-received (retaining the curvature of the inner and outer pipe surfaces) specimens loaded in four-point bending. Dissolved oxygen was controlled to <10 ppb and temperature was controlled to ±2 °C in all the tests (Data in Appendix 2). The results show that SSC was more severe at 5 °C compared to 24 °C in the simulated Produced Water environment and the as-received surface condition provided improved SSC resistance compared to the fully-machined surface condition. It was noted that the inner loading rollers and edges may exacerbate cracking in the four-point bend test.

6.3.1 Crack Locations

Three regions were defined on the tensile test surface of the four-point bend test specimens to categorise the location of cracking in each specimen. The regions are defined as the central region, inner loading rollers and chamfered edges as detailed in Figure 6.15.

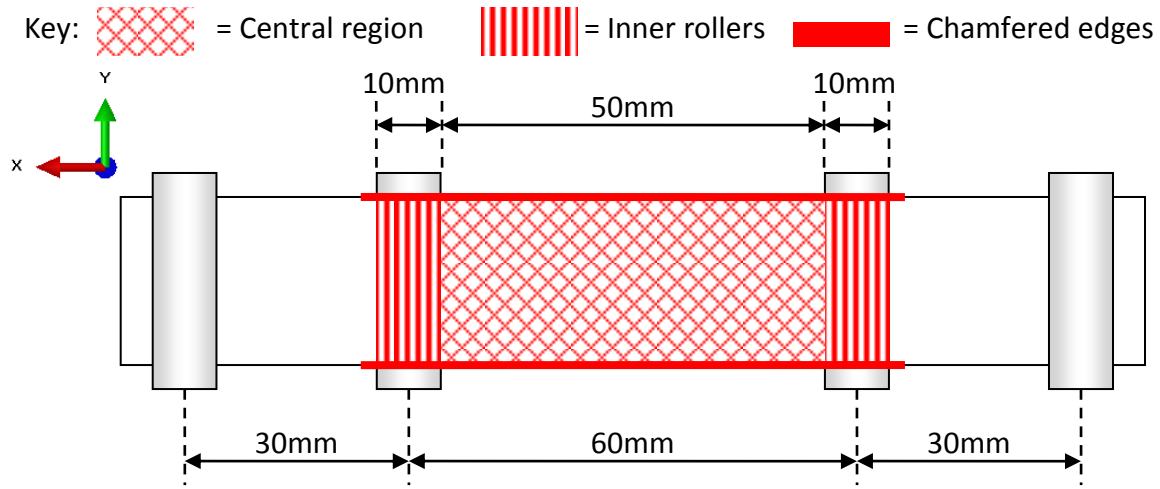

Figure 6.15 Crack evaluation regions defined on tensile face of four-point bend SSC specimen

6.3.2 Produced Water Test Results (69 mbar H_2S)

Figure 6.16 presents the total number of cracks observed in as-received and fully-machined specimens tested in simulated Produced Water at 5 °C and 24 °C when exposed to 69 mbar H_2S. The results show the as-received surface is more resistant to SSC than the fully-machined surface and that more cracking occurred at 5 °C than at 24 °C in the fully-machined condition:

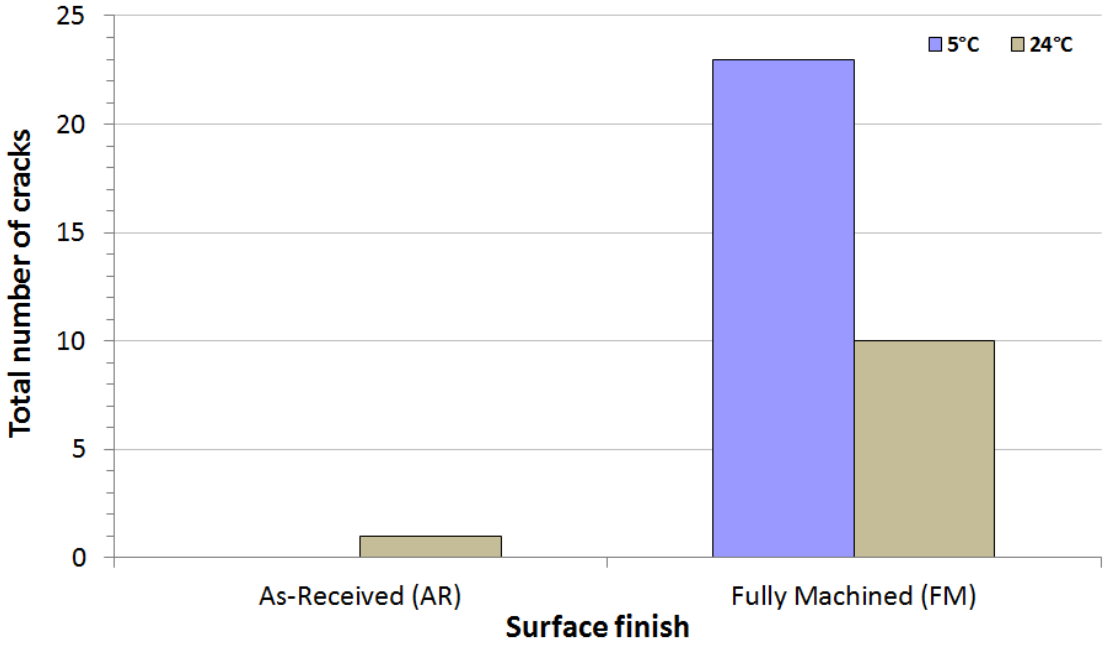

Figure 6.16 Total number of cracks observed in as-received and fully-machined specimens tested at 5 °C and 24 °C in Produced Water when exposed to 69 mbar H_2S partial pressures

Figure 6.17 details the crack locations on the tensile test surface. No cracks were observed where the original pipe surface remained intact; the single crack seen in as-received specimen P1 (Figure 6.18) was located on the chamfered edge were the pipe surface had been removed. All cracking observed in the fully-machined specimens tested at 24 °C occurred on the chamfered edges or in the inner roller regions. The specimens tested at 5 °C also had cracks in the central region as well as the edges and the roller regions.

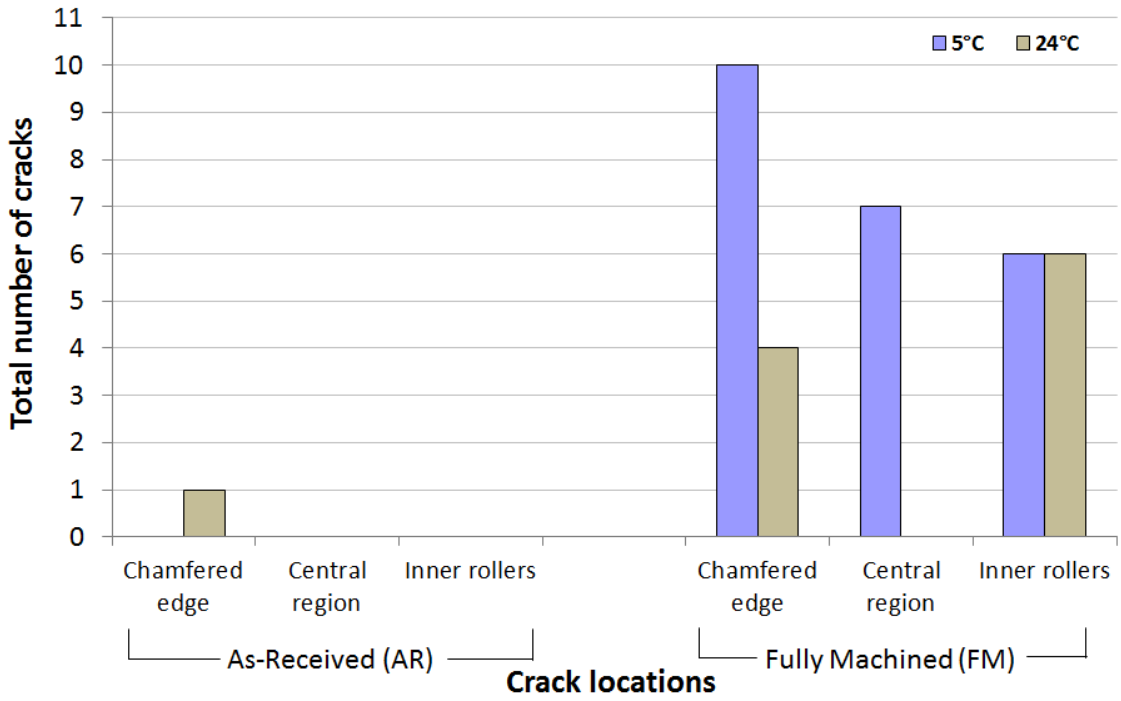

Figure 6.17 Total number of cracks by location on the tensile test surface of as-received and fully-machined specimens tested at 5 °C and 24 °C in Produced Water when exposed to 69 mbar H_2S. No cracks occurred where the original pipe surface remained intact. The absence of cracking in the central region of the fully-machined specimens tested at 24 °C indicates that 5°C is a more severe test condition

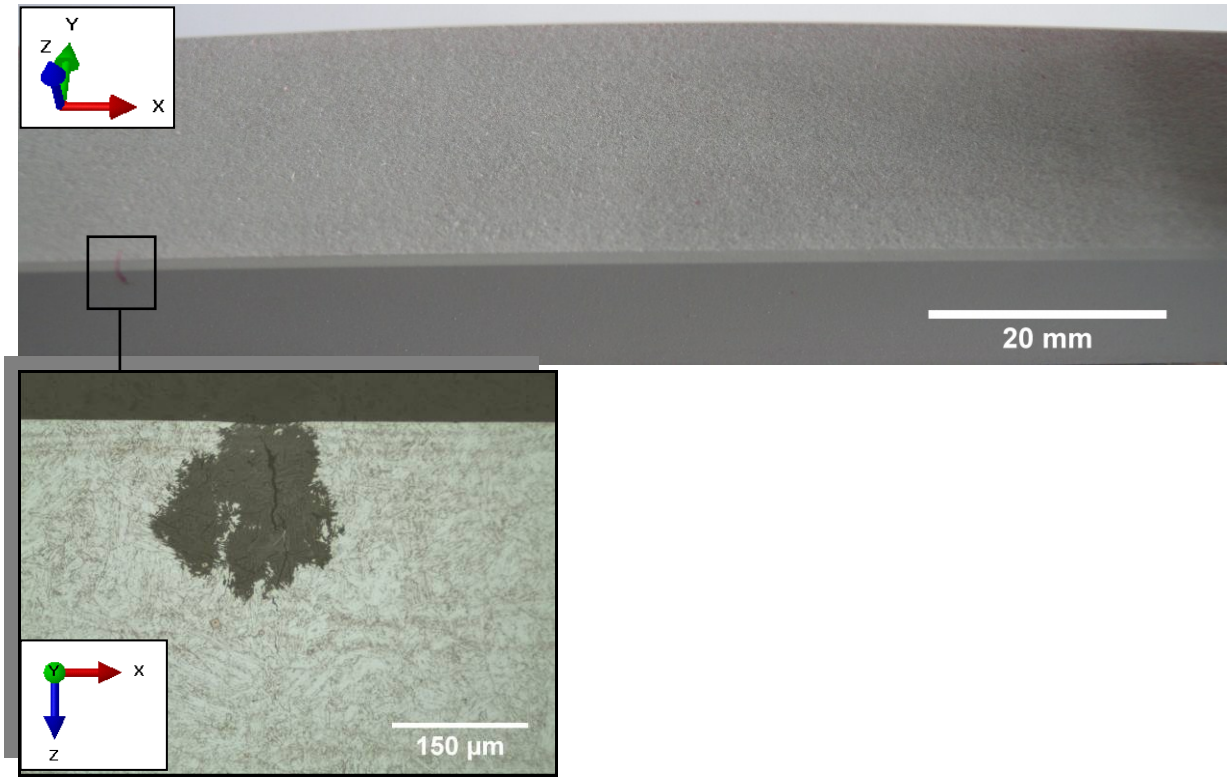

Figure 6.18 Single SSC crack located on the chamfered edge of as-received specimen P1 (24 °C). No cracks were observed where the original pipe surface remained intact

Figure 6.19 shows the distribution of cracks in terms of maximum crack depth penetration through the thickness of the specimens. The results show that the deepest cracks occurred in the fully-machined specimens tested at 5 °C.

Figures 6.20 to 6.23 show the extent of cracking seen on fully-machined specimens P3, P4, P7 and P8 revealed by DPI. Even though the chamfered edges and inner roller regions have influenced crack susceptibility, cracking can still be observed away from these features (e.g. Figure 6.22).

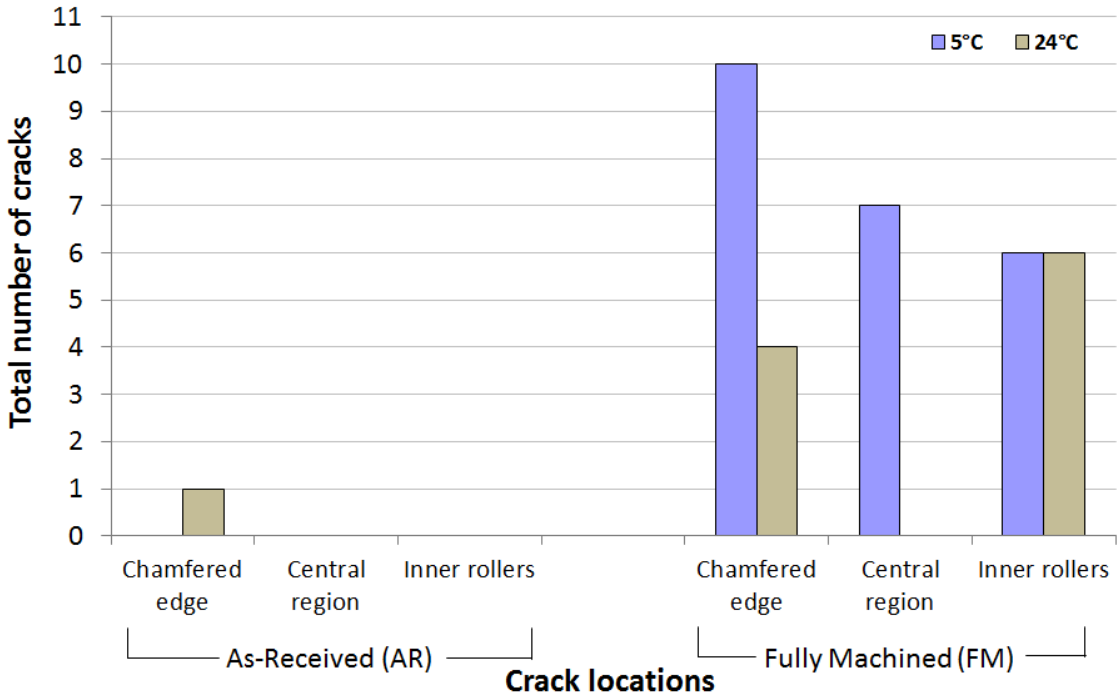

Figure 6.19 Maximum crack depth penetration observed in as-received and fully-machined specimens tested at 5 °C & 24 °C in Produced Water when exposed to 69 mbar H_2S. The deepest cracks occur in the fully-machined specimens tested at 5 °C

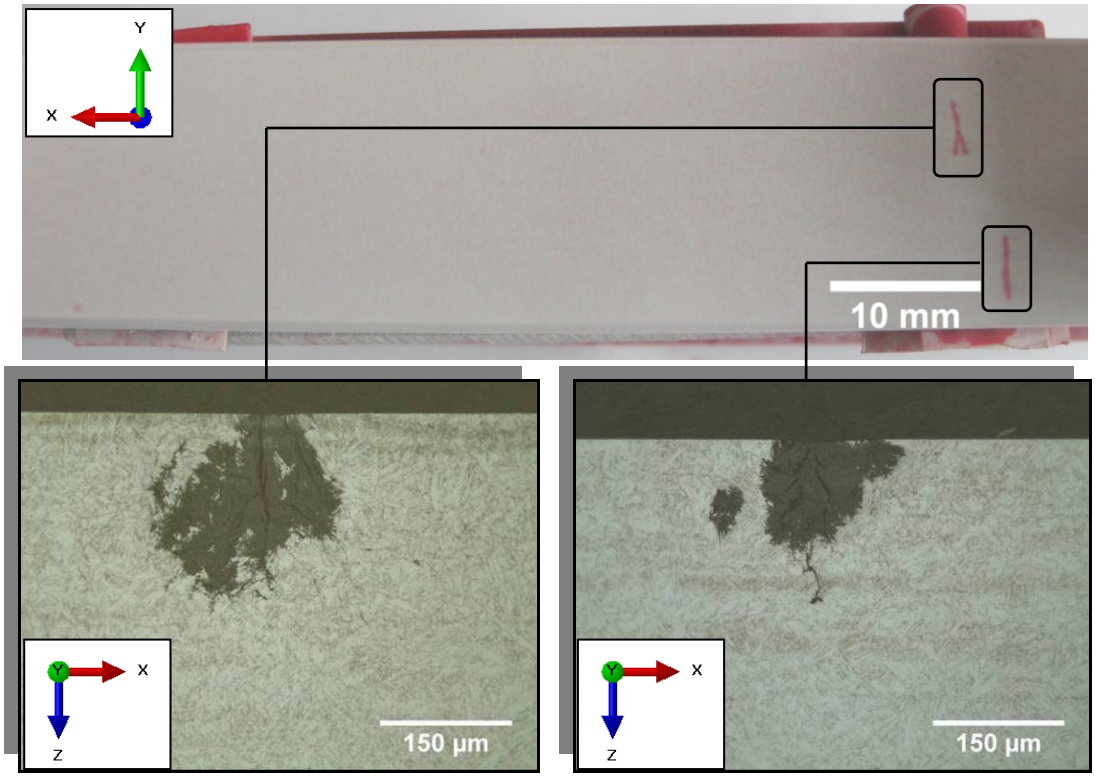

Figure 6.20 SSC cracks located at inner loading roller position on the tensile surface of fully-machined specimen P3 (Specimen tested in Produced Water at 24 °C and exposed to 69 mbar H_2S)

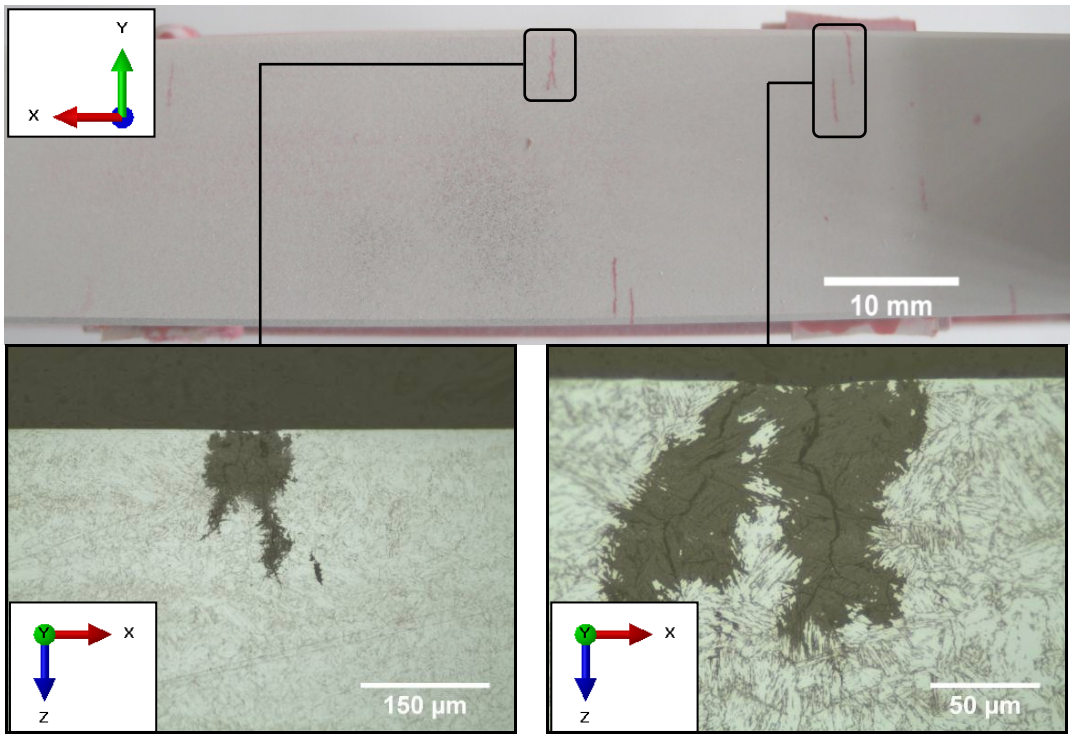

Figure 6.21 SSC cracks located on the tensile surface of fully-machined specimen P4 (Specimen tested in Produced Water at 24 °C and exposed to 69 mbar H_2S). The majority of cracks are either at the inner loading roller position or at the edges of the specimen

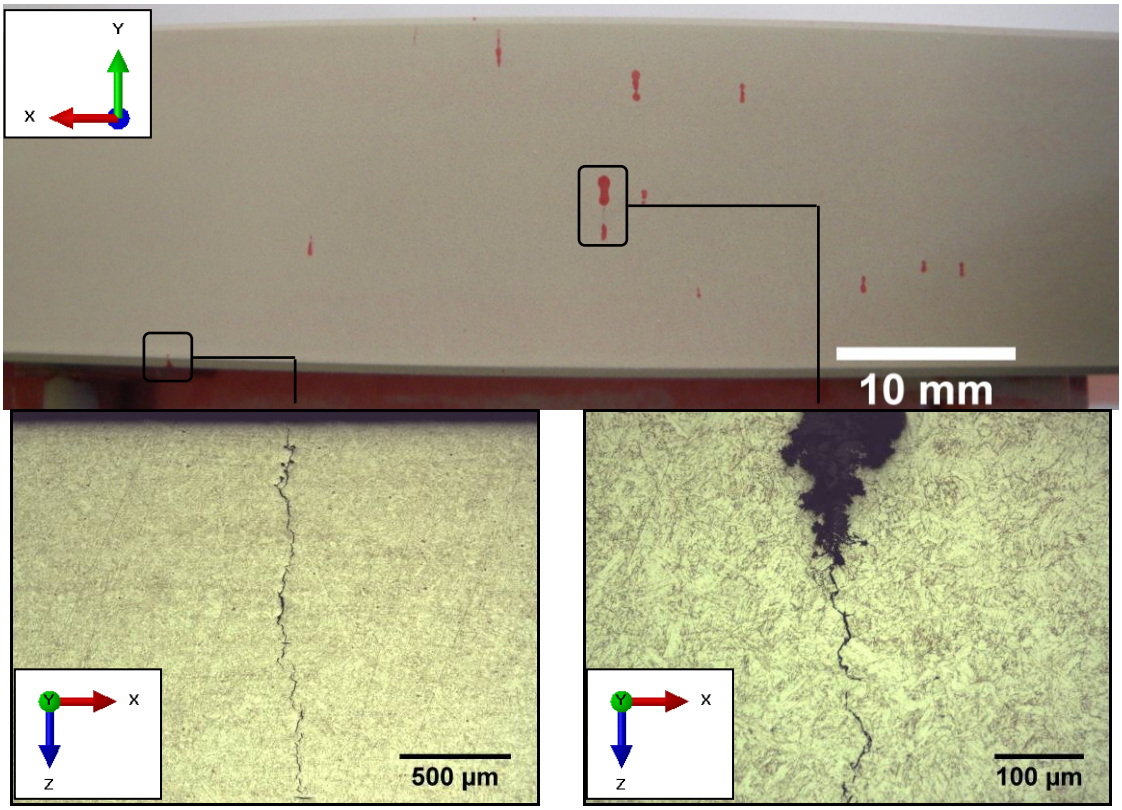

Figure 6.22 SSC cracks located on the tensile surface of fully-machined specimen P7 (Specimen tested in Produced Water at 5 °C and 69 mbar H_2S). Cracks are distributed over the entire test face

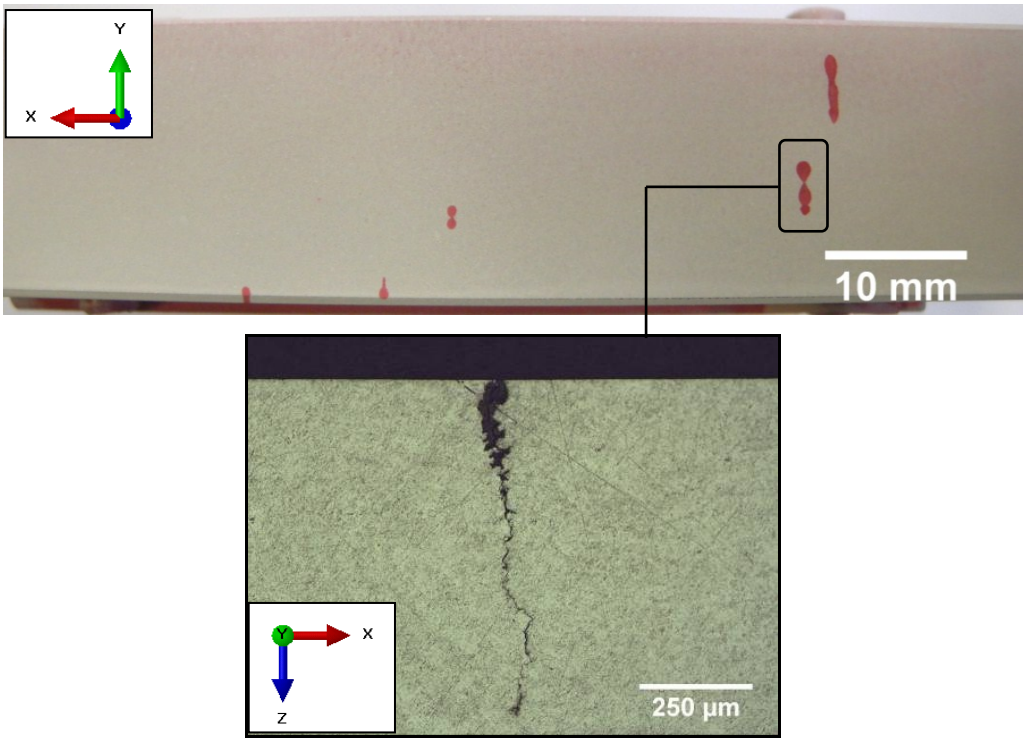

Figure 6.23 SSC cracks located on the tensile surface of fully-machined specimen P8 (Specimen tested in Produced Water at 5 °C and 69 mbar H_2S). The longest cracks are located at the inner loading roller position

6.3.3 Produced Water Test Results (35 mbar H_2S)

Figures 6.24 and 6.25 present the total number of cracks observed in as-received and fully-machined specimens tested in simulated Produced Water at 5 °C and 24 °C when exposed to 35 mbar H_2S. The results also show that the as-received surface is more resistant to SSC than the fully-machined surface and that more cracking occurred at 5 °C than at 24 °C in the fully-machined condition. The key result here is that there was no cracking in the fully-machined specimens tested at 24 °C, but there was significant cracking in the fully-machined specimens tested at 5 °C.

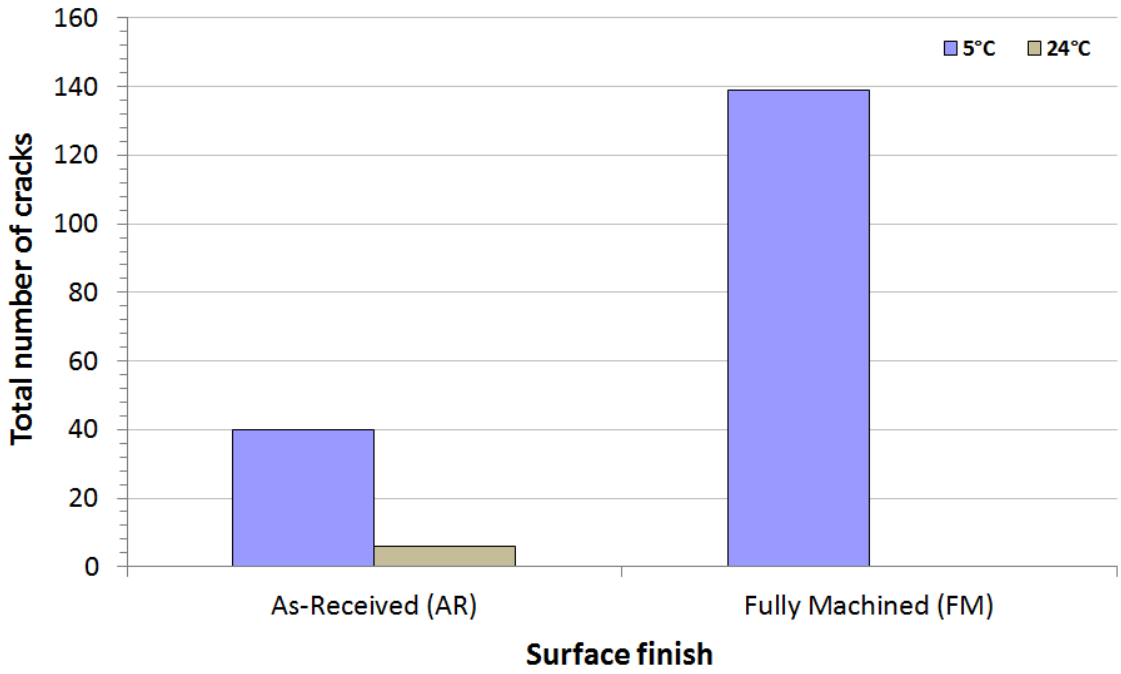

Figure 6.24 Total number of cracks observed in as-received and fully-machined specimens tested at 5 °C and 24 °C in Produced Water when exposed to 35 mbar H_2S partial pressures

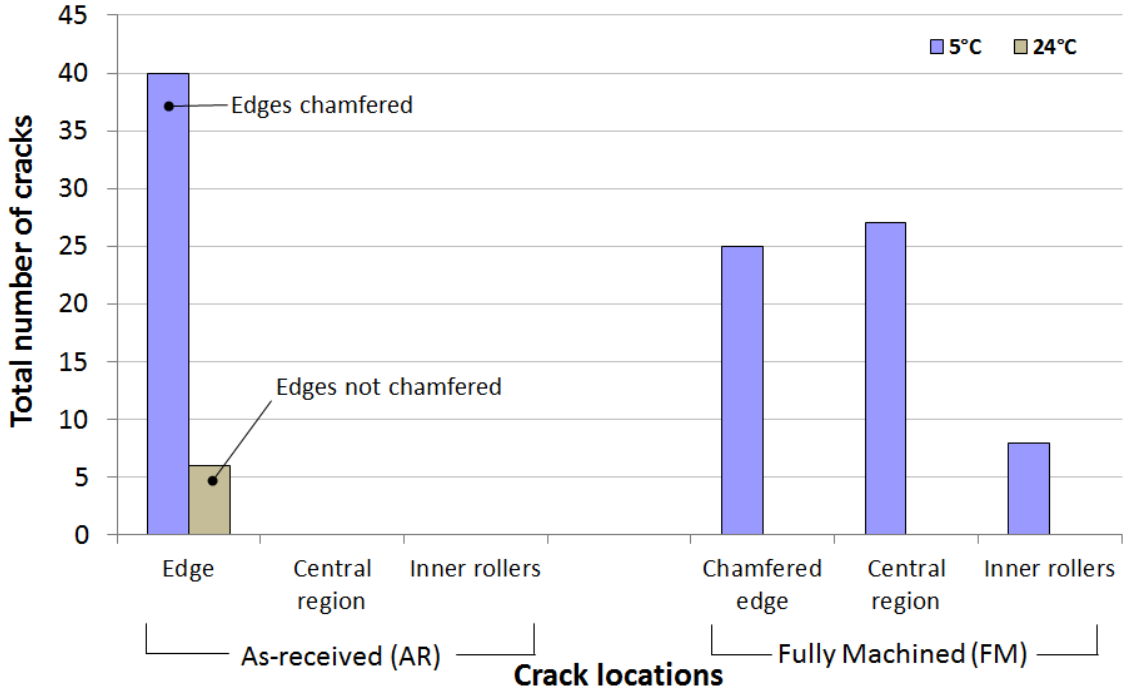

Figure 6.25 Total number of cracks by location on the tensile test surface in as-received and fully-machined specimens tested at 5 °C and 24 °C in Produced Water and 35 mbar H_2S. No cracks occurred where the original pipe surface remained intact. Cracks occurred in the fully-machined specimens tested at 5 °C but not at 24 °C indicating that 5 °C is a more severe test condition.

Another similarity with the 69 mbar H_2S tests is that the as-received specimens tested at 5 °C only cracked along the chamfered edges (Figure 6.26), however it can be seen that omitting the chamfer (i.e. testing with the edges left as-machined) does not eliminated edge cracking (Figures 6.25 and 6.27).

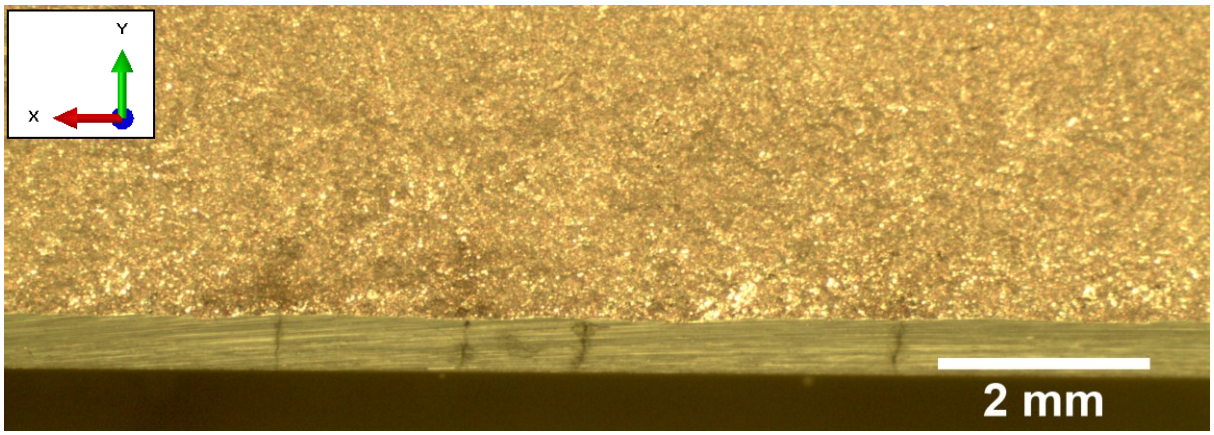

Figure 6.26 SSC cracks located on the chamfered edge of as-received specimen P14 (Specimen tested in Produced Water at 5 °C and 35 mbar H_2S). Visible grinding marks may have initiated cracking

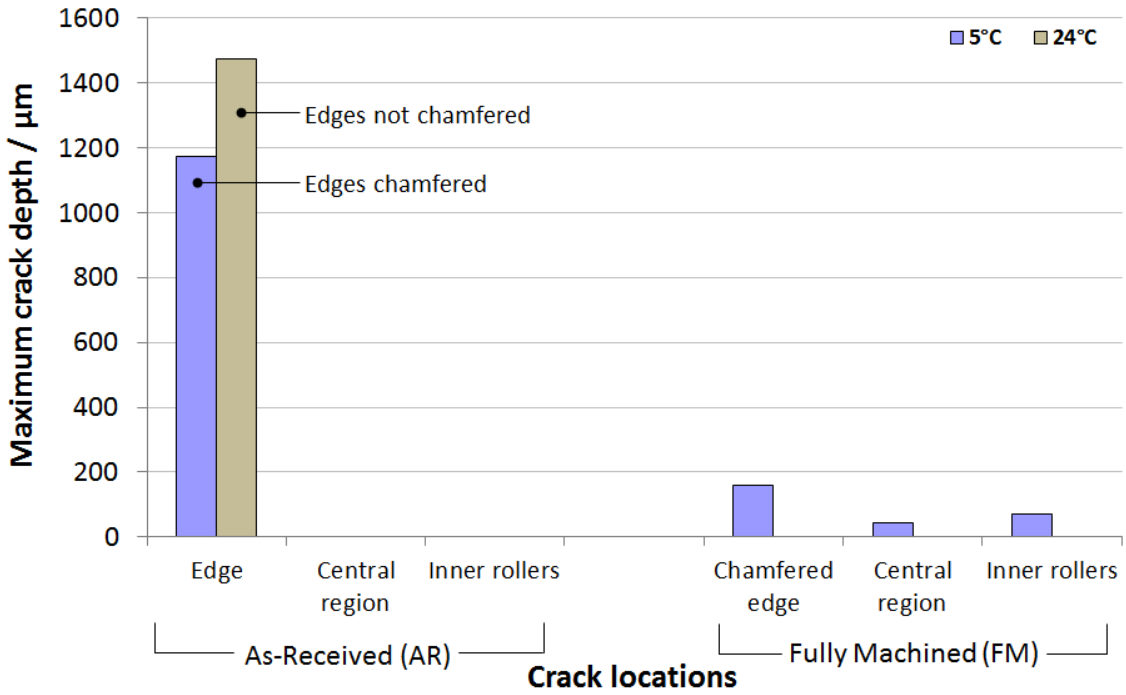

Figure 6.27 Maximum crack depth by location on the tensile test surface in as-received and fully-machined specimens tested at 5 °C and 24 °C in Produced Water (35 mbar H_2S). For the as-received specimens, no cracks were observed where the original pipe surface remained intact, but cracking occurred at the edges of the tensile surface (the deepest cracks occurred on the specimens without edge chamfers). For the fully-machined specimens, cracking only occurred at 5°C

The tensile test face, chamfers and sides of the fully-machined test specimens were wet ground to a 600 grit finish. The chamfers and sides of the as-received specimens were also prepared to the same finish. This was done using an automatic grinder/polisher fitted with a 600 grit silicon carbide pad and water coolant. The coarseness of this finish is evident on a macroscopic scale and could be a contributing factor in the increased SSC susceptibility observed on the surfaces prepared in this way. Figure 6.28 shows a fully-machined specimen tested at 5 °C with several small cracks distributed over the test face and edges. Grinding marks from the 600 grit silicon carbide paper are clearly visible but further work is required to understand if this contributed to crack initiation on the fully-machined test specimens.

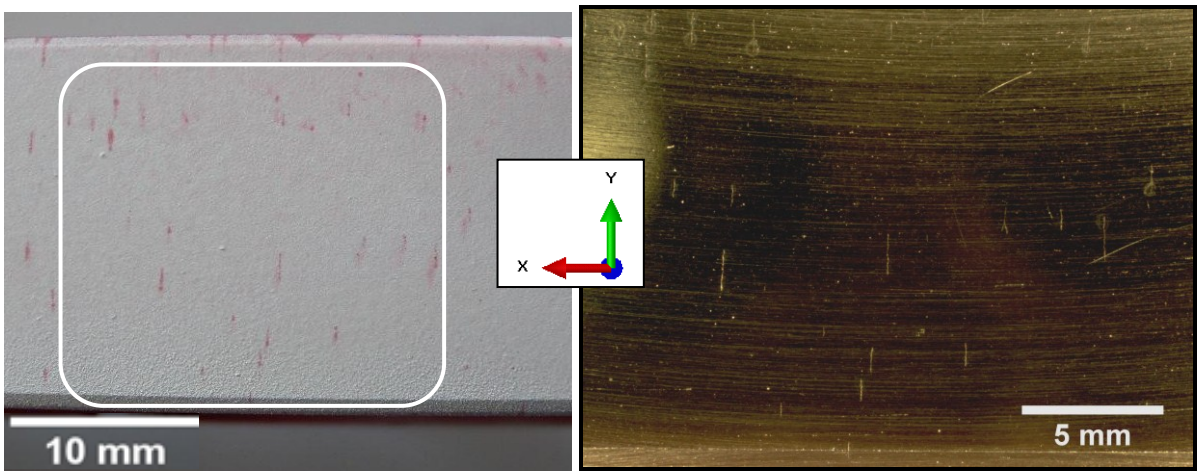

Figure 6.28 SSC cracks on the test face of fully-machined specimen P17 (PW, 5 °C, 35 mbar H_2S). Insert shows grinding lines from 600 grit SiC paper

6.3.4 Condensed Water Test Results (69 mbar H_2S)

Figure 6.29 presents the results of the Condensed Water SSC tests at 69 mbar H_2S using in-situ pH monitoring to control solution pH to 3.5 ±0.1. During the 24 °C tests the solution pH remained stable for the 30 day test period so no adjustment was required, but during the 5 °C test the solution pH started to rise after approximately 24 hours so the acid injection system was used to adjust pH back to 3.5. After this initial adjustment the pH remained stable for the remainder of the test and no further adjustments were required.

Only one as-received specimen cracked in the 24 °C test and all the cracks were located along the thickest edge (Figure 6.30). Although this result does not support previous results that 5 °C is a more severe test condition than 24 °C, it does show that specimen geometry may influence crack susceptibility. Cracking in this material is typically intergranular and follows prior austenite grain boundaries as can be seen in Figures 6.5 and 6.22. The crack shown in Figure 6.30 may also be intergranular but as shown in the insert

there is an appreciable amount of metal dissolution inside the crack making the mode difficult to identify.

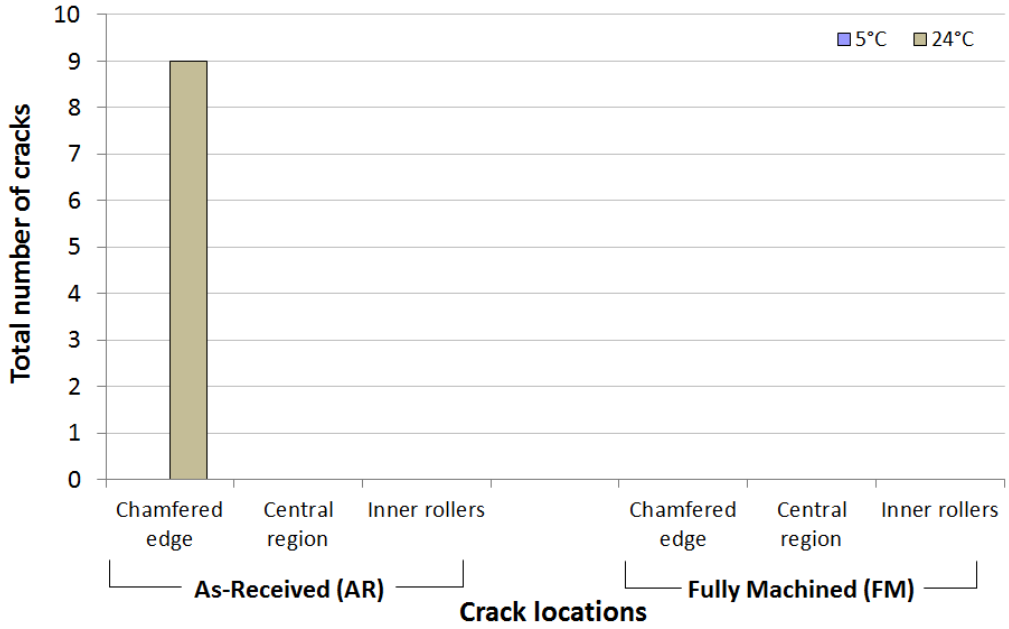

Figure 6.29 Maximum crack depth by location on the tensile test surface in as-received and fully-machined specimens tested at 5 °C and 24 °C in Condensed Water and 69 mbar H_2S. Only one as-received specimen cracked at 24 °C and all the cracks were located along one chamfered edge.

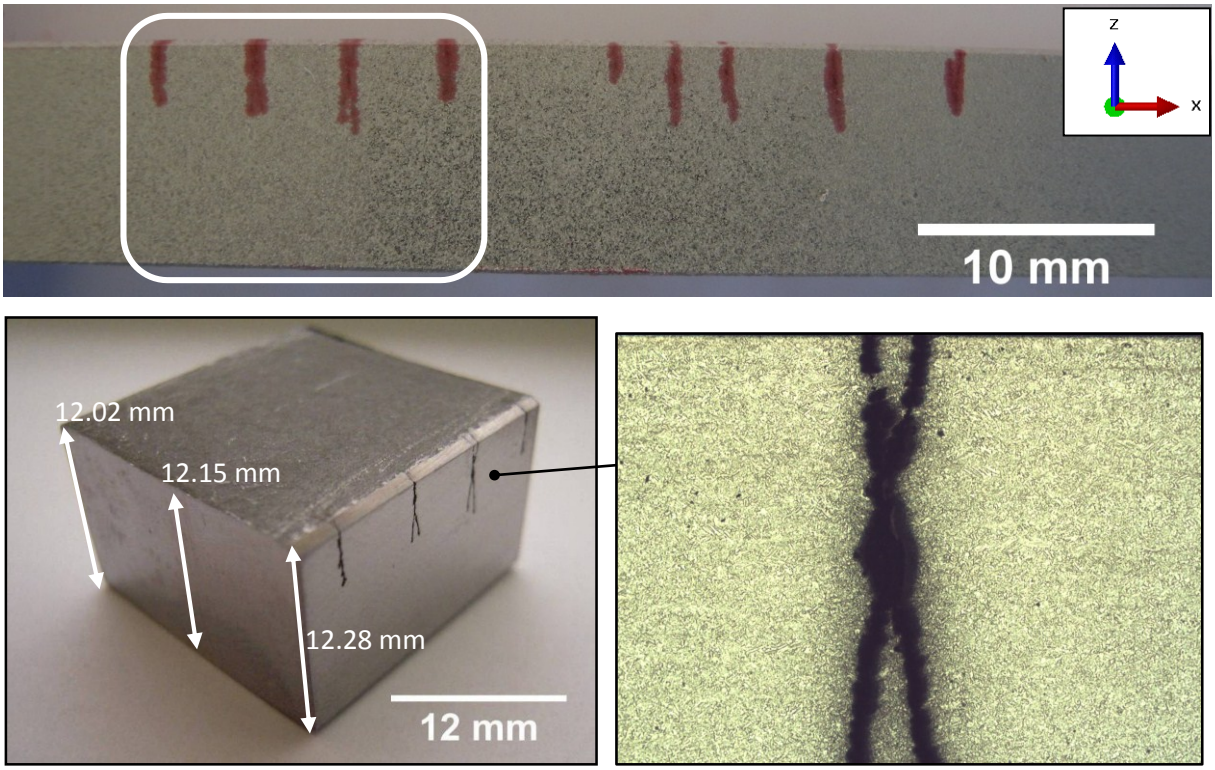

Figure 6.30 SSC cracks located along one chamfered edge of specimen C1 (CW, 24°C, 69 mbar H_2S). Inserts show the thickest edge cracked and a micrograph one crack, etched with Vilella's reagent.

6.3.5 Corrosion Coupon Test Results

The mass loss results for the unstressed corrosion coupons is given in Figure 6.31 for all the test environments. The apparent trend of greater mass loss at 24 °C may be misleading given the low magnitude of mass loss which was caused by small amounts of crevice corrosion between the PTFE strap and the hole in the specimen. Pitting was not observed on the surface of any of the test coupons and the worst case corrosion rate (using equation 4.12) was 0.002 mm/year which is considered negligible.

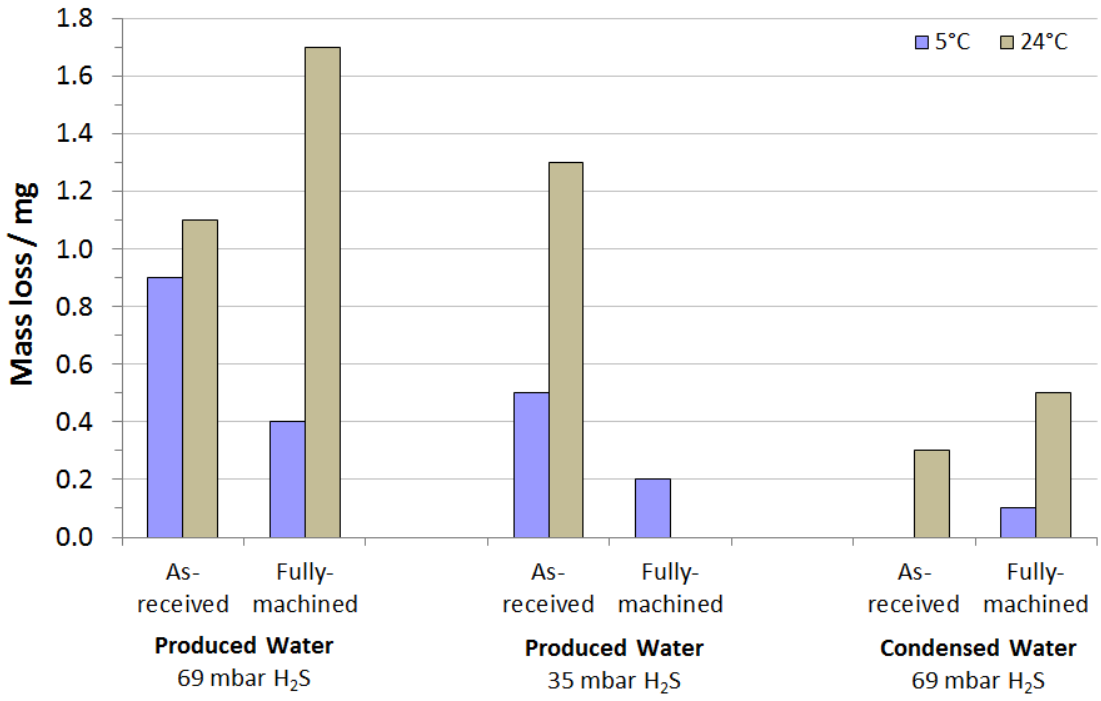

Figure 6.31 Mass loss results for unstressed corrosion coupons in all SSC test environments

6.3.6 Summary of the Seabed Temperature SSC Investigation

The seabed temperature SSC test results are summarised in Figure 6.32 which highlights the severity of the cracking observed in the single as-received specimen tested in the Condensed Water environment at 69 mbar H_2S. The figure shows that weldable 13%Cr supermartensitic stainless steel is more susceptible to SSC at 5 °C compared to 24 °C in the high chloride Produced Water environment.

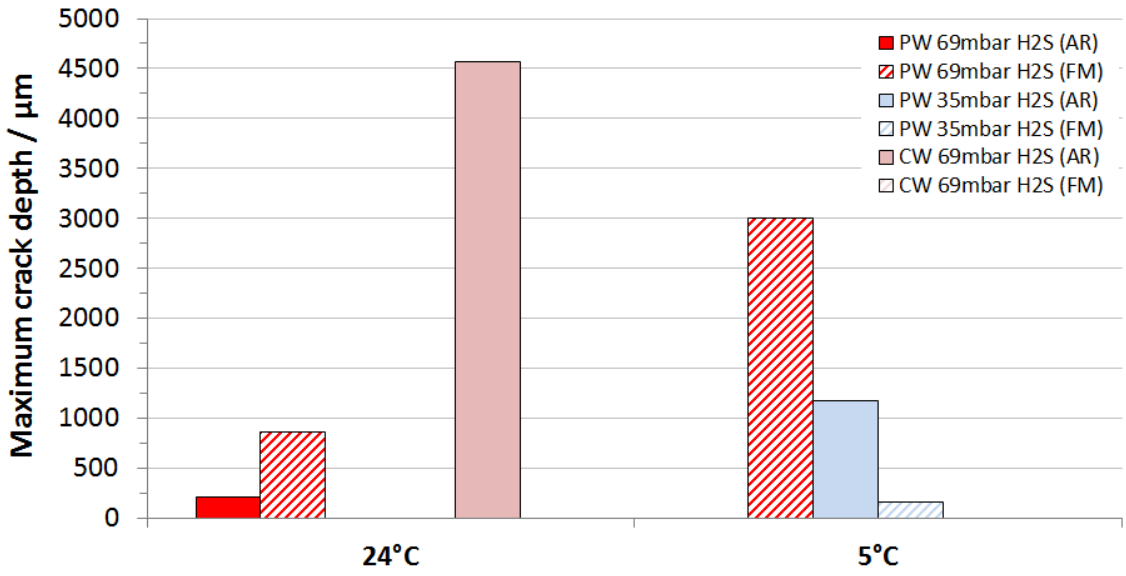

Figure 6.32 Summary of seabed temperature SSC test results (maximum crack depth vs temperature)

Other key observations include:

1. The high chloride Produced Water environment is a more severe test condition than the lower chloride Condensed Water environment. Cracking was observed in the fully-machined specimens tested at 5 °C in Produced Water (69 mbar H_2S and 35 mbar H_2S) but no cracking was observed in the fully-machined specimens tested at 5 °C in Condensed Water (69 mbar H_2S).

2. The as-received pipe surface provides better SSC resistance than the fully-machined surface ground to a 600 grit finish. No cracks were observed where the as-received pipe surface remained intact but cracks did occur at the edges of the as-received specimens and on the surface of the fully-machined specimens.

3. Anomalous cracking was observed on the chamfered edges and at the inner roller positions, highlighting that these features may promote SSC in the four-point bend test.

4. When cracking at the chamfered edges and in the region of the inner rollers is discounted, 5 °C proves to be a more severe test condition than 24 °C. This was shown by the amount of cracking seen in the central region of the fully-machined specimens tested in Produced Water at 69 mbar H_2S and 35 mbar H_2S. Cracks occurred at 5 °C but not at 24 °C.

5. Specimen cross-sectional asymmetry may also influence crack susceptibility in the four-point bend test. This was shown in the Condensed Water tests where a single specimen cracked along one edge which was notably thicker than the edge which did not crack.

6. General corrosion was not observed with this material when exposed to 69 mbar H_2S in Produced and Condensed Water environments (pH 3.5 – pH 4.5).

7. Pitting corrosion was not observed in the unstressed corrosion coupons.

6.4 Discussion

6.4.1 Improving Current SSC Test Protocol

6.4.1.1 Reducing Oxygen Contamination

Omura *et al*. [30] showed that placing the SSC test vessel inside a nitrogen chamber can reduce the level of dissolved oxygen in the test solution, but depending on the flow rate of nitrogen used to purge the system, dissolved oxygen could rise to 25 ppb. Oxygen contamination can increase the rest potential of modified 13%Cr stainless steels [76] and it has been suggested that oxygen levels of 50 ppb in the test solution it can greatly accelerate corrosion in these steels [77].

The key improvement made in Section 6.2 was incorporating a H_2S-resistant dissolved oxygen sensor inside the test vessel for in-situ oxygen monitoring during the SSC test. This setup ensured that the results of the seabed temperature SSC investigation were not skewed by excessive levels of dissolved oxygen in the test solution. It should be noted that oxygen solubility increases as temperature decreases [170,171]. The in-situ oxygen monitoring therefore increases the reliability of the test method and ensures that the SSC tests can be performed with dissolved oxygen levels below 10 ppb as defined in EFC17 [7].

6.4.1.2 Controlling pH in Simulated Condensed Water Test Solutions

In Section 6.1, the pH instability of the simulated Condensed Water solution, when acidified with HCl, reflects similar experiences reported by Omura *et al*. [30] and Augustin *et al*. [92]. Both authors reported that better pH stability was achieved when acetic acid was used instead of HCl. Other reports indicate that the pH of Condensed Water solutions

acidified with HCl remains stable during the SSC test [75]. There is currently no consensus how the use of artificial acetate buffers influence pH and corrosion rates in 13%Cr stainless steels. Furthermore, no work has been published to date on in-situ adjustment of solution pH during an SSC test without introducing oxygen into the test solution. The acid injection system detailed in Section 6.2 allows pH adjustment of Condensed Water solutions under de-aerated conditions so solution pH can be maintained to ±0.1 as required by EFC17 [7]. However, the main limitation of this system is that pH can only be lowered to make the solution more acidic. Since there is no way of increasing the pH to be more alkaline, care must be taken not to over-acidify the test solution below pH 3.4, because the depassivation pH for this material is approximately 3.0 to 3.5 [87].

The original test vessel at Exova was pressurised at 2 bar to create a positive internal pressure as a safeguard against oxygen ingress. The new system allows tests to be performed at atmospheric pressure thereby reducing setup time. With this method, the H_2S partial pressure is set directly by the H_2S gas concentration in the H_2S/CO_2 gas mixture.

6.4.2 SSC Test Results

Published SSC test data on weldable 13%Cr supermartensitic stainless steel is limited. The most directly comparable results (at room temperature) using the four-point bend loading method were published by Enerhaug *et al.* [26] and Ueda *et al.* [49]. Their work used root-intact welded specimens so the SSC resistance of the parent pipe can be compared to the parent as-received specimens tested in this thesis. The results from the welded specimens show that 13%Cr supermartensitic stainless steel is resistant to SSC at 10 mbar

H_2S in 31,400 mg/l Cl^- (pH 3.17) [49] and at 40 mbar H_2S in 68,000 mg/l Cl^- (pH 4.0) [26]. No failures in the parent metal were reported. Figure 6.33 presents these results alongside the seabed temperature SSC investigation results from this thesis (pH 4.5 100,000 mg/l Cl^-).

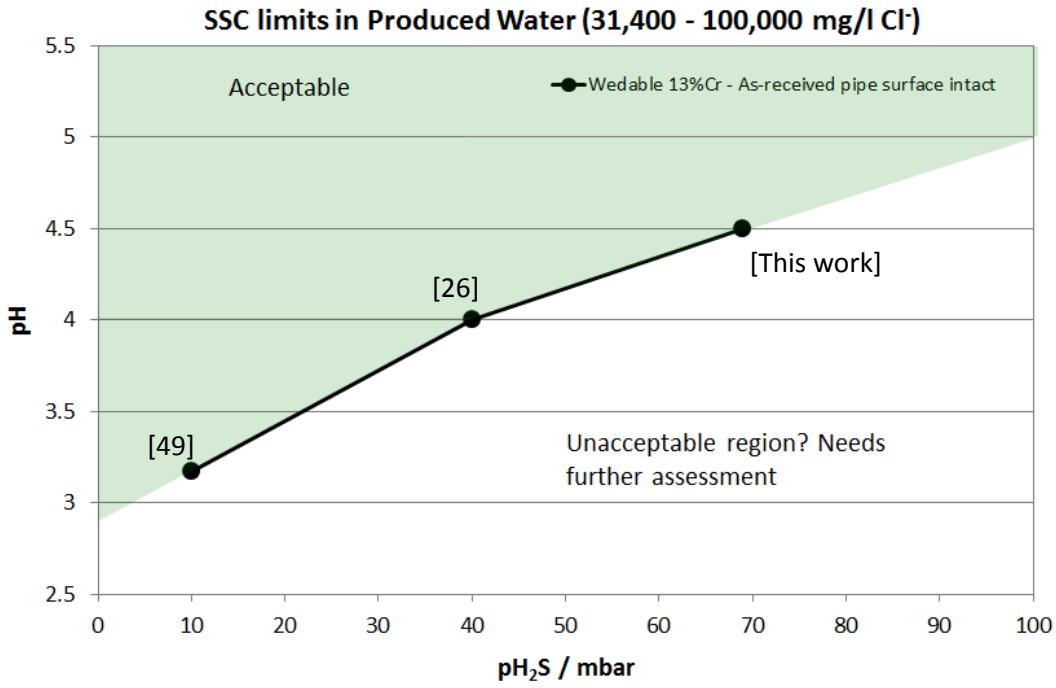

Figure 6.33 SSC limits for weldable 13%Cr supermartensitic stainless steel with the as-received pipe surface intact. Results from published literature [26,49] and the Seabed Temperature SSC Investigation presented in this thesis. All specimens were tested using the four-point bend loading method stressed to 100% AYS in Produced Water (31,400-100,000 mg/l Cl^-) at 24°C.

Metallographic examination of the cracks generated in the SSC tests presented in this thesis showed that crack propagation was intergranular in nature, with areas of metal dissolution/pitting at the surface exposed to the test environment (see Figure 6.5). It is often reported that pitting is the precursor to SSC in 13%Cr martensitic stainless steels [14,29,80,172] because localised breakdown of the passive film facilitates hydrogen entry into the steel, combined with the stress concentration associated with the corrosion pit facilitates cracking. Furthermore, hydrogen permeation studies performed by Kimura *et al.*

[40] revealed that SSC resistance is dependent on pitting resistance, not strength, at pH 4.5. In contrast, when pH ranges from 3.0 to 4.5, strength was shown to be an influencing factor.

Retained austenite is recognised as being beneficial to the SSC resistance of 13%Cr martensitic stainless steels [99], potentially due to the preference for hydrogen trapping in the softer austenite phase [100], reducing the likelihood of embrittlement in the harder martensite phase. Nose and Asahi [98] showed that 10% retained austenite was beneficial to the SSC resistance of weldable 13%Cr martensitic stainless steels. XRD measurements presented in Chapter 5 of this thesis showed that the as-received pipe contained an average volume fraction of 12.9% retained austenite in its unstressed condition. It should be noted that cold work can transform retained austenite into fresh martensite [100,103] and potentially reduce SSC resistance. The effect of cold work on retained austenite has not been investigated in this thesis.

6.4.3 Influence of Temperature on SSC Resistance

With controlled levels of oxygen and stable solution pH, the results of the seabed temperature SSC investigation showed that 5 °C was a more severe test condition than room temperature (24 °C) in the high chloride Produced Water environment, thereby supporting the observations made by Bodycote's scoping experiment in 2005 [3]. This results challenges the widely accepted notion that 13%Cr martensitic stainless steel behave in the same way as carbon steels in that the risk to SSC is most severe at room temperature [10,28,74,77].

Chambers *et al.* [75] tested UNS S41426 supermartensitic stainless steel at 24 °C and 5 °C using the tensile method (stressed to 90% AYS) in Produced Water (pH 4.5, 100,000 mg/l Cl^-) at 35 mbar H_2S and reported that SSC occurred at 24 °C but not at 5 °C. This is the opposite result to that found in the seabed temperature SSC investigation presented in this thesis, where cracking occurred at 5 °C but not at 24 °C when exposed to 35 mbar H_2S. Both investigations tested the fully-machined surface and since both testing programs were performed at pH 4.5, the strength differences between the two material grades is not considered to be an influencing factor on SSC resistance [96]. The two fundamental differences between the tests are as follows:

1. The specimens tested in the seabed temperature SSC investigation in this thesis were stressed to a higher level (100% AYS in four-point bending) than the tensile specimens tested by Chambers *et al*. (90% AYS in tension). However, if the higher loading level was the cause of cracking at 5 °C it would be expected that the four-point bend tests would have also cracked at 24 °C.

2. Chambers *et al.* [75] noted that their work was done prior to the appreciation for the effect of dissolved oxygen on martensitic stainless steels, and thereby stressed that oxygen contamination was a possibility. Therefore it is possible that the cracking observed at 24 °C was caused by oxygen contamination. If there was no oxygen contamination at 5 °C, the absence of cracking at 5 °C could be due to the lower loading stress.

The idometric titration tests in this thesis showed that H_2S solubility increases as temperature and salinity (chloride content) decreases. This could explain why cracking was more severe at 5 °C than at room temperature: at 5 °C there is an effectively higher H_2S partial pressure (pH_2S) in solution than at 24 °C. By the *direct proton transfer* theory, Crolet & Bonis [21] proposed that forced proton entry locally dilates the crystal lattice near the surface which generates internal stresses that can initiate cracking. In this theory, the coexistence of charging and degassing means that it is the *charging rate* that increases with pH_2S, not the final concentration of absorbed hydrogen in the metal. Indeed, Hinds *et al.* reported that the subsurface hydrogen concentration in a super 13%Cr steel with 12% retained austenite did not vary significantly over the temperature range of 5 °C to 70 °C [74]. An increased rate of hydrogen entry at 5 °C may therefore explain why more cracks and deeper cracks were observed in the SSC specimens tested at 5 °C compared to those tested at 24 °C.

The preceding argument assumes that the solubility of H_2S/CO_2 gas mixtures follows the same trend as pure H_2S gas. This was considered a valid assumption because the solubility of both H_2S and CO_2 is influenced by temperature and salinity in a similar way [169,173]. It should also be noted that the solubility of H_2S increases as pressure increases [174] which is of importance when performing autoclave tests at elevated temperature and pressure.

6.4.4 Influence of Chlorides, H_2S and pH on SSC Resistance

It is well known that chlorides attack the passive film in stainless steels [73, 83-85] and this provides a gateway for pitting corrosion, resultant hydrogen entry and hydrogen embrittlement. Marchebois *et al.* [39] stressed that chloride concentration is very influential on 13%Cr supermartensitic stainless steels, particularly when combined with H_2S and low solution pH. The depassivation pH in simulated Produced Water (100,000 mg/l Cl-) should be between 3.0 and 3.5 [87], so at pH 4.5 the oxide layer is expected to be in the passive state. This is consistent with the observed test results presented in this thesis; no general corrosion was observed in the Produced Water tests which suggests the material is in a passive state. Furthermore, no general corrosion was observed at pH 3.5 in the Condensed Water tests which also indicates passive film stability. In the passive state, crack initiation will be controlled by pitting which is influenced by chloride concentration and H_2S partial pressure (pitting will occur at lower potentials in H_2S containing environments [14]). When pitting occurs, adsorbed sulphur species may lower the activation energy for hydrogen entry into the steel [15], increasing the likelihood of SSC. Further work investigating the effect of temperature on passive film stability in this system is in progress [175].

Based on the Produced Water and Condensed water SSC test results presented in Chapter 6 of this thesis, it can be concluded that chlorides are more detrimental to SSC resistance than H_2S partial pressure alone due to the passive state of the oxide film and the aggressiveness of chlorides with respect to localised dissolution. The role of H_2S becomes more important when the passive film is compromised (either locally or during active dissolution). In the passive state, the material was resistant to SSC in the low-chloride

Condensed Water solution even though H_2S solubility was higher (than Produced Water). In comparison, failures were observed the higher-chloride Produced Water tests when exposed to lower levels of H_2S (Compare Figure 6.24 to Figure 6.29). Similar trends have been reported in the literature [39,75,86,105]. Cooling *et al*. [20] demonstrated this for down-hole tubular 95 ksi (655 MPa) grade 13%Cr and showed that SSC resistance was worse in simulated Produced Water (120,000 mg/l Cl^-) compared to simulated Condensed Water (1000 mg/l Cl^-) environments when tested in the range of 10 mbar to 1 bar H_2S.

6.4.5 Influence of Surface Finish on SSC Resistance

The seabed temperature SSC investigation presented in this thesis showed that the SSC test results were heavily influenced by surface finish. The qualification of weldable 13%Cr martensitic stainless steel for the Åsgard Field reported that cracking occurred preferentially in the HAZ on the machined edges of four-point bend SSC specimens but not on the as-received pipe surface [26]. This corresponds to the observations made during the SSC tests presented in this thesis in that the as-received surface condition provides enhanced SSC resistance when compared to the 600-grit fully-machined surface condition. The fully-machined surface condition is commonly used as a standard finish to rank a material in a particular environmental condition (chloride level, pH, H_2S). Given the increased SSC susceptibility in the fully-machined condition, preparing specimens in this way represents a very conservative test, since the pipes in service will have a grit-blasted finish.

Hinds *et al.* [168] showed that grinding operations on a 316L austenitic stainless steel generated a heavily deformed nanocrystalline layer with near-surface residual tensile

stresses in the order of 500 MPa (for a surface with a R_a value of 0.16 µm corresponding to a 600 grit finish), leading to preferential pitting. Preferential pitting at physical defects introduced by the machining and grinding processes was also observed in a 304 austenitic stainless steel [176]. SSC and macroscopic grinding marks are clearly visible along the chamfered edge of the 13%Cr specimen in Figure 6.28.

In Chapter 5 of this thesis it was shown that the as-received surface was rougher and harder than the fully-machined surface. Normally, pitting is more likely on a rougher surface because microscopic crevices trap metal ions which create a locally acidified solution and facilitate further dissolution. Harder material is also generally more susceptible to SSC. The apparent increase in hardness may be caused by residual compressive stresses generated by the alumina blasted surface treatment in the as-received condition, as described by Griffiths *et al*. [146]. Residual compressive stresses can slow the rate of hydrogen diffusion in steels and therefore improve resistance to hydrogen embrittlement [167]. This may account for the superior SSC resistance observed in the as-received specimens compared to specimens prepared with a fully-machined surface condition. However, the application of a tensile stress, either through a four-point bend test or during service conditions, may relax any residual compressive stresses generated by the alumina blasting process [177]. An ideal finish would be a smooth grit blasted surface to provide the beneficial residual compressive stresses but with a reduced risk of pitting corrosion as a smooth surface allows cations to diffuse away from active sites.

6.4.6 Influence of Test Method on SSC Resistance

The four-point bend test method applies stress to a relatively large surface area of a test specimen and is particularly suited for testing as-received surfaces and root-intact welded specimens. However, test configuration and specimen geometry may influence the stress and strain distribution in a four-point bend test. The asymmetric cross-section of Specimen C1 (Figure 6.30) resulted in preferential cracking along the thickest edge of the specimen. This asymmetry was a consequence of poor specimen preparation; the specimen was not machined with both sides at a tangent to the pipe surface. A thicker edge will be more highly strained for a given deflection compared to a thinner edge and this is investigated further in Chapter 7

Machined edges are known to be susceptible to cracking as previously noted and it has been shown that cracking will occur on both chamfered and non-chamfered edges (Figures 6.25 and 6.27) as well as the inner loading roller positions. Therefore, any cracking associated with edges or roller positions (see Figures 6.20 and 6.26) should be treated with caution and taken as an artefact of the four-point bend test method.

Zhai *et al.* [143] showed that there is a relationship between roller spacing and specimen thickness which can generate peak stresses on the tensile surface above the inner loading rollers. The SSC tests presented in this chapter used 10 mm thick specimens loaded with rollers spaced on 60/120 mm centres giving an inner-roller spacing/thickness ratio of 6 and an outer-roller/inner roller ratio of 2. According to Zhai *et al*., both of these ratios will

generate peak stresses at the roller positions.[30] Lube *et al.* [144] identified these peak stresses as 'wedging stresses' that lead to additional tensile stresses on the tensile surface which act to open cracks along the transverse direction. Some of the largest cracks observed in the seabed temperature SSC investigation were in the vicinity of the inner loading rollers so this could be due to so called 'wedging stresses'.

The loading rollers are constrained within the test rig in such a way that they are not free to rotate when a load is applied to the test specimen. When loaded, the specimen is stretched over the roller which will generate frictional forces at the contacting surfaces. The influence of friction at the loading rollers is investigated further in Chapter 7 using strain-gauged flexural bend test specimens and finite element analysis. Chapter 7 also investigates the four-point bend test method to provide insight on how the stress and strain response of parent fully-machined and as-received SSC test specimens may have influenced the cracking observed in this chapter.

[30] These ratios are unavoidable due to limitations on specimen thickness, loading jig size and test vessel size.

CHAPTER 7: RESULTS & DISCUSSION
Stress & Strain Investigation of the Four-Point Bend Test

7.1 Flexural Bend Tests

Four-point bend tests were performed at room temperature, 130 °C and 5 °C to investigate the flexural properties of the weldable 13%Cr supermartensitic stainless steel pipeline material supplied by Nippon steel & Sumitomo Metal Corporation.[31] Flexural properties such as Bending Modulus, Poisson's ratio and 0.2% offset strain were measured at each temperature. Specimens were taken from the longitudinal and transverse orientation of the pipe with thicknesses ranging from 10 mm to 2.5 mm. An assessment was made on the repeatability of the flexural bend test as well as potential sources of error.

7.1.1 Room Temperature Flexural Bend Test Results

Room temperature flexural bend tests were performed on fully-machined specimens measuring 130 mm long x 20 mm wide cut from the longitudinal pipe orientation with thicknesses of 2.5 mm, 5 mm and 10 mm. In addition, flexural bend tests were performed on specimens measuring 70 mm long x 20 mm wide x 4 mm thick cut from the transverse pipe orientation.

[31] The 130 °C test temperature was stipulated by Nippon steel & Sumitomo Metal Corporation and reflects typical operating temperatures this grade of pipeline material would be exposed to in service

7.1.1.1 Flexural Properties in the Longitudinal Direction (24°C)

The room temperature flexural bend test results for specimens cut from the longitudinal orientation of the pipe are given in Figures 7.1 to 7.4. The average value of 0.2% offset strain measured **7297 με** across specimens FB1 to FB10, the elastic bending modulus ranged from 181 – 206 GPa and Poisson's ratio was between 0.29 and 0.32. The average 0.2% offset strain measured for the 10 mm thick specimens (FB1 to FB4) was **7292 με**. Figure 7.1 shows that specimen thickness, in the range of 2.5 mm to 10 mm, does not directly influence the value of 0.2% offset strain determined from the flexural bend tests. The 0.2% offset strain was repeatable to ±100 με across the thickness range tested. The results are summarised in Table 7.1.

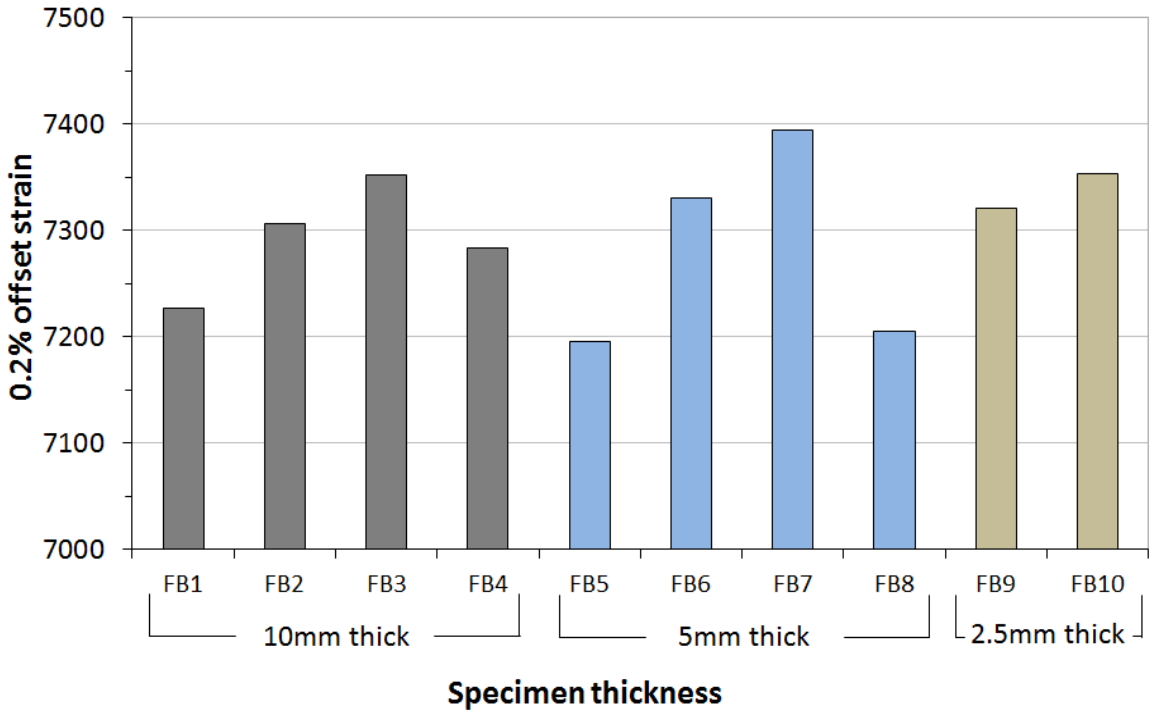

Figure 7.1 Flexural bend test results for 10, 5 & 2.5 mm thick specimens (FB1 – FB10) at 24°C. The 0.2% offset strain can be measured with a repeatability of ±100με

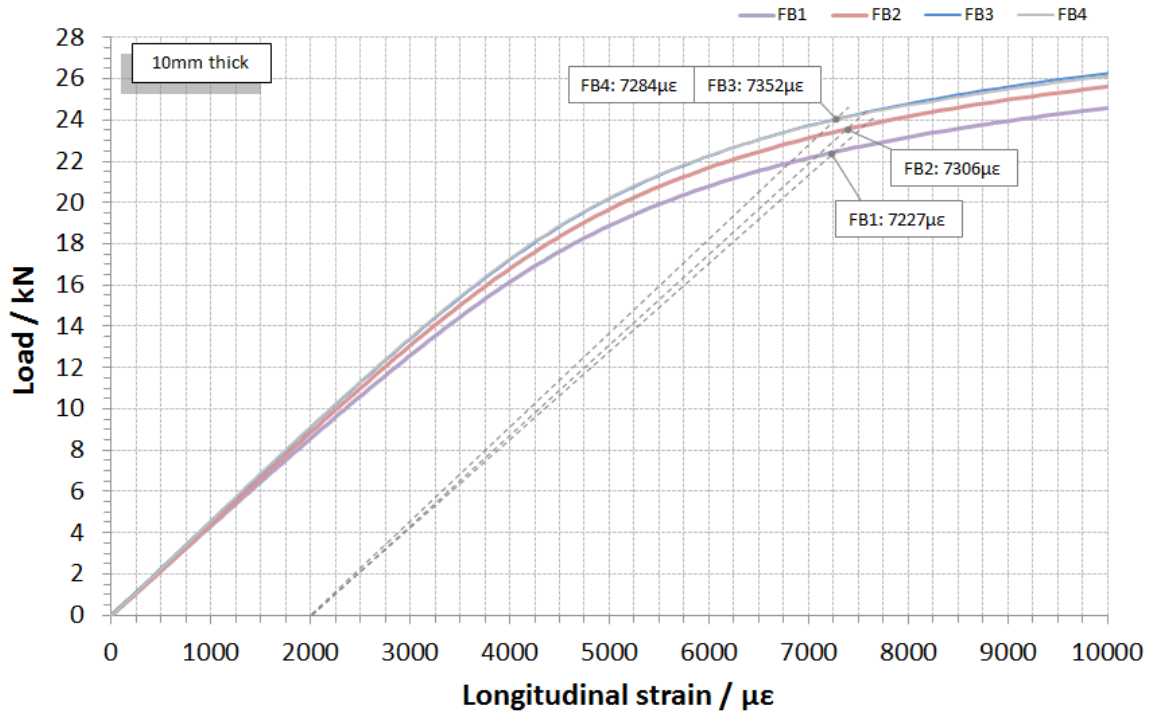

Figure 7.2 Flexural-bend curves for 10 mm thick specimens (FB1-FB4) at 24°C. Figure shows 0.2% offset strain for each test.

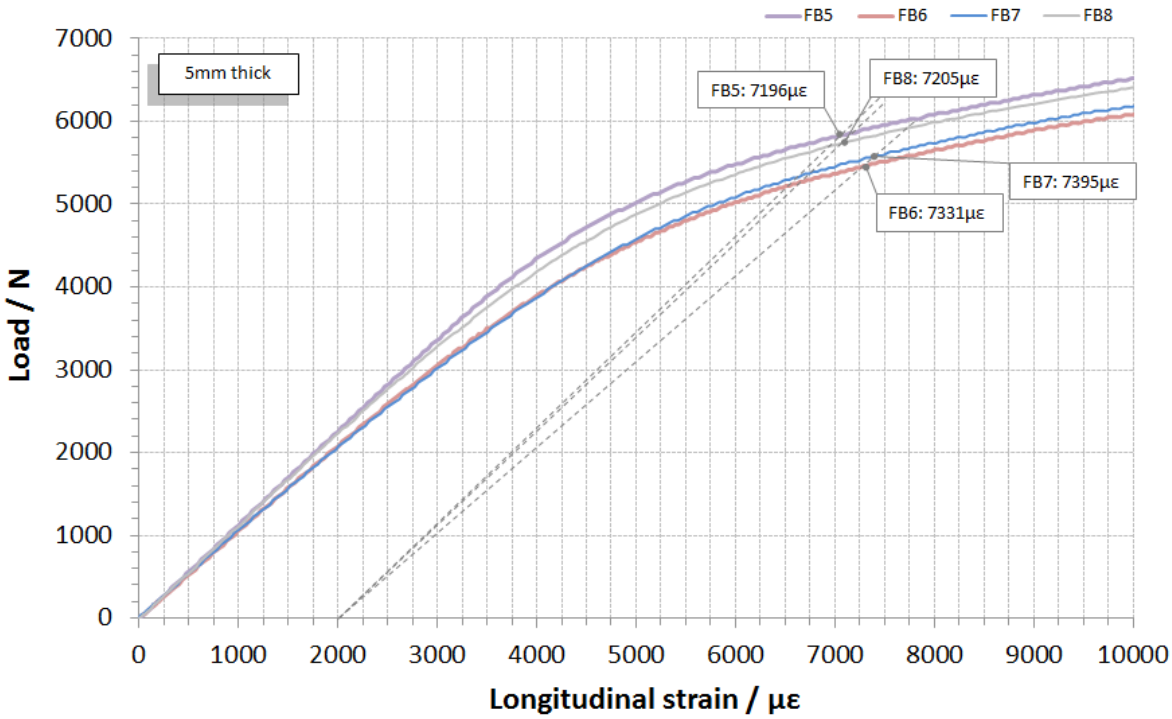

Figure 7.3 Flexural-bend curves for 5 mm thick specimens (FB5-FB8) at 24°C. Figure shows 0.2% offset strain for each test.

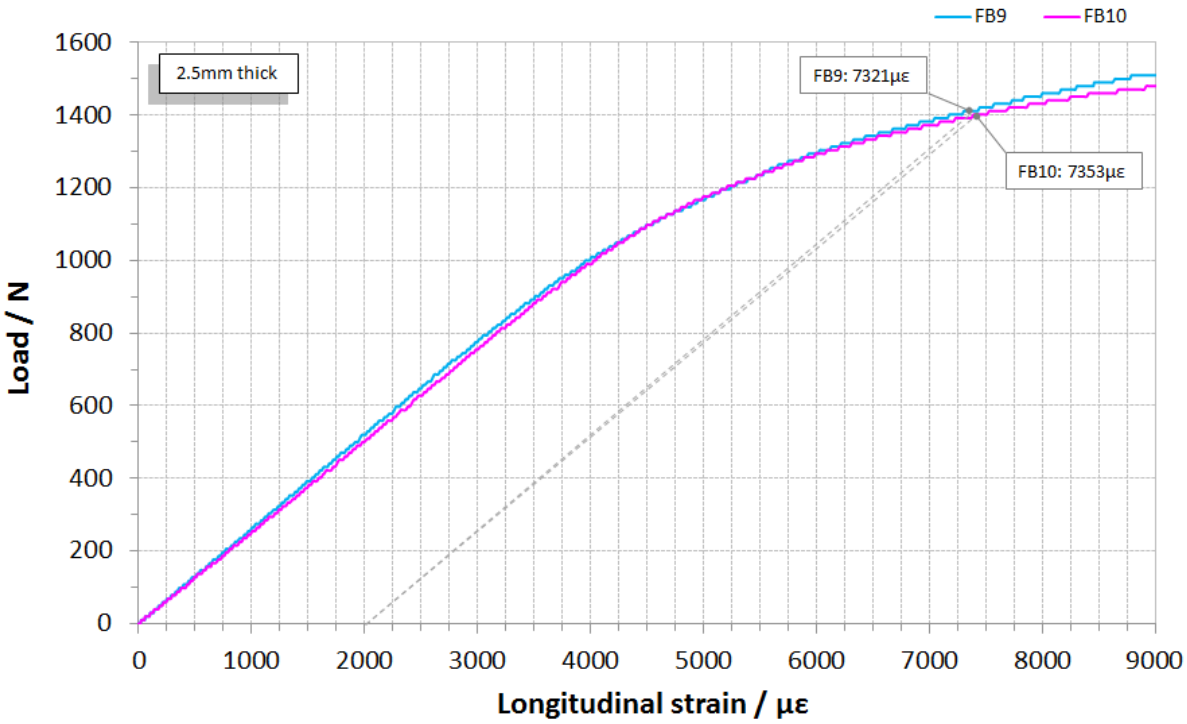

Figure 7.4 Flexural-bend curves for 2.5 mm thick specimens (FB9-FB10) at 24°C. Figure shows 0.2% offset strain for each test.

Table 7.1 Summary of the flexural-bend test results at 24°C: longitudinal specimens

Sample Ref.	Specimen Size (mm) (L x W x D)	Elastic properties		Properties at 0.2% offset strain			
		Modulus (GPa)	Poisson's ratio	Strain (με)	Poisson's ratio	Load (kN)	deflection (mm)
FB1	130x20x10	193	0.30	7227	0.33	22.5	2.53
FB2		198	0.30	7306	0.33	23.5	2.37
FB3		205	0.30	7352	0.33	24.1	2.41
FB4		206	0.29	7284	0.32	24.0	2.41
FB5	130x20x5	203	0.30	7196	0.34	5.9	4.71
FB6		188	0.30	7331	0.32	5.5	4.90
FB7		188	0.39	7395	0.30	5.6	4.93
FB8		201	0.29	7205	0.34	5.8	4.59
FB9	130x20x2.5	188	0.32	7321	0.38	1.4	>10
FB10		181	0.30	7353	0.33	1.4	>10

Note: deflection of the 2.5mm thick specimens exceeded the 10mm stroke of the displacement transducer

7.1.1.2 Poisson's Ratio Measurements (24°C)

Poisson's ratio was determined from the longitudinal and transverse strain measurements taken during the room temperature flexural bend tests described previously. The average Poisson's ratio in the elastic region was then used in the finite element models described later in this chapter. Figures 7.5 to 7.7 show how the Poisson's ratio of specimens FB1 to FB10 changes during deformation in the flexural bend test. The measurements were taken from the biaxial strain gauge on the tensile test surface and expressed as a ratio of transverse to longitudinal strain components. The figures show that the 10 mm thick specimens give more repeatable results than the 5 mm thick and 2.5 mm thick specimens. As thickness reduces, repeatability worsens. For this reason, 10 mm thick specimens were used as a standard for the remaining flexural bend tests performed in this project.

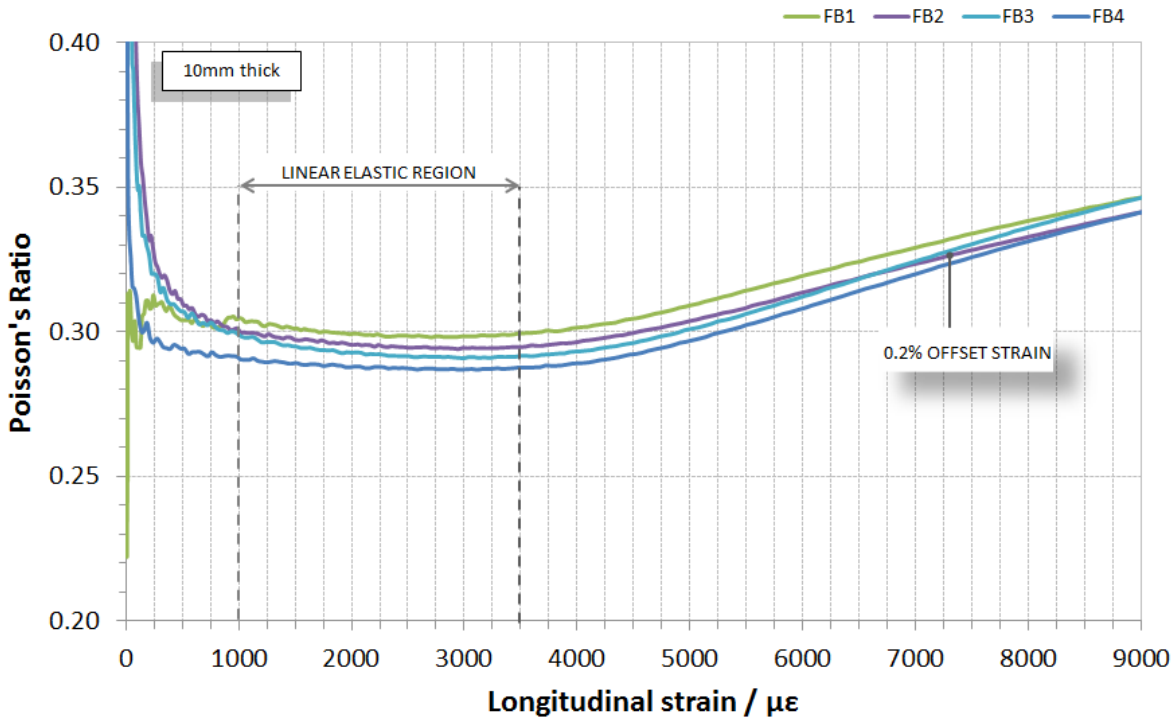

Figure 7.5 Change in Poisson's Ratio during the flexural bend test: 10 mm thick specimens at 24°C

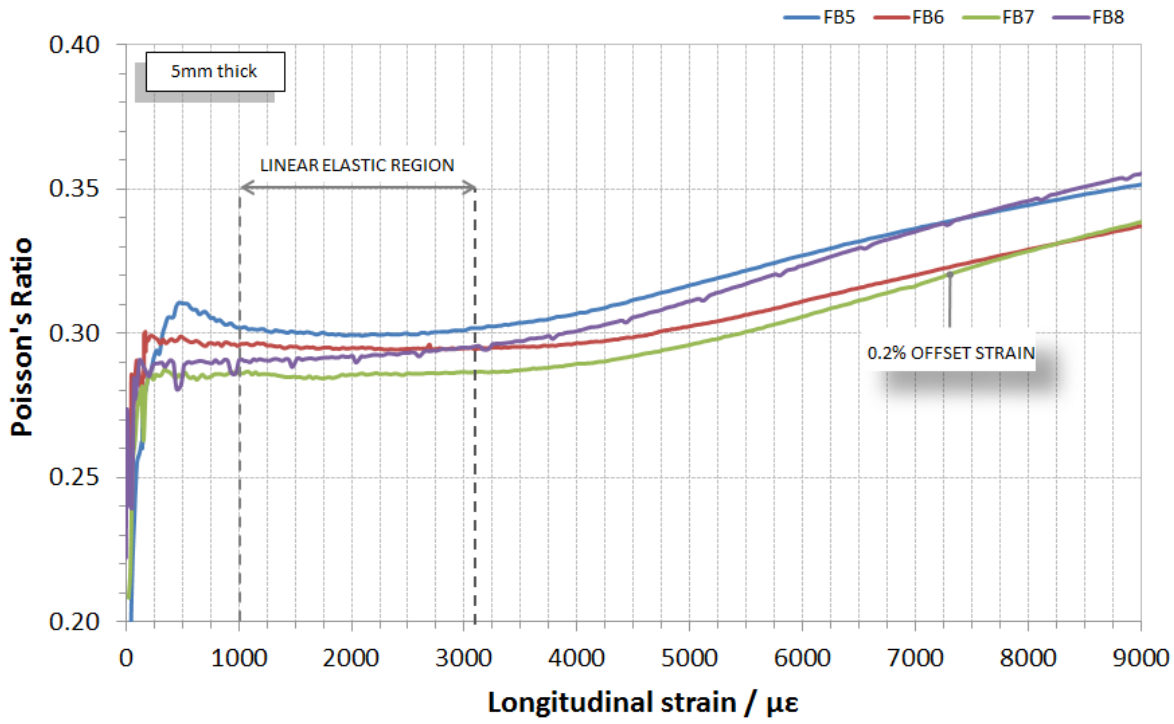

Figure 7.6 Change in Poisson's Ratio during the flexural bend test: 5 mm thick specimens at 24°C

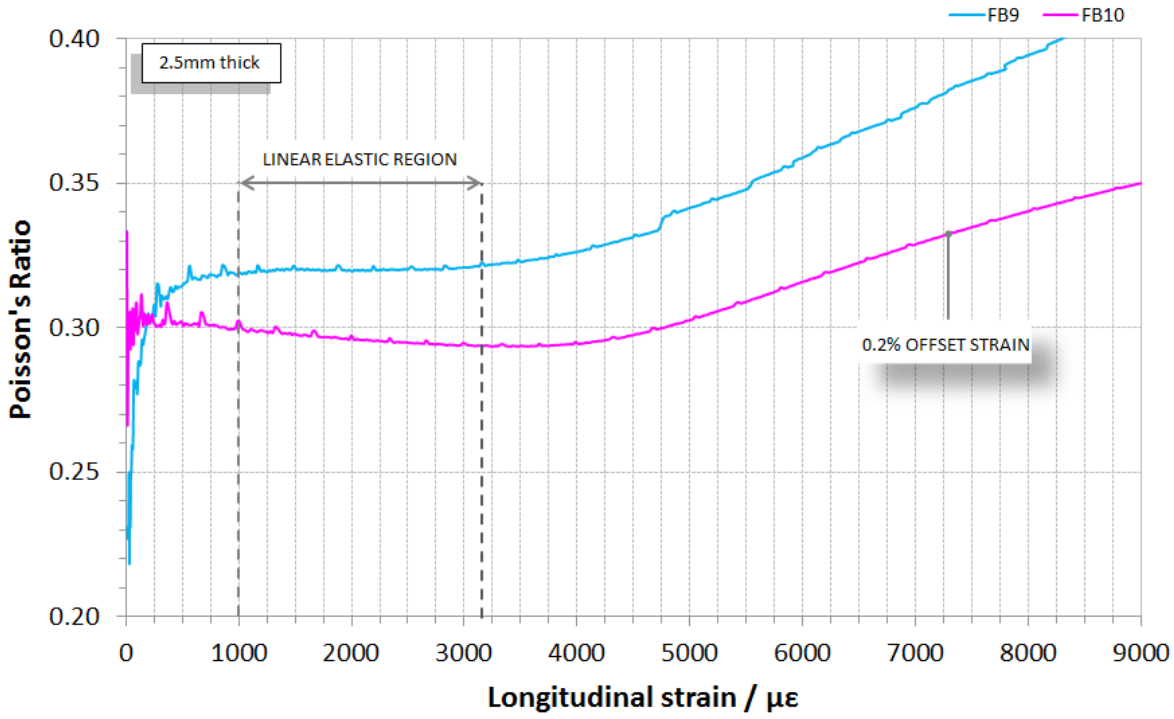

Figure 7.7 Change in Poisson's Ratio during the flexural bend test: 2.5 mm thick specimens at 24°C

7.1.1.3 Flexural Bend Properties in the Transverse Direction (24°C)

The room temperature flexural bend test results for specimens cut from the transverse orientation of the pipe are given in Figure 7.8. The average value of 0.2% offset strain was higher than the longitudinal specimens, measuring **7439 με** across specimens FB11 to FB13, the elastic bending modulus ranged from 190 – 199 GPa and Poisson's ratio was between 0.27 and 0.29. The results are summarised in Table 7.2.

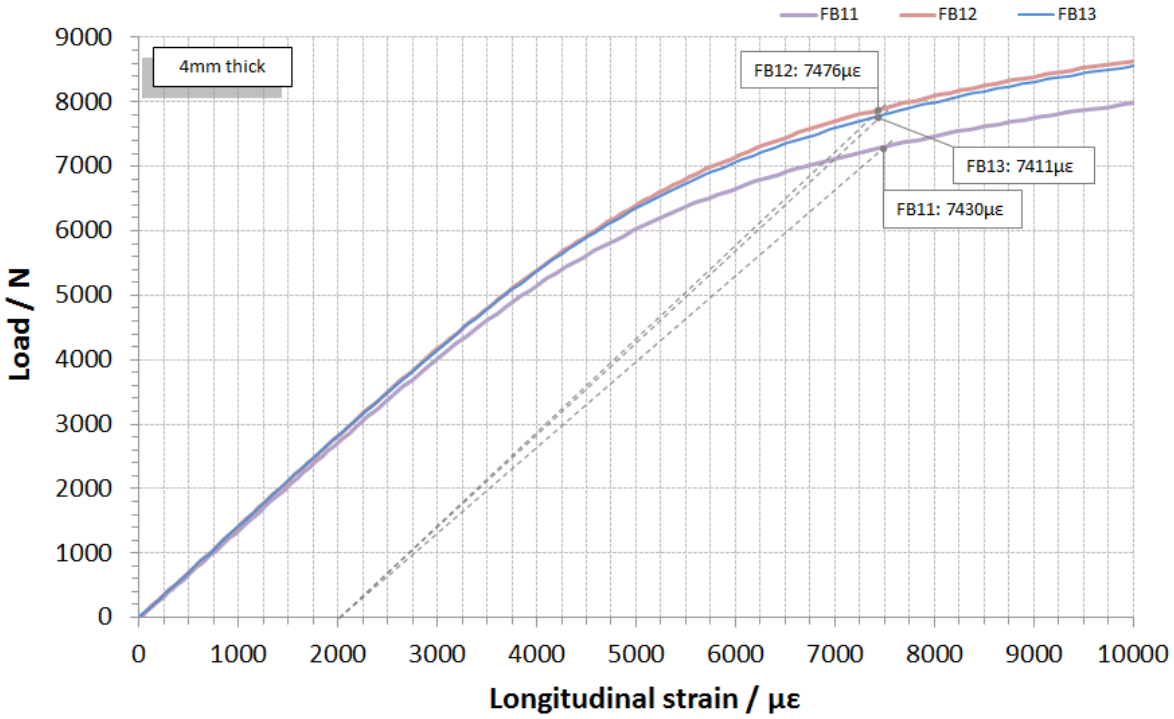

Figure 7.8 Flexural-bend curves for transverse section specimens (FB11-FB13) at 24°C. Figure shows 0.2% offset strain for each test.

Table 7.2 Summary of the flexural-bend test results at room temperature: transverse specimens

Sample Ref.	Specimen Size (mm) (L x W x D)	Elastic properties		Properties at 0.2% offset strain			
		Modulus (GPa)	Poisson's ratio	Strain (με)	Poisson's ratio	Load (kN)	deflection (mm)
FB11	70x20x4	190	0.27	7430	0.27	7.4	1.51
FB12		199	0.27	7476	0.28	7.8	1.48
FB13		199	0.29	7411	0.30	7.8	1.53

7.1.2 Flexural Bend Test Results at 130 °C

The results of the 130 °C flexural bend tests are given in Figure 7.9 and are compared with the 10 mm thick longitudinal specimens tested at room temperature. This comparison shows there is no change in the flexural response at 130 °C when compared to 24 °C. In the 130 °C tests, the average value of 0.2% offset strain measured **7327 με** and the elastic bending modulus ranged from 190 – 198 GPa which is consistent with the 24 °C test results.

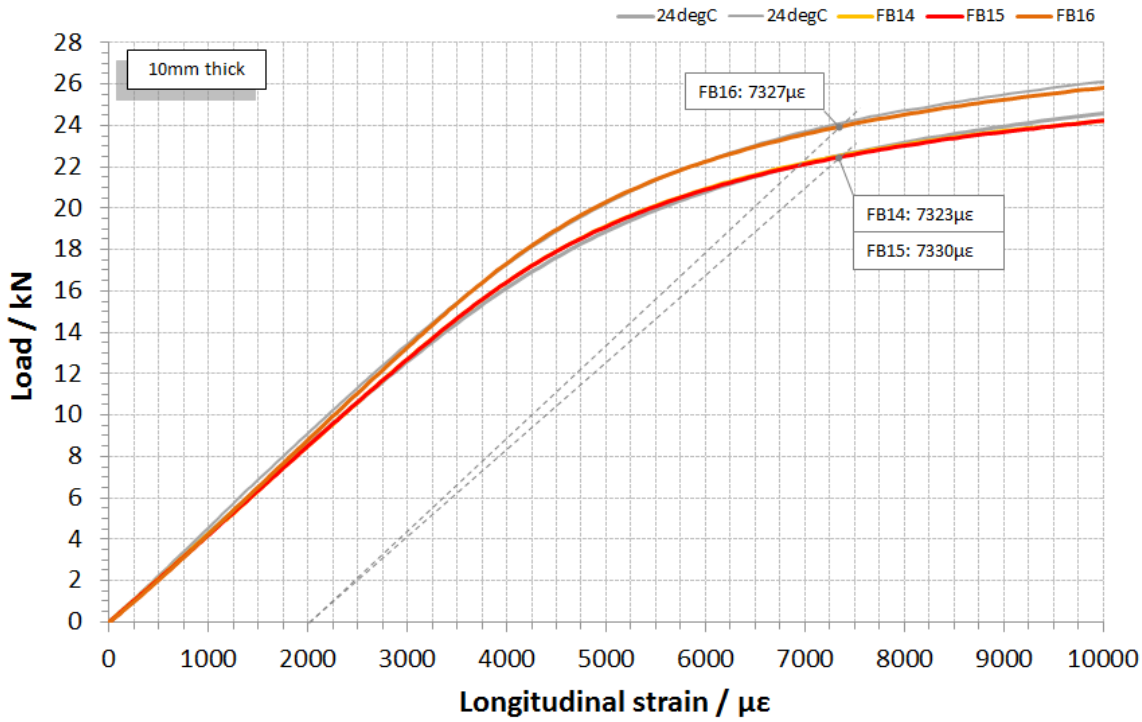

Figure 7.9 Flexural-bend curves for 10 mm thick specimens (FB14 to FB16) at 130 °C. Figure shows the 0.2% offset strain and includes the 24 °C curves for comparison

Table 7.3 Summary of the flexural-bend test results at 130 °C: longitudinal specimens

Sample Ref.	Specimen Size (mm) (L x W x D)	Elastic properties		Properties at 0.2% offset strain			
		Modulus (GPa)	Poisson's ratio	Strain (με)	Poisson's ratio	Load (kN)	deflection (mm)
FB14	130x20x10	193	0.29	7323	0.34	22.5	2.88
FB15		190	0.29	7330	0.34	22.5	2.93
FB16		198	0.29	7327	0.32	23.9	2.86

7.1.3 Low Temperature Flexural Bend Test Results (5 °C & 24 °C)

Figure 7.10 shows the load-strain curves for flexural bend tests performed at 5 °C and 24 °C. All the specimens were 10 mm thick and cut from the longitudinal orientation of the pipe. The average value of 0.2% offset strain measured **7276 με** at 24 °C and **7318 με** at 5 °C, showing that there is no significant difference between the flexural responses at these two temperatures.

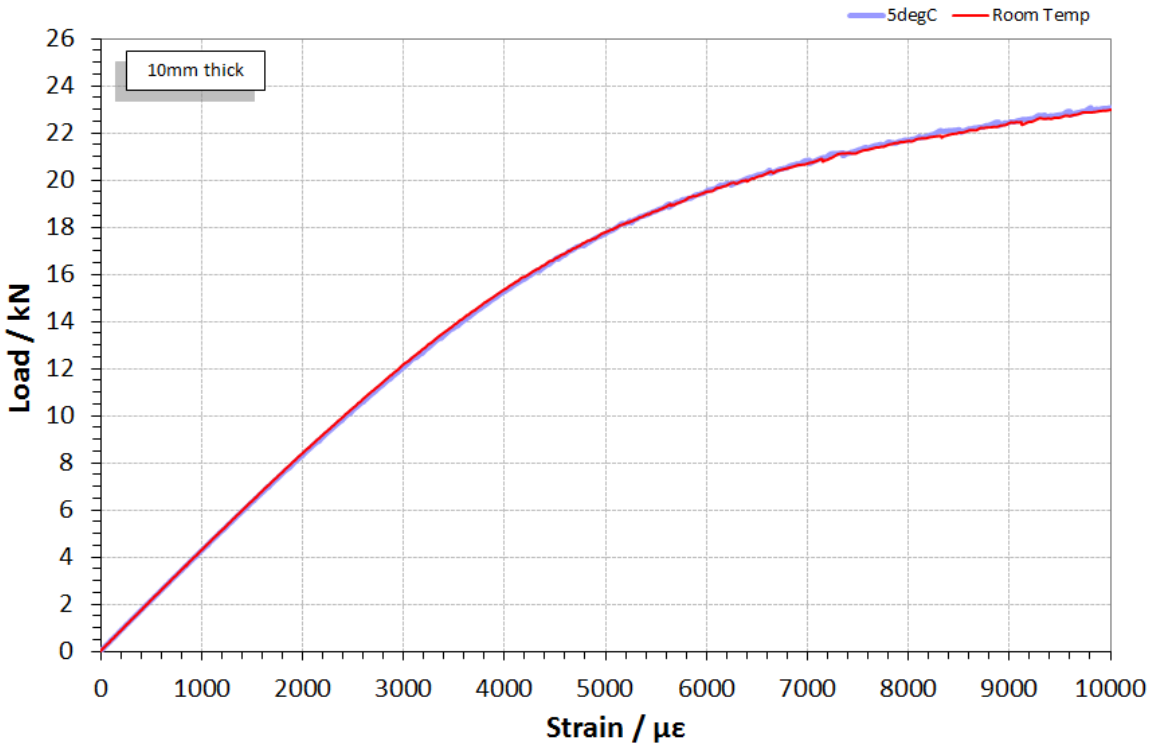

Figure 7.10 Flexural-bend curves for 10 mm thick specimens at 5 °C and 24 °C. Longitudinal section specimens tested

Table 7.4 Summary of the flexural bend test results at 5 °C and 24 °C

Temp (°C)	$\varepsilon_{0.2}$ (με)	$Load_{0.2}$ (kN)
5	7329	21.1
5	7307	21.0
24	7247	20.9
24	7304	21.0

7.1.4 Measurement Errors Associated with the Flexural Bend Test

7.1.4.1 Gradient of the Load-Strain Curve

The precision of the 0.2% offset strain measured from the load-strain curve is sensitive to the gradient of the linear-elastic portion of the curve as shown Figure 7.11 for the 10 m thick room temperature flexural-bend test specimens presented in Section 7.1.1.1. The standard deviation is ±51 με for 10 mm thick specimens, ±97 με for 5 mm thick specimens and ±22 με for the 2.5 mm thick specimens. This represents a typical error of ±1). Note that only two 2.5 mm thick specimens were tested so the error may be greater when more samples are considered.

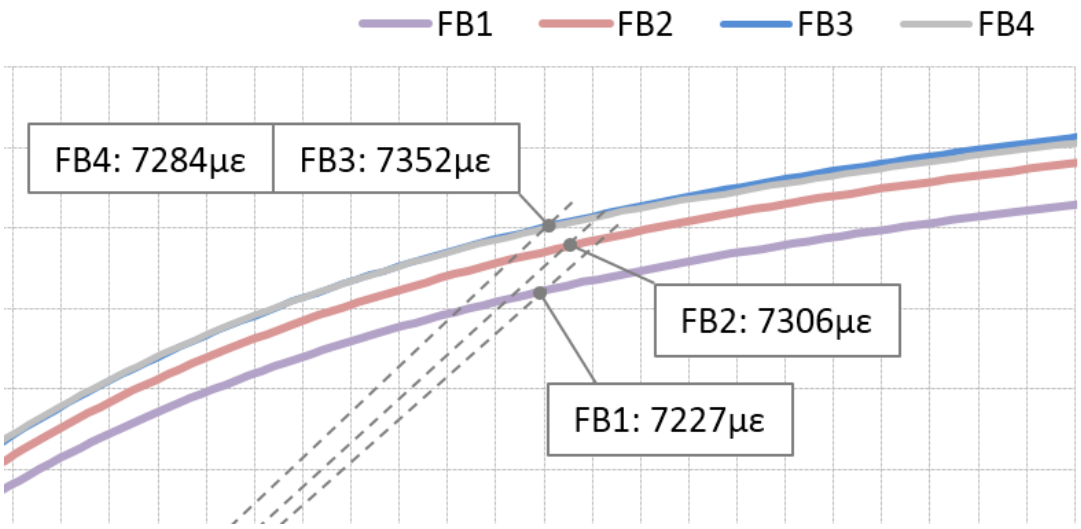

Figure 7.11 Errors in the 0.2% offset strain due to differences in gradient of the linear region from load-strain curve (10 mm thick specimens)

7.1.4.2 Strain Gauge Misalignment

Table 7.5 shows the measured flexural-bend properties of two specimens with the measurement strain gauge misaligned by β=1° and β=3° compared to a correctly aligned strain gauge (β=0°). The corresponding error is negligible and consistent between measured and theoretical values (Table 7.6). Even with a relatively large gauge misalignment of 3°, the

errors associated with the 0.2% offset strain are in the order of 38 με (0.52%). The theoretical error for the same amount of misalignment is comparable at 27 με (0.40%).

Table 7.5 Measured parameters at the 0.2% offset strain with the measurement strain-gauge misaligned by angle β to the principal axis

β	Specimen Size (mm) (L x W x D)	Elastic properties		Properties at 0.2% offset strain			
		Modulus (GPa)	Poisson's ratio	Strain (με)	Poisson's ratio	Load (kN)	deflection (mm)
0°	130x20x10	207	0.30	7310	0.34	24.3	2.66
1°		209	0.29	7308	0.32	24.4	2.59
3°		212	0.28	7272	0.34	24.4	2.58

Table 7.6 Measured error (n) at the 0.2 % offset strain compared to theoretical value for gauge misalignments of β=1° & β=3° to the principal axis

β	Measured error		Theoretical error	
	$(\varepsilon_{L0} - \varepsilon_{L\beta})$	(%)	n_L	n_L (%)
1°	2με	0.03	3με	0.04
3°	38με	0.52	27με	0.40

7.1.4.3 Specimen Misalignment in the Loading Rollers

Table 7.7 shows the difference in measured flexural-bend properties between a specimen correctly aligned in the loading rollers (θ=0°) with a specimen purposely misaligned by 2° in the loading rollers. The difference in the measured value of 0.2% offset strain between the two specimens was 53 με (0.73%).

Table 7.7 Measured parameters at 0.2% offset strain with specimen alignment (θ) in the loading rollers

θ	Specimen Size (mm) (L x W x D)	Elastic properties		Properties at 0.2% offset strain			
		Modulus (GPa)	Poisson's ratio	Strain (με)	Poisson's ratio	Load (kN)	deflection (mm)
0°	130x20x10	207	0.30	7310	0.34	24.3	2.66
2°		202	0.30	7363	0.34	24.0	2.57

7.1.5 Summary of the Flexural Bend Tests

1. Based on the 10 mm thick fully-machined specimens cut from longitudinal orientation of the pipe, the average 0.2% offset strain measured **7292 με** at room temperature, **7327 με** at 130 °C and **7318 με** at 5 °C. The corresponding deflection required to achieve the 0.2% offset strain ranged from 2.37-2.93 mm at room temperature and 2.86-2.93 mm at 130 °C.

2. The use of 10 mm thick test specimens provides the most accurate Poisson's ratio measurement in bending and also improves the accuracy of the 0.2% offset strain measurement to ±0.85%.

3. The most significant errors generated from a flexural bend test come from manually measuring the 0.2% offset strain from the load-strain curve. Here, errors in the order of ±1.0% are easily incurred. Other errors such as misalignment of strain gauges or specimen misalignment in the loading rollers are minimal, even when large misalignments are considered. For example when the loading strain gauge is misaligned by 3° to the principal axis, the corresponding error is only ±38 με. When the specimen is misaligned in the loading rollers by 2°, the corresponding error is 53 με.

7.2 Tensile & Flexural-Bend Test Comparison

This section uses finite element analysis to compare the tensile and flexural-bend test methods and explains the difference observed in the 0.2% offset strain generated by both methods. The results are used to verify if the 0.2% offset strain determined from a tensile stress-strain curve should be used to set the load in a four-point bend test specimen to achieve the correct level of 0.2% plastic strain on the tensile test face.

7.2.1 Stress Distribution in Pure Tension and Four-Point Bending

In a uniaxial tensile test, stress is distributed uniformly through the thickness of the gauge-length whereas in a four-point bend test, stress changes from tension on one face to compression on the other, resulting in a through-thickness stress gradient. This difference is illustrated by the finite element models in Figure 7.12 when both are loaded to approximately 740 MPa.

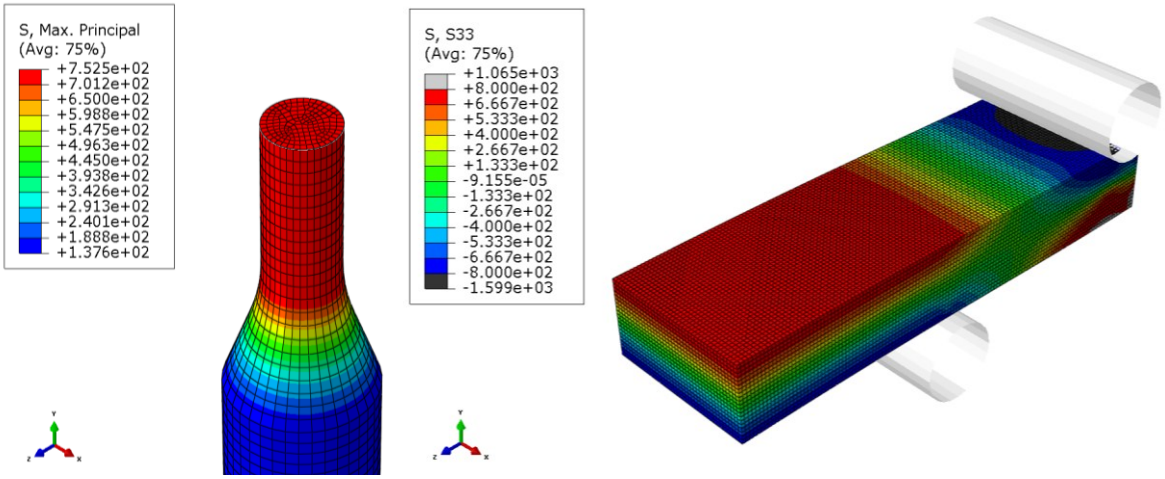

Figure 7.12 Stress distribution in tensile (left) and four-point bend (right) test specimens. FE models loaded to 0.2% offset yield stress (≈740 MPa)

7.2.2 Comparing the 0.2% Offset Strain in Tension and Flexure

Figure 7.13 shows the difference in the 0.2% offset strain determined from room temperature tensile and flexural-bend tests made on specimens cut from the longitudinal orientation of the supplied pipe. This difference is quantified in Table 7.8 for tests carried out at 5 °C, 24 °C and 130°C. At 24 °C, the 0.2% offset strain from a tensile test is 18% lower than the 0.2% offset strain determined from a flexural bend test. At 5 °C and 130 °C, the difference is 24%.

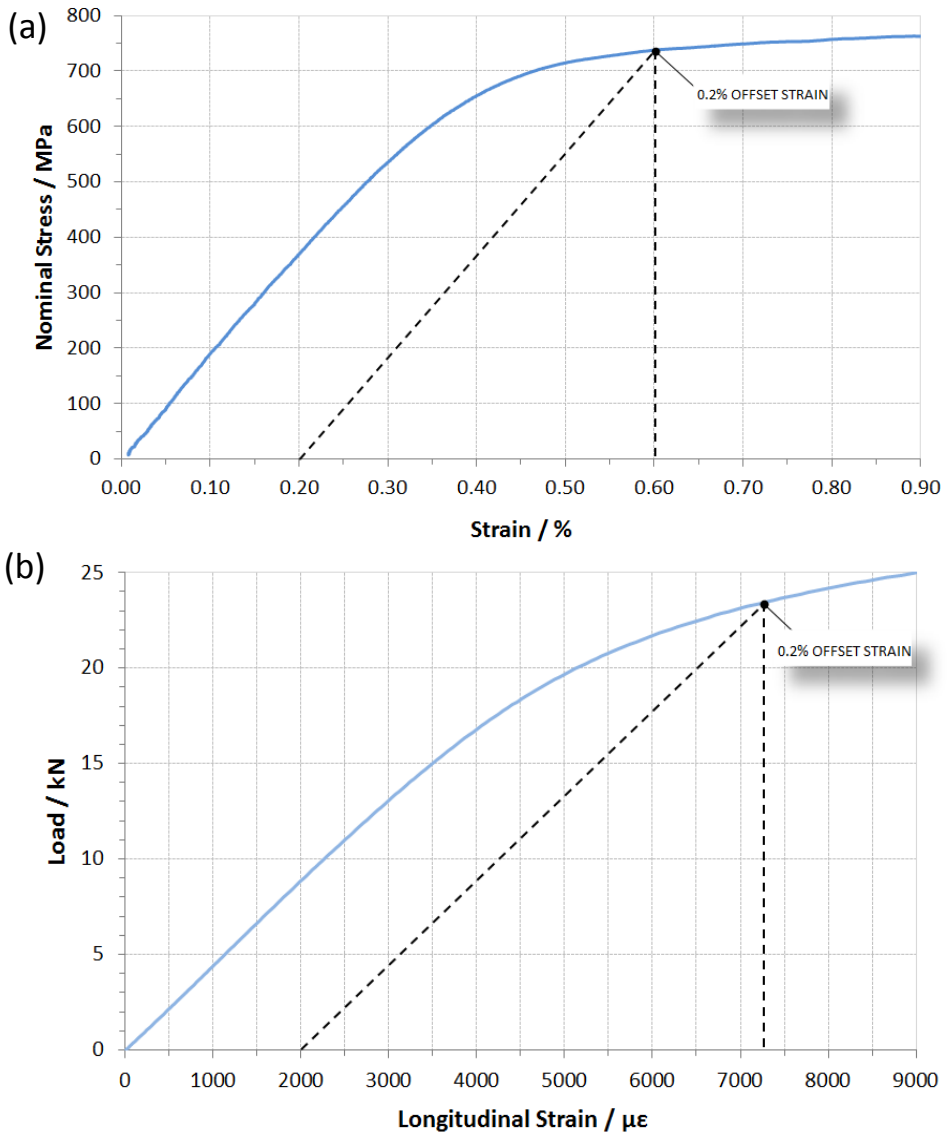

Figure 7.13 (a) Stress-Strain curve from a uniaxial tensile test & (b) Load-Strain curve from a flexural bend test. Note the higher 0.2% offset strain generated by the flexural bend test.

Table 7.8 Comparison of tensile and flexural bend test results at 5 °C, 24 °C and 130 °C

Orientation	Test Temp. (°C)	Average tensile 0.2% yield stress (MPa)	Average strain at 100% AYS (με)		Difference in strain at 0.2% offset
			Tension*	Flexure	
Longitudinal	5	712	5557	7318	24%
Longitudinal	24	739	5970	7292	18%
Transverse	24	744	6070	7439	18%
Longitudinal	130	706	5589	7327	24%

**Tensile stress/strain data taken from Chapter 5, Section 5.3*

The finite element method was used to generate load-strain, stress-strain and stress-load curves from models of the tensile and flexural bend test methods. The results from the FE models were validated using linear elastic equations and taking data from the elastic regions of the stress-load curves as shown in Figure 7.16

The **load-strain curves** in Figure 7.14 show that the 0.2% offset strain in tension equals 6000 με whereas the 0.2% offset strain in bending equals 7100 με. This is in good agreement with the experimental tensile and flexural bend test results given in Figure 7.13 and Table 7.8. The **stress-strain curves** in Figure 7.15 show that the 0.2% offset strain measures approximately 6200 με in both tension and bending, suggesting that the 0.2% offset strain from tensile stress-strain data is a valid measure of the 0.2% offset strain in four-point bending. The **stress-load curves** in Figure 7.16 show why the load-strain curve from a flexural bend test gives a higher 0.2% offset strain than a stress-strain curve from a tensile test: In uniaxial tension, load increases linearly with stress whereas in bending, the load-stress relationship becomes non-linear in the plastic regime.

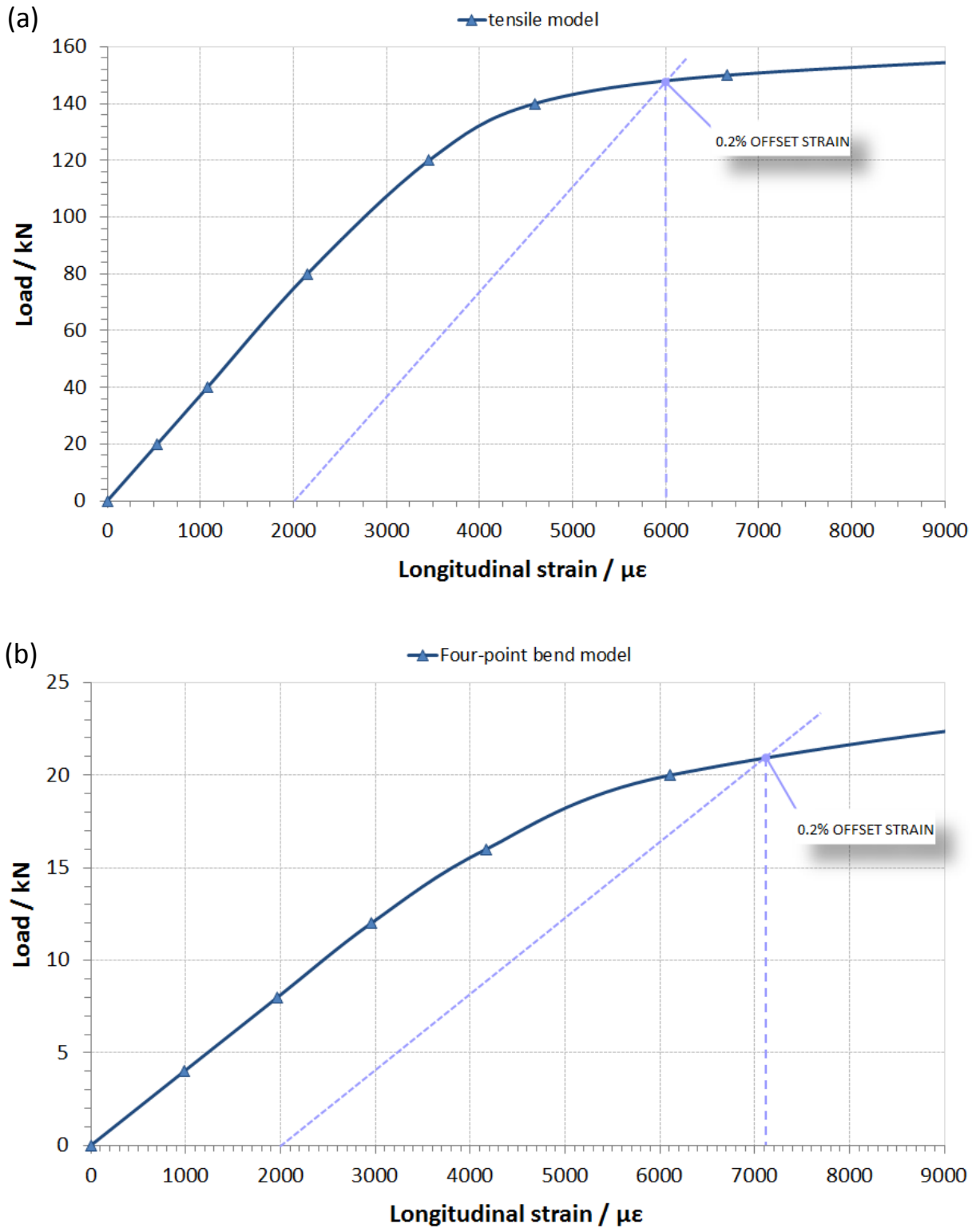

Figure 7.14 Load-Strain curves from FE models of tensile test (a) & flexural-bend test (b). The 0.2% offset strain is higher for the flexural bend test method.

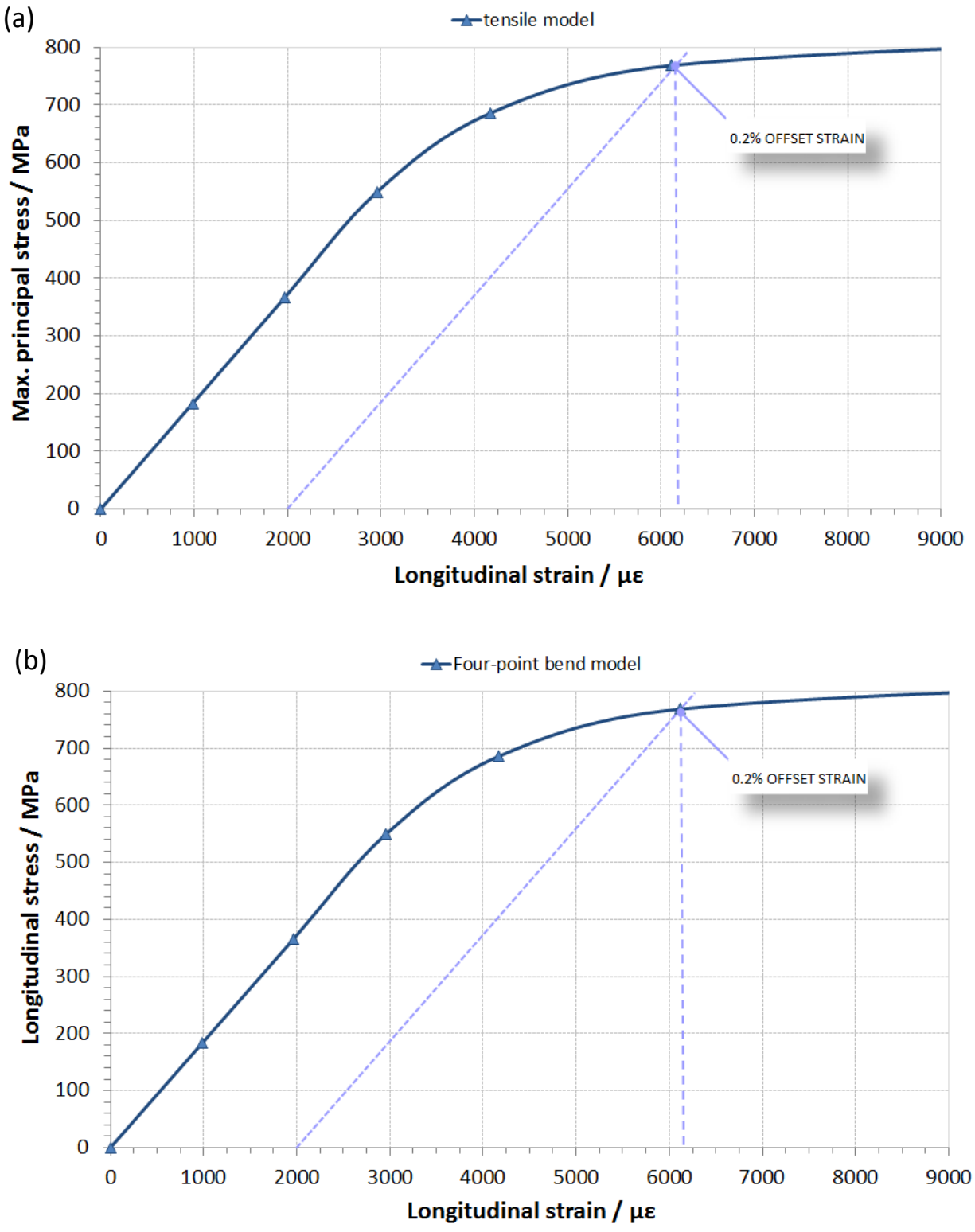

Figure 7.15 Stress-Strain curves from FE models of tensile test (a) & flexural-bend test (b). The 0.2% offset strain is the same for both loading methods.

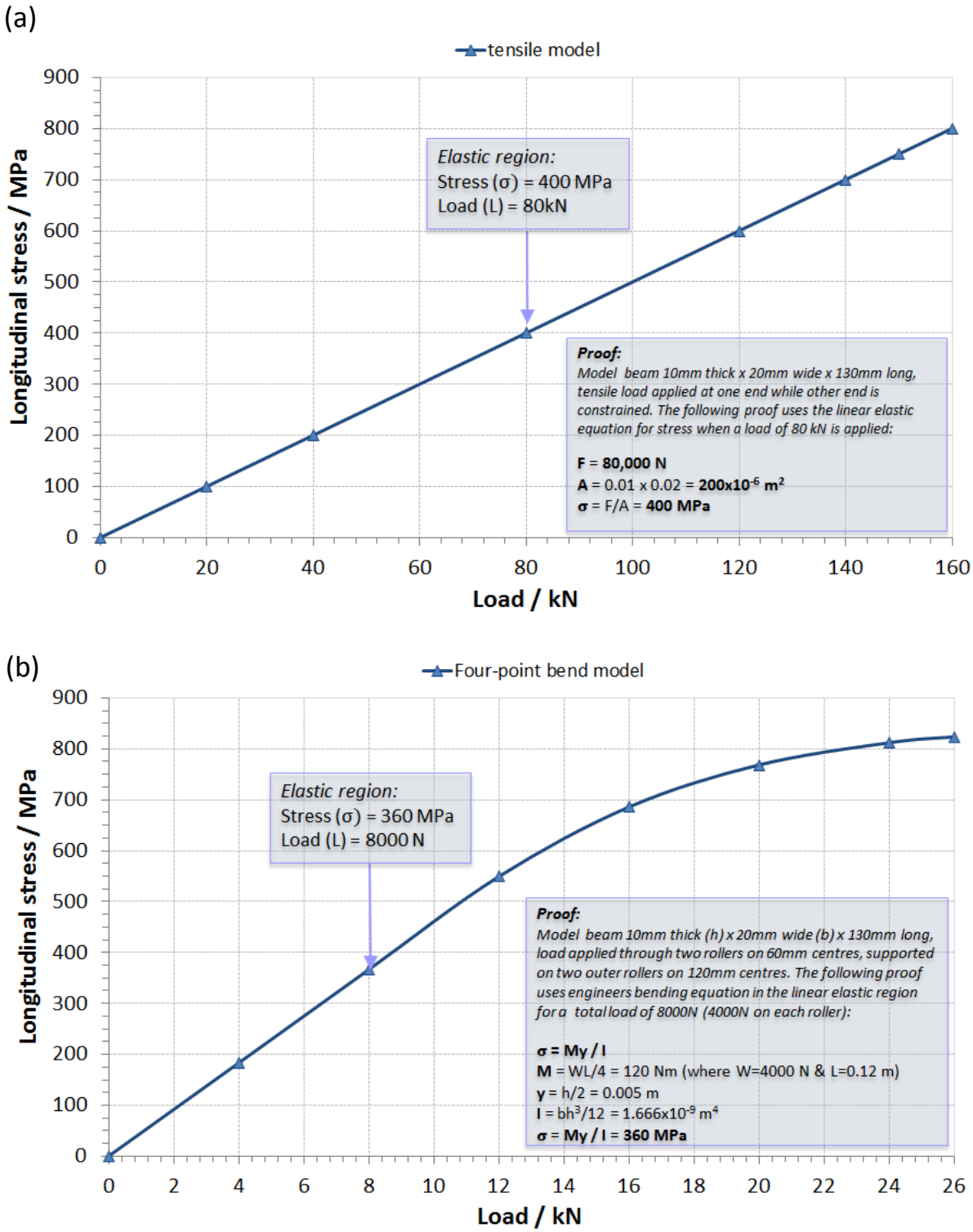

Figure 7.16 Stress-Load curves from FE models of tensile test (a) & flexural-bend test (b). In tension, load increases linearly with stress. In bending, the load-stress relationship becomes non-linear in the plastic regime.

Figure 7.17 shows the evolution of elastic and plastic strain components on the surface of the flexural-bend FE model during loading. This shows that a loading strain of 6000 με (determined from a tensile test) produces a surface plastic strain of 0.2% (Load Step 6) while a loading strain of 7300 με (determined from a flexural-bend test) produces a surface plastic strain of approximately 0.3% (Load Step 8).

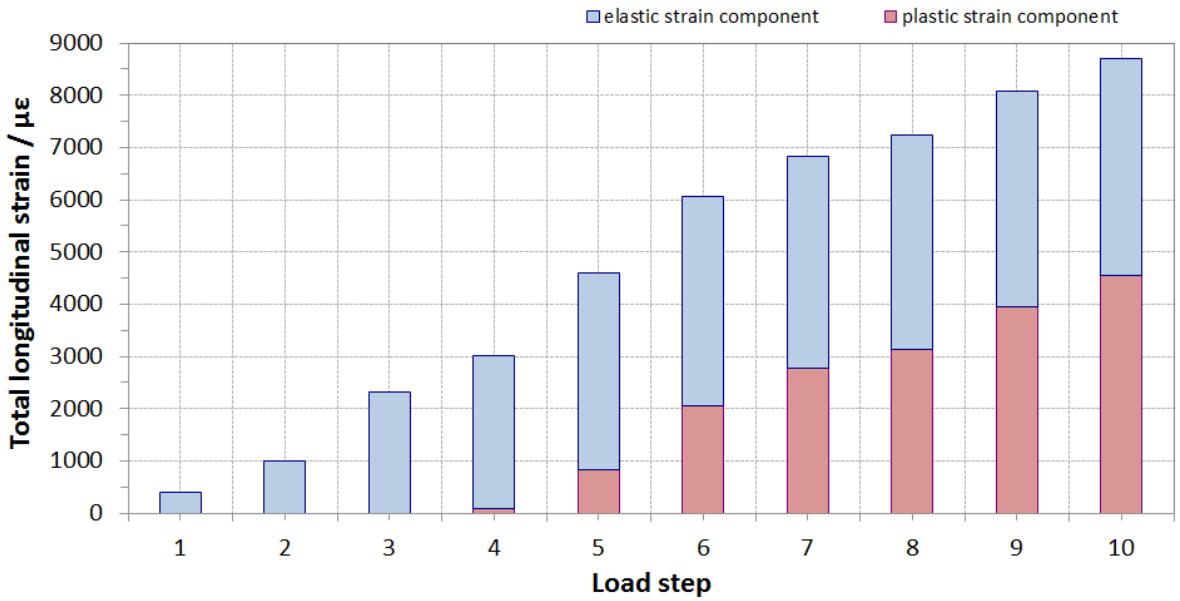

Figure 7.17 FE results of a four-point bend test showing elastic and plastic strain components. Load Step 6 corresponds to the loading strain set by tensile stress-strain data and Load Step 8 corresponds to the loading strain set by flexural-bend load-strain data.

Figure 7.18 shows the stress and strain gradients generated through the thickness of the flexural bend model at the mid-length, mid-width position at Load Step 6 (6000 με) and at Load Step 8 (7300 με). When the beam is fully elastic, both stress and strain increase linearly with distance from the neutral axis. When plastically deformed, stress becomes non-linear in the plastic zone near the surfaces while strain continues to increase linearly. Note the steep change in stress gradient at approximately 2 mm from the surface, highlighting the depth of plastic strain in the specimen (loaded to 7300 με).

When the loading strain is increased from 6000 με to 7300 με, the increase in stress is only 11 MPa (1.5% of the target AYS value). This small increase in stress for a relatively large increase in strain is due to the shallow gradient of the stress-strain curve in the plastic regime where strain exceeds 0.5% (see Figure 7.13a).

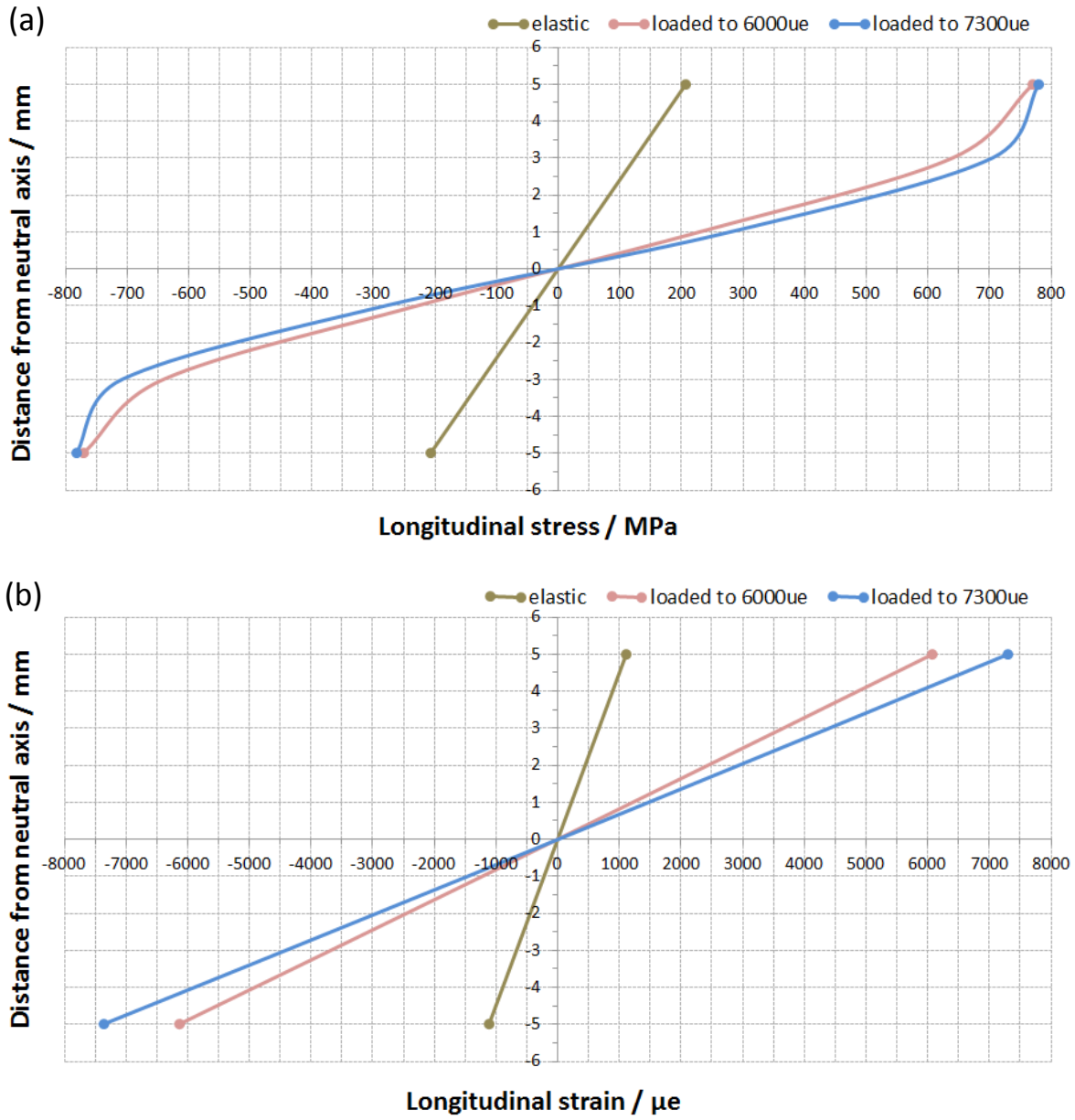

Figure 7.18 Through-thickness Stress (a) & Strain (b) gradients in a 10 mm thick four-point bend specimen. The FE model was loaded to 6000 με and 7300 με, corresponding to loading levels set by tensile stress-strain data and flexural load-strain data respectively.

7.2.3 Summary of the Tensile & Flexural Bend Test Comparison

1. Physical tests and finite element models show that the 0.2% offset strain measured from a uniaxial tensile is approximately 18-24% lower than the 0.2% offset strain measured from a flexural bend test. The 0.2% offset strain from a tensile stress-strain curve is approximately 6000 με and the 0.2% offset strain from a flexural bend test is approximately 7300 με. Some companies prefer to set the loading strain of four-point bend SSC/SCC test specimens using flexural bend data as it is a more conservative approach.

2. Finite element analysis was used to show that the higher 0.2% offset strain given by a flexural-bend load-strain curve is due to the non-linear relationship between load and stress during plastic deformation. In contrast, a tensile test specimen has a linear relationship between load and stress in the plastic regime (when tested up to 10000 με). The consequence of this is a tensile load-strain curve is directly comparable to a tensile stress-strain curve but a flexural-bend load-strain curve IS NOT comparable to a tensile stress-strain curve. Therefore, the flexural-bend load-strain curve SHOULD NOT be treated in the same way as a tensile stress-strain curve.

3. For the reasons given in point 2, the 0.2% offset value from the flexural-bend load-strain curve will result in a surface plastic strain of approximately 0.3%. In terms of stress, this only equates to an additional 11 MPa (101.5% AYS), hence strain is a more important consideration when loading four-point bend specimens from flexural bend data.

7.3 Full-Field Stress & Strain Analysis

Finite Element Analysis was used to show the full-field stress and strain distribution generated on the tensile test surface of parent four-point bend SSC test specimens representative of those tested in Chapter 6. Both fully-machined and as-received cross-sectional geometries were modelled (see Figure 4.4) and loaded to a nominal strain of 7300 με at the mid-length, mid-width position on the test surface to match the loading conditions used in the SSC tests.

The work presented in this chapter investigates the anticlastic bending effect [117], the influence of roller contact friction and how edge chamfers and fillet radii influence the stress and strain distribution on the tensile test surface of the four-point bend specimens. Where appropriate, the finite element models were verified with measurements made on four-point bend specimens fitted with strain gauges and four-point bend specimens analysed by DIC. To conclude this chapter, a model with the same physical geometry as the as-received specimen that displayed anomalous cracking behaviour in the condensed water tests from the seabed temperature SSC investigation is analysed to show that cracks were generated in the area where strain was concentrated.

7.3.1 Surface Stress & Strain Distribution in Four-Point Bending

7.3.1.1 Fully-Machined Geometry

Figure 7.20 shows the maximum principal stress distribution on the tensile surface of a 130x20x10 mm fully-machined specimen loaded to a nominal longitudinal strain of 7294 με. Assuming frictionless contact with the rollers, the model predicts a small stress concentration in the order of 26 MPa (3% of the nominal loading stress) located below the inner loading rollers on the tensile surface:

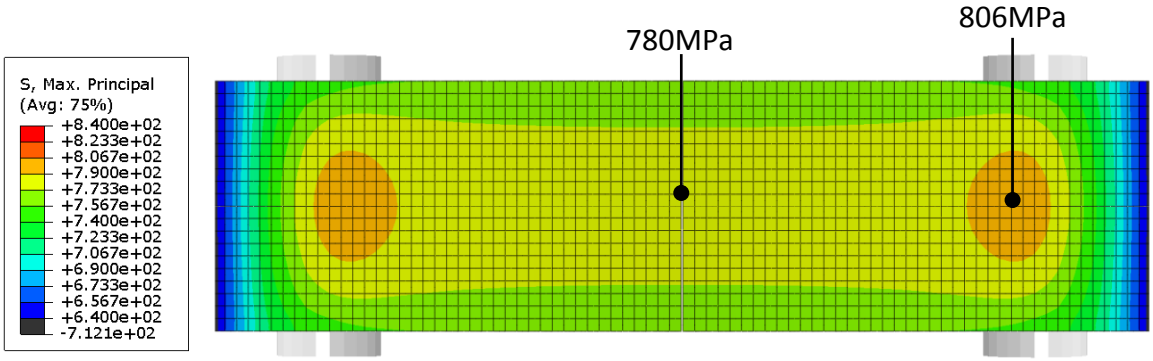

Figure 7.20 Maximum Principal Stress on the tensile surface of a fully-machined four-point bend specimen loaded to 7294 με (assuming frictionless contact between the rollers & the test specimen). Stress is concentrated on the tensile test surface below the inner loading rollers.

Figures 7.21 and 7.22 show the corresponding longitudinal and transverse strain distributions. In contrast to stress, strain is not concentrated at the roller positions but there is a transverse strain concentration along the edges of the specimen. Longitudinal strain is relatively uniform between the inner loading rollers, with the model predicting an area of ±16 mm from the centreline where longitudinal strain is uniform to a tolerance of -1.0% of the nominal loading strain. The DIC measurements in the figures confirm the predictions of the finite element models, but it must be noted that the resolution of the DIC measurements was limited due to the large analysis area used.

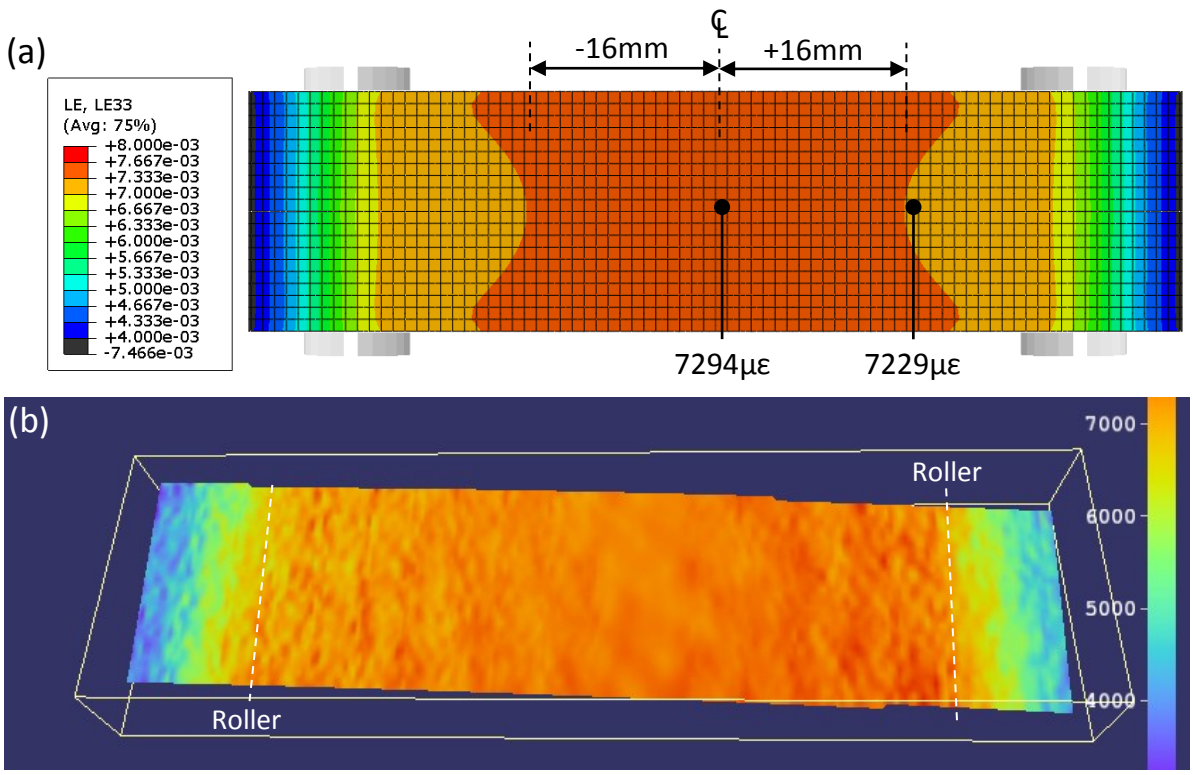

Figure 7.21 Finite element model (a) and DIC measurement (b) showing longitudinal strain on the tensile surface of a fully-machined four-point bend specimen loaded to 7300 με. FE model assumes frictionless contact between the rollers & the test specimen.

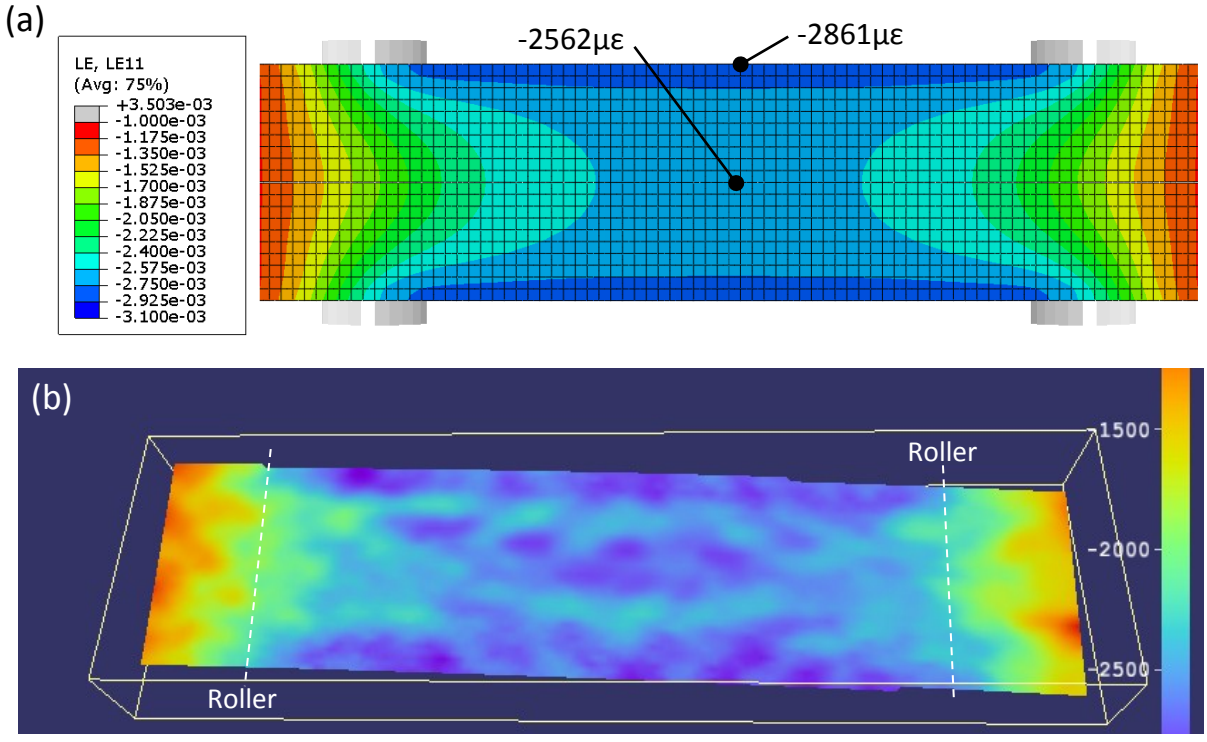

Figure 7.22 Finite element model (a) and DIC measurement (b) showing transverse strain on the tensile surface of a fully-machined four-point bend specimen loaded to 7300 με. FE model assumes frictionless contact between the rollers & the test specimen.

7.3.1.2 As-Received Geometry

Figure 7.23 shows the maximum principal stress distribution on the tensile surface of a 130x20x12.7 mm as-received specimen loaded to a nominal longitudinal strain of 7360 με. The stress distribution is similar to the fully-machined model (Figure 7.20) in that surface stress reduces at the edges but concentrated at the inner loading roller positions. The magnitude of this stress concentration is 25 MPa (3% of the nominal loading stress).

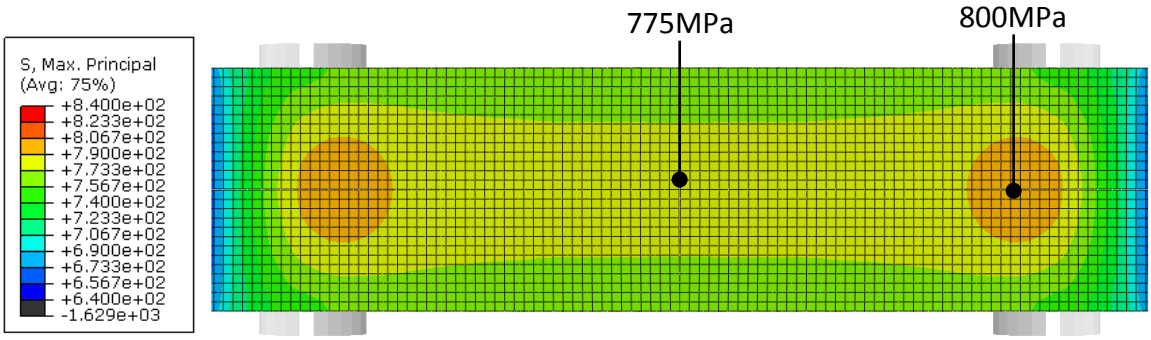

Figure 7.23 Maximum Principal Stress on the tensile surface of an 'as-received' four-point bend specimen loaded to 7360 με (assuming frictionless contact between the rollers & the test specimen). Stress is concentrated on the tensile test surface below the inner loading rollers.

Figures 7.24 and 7.25 show the corresponding longitudinal and transverse strain distributions. The concave shape of the tensile surface generates a longitudinal strain concentration of 7814 με along the edges. This effect was not apparent in the DIC measurements (Figure 7.24b), but could be due to the digital image resolution used. The DIC measurement shows a slight strain concentration on the tensile surface at one roller position which could have been caused by elevated contact friction (see Section 7.3.3) or some asymmetry in the loading arrangement. The transverse strain distribution is similar to the fully-machined geometry (see Figure 7.22). In both cases transverse strain concentrates along the edges of the specimen, but the concave surface geometry of the as-received specimen appears to exacerbate this strain concentration.

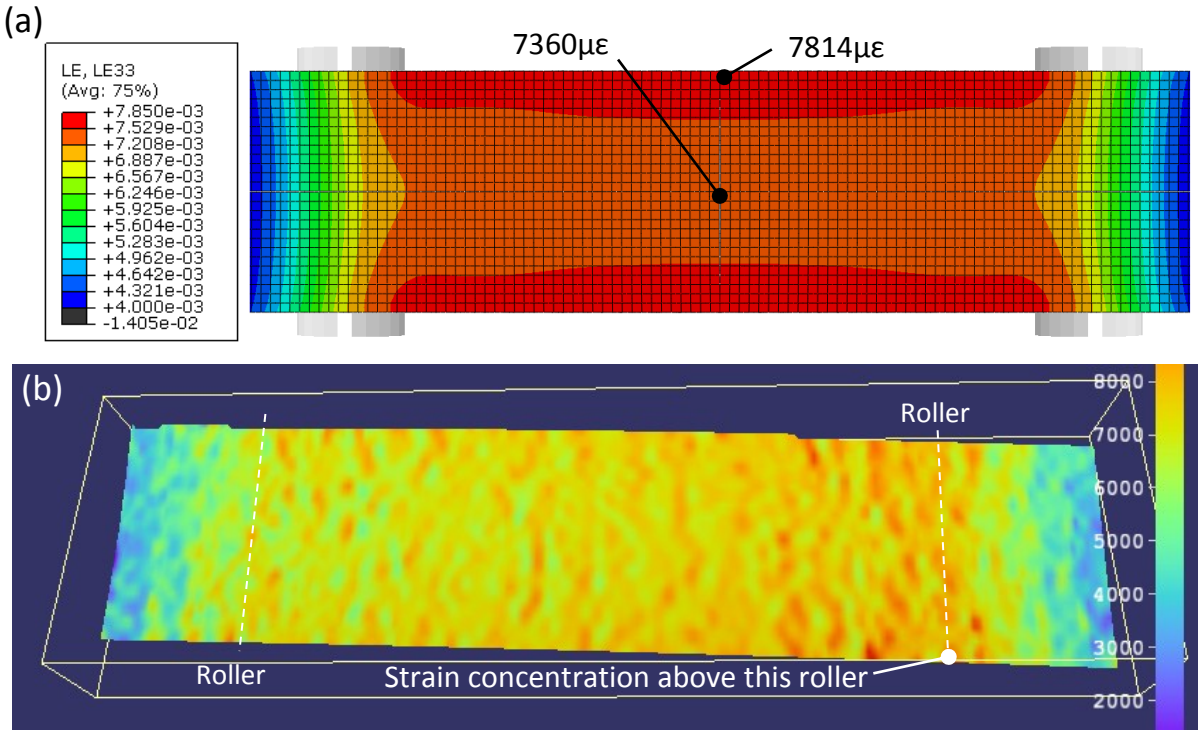

Figure 7.24 Finite element model (a) and DIC measurement (b) showing longitudinal strain on the tensile surface of an as-received four-point bend specimen loaded to 7360 με. FE model assumes frictionless contact between the rollers & the test specimen.

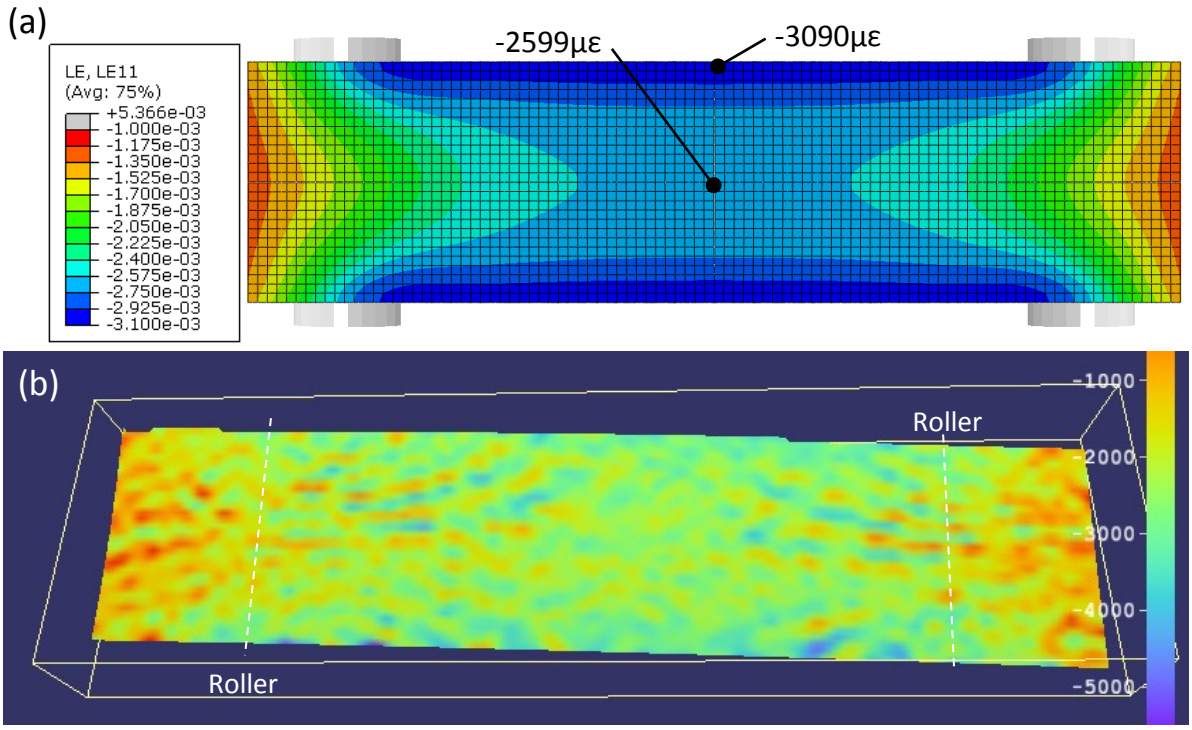

Figure 7.25 Finite element model (a) and DIC measurement (b) showing transverse strain on the tensile surface of a fully-machined four-point bend specimen loaded to 7360 με. FE model assumes frictionless contact between the rollers & the test specimen.

7.3.2 The Anticlastic Bending Effect

Section 7.3.1 showed that transverse strains on the tensile test surface were higher at the edges of the specimen for both the fully-machined and as-received geometries when loaded in four-point bending. This is because the edges of the specimen are unconstrained and therefore free to contract more than the material away from the edges. Furthermore, longitudinal tensile stresses produce lateral contraction and longitudinal compressive stresses produce lateral expansion throughout the beam. The net effect is that the cross-sectional shape of the beam distorts from a rectangular shape to a curved shape so the tensile surface becomes concave and the compressive surface becomes convex. This is called *anticlastic bending* [117] and can be seen by the z-axis displacement measurements for a 10 mm thick fully-machined specimen loaded to approximately 7300 με in Figures 7.26 and 7.27.

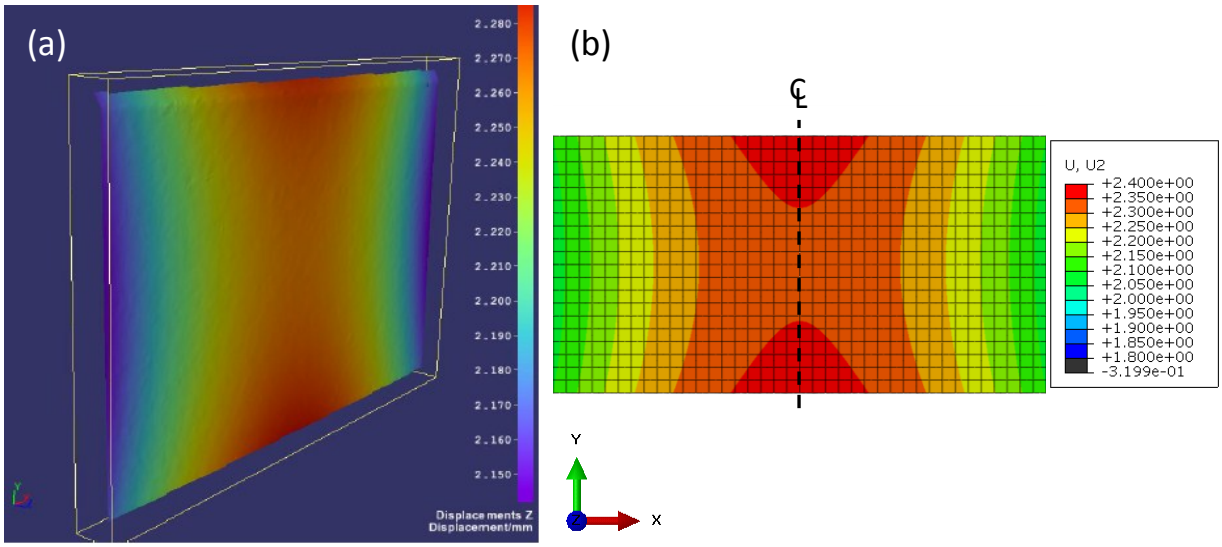

Figure 7.26 Anticlastic bending on the tensile test surface of a 10 mm thick fully-machined beam loaded to 7300 με. Full-field maps showing z-axis displacement across the width of the beams using (a) DIC & (b) FEA

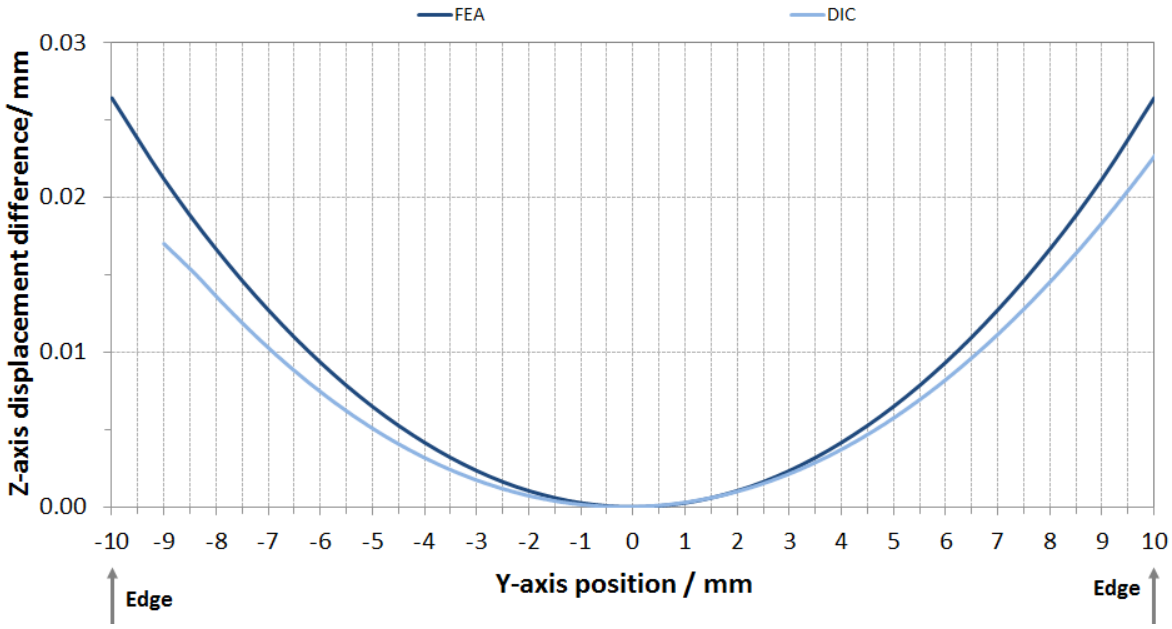

Figure 7.27 Line plots showing z-axis displacement on the tensile surface across the width of a 10 mm thick fully-machined beam loaded to 7300 με in four-point bending (a) DIC measurement & (b) FEA prediction. The finite element model predicts a steeper displacement gradient than measured by DIC. This difference is likely to be influenced by assumptions made in the model, such as Poisson's ratio, homogeneous material properties etc.

The use of thinner four-point bend specimens results in a more pronounced anticlastic bending effect which causes the longitudinal strain gradient to increase across the width of the tensile test surface. This can be observed in Figure 7.28 which compares the displacement and strain response on the tensile test surface for a standard 10 mm thick fully-machined specimen and a 2.5 mm thick fully-machined specimen. When a 2.5 mm thick specimen is loaded in four-point bending, the edge strains are approximately 600 με greater than the longitudinal strain measured at the edges of a 10 mm thick specimen.

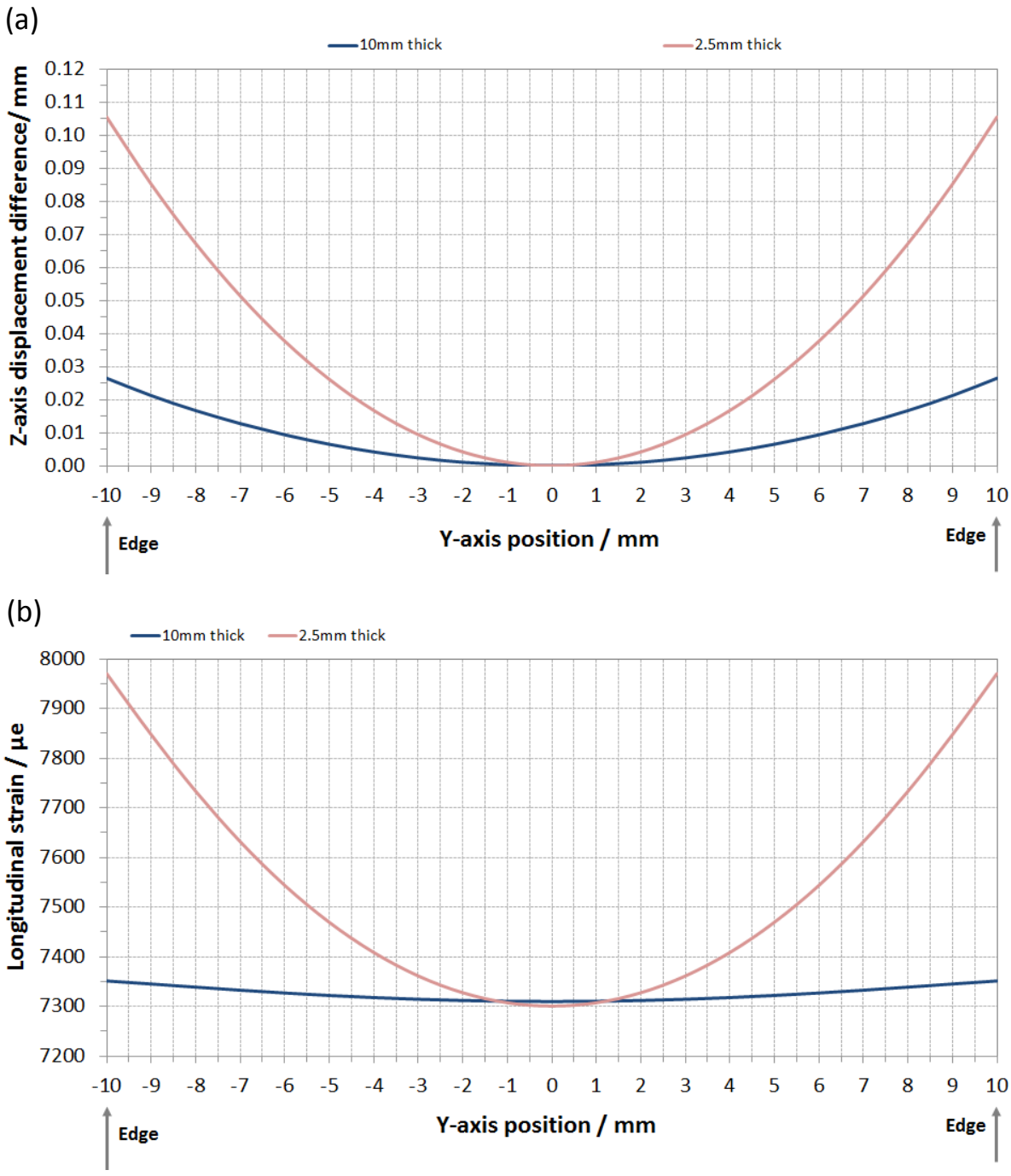

Figure 7.28 FEA of 10 mm & 2.5 mm thick beams: (a) z-axis displacement across the mid-width, (b) Longitudinal strain gradient across the mid-width. The anticlastic bending effect is more severe in the 2.5 mm thick specimens.

7.3.3 Friction at the Loading Rollers

The finite element analysis results in Figure 7.29 show that friction at the loading rollers does not influence the flexural response of the beam at the mid-point of the tensile surface where the loading strain gauge is attached. Friction coefficients 0, 0.5 and 0.7 were considered and compared with flexural bend test results for 10 mm thick fully-machined specimens.

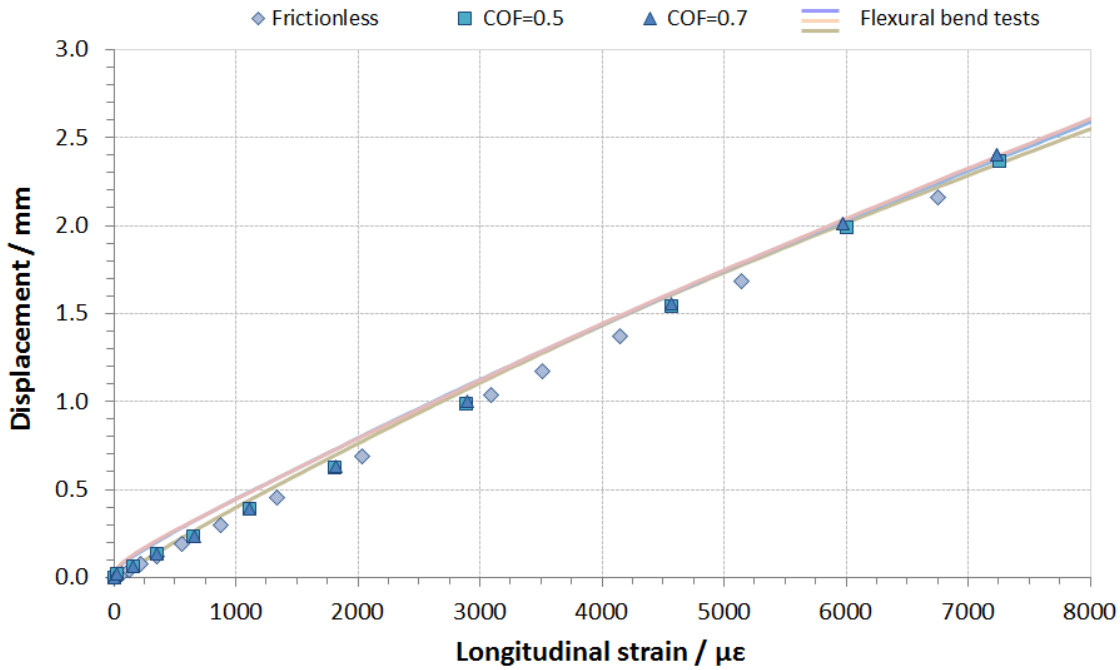

Figure 7.29 Influence of friction at the loading rollers on the flexural response of a 10 mm thick fully-machined beam loaded in four-point bending. FE model shows that increasing roller contact friction does not influence the displacement/strain response at mid-point of beam.

The magnitude of stress concentration generated at the inner roller positions on the tensile surface increases with friction (Figure 7.30). Furthermore, the position of maximum principle stress concentration shifts further away from the centre of the beam (0 mm position) as the coefficient of static friction increases.

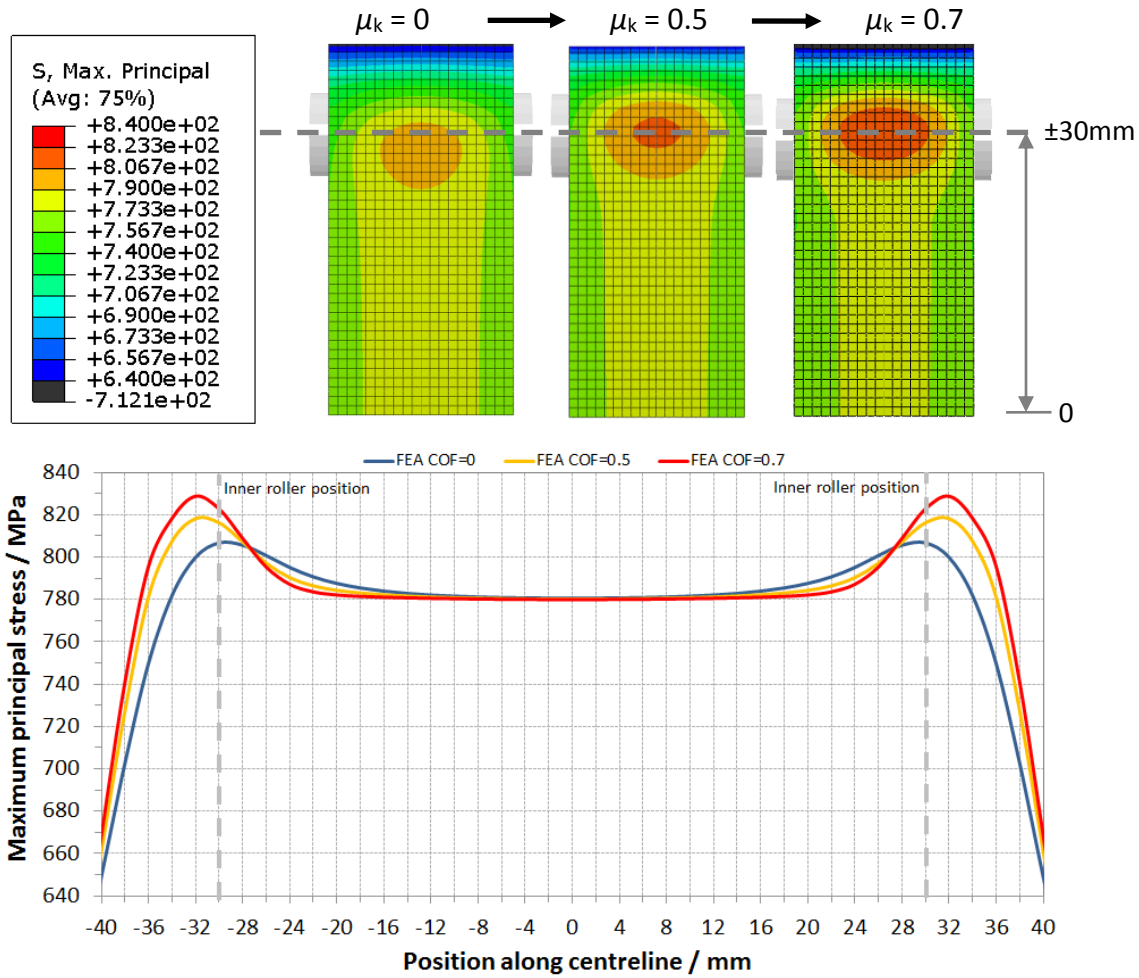

Figure 7.30 Influence of roller contact friction (μ_k) on surface stress concentration (10 mm thick fully-machined specimen). Line plot along centreline of beam shows that stress increases with friction.

When surface strain is considered, the introduction of contact friction creates a localised area of strain concentration at the inner roller positions. Longitudinal strain is concentrated across the width of the beam and transverse strain is concentrated at the edges of the beam (Figure 7.31). Both longitudinal and transverse strain concentrations tend to increase with friction. Strain gauge measurements along the centreline of the beam indicate that roller contact friction could be as high as 0.7 in real test samples.

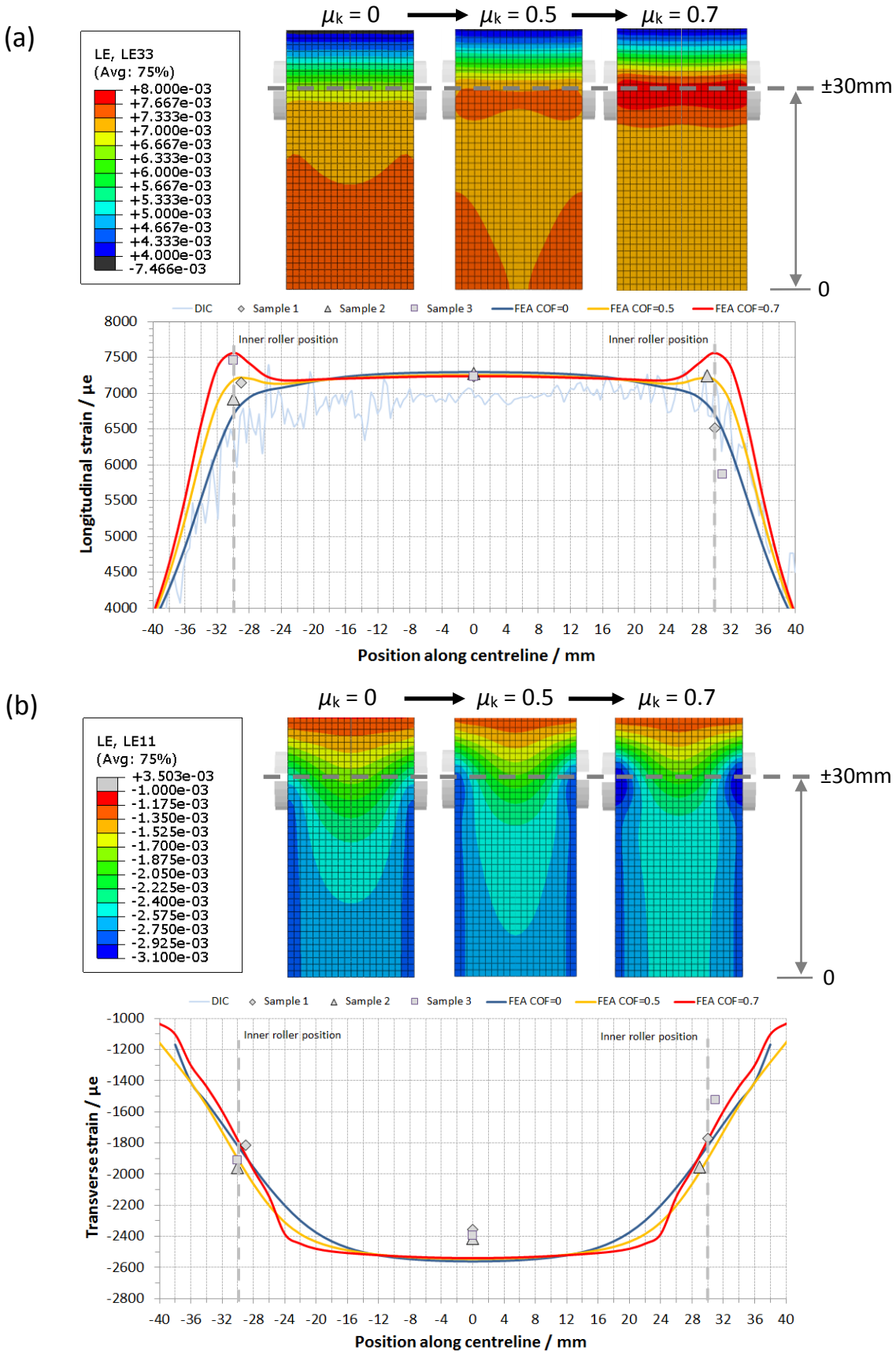

Figure 7.31 Influence of roller contact friction (μ_k) on surface strain concentration showing (a) longitudinal and (b) transverse strains for a 10 mm thick fully machined four-point bend specimen. Line plot along centreline of beam shows that strain concentration increases with friction.

7.3.4 Influence of Edges on the Fully-Machined Geometry

The line plot in Figure 7.32 is a finite element prediction of how chamfer angle influences stress at the edge of a 10 mm thick fully-machined beam loaded in four-point bending to 7300 με. Stress is lower at the edges than at the centre of the tensile surface regardless of edge preparation, but chamfering will further reduce the magnitude of stress.

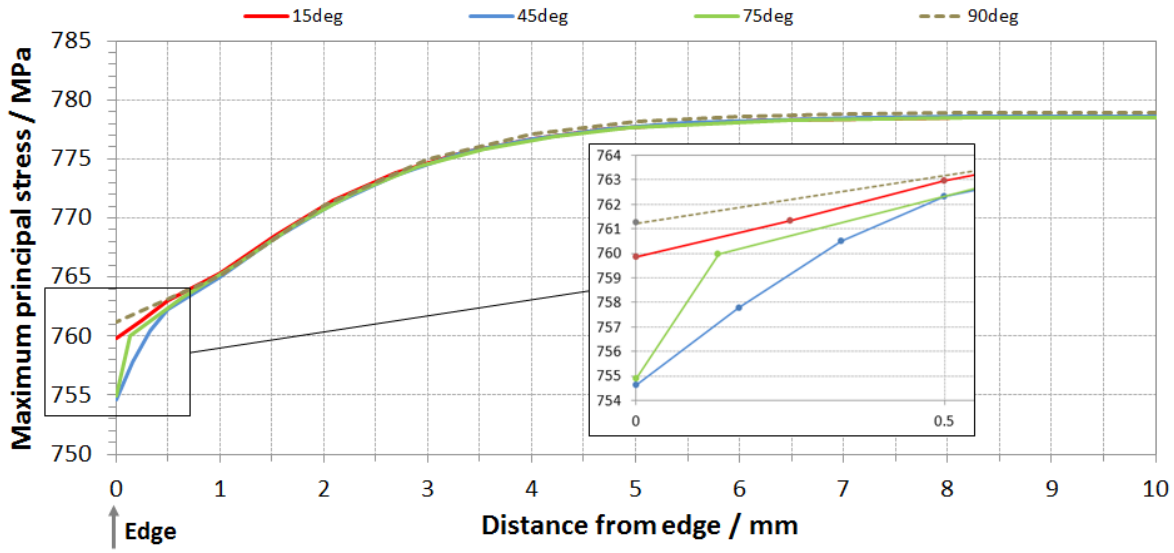

Figure 7.32 FEA prediction of how chamfer angle effects the maximum principal stress at the edges of a beam loaded in four-point bending. The 10 mm thick model simulated loading to 7300 με on the tensile test surface with 15°, 45°, 75° and 90° (as-machined) edge angles.

Unlike stress, strain tends to increase at the edges of the specimen due to the anticlastic bending effect. Figure 7.33 shows the full-field DIC measurements for two fully-machined specimens with chamfered edges. Although strain appears to be reduced at the 15° and 45° edges, it is unclear if chamfer angle really influences the results. This is because the DIC analysis area did not fully reach the 75° and 90° edges. Furthermore, the strain difference could be due to asymmetric loading of the samples – note in the figure how the highest strain is always on the bottom edge and the lowest strain is always on the upper edge.

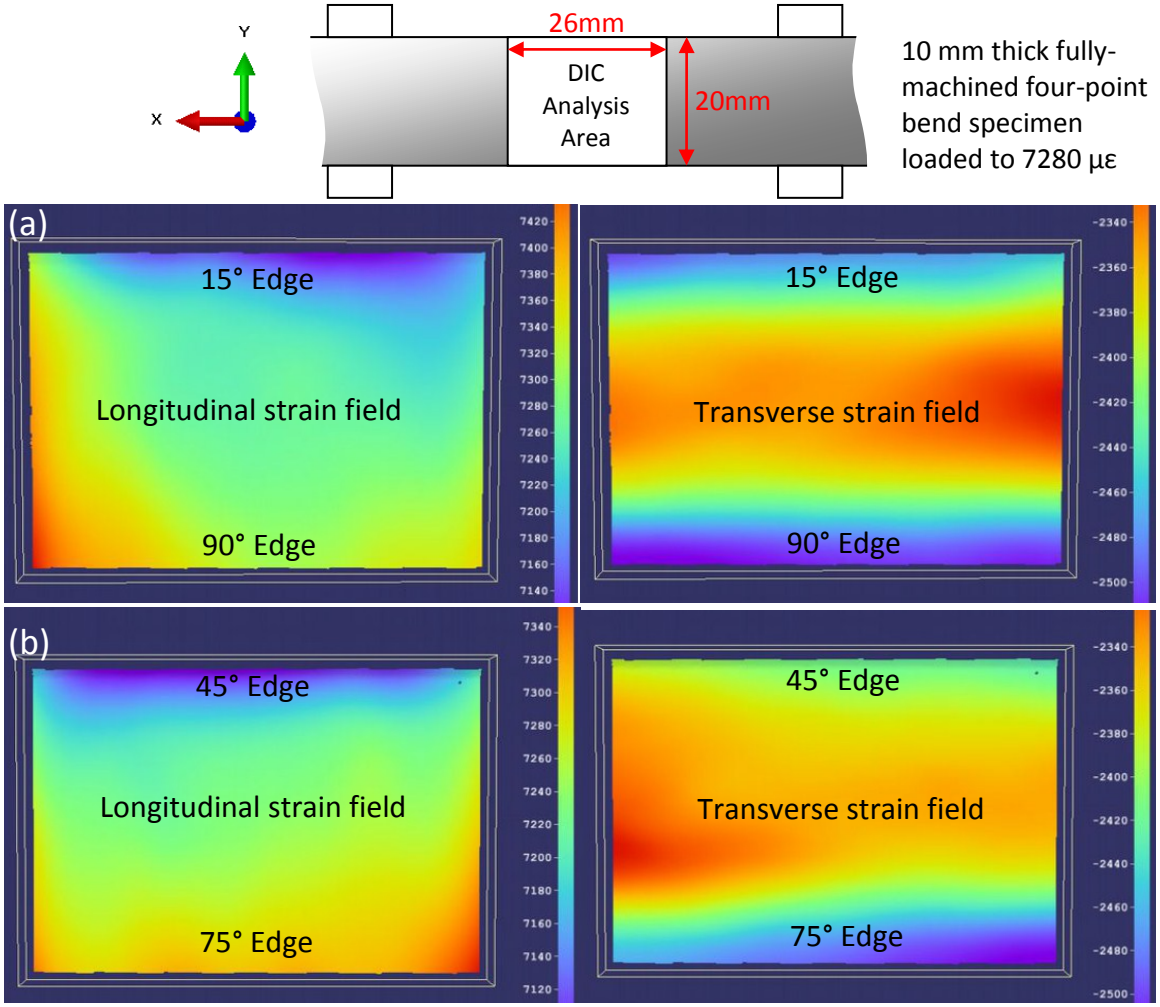

Figure 7.33 Full-field longitudinal and transverse strains on the tensile surface with different edge chamfers: (a) with 15° and 90° edges and (b) with 45° and 75° edges.

The finite element predictions in Figure 7.34 suggest that both longitudinal and transverse strains will be reduced at the edges when edge chamfers are applied. It could be argued that a 75° chamfer is most effective as this reduces longitudinal strain more than the other chamfer angles. If this is the case, it supports the conclusion that loading asymmetry is skewing the strain field seen in the DIC measurements above.

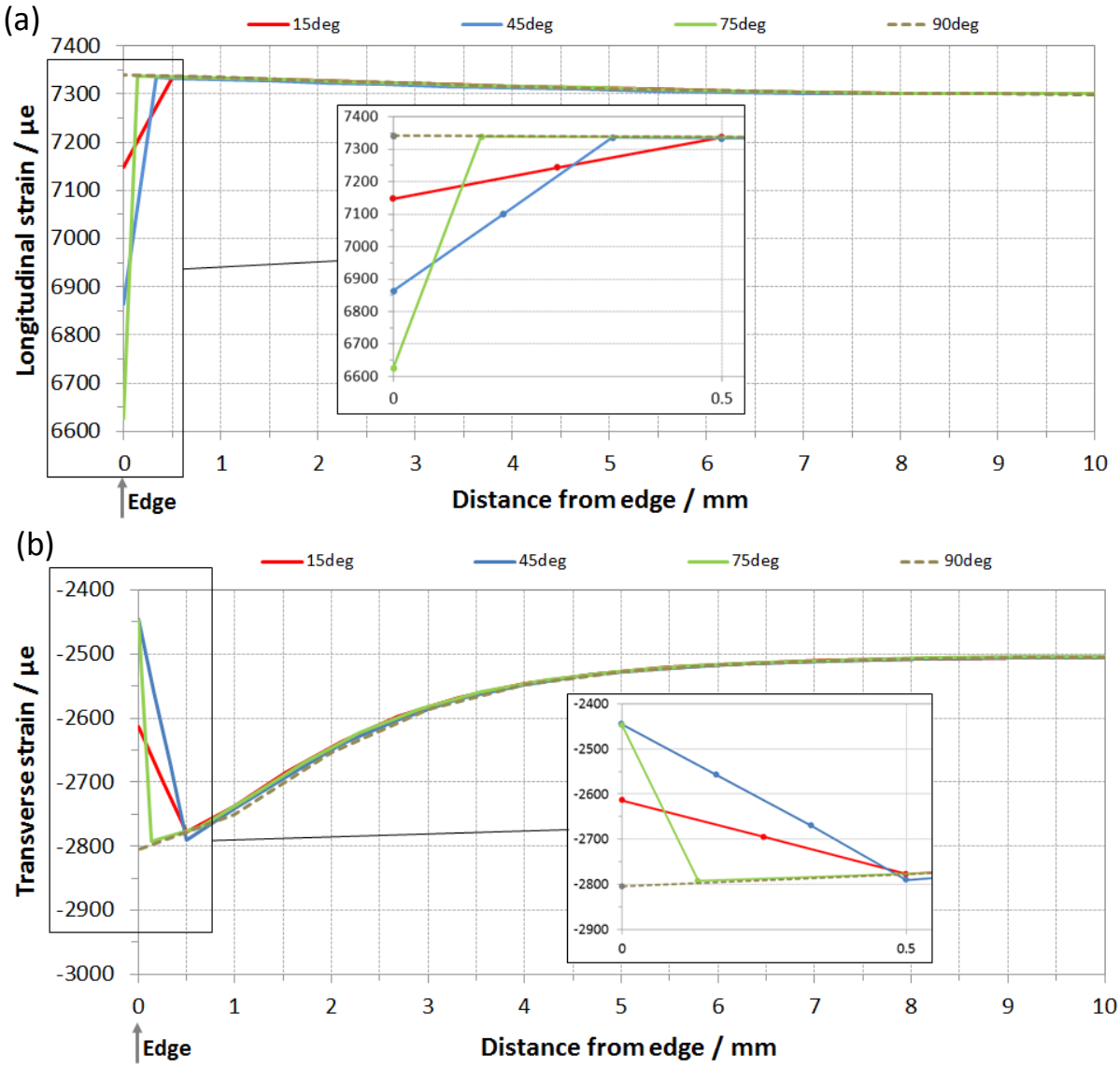

Figure 7.34 FEA showing the effect of edge chamfer angle on (a) longitudinal strain and (b) transverse strain at the edges of the tensile test surface for a 10 mm thick fully-machined specimen loaded to 7300 με in four-point bending.

The finite element results in Figure 7.35 show that an edge fillet becomes more effective as its size increases for both stress and strain. A fillet radius of 0.5 mm gives the same edge stress as a 45° chamfer (approximately 755 MPa) but a 2 mm radius reduces the edge stress to 705 MPa. Similarly, the longitudinal and transverse strain reduction generated by a 0.5 mm fillet is comparable to a 45° chamfer. For a 2 mm fillet, longitudinal strain is reduced from 7300 με to 4500 με.

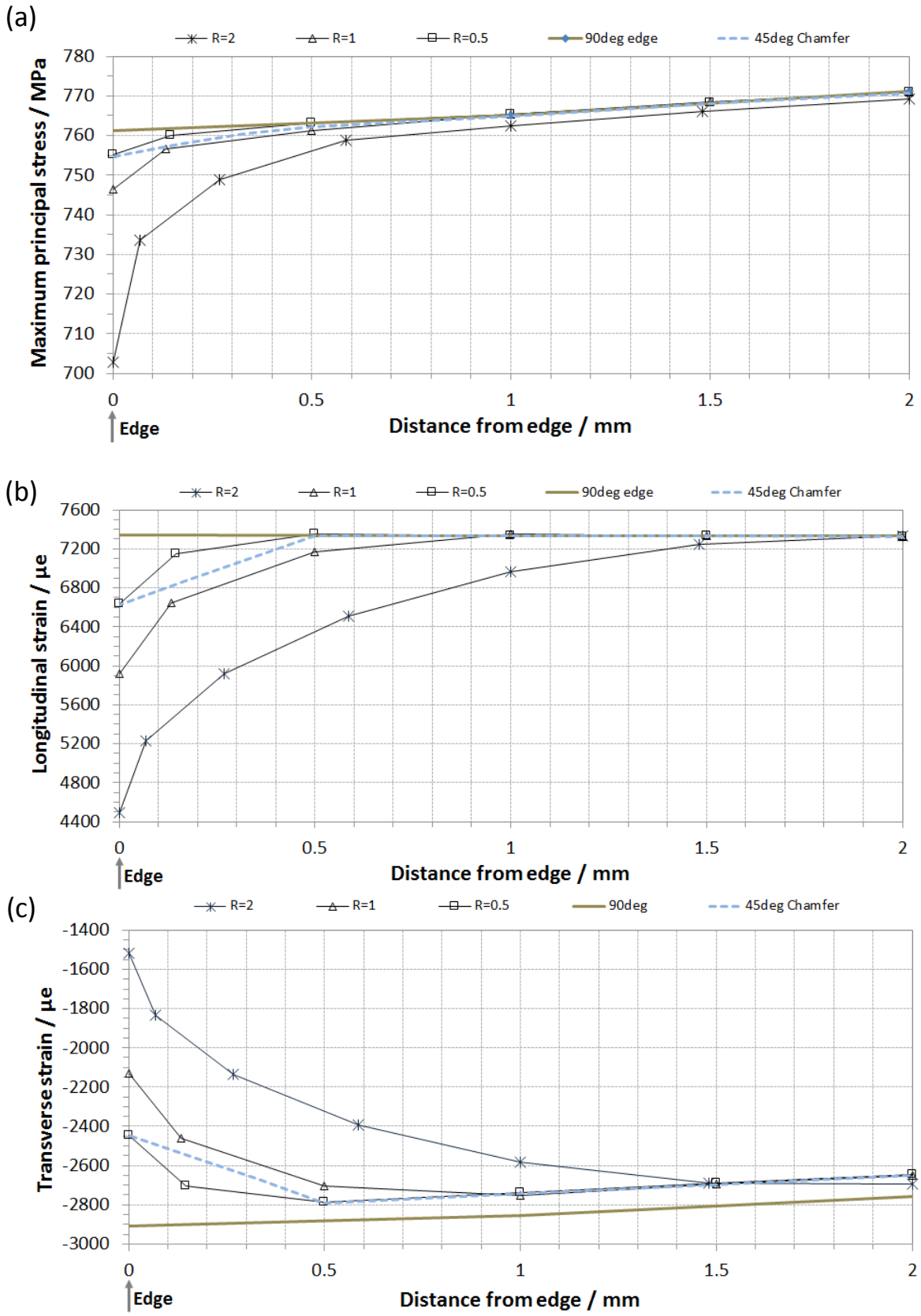

Figure 7.35 FEA showing the effect of fillet radii size on (a) maximum principal stress, (b) longitudinal strain and (c) transverse strain. Radii applied to the long edge of the tensile test surface using a 10 mm thick fully-machined beam loaded to 7300 με in four-point bending.

7.3.5 Influence of Edges on the As-Received Geometry

When chamfers or fillets are applied to the edges of curved as-received specimens, a similar reduction in stress and strain can be observed. Figure 7.36 compares a 45° edge chamfer with a 0.5 mm fillet in terms of longitudinal and transverse strain reduction. Note that cracks were observed in the SSC tests on the chamfered edges which corresponds to the location of peak strain (chamfering simply moves this peak strain away from the edge with a reducing in strain that follows the dashed line in Figure 7.36.

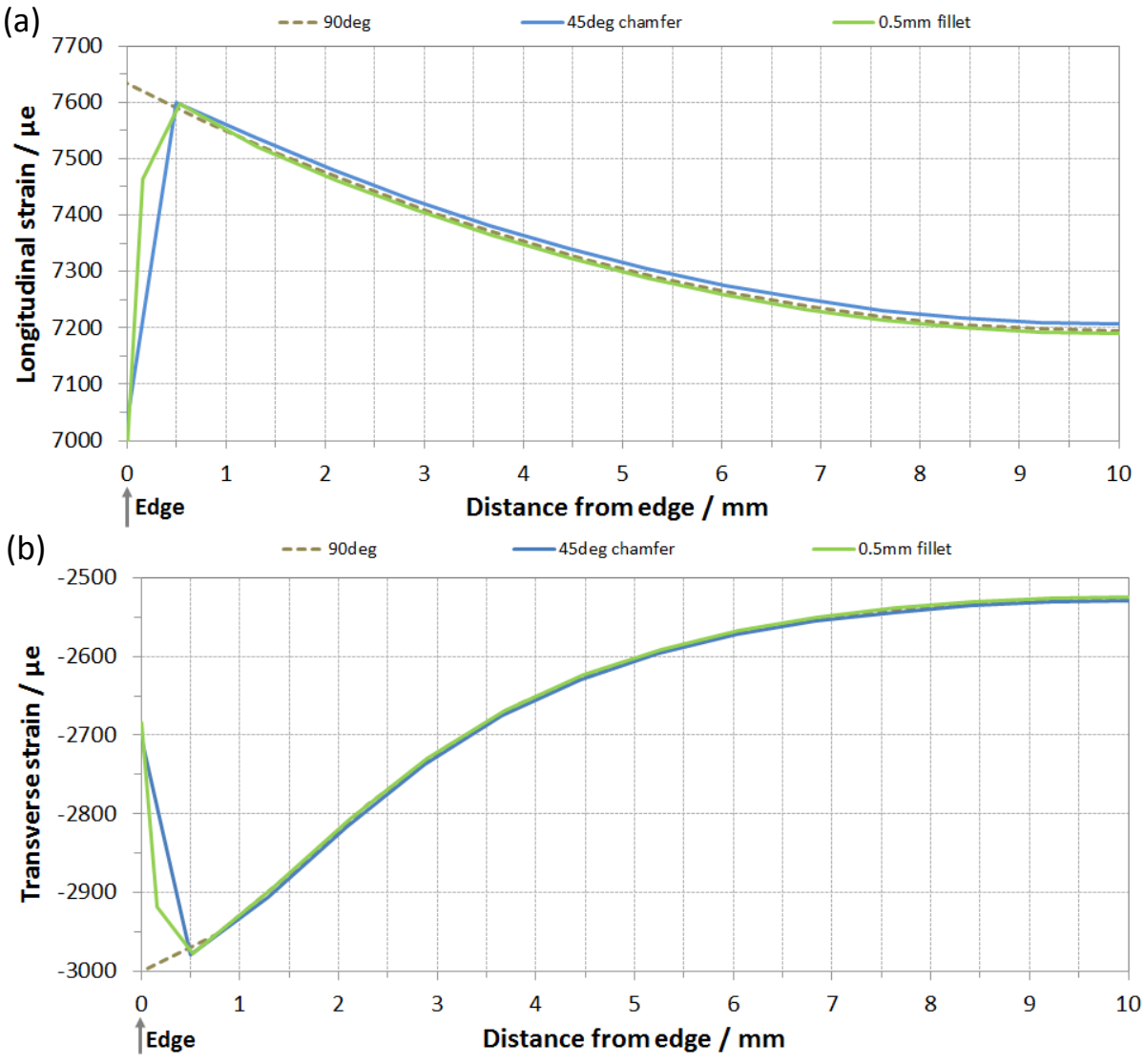

Figure 7.36 FEA showing the effect of 45° edge chamfer and 0.5 mm fillet on (a) longitudinal strain and (b) transverse strain at the edge of the tensile test surface. Curved as-received specimen loaded to 7300 με in four-point bending.

7.3.6 Anomalous Case of Cracking in the Condensed Water SSC Test

A finite element model was made to represent as-received specimen C1 from the 69 mbar H_2S condensed water SSC tests in Chapter 6. This particular specimen cracked along one edge which was 0.2 mm thicker than the edge that did not crack. The model was loaded to approximately 7300 με at the mid-length, mid-width position with the assumption that the cross-sectional area remained constant along the length of the beam and frictionless contact at the loading rollers. The finite element analysis predicted strains up to 7781 με at the thickest edge where cracking occurred and strains up to 7591 με on the opposing edge where no cracking occurred (Figure 7.37). Stress was not concentrated on either edge.

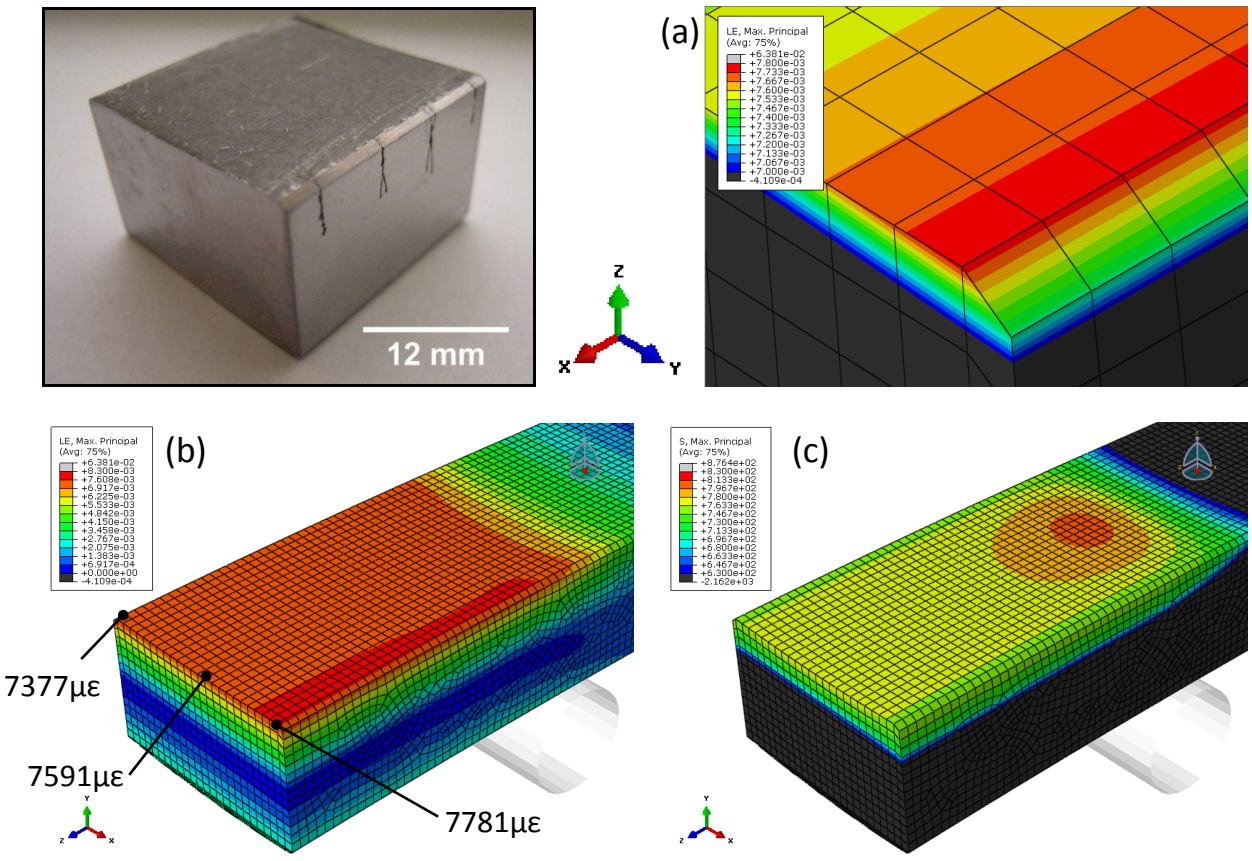

Figure 7.37 Finite element model of specimen C1 showing (a) & (b) strain concentration along cracked edge, (c) stress is not concentrated at the edges of the specimen.

7.3.7 Summary of the Full-Field Stress & Strain Analysis

The full-field stress and strain analysis highlighted several limitations of the four-point bend test. Some of these are unavoidable with the current set up (such as fiction at the loading rollers) while others can be mitigated to a certain extend (chamfering and radii to reduce edge strain). Crucially, thin specimens exacerbate the anticlastic bending effect so full thickness specimens should always be used in preference to reduced thickness specimens. When curved specimens are used, they must be machined to ensure a symmetrical cross-section to avoid thickness differences in the beam which can lead to preferential cracking on the more highly strained thicker edge. Ideally the loading jig should be designed to prevent asymmetrical loading and allow the rollers to rotate, reducing fiction with the test specimen. However, the need for galvanic isolation between the specimen and loading jig makes the latter requirement technically challenging. The following list summarises some other key points from the full field stress and strain investigation:

1. For both the fully-machined and as-received specimen geometries, finite element analysis showed that maximum principal stress is greatest near the inner loading rollers on the tensile test surface. The magnitude of this stress concentration is 26 MPa and 33 MPa for the respective geometries. In contrast, stress is lower along the longitudinal edges compared to the mid-point of the test surface.

2. For both the fully-machined and as-received specimen geometries, contact friction between the rollers and the test specimen causes strain to concentrate on the tensile surface near the inner loading rollers. The magnitude of this strain concentration increases with increasing coefficient of kinetic friction.

3. FEA indicates that longitudinal strain is relatively uniform between the inner loading rollers on the tensile test surface of a fully-machined test specimen. However, the DIC measurements highlighted that some non-linearity can exist in real test specimens, possibly due to elevated friction at the rollers or some asymmetry in the loading arrangement.

4. The highest transverse strains were generated along the edges of the tensile test surface. This applies to both fully-machined as as-received geometries. When contact friction is introduced at the rollers, the magnitude of transverse strain increases, particularly at the edges near the inner loading rollers on the tensile surface.

5. For the as-received specimen geometry, longitudinal strain is approximately 445 με higher at the edges of the tensile test surface when compared to the mid-point of the test surface.

6. Stress and strain is reduced at the longitudinal edges by chamfering and the use of fillet radii. FEA shows that extent of strain reduction is influenced by chamfer angle and fillet radius size.

7. The FE model of specimen C1 from the Condensed Water SSC tests indicates that the cracked edge was more highly strained than the edge without cracks. The model predicted strains up to 7781 με along this edge, which is approximately 7% higher than the nominal loading strain.

7.4 Discussion

7.4.1 Flexural Properties at 24 °C, 130 °C & 5 °C

The flexural bend test results showed that the 0.2% offset strain as determined from the load-strain curve was relatively consistent across the three test temperatures, averaging 7297 με at 24 °C, 7327 με at 130 °C and 7318 με at 5 °C. For the 10 mm thick specimens, the elastic bending modulus averaged 200 GPa at 24 °C and reduced to 193 GPa at 130 °C. Poisson's ratio was not influenced by the change in test temperature. These results are consistent with expected physical properties and in good agreement with published data for similar grades of stainless steel [157]. Microstructural changes were not expected at the elevated test temperature or from the 175 °C heat treatment used to cure the high temperature strain gauges because this is well below the A1 temperature for this material (approximately 600 °C). Furthermore, martensite tempering to precipitate carbides typically occurs at 200 °C but the low carbon content and additions of molybdenum will increase the temperature where softening will occur [54].

The deflection required to strain a four-point bend specimen to the 0.2% offset strain increases with temperature. This becomes significant when four-point bend stress corrosion test specimens are loaded at room temperature then heated to an elevated test temperature. Since the displacement is fixed at room temperature, load will relax as temperature is increased and the specimen will be overstrained. However, this decrease is most marked for duplex stainless steels compared to 13%Cr supermartensitic stainless steels [178]. Furthermore, Turnbull *et al*. [116] showed that load and strain relaxation was less than 3% in a four-point bend supermartensitic stainless steel specimen with super-duplex

stainless steel weld filler, when tested at 130 °C and maintained at that temperature for 30 days (i.e. the duration of a typical SSC test).

It is common to load four-point bend SSC/SCC test specimens to the 0.2% offset strain determined from flexural bend tests using the principal strain (ε_p) determined from longitudinal (ε_1) and transverse strain (ε_2) measurements, taking Poisson's ratio (v) from reference data [178]:

$$\varepsilon_p = \frac{\varepsilon_1 + v\varepsilon_2}{1 - v^2} \tag{7.1}$$

Since Poisson's ratio is a measure of transverse to longitudinal strain ($v = \varepsilon_2/\varepsilon_1$), substituting $v = \varepsilon_2/\varepsilon_1$ into equation 7.1 simplifies the equation to:

$$\varepsilon_p = \varepsilon_1 \tag{7.2}$$

Therefore, fully-machined four-point bend SSC/SCC test specimens can be loaded accurately from the longitudinal strain measurement alone, removing the need for biaxial strain gauges and therefore simplifying the test method.

It was reported in the literature that the effective Poisson's ratio for a supermartensitic stainless steel remains relatively constant when loaded in four-point bending to 10000 με [115]. In uniaxial tension, the Poisson's ratio of steel is known to increase during plastic deformation [117]. This was the observation made from the Poisson's ratio measurements in Section 7.1.1.2. There was a small but distinct increase in Poisson's ratio when the beam was plastically deformed as shown in Figure 7.38. Furthermore, the 10 mm thick specimens appear to provide a more stable Poisson's ratio measurement

compared to the 2.5 mm thick specimens. It is believed that this is due to the anticlastic bending effect [117] and the observation that the strain gradient generated across the width of the beam increased as thickness was reduced.

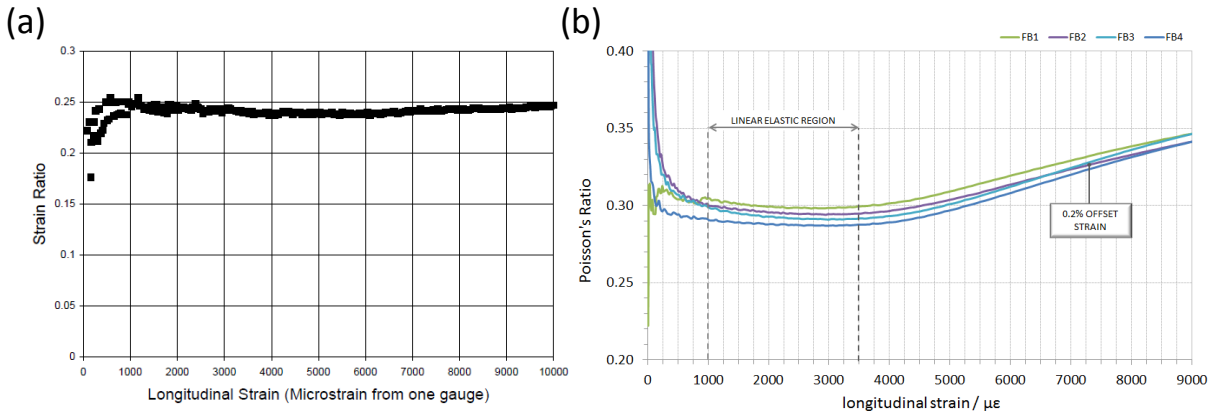

Figure 7.38 (a) Literature data showing the effective Poisson's ratio for a supermartensitic stainless steel loaded in four-point bending [115], compared to (b) Poisson's ratio measured in room temperature flexural bend tests

7.4.2 Errors Associated with the Flexural Bend Test

The errors associated with flexure tests have been analysed by Baratta *et al*. [179]. Their work identified that the major source of error arises from external influences such as load bearing friction; eccentric loading; beam twisting; contact-point tangency shift; wedging stresses and neglecting corner chamfers. The work in Section 7.1.4 identified two major sources of error caused by eccentric loading and friction at the loading rollers. Both of these can be reduced to some extent by proper design of the loading fixtures. Please note that the influence of friction at the contact points will be discussed subsequently in this chapter.

In Section 7.1.4.2 and Section 7.1.4.3, the errors associated with strain gauge misalignment were shown to be negligible, and only become significant at angles around 45° to the principal axis [125,126]. For a gauge misalignment of 1°, the associated error on the

measured 0.2% offset strain was only 3 με (0.04%). The main source of error comes from the gradient of the linear region of the load-strain curve, generating errors in the order of ±1.0%.

The DIC measurements in Section 7.3.1 highlighted that the surface strain distribution can be non-linear in real test specimens. This was highlighted in Figure 7.24b which shows that longitudinal strain is slightly concentrated on the test surface near one of the loading rollers, possibly due to eccentric loading or elevated friction at the roller. This is likely to be the main source of error resulting from specimen loading.

7.4.3 Loading Specimens from Flexural Bend or Tensile Test Data

Tensile material properties (determined from uniaxial tensile tests) are often used to predict the behaviour of a material under forms of loading other than uniaxial tension. For example, NACE MR0175 / ISO 15156-3 [4] specifies the use of tensile stress-strain data to determine the strain at 100% Actual Yield Strength (AYS) for loading SSC/SCC test specimens in four-point bending. Although the validity of this approach has been questioned and actively discouraged in the literature [115], recent work has mitigated the concerns that the tensile method underestimates the total strain needed to achieve 0.2% plastic strain [180].

The flexural bend and tensile test method comparison in Section 7.2.2 confirmed that the 0.2% offset strain measured from a uniaxial tensile test is lower than the 0.2% offset strain measured from a flexural bend test. The difference between the two methods is approximately 18% which corresponds to other published work [116]. This is topic has been discussed by NACE Task Group TG494 (Four-Point Bend Test Procedure) and there is mixed

opinion as to which method is more appropriate for setting the loading strain in a four-point bend SSC/SCC specimen. Although it would seem intuitive to use flexural bend data to determine the loading strain for a specimen loaded in four-point bending, it has been argued that the load-strain curve generated during a flexural bend test cannot be used in the same way as a stress-strain curve is used from a uniaxial tensile test to determine the level of strain at a nominal 0.2% offset yield strength [181].

The FEA results in Section 7.2.3 identified that the difference in 0.2% offset strain is linked to the use of 'load' as a reference variable in the flexural-bend test. Figure 7.16 showed the relationship between load and stress for both the tensile and flexural-bend test methods when loaded to a nominal strain of 1.0%. In pure tension, load increases linearly with stress during elastic and plastic deformation so load can be directly related to stress. This is the basis of generating a stress-strain curve from a tensile test. Tensile force is recorded as a function of the increase in gauge length and force-elongation data is normalised with respect to specimen dimension, to create a stress-strain curve that is identical in shape to the force-elongation curve [182].

In four-point bending, the load-stress relationship becomes non-linear with the onset of plastic deformation (at approximately 500 MPa), hence load cannot be directly related to stress in this regime. This non-linearity is a consequence of work hardening in the plastic zones near the surface which resists the applied load. Consequently, the 0.2% offset strain measured from the load-strain curve in a flexural bend test does not correspond to 0.2% plastic strain on the test face. The finite element models show that the surface plastic strain

is closer to 0.3% as shown in Figure 7.17. This work has since been verified by an independent study performed at NPL [180]. The magnitude of stress and strain will be a function of the work hardening characteristics of the material. For the supermartensitic stainless steel modelled in this thesis, loading the four-point bend specimen to the 0.2% offset strain determined from a flexural bend test (7300 με) results in a surface stress only 11 MPa greater than loading the same specimen to the 0.2% offset strain determined from a uniaxial tensile test (6000 με).

7.4.4 Surface Stress & Strain Distribution in Four-Point Bending

7.4.4.1 General Stress & Strain Distribution

The FE models in Section 7.3.1 predicted that the full-field stress and strain distribution on the tensile test surface was remarkably similar for both the fully-machined and as-received geometries loaded in four-point bending (see Figure 4.4 for the different cross-sectional geometries). The key observation is that stress concentrates near the inner loading rollers on the tensile surface but is lower at the edges, for both specimen geometries, compared to the centre of the tensile surface. The reduction in stress at the edges of the specimen supports the finite element analysis made by Huurman and Pronk [142] and can be attributed to the anticlastic bending effect [117]. Longitudinal strain is relatively uniform on the tensile surface but increases at the edges, more significantly in the as-received specimen with the concave surface geometry. Transverse strain is greatest along the longitudinal edges of the tensile surface, again more pronounced in the as-received geometry. These models assumed frictionless contact at the rollers where in fact there will inevitably be frictional forces generated at these contact points. The presence of friction in a

flexure test with fixed load and support points gives rise to couples at these locations as well as axial forces in the neutral axis [179].

7.4.4.2 The Anticlastic Bending effect

The high transverse strains at the edges of the specimens predicted by the FE models (see Figures 7.22a and 7.25a) are due to anticlastic bending. This is where the longitudinal tensile stresses produce lateral contraction and the longitudinal compressive stresses produce lateral expansion, resulting in the tensile surface distorting to a concave shape [117]. This was demonstrated by Huurman and Pronk [142] by a 3D FE model of a rectangular-section beam in four-point bending (Figure 7.39). Stress is lower at the edges of the inner loading point which agrees with FEA results presented in Section 7.3.1.

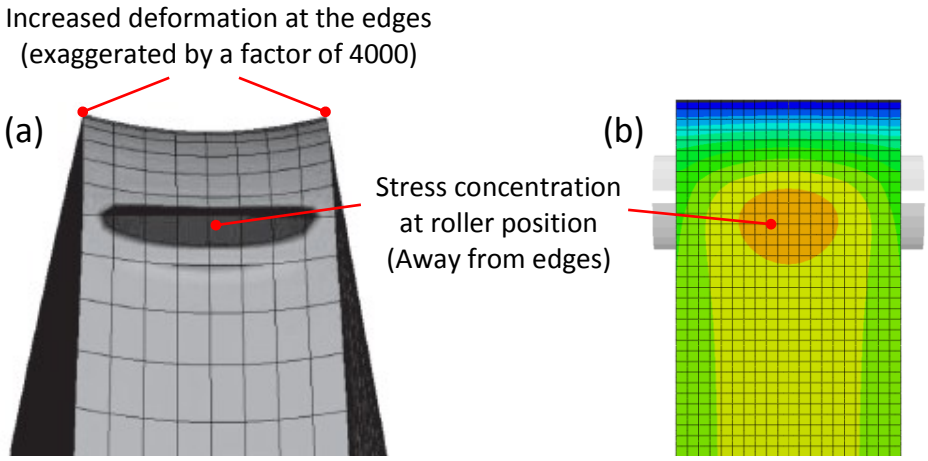

Figure 7.39 (a) FE model from literature showing anticlastic bending and reduced stress at the edges of the beam [142] & (b) FE model of a fully-machined specimen also showing reduced stress at the edges. Both examples show the tensile surface at the inner loading point

The FEA in Section 7.3.2 showed that the anticlastic bending effect is exacerbated when as specimen thickness is reduced. A possible explanation for this is that thinner specimens have less constraining material through the thickness to resist deflection, thereby resulting in a more severe anticlastic bending effect. This has implications for small-scale testing. Miniature test specimens are used when characterising expensive alloys that are

typically only available in small quantities [128]. Other examples include testing electro-ceramic components which are too small for commonly used flexure specimens to be cut from them (1.5 mm thick specimens considered) [144], testing thin specimens for spring applications (0.25 to 1.3 mm thick) [183], small specimen testing for the nuclear industry [184] or fatigue testing with compact test specimens (2 mm thick specimens considered) [143]. None of these references addressed the issue of stress and strain distribution across the width of the test face. In the context of four-point bend SSC testing, it would be prudent to use 10 mm thick specimens where possible to minimise the anticlastic bending effect. However, there is a balance between maximising specimen size and accommodating the loading jig in the test vessel or autoclave.

7.4.4.3 Effect of Friction at the Rollers

Localised contact at the loading rollers can generate 'wedging stresses' that produce a tensile stress concentration at the roller position on the tensile surface of the beam [144,179]. NPL showed that the assumption of negligible friction at the rollers in a four-point bend test may not be reliable; meaning a higher load is required to achieve the target loading strain [180]. The work presented in this thesis focused on how friction influences the stress and strain concentration generated near the rollers on the tensile test surface. When friction was introduced to the finite element models, the results showed that contact friction between the rollers and the test specimen increases the magnitude of stress and strain concentration generated on the tensile surface. In practice, this would go unnoticed during normal loading operations where a single strain gauge is located at the mid-point of the beam. At the roller positions, the maximum principle stress and longitudinal strain concentration shifts further away from the centre of the beam as the friction coefficient

increases. This effect is a reflection of *contact point tangency shift* which is a function of contact radii, specimen thickness and the ratio of the modulus of elasticity to the bend strength [179]. Figure 7.40 shows how contact point tangency shift can result in a span length change in four-point bending.

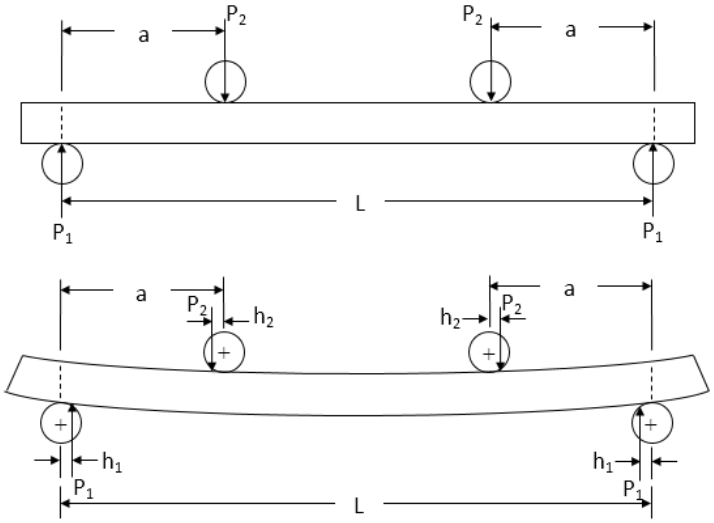

Figure 7.40 Contact point tangency shift in four-point bending [179], resulting in span lengthening between the upper loading points as shown by h_2.

If the rollers in the loading fixture were free to rotate, then a *coefficient of rolling friction* (μ_r) would apply which is typically 0.03 for steel-ceramic pairings [144]. However, the rollers are constrained in the fixture such that the specimen slides over fixed contact points during deformation. In this case, a *coefficient of kinetic friction* (μ_k) applies and has a typical value of 0.5 for steel-ceramic pairings [158]. Strain gauge measurements from flexural bend tests were consistent with finite element models based on frictionless contact, μ_k=0.5 and μ_k=0.7, highlighting the variation that exists in real loading conditions. Zhai *et al.* [143] investigated the relationship between inner-roller spacing (t) and specimen thickness (h) on the surface stress distribution in four-point loading. A t/h ratio between 1.2 and 1.5 provides a region of uniform stress between the inner rollers with small peak stresses at the roller positions. The t/h ratio for the SSC specimens modelled in this chapter is 6 (t=60, h=10).

With reference to Figure 2.54, the surface stress profile for a t/h ratio of 3 is similar to the surface stress profile measured in the finite element models (Figure 7.30). To achieve a t/h ratio of 1.2 to 1.5 and hence reduce the peak stresses generated at the roller positions would require 40-50 mm thick specimens if the 60 mm inner roller span were retained. This is unfeasible since specimen thickness is limited to the thickness of the pipe (12.7 mm). Based on a 10 mm thick specimen, the loading jig would require a 12-15 mm long inner roller span. The reduced test area may be adequate for testing parent material but could be unsuitable for testing root-intact welded specimens as loading requires strain gauges to be placed either side of the weld. If the strain gauges fall outside the area of uniform stress (between the rollers) then achieving the correct loading strain would become problematic.

7.4.4.4 Influence of Edge Preparation on Stress & Strain Concentration

The FE models showed that stress decreases at the edges whereas strain increases at the edges of the test surface. The magnitude of strain concentration is greater for the curved as-received specimen compared to the flat fully-machined surface. Both chamfering and radii are effective at reducing stress. The FE models predict that chamfer angle may influence the extent of strain reduction, but it is unlikely that edge chamfers will be accurately applied to SSC test specimens during sample preparation. Therefore the application of any chamfer, regardless of angle, is beneficial for reducing both stress and strain at the edges. Fillets become more effective as radius increases (see Figure 7.35). Baratta *et al*. [179] identified that rounding the edges of brittle ceramic materials reduced premature failure when loaded in four-point bending. Chamfering on the other hand did not because it adds additional ground edges to the specimen, increasing the number of flaws

generated from the grinding operation from which cracks can initiate. It has already been discussed in Chapter 6 how grinding processes can introduce physical defects into stainless steels generating sites for preferential pitting corrosion [168,**Error! Bookmark not defined.**]. Therefore the practice of grinding chamfers onto the edges of four-point bend stress-corrosion test specimens may not be appropriate. The general consensus amongst the NACE four-point bend task group TG494 is that the edges should be prepared with a small fillet by lightly abrading with a fine grit paper to remove sharp edges [181]. Any cracks at the edges are therefore considered to be an artefact of the test method and discounted.

7.4.4.5 Anomalous case of Cracking in the Condensed Water SSC Test

The FE model of the Condensed Water SSC test specimen highlighted how an asymmetric cross-section could influence strain distribution on the tensile test surface. FEA predicted strain concentrations in excess of 400 με above the nominal loading strain along the thick edge and reduced strain along the thinner edge (approximately 214 με above the nominal loading strain). Since cracking occurred along the thicker edge in the SSC tests, it is feasible that the specimen could have been overloaded by a strain concentration along the thick edge as shown in Figure 7.37. The finite element model provides supporting evidence that the cracks generated in specimen C1 in the Condensed Water SSC tests was an artefact of the four-point bend test and not indicative of SSC resistance in the given test environment.

CHAPTER 8: OVERALL DISCUSSION

8.1 Investigation of Seabed Temperature SSC Resistance

8.1.1 Factors Influencing Crack Initiation

SSC susceptibility is highly dependent on passive film stability since a stable passive film acts as a barrier to general corrosion and hydrogen uptake. It has been reported that conventional 13%Cr stainless steels display general corrosion at pH 3.5 in Condensed Water test environments [83], indicating active dissolution of the oxide film. The supermartensitic stainless steel investigated in this thesis did not show any signs of general corrosion in either the Produced Water (pH 4.5) or Condensed Water (pH 3.5) tests which indicates that the oxide film remained in a passive state, even though SSC was observed. Crack initiation must therefore be linked to localised breakdown of the passive film and pitting, which will be facilitated by chlorides in the test solution and physical defects induced by machining processes. H_2S also promotes pitting because this leads to the adsorption of a sulphur species that retards re-passivation and stabilises what would otherwise be metastable pits if H_2S was not present. Furthermore, the mechanism of hydrogen promotion by Dean [15] suggests that the conjugate base of H_2S adsorbs on the steel surface and catalytically promotes hydrogen entry through a transition state complex $[HSH]_{ads}$, resulting in local embrittlement at the pit site. Corrosion pits act as local stress-raisers that can initiate cracking. Indeed, Horner *et al*. [11] showed that stress corrosion cracks can initiate at the side of a pit wall close to the pit mouth where there is a high level of localised plastic strain.

In SSC, crack initiation at pit walls may be exacerbated by local embrittlement since hydrogen has a propensity travel to sites of plastic strain.

8.1.2 Factors Influencing Crack Propagation

Following the initiation stage, SSC propagates in a direction approximately perpendicular to the applied tensile stress. The loading stress acts to open the crack but decreases from the surface due to the linear gradient of bending stresses through the thickness of the beam, hence complete fracture of the test specimens was not observed. However, cracks up to 4.5 mm deep were measured in the Condensed Water tests and up to 3 mm deep in the Produced Water tests (Figure 6.32).

Locally, crack propagation will be influenced by plasticity at the crack tip and local embrittlement by absorbed hydrogen. Hutchings and Turnbull [185] showed that dislocations provide reversible trap sites in AISI 410 steel and Hinds *et al.* [74] showed that reversible trap sites control the diffusivity of hydrogen in a super 13%Cr steel. Cracking is associated with reversible trapped hydrogen and since the density of dislocations would be expected to increase with deformation, the large plastic zone produced in the four-point bend specimens (penetrating approximately 2 mm from the tensile surface as shown in Figure 7.18) provides a source of hydrogen for crack propagation. Furthermore, plastic strain concentration at the edges and roller positions provide sites of increased dislocation density and therefore become sites for preferential hydrogen trapping. Note that the deepest cracks were observed at the specimen edges in the Seabed Temperature SSC Investigation (Chapter 6).

8.1.3 Effect of Temperature on SSC Resistance (5 °C versus 24 °C)

The four-point bend SSC results presented in Chapter 6 showed that specimens tested in the fully-machined condition were more susceptible to SSC at 5 °C than those tested at 24 °C. This supports the observations made by Bodycote in 2005 [3] but contradicts other published work on similar grade (UNS S41426) materials [75]. Poor control of test variables, particularly dissolved oxygen could be accountable for the conflicting data in the literature.

The solubility of H_2S in water increases as temperature decreases (see Figure 6.14), which implies that the specimens tested at 5 °C were exposed to an effectively higher H_2S partial pressure (pH_2S) compared to the specimens tested with the same gas mixture at 24 °C. The evidence provided in the Seabed Temperature SSC Investigation suggests that both crack initiation and crack propagation is greater at lower test temperatures since the highest number of cracks and some of the deepest cracks were observed in the specimens tested at 5 °C. H_2S promotes crack initiation through pitting and increased hydrogen charging as discussed previously. However, the increased number and depth of cracks could be explained by an increase in hydrogen *charging rate* with reduced temperature, since charging rate increases with pH_2S as proposed by Crolet & Bonis [21].

The material safely operates on the upper shelf at 5 °C and there is little change in mechanical properties when compared to 24 °C. Alhough not investigated in this thesis, it is possible that the fracture toughness could be reduced at 5 °C, since this effect has been reported for low alloy steels in the temperature range of 24 °C to 5 °C [75,161].

8.1.4 Effect of Chlorides on SSC Resistance (PW versus CW)

It should be noted that H_2S solubility increases as salinity decreases [169], yet the results presented in Chapter 6 showed that SSC was more severe in the high chloride Produced Water environment compared to the low chloride, low pH Condensed Water environment. This highlights that chlorides are more detrimental to SSC resistance than pH_2S and pH, as commonly reported in the literature for 13%Cr stainless steels [39,75,86,105]. It should be noted that when the solution pH falls below the depassivation pH, general corrosion will occur and hydrogen uptake will increase significantly.

8.1.5 Effect of Surface Finish on SSC Resistance (FM versus AR)

The Seabed Temperature SSC Investigation presented in this thesis highlighted that the grit-blasted as-received pipe surface was inherently resistant to SSC in all the test environments, indicating that surface finish and specimen preparation heavily influence the SSC susceptibility of this material. Residual compressive stresses imparted by the grit blasting process generate an apparent increase in hardness [146], as measured by the nanoindentation hardness tests in Chapter 5. These residual compressive stresses slow the rate of hydrogen diffusion in steels and improve resistance to hydrogen embrittlement [167]. This could explain the superior SSC resistance of the as-received specimens compared to the fully-machined specimens in the Produced Water test environments. The fully-machined specimens were ground to a 600-grit finish which removes the as-received pipe surface and relieves the beneficial residual compressive stresses induced from the grit blast process. In 316L stainless steels, grinding operations can generate near surface residual tensile stresses [168], although these will be relaxed to some extent when the specimen is

loaded to 0.2% plastic strain. Furthermore, machining and grinding processes can generate physical defects from which pitting can occur, as observed in 316L and 304 austenitic stainless steels [168, 176]. Grinding marks on the chamfered edge, as shown in Figure 6.26, could be responsible for local breaks in the passive film as well as stress concentrators which could initiate pitting corrosion and promote SSC propagation.

8.2 Suitability of the Four-Point Bend Test Method

Preferential cracking at the edges and inner loading roller positions highlight the limitations of the four-point bend test method for assessing the SSC resistance of 13%Cr stainless steels. The FEA in Chapter 7 showed that these areas are hot spots for plastic strain concentration and which may also be sites for preferential hydrogen trapping as discussed previously. Furthermore, strain concentrates more at the edges of the curved as-received specimens than on flat-surfaced fully-machined specimens which may account for the case of anomalous cracking in the Condensed water SSC tests (Figure 7.37). In reality, strain concentrations can also be magnified by eccentric loading and asymmetric specimen geometry [178] as highlighted by the DIC measurements in Chapter 7.

Although chamfers and fillet radii are effective at reducing stress and strain along the edges of the test surface (Figure 7.35), the process of removing material at the edges of the specimen locally changes the test surface and will introduce physical defects. These defects may act as stress concentrators and microscopic crevice sites which can promote pitting corrosion and make the material more susceptible to SSC.

FEA highlighted that contact friction at the inner loading rollers increases the stress concentration on the tensile test surface and generates a strain concentration in the same region which is not predicted when frictionless contact is assumed. NPL showed that the assumption of frictionless contact at the rollers may not be reliable [182], hence it should be expected that there will be some strain concentration on the tensile test surface near the inner loading rollers which could influence SSC initiation. To support this, the Seabed Temperature SSC Investigation showed that some of the largest cracks were observed near the inner loading rollers on the tensile surface of the fully-machined test specimens as demonstrated in Figure 8.1.

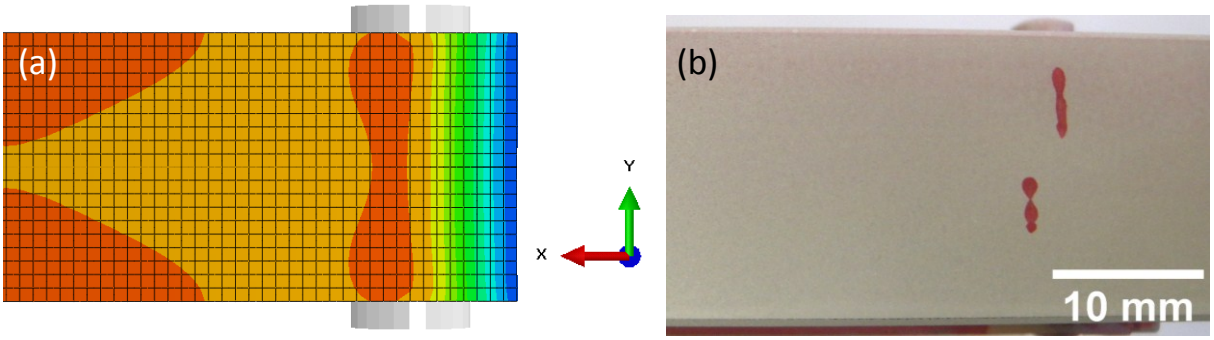

Figure 8.1 Strain concentration and preferential SSC at the inner loading roller: (a) FE model with μ_k = 0.5, (b) SSC test specimen

The peak stresses generated on the tensile surface above the inner loading rollers could be reduced by testing smaller size specimens [143]. However, it was shown in Chapter 7 that reducing specimen thickness increased the anticlastic bending effect which results in an even higher strain generated at the edges of the specimen [117].

It has already been reported that loading four-point bend specimens from tensile stress-strain data results in a loading strain approximately 18% lower than that determined

form a flexural bend test [116]. However, the FEA in Chapter 7 showed that the 0.2% offset strain measured from the load-strain curve in a flexural bend test corresponds to approximately 0.3% plastic strain in the material, therefore tensile stress-strain data should be used to set the loading strain in four-point bend specimens to achieve a surface strain of 0.2% plastic strain. This result has also been verified by NPL [181]. This indicates that the SSC test specimens in Chapter 6 were loaded to 0.3% plastic strain which may have exacerbated the level of cracking seen in the fully-machined specimens. Excessive plastic strain can rupture of the passive film, but this should have been mitigated by the 48 hour air-passivation carried out prior to testing. More likely is the transformation of retained austenite into fresh martensite by deformation-induced martensitic transformation [100,103]. Given that 10% or more retained austenite is believed to be beneficial to the SSC resistance of 13%Cr stainless steels [98], the measured volume fraction of 12.9% retained austenite could have been reduced at the surface during loading. Further investigation is required to confirm if this is the case.

CHAPTER 9: SUMMARY & CONCLUSIONS

9.1 Summary

The primary aim of this EngD project was to determine if the weldable 13%Cr supermartensitic stainless steel supplied by Nippon Steel & Sumitomo Metal Corporation was more susceptible to SSC at seabed temperatures of 5 °C than at room temperature. The secondary aim of this project was to investigate the suitability of the four-point bend test method as a means of loading SSC test specimens through a stress and strain investigation.

The work presented in the *Verification of the Scoping SSC Tests* (Section 6.1) highlighted issues with the existing test procedure and apparatus used for testing the SSC resistance of corrosion resistant alloys. The main problem with the existing SSC test method was the uncertainty of whether dissolved oxygen remained below 10 ppb in the test solution for the duration of the test. It was also found that the pH of the simulated Condensed Water solution was unstable and tended to drift to a more alkaline value over the duration of the test. With regards to specimen preparation, it was observed that removing a small area of the as-received pipe surface for strain gauge application promoted SSC, highlighting the importance of maintaining surface integrity when testing 13%Cr materials. Consequently, the standard Exova four-point bend test procedure was updated so that strain gauges were attached directly to the as-received surface for specimen loading. The observations made during this work defined the first major objective for this EngD project, defined as *SSC Test Protocol Development & Modification* (Section 6.2).

In the SSC Test Protocol development & Modification phase, a new SSC test rig was designed with in-situ oxygen monitoring and a pH control system. The four-point bend test rig was also redesigned to provide improved strain stability in the test specimen. Idometric titrations were performed to show that the solubility of hydrogen sulphide increases as temperature is reduced from 24 °C to 5 °C, increasing the effective partial pressure (pH_2S) in solution and potentially increasing the rate of hydrogen uptake through pit sites, providing a possible explanation for the increased SSC seen at 5 °C.

Following the development & modification phase, the *Seabed Temperature SSC Investigation* (Section 6.3) was implemented to complete the first aim of the project. This investigation showed that the as-received pipe surface was resistant to SSC in all the test conditions and the fully-machined surface was resistant to SSC in the Condensed Water environment (at 69 mbar H_2S). However, the fully-machined surface was more susceptible to SSC at 5 °C compared to 24 °C in the high-chloride Produced Water environment. Given that H_2S solubility increases as temperature and salinity decreases, the SSC results suggested that chlorides are more detrimental to SSC resistance than H_2S partial pressure and solution pH when the passive film is stable. It is also possible that passive film behaviour may be influenced by temperature changes in the range of 5 °C to 24 °C in Produced Water and Condensed Water environments. This was not investigated in this thesis but is an active area of current research [175]. Observing the crack locations on the test surface of the specimens indicated that SSC would concentrate along the chamfered edges and on the test face near the inner loading rollers. These observations initiated the second stage of the project: *Stress & Strain Investigation of the Four-Point Bend Test* (Chapter 7).

The first objective of the stress and strain investigation was to develop a new test rig to perform flexural bend tests with accurate temperature control. With accurate flexural-bend and tensile test data, finite element analysis was used to show that the 0.2% offset strain taken from a tensile stress-strain curve corresponds to 0.2% plastic strain in a four-point bend test. The 0.2% offset strain taken from a flexural bend test corresponds to approximately 0.3% plastic strain due to the non-linear relationship between stress and load during plastic deformation.

The second objective of the stress and strain investigation was to map the full-field stress and strain distribution on the test surface of fully-machined and as-received test specimens. This was achieved using FEA and validated with DIC and strain gauge measurements. The work highlighted stress and strain concentrations associated with friction at the inner loading rollers, which are unavoidable due to the geometry of the test specimen and the corresponding loading arrangement. Strain concentrations located at the edges of the specimens correspond to the location of cracking observed in the SSC tests. Although chamfering and fillet radii can be used to reduce strain at the edges of the test specimens, the application of chamfers or fillets locally changes the test surface and increases the risk of SSC. Therefore any cracks located at the edges or at the inner loading roller positions should be treated as an artefact of the test system and not a true indication of material performance.

9.2 Conclusions

1. The ductile-brittle transition temperature is approximately -100 °C which means that this material is safely operating on its upper shelf when exposed to seabed temperatures of 5 °C. Furthermore, mechanical properties[32] in tension and bending are not significantly influenced when temperature is reduced from 24 °C to 5 °C. (Chapter 5)

2. Weldable 13%Cr supermartensitic stainless steel is more susceptible to SSC at 5 °C compared to 24 °C when tested in the high chloride Produced Water environment. This was highlighted by the highest number of cracks, and also the deepest cracks, observed in the fully-machined specimens tested at 5 °C (Section 6.3). This may be due to the increase in H_2S solubility as temperature decreases (Section 6.2.3).

3. The SSC resistance of weldable 13%Cr supermartensitic stainless steel is strongly influenced by surface condition: The as-received pipe surface was inherently immune to SSC in all test conditions. The 600-grit fully-machined surface condition is susceptible to SSC in simulated Produced Water when exposed to 35 mbar H_2S (Section 6.3). The protection imposed by the as-received pipe surface may be linked to residual compressive stresses induced by the alumina blasting process. Conversely, the reduced SSC resistance of the fully-machined surface condition may be linked to physical defects generated by grinding to a 600 grit finish which provides sites for preferential pitting and SSC initiation.

[32] An assessment of fracture toughness at 5 °C and 24 °C was not performed in this thesis, and is therefore a recommendation of future work.

4. Cracks generated at the chamfered edges of the as-received test specimens could be attributed to removal of the protective pipe surface and small physical defects introduced by the grinding process which act as local stress concentrators on the chamfer (Section 7.3).

5. The SSC results suggest that chloride content is more detrimental to the SSC resistance of weldable 13%Cr supermartensitic stainless steel than H_2S concentration and pH: At 5 °C, the material was resistant to SSC in the Condensed Water environment when exposed to 69 mbar H_2S, but failed in the Produced Water environment when exposed to 35 mbar H_2S (Section 6.3).

6. Environmental parameters, such as dissolved oxygen, pH and temperature need to be closely controlled when conducting SSC testing of weldable 13%Cr supermartensitic stainless steels to provide reliable and reproducible results in laboratory tests. The new SSC test rig development implemented at Exova allows tests to be performed to the requirements of EFC17 and ISO 15156 guidelines by controlling dissolved oxygen to <10 ppb, temperature to ±2 °C and pH to ±0.1 (Section 6.2).

7. When loading 13%Cr stainless steels SSC test specimens in four-point bending, the loading strain should be monitored for at least 1.5 hours after applying the initial load to ensure strain stability. After this time, the strain gauge can be removed with confidence that the loading strain will be stable for the 30 day SSC test (Section 6.2).

8. The load-strain curve generated from flexural bend test data should not be treated in the same way as that from tensile stress-strain data. This is because the relationship between stress and load in the flexural bend test becomes non-linear in the plastic regime. Consequently, the 0.2% offset strain determined from a flexural bend load-strain curve corresponds to approximately 0.3% plastic strain in the material (Section 7.2).

9. Friction at the loading rollers can generate stress and strain concentrations on the test face, the location of which coincides with the location of preferential SSC observed in the seabed temperature SSC investigation (Sections 6.3 & 7.3).

10. Anticlastic bending increases strain at the edges of the tensile test face of a specimen loaded in four-point bending. This effect is magnified in as-received geometries and when the thickness of fully-machined specimens is reduced. Therefore full-thickness specimens should be used where possible (Section 7.3.2).

11. Chamfering and fillet radii will reduce stress and strain at the edges of a four-point bend specimen. Chamfer angle has little influence on the extent of stress and strain reduction at the edges whereas fillet radius becomes more effective as the radius is increased. However, edge preparation does not necessarily reduce the likelihood of SSC for the reasons given in Point 4. Therefore cracks generated on the chamfered edges should be treated as an artefact of the test method (Section 7.3.4 & Section 7.3.5).

CHAPTER 10: FURTHER WORK

The work presented in this thesis focused on the Seabed Temperature SSC resistance of parent weldable 13%Cr supermartensitic stainless steel using the four-point bend test method. The following future work was identified during the course of this research project:

1. SSC tests at 5 °C using four-point bend specimens loaded from tensile data, compared to specimens loaded from flexural bend data.

2. Full ring SSC tests in simulated Produced Water environments at 5 °C and 24 °C. The full ring rest method eliminates the influence of edges and roller friction associated with the four-point bend test method. Full ring tests would be used to determine the SSC limits of the as-received pipe surface in Produced Water. This work would also require a development phase to build a full-ring test rig that incorporates the oxygen sensor, nitrogen cabinet and pH controller as used in the four-point bend tests.

3. Investigate the influence of surface finish on SSC susceptibility using fully-machined four-point bend specimens with different surface grinding finishes (e.g. grit 600 to 1 µm diamond finishes). It is recommended that the tests are done at 5 °C in Produced Water with 69 mbar H_2S as these conditions generated SSC in the fully-machined specimens prepared to a 600 grit finish. This work should be supported by electrochemical tests to investigate passive film stability in these environments.

4. Hydrogen uptake measurements at 5 °C and 24 °C in simulated Produced Water environments (70 mbar H_2S), fracture toughness tests at 5 °C and 24 °C and XRD to determine the effect of cold work on retained austenite.

5. Use DIC to measure the full-field surface strain distribution of root-intact welded four-point bend specimens loaded in four-point bending. Investigate how weld root profile influences strain concentrations at the fusion line of the weld. Investigate the effects of pipe misalignment on strain distribution, including the use of full-thickness and reduced thickness specimens. Investigate specimens with under-matching (i.e., 22%Cr duplex), matching (i.e., 13%Cr) and over-matching (i.e., 25%Cr super-duplex) weld metal and the effect this has on strain concentration at the fusion line. It is recommended that the DIC analysis focuses on the weld root rather than the entire specimen, using a reduced analysis area to improve the DIC image resolution (as done with the edge analysis setup described in Section 4.3.5.4). Focusing on the weld root would allow strain gauges to be attached to the tensile surface either side of the weld for more accurate loading (compared to loading from strain gauge measurements on the compressive face).

APPENDIX 1: THERMAL STABILITY TRIALS

Several trials were conducted as part of the flexural bend test development phase to ensure that the heat chamber provided uniform and stable heating to the test specimen at temperatures up to 200 °C.

A 130x20x10 mm four-point bend calibration sample was machined from 13%Cr material and fitted with eight thermocouples (Figure A3.1). The thermocouples were secured to the surface of the specimen using aluminium tape (Figure A3.2) and were used to measure the thermal gradient through the thickness and across the length of the beam in the following trials.

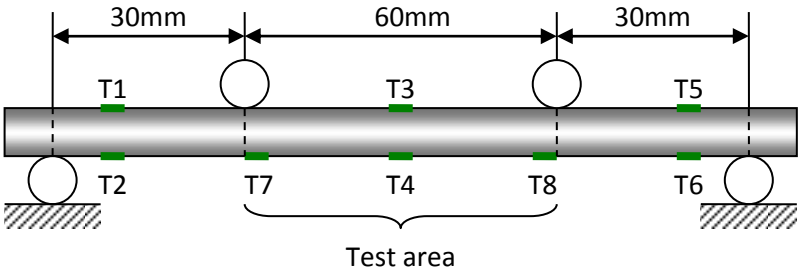

Figure A1.1 Thermocouple positions on test sample

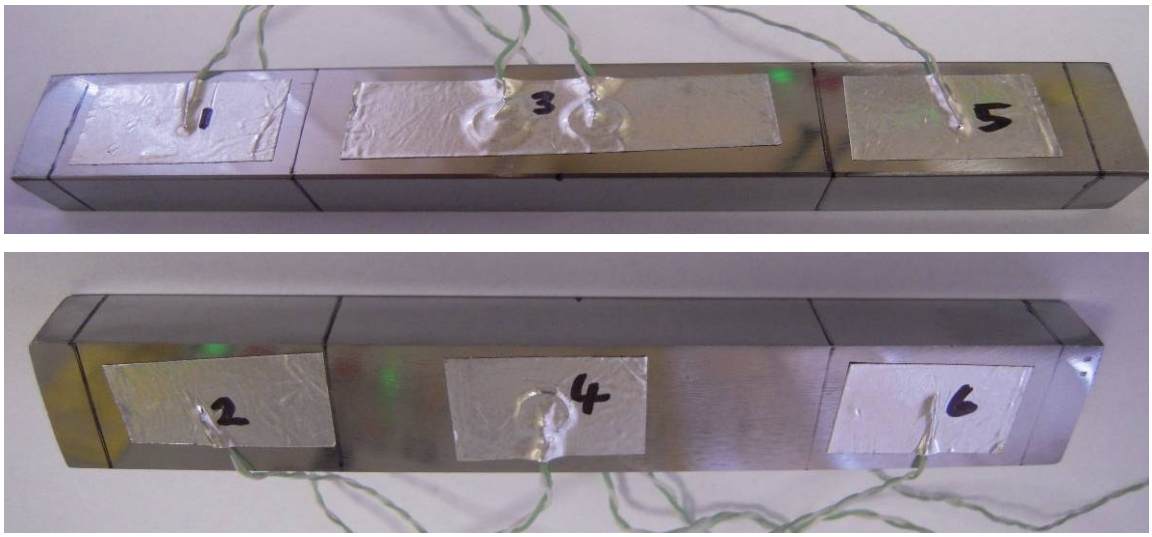

Figure A1.2 Thermocouples held in position using aluminium tape

A1.1: ON/OFF Control

This setup used a 200 W heater pad controlled by an On/Off controller. Figure A1.3 shows the temperature control achieved with this system:

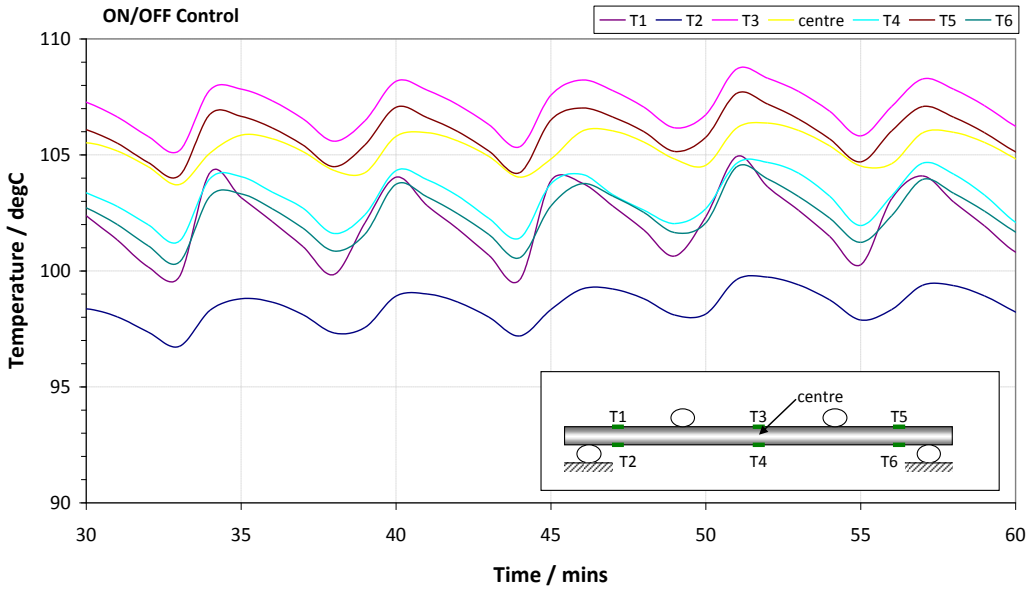

Figure A1.3 Temperature control at 100 °C using ON/OFF control

RESULTS:

- For a target temperature of 100 °C, the thermal gradient across the specimen was ±5 °C (worst case), ranging from 98 °C to 108 °C.
- Using ON/OFF control causes the specimen temperature to fluctuate by 6 °C (±3 °C) about the set-point.

A1.2: PID Control

Several trials were conducted with the Leicester 'LHS15 system' air heater and CSS controller to identify the optimal air pressure and controller settings for optimal temperature control and low thermal gradient through the calibration sample. The factory default settings in the CSS controller were as follows:

- Proportional band (P) = 30
- Integral band (I) = 0.2
- Derivative band (D) = 0.001
- Maximum power output (hpH) = 100 % (650 °C)

Figure A1.4 shows the response when heating to 200 °C with these settings with an air pressure of 0.025 MPa. The heating time is fast but the target temperature overshoots by 6 °C and the system oscillates for 30 minutes before settling down:

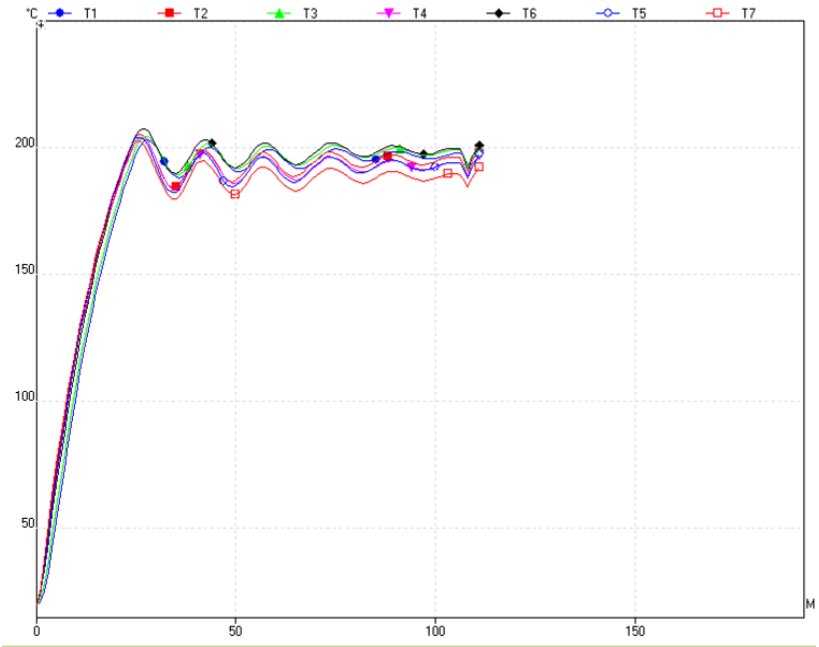

Figure A1.4 Heating curve with factory default settings

The factory default settings and air pressure was adjusted to find the optimal parameters for testing at 50 °C, 100 °C, 150 °C and 200 °C. Table A1.1 summarises the optimal settings and the following figures show example heating curves taken from the calibration specimen thermocouples. The heating curves show that the worst case thermal gradient across the calibration specimen was ±0.5 °C up to 50 °C and ±3.0 °C up to 200 °C.

Table A1.1 CSS Controller settings for elevated temperature flexural bend tests

Controller Settings					Air pressure (MPa)	Worst case set-point deviation (°C)	Worst case Thermal gradient (°C)
Set-point (°C)	P	I	D	hPH (%)			
≤50	24	0.01	0	30	0.075	49-50	±0.5
≤100						99-101	±1.0
≤150				80		147-151	±2.0
≤200					0.025	196-202	±3.0

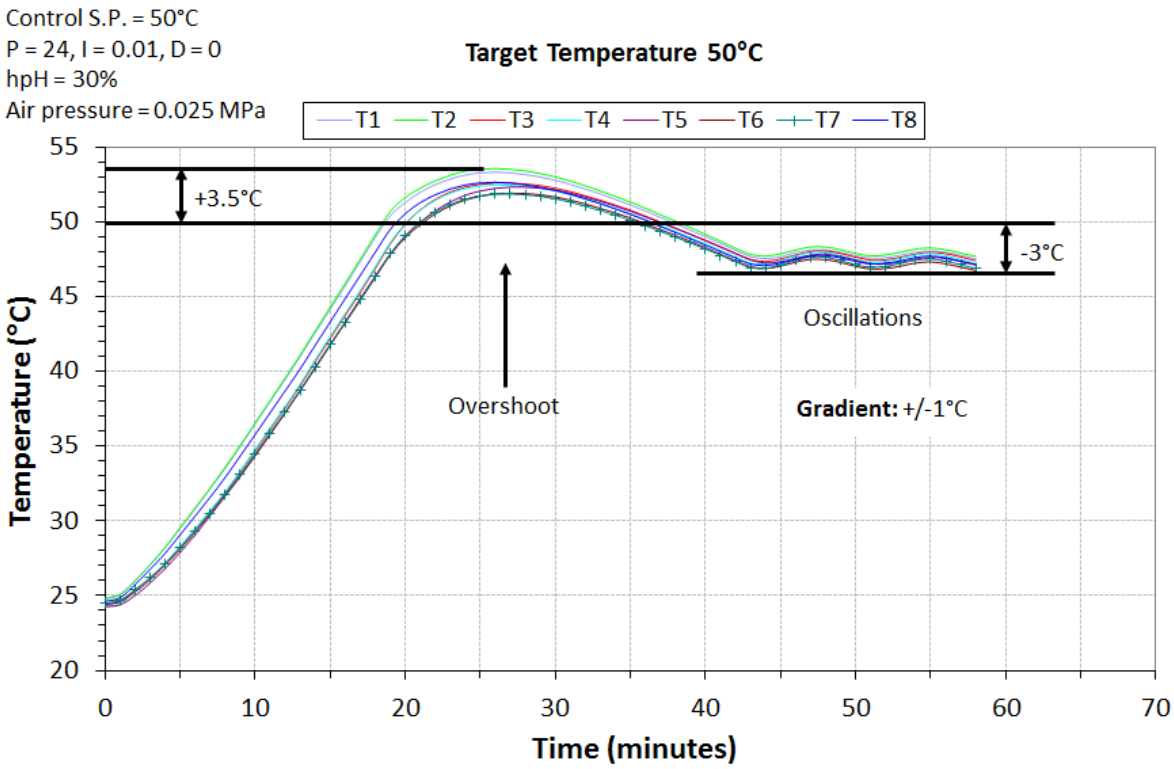

Figure A1.5 Heating curves for calibration specimen: 50 °C, air pressure 0.025 MPa

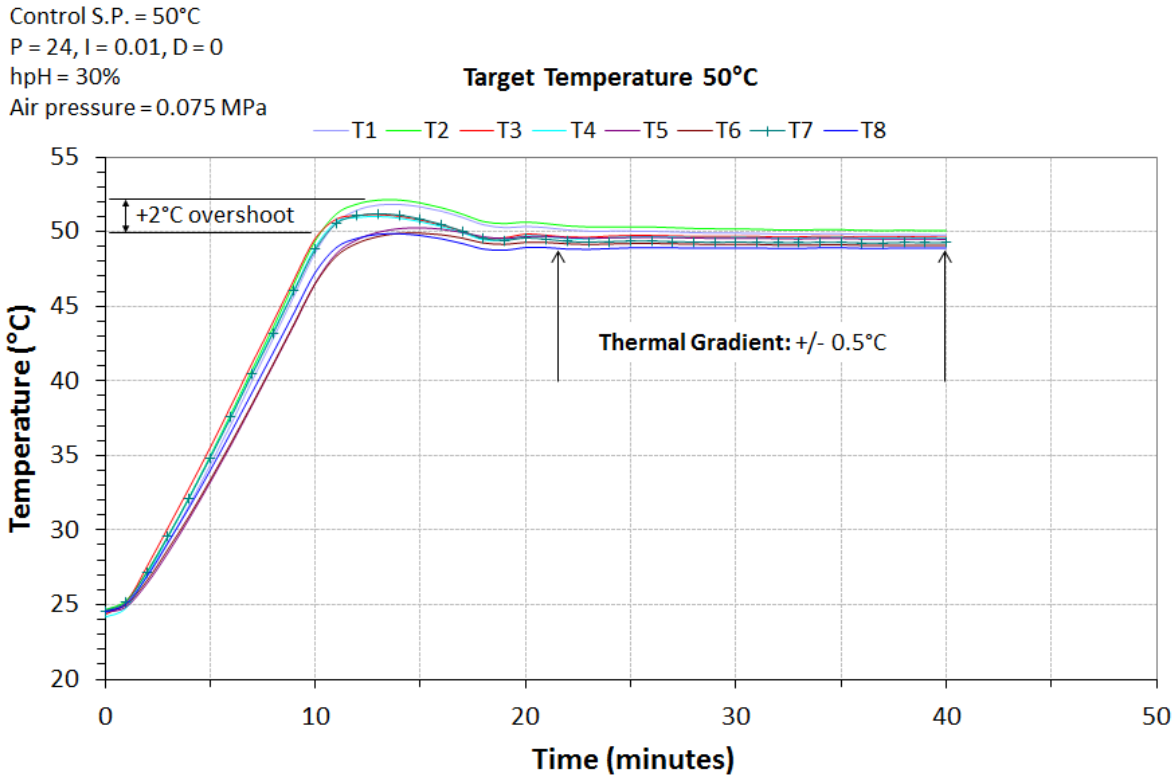

Figure A1.6 Heating curves for calibration specimen: 50 °C, air pressure 0.075 MPa

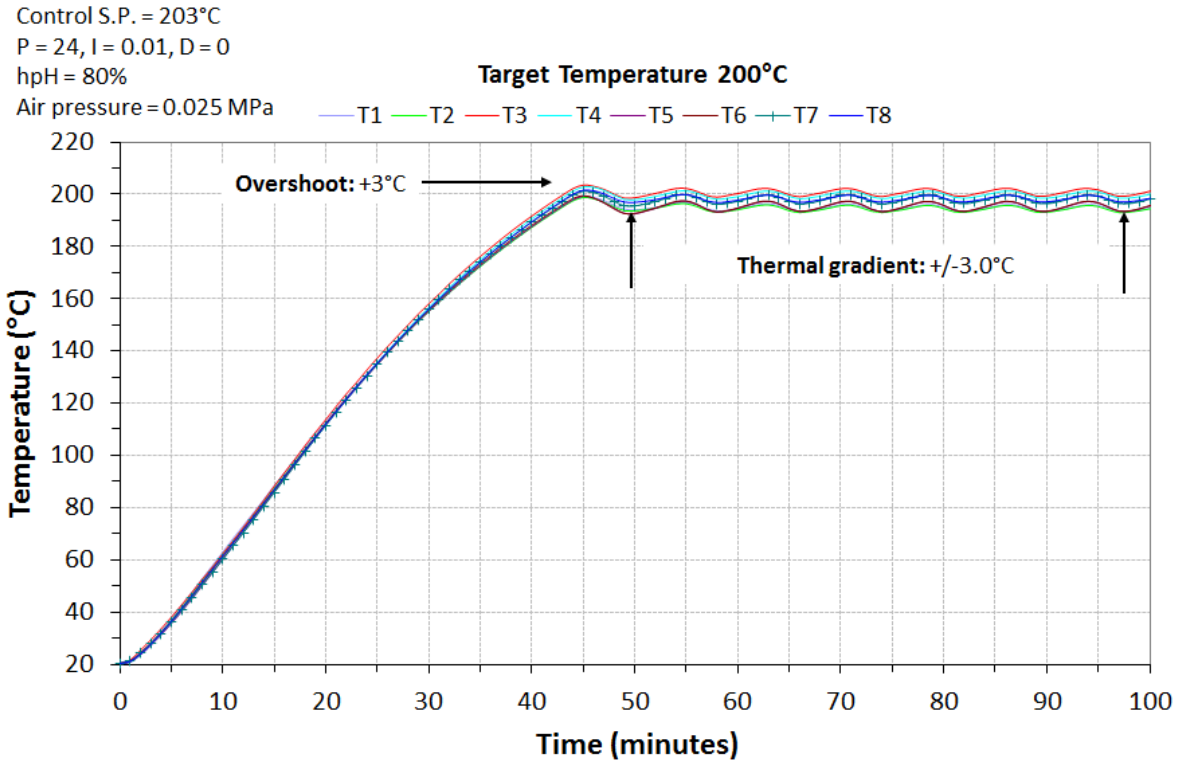

Figure A1.7 Heating curves for calibration specimen: 200 °C, air pressure 0.025 MPa

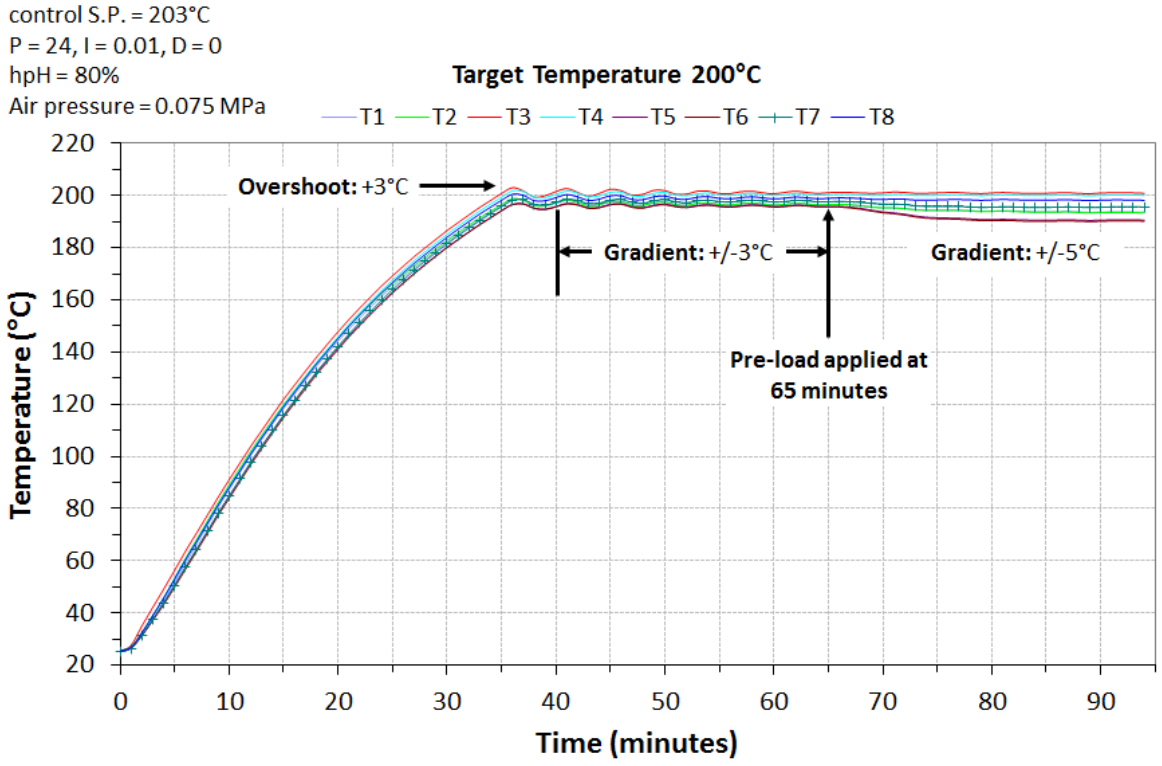

Figure A1.8 Heating curves for calibration specimen: 200 °C, air pressure 0.075 MPa

The following key observations were made from these trials:

Influence Power output (hpH): At low target temperatures (50 °C & 100 °C) the power output needs to be as low as possible. If it is set too high, then heating can considerably overshoot the target temperature. At high target temperatures (150 °C & 200 °C) the power output needs to be sufficient to achieve the target temperature.

Influence of air flow: At target temperatures of 50 °C, 100 °C & 150 °C the optimal air flow needs to be around 0.075 MPa to reduce overshoot on heating. At 200 °C the optimal air flow needs to be 0.025 MPa. This is because the temperature gradient across the sample worsens with increased air flow at higher temperatures.

Influence of thermal conduction: Tests proved that application of pre-load increases the thermal gradient in the sample. This is because the loading rod acts as a heat sink and conducts heat away from the sample, increasing the gradient from ±2 °C to ±4 °C. Therefore the pre-load must not be applied during the heating/soaking period. The pre-load must be applied just before the test is about to start.

Thermocouple attachment: If the thermocouple is not in direct contact with the specimen then it measures air temperature rather than specimen temperature giving misleading results. It was found that aluminium tape was good for maintaining adhesion at temperatures up to 200 °C.

Deflector plate: The shape of the deflector plate influences the thermal response of the system. The optimal design was found to be an inverted 'T' shape that shields the sample and loading fixtures from direct air heating (rectangular shaped plates of varying widths increased the thermal gradient).

APPENDIX 2: SSC TEST SOLUTION TEMPERATURE & DISSOLVED OXYGEN MEASUREMENTS

A2.1 Produced Water 69 mbar H_2S

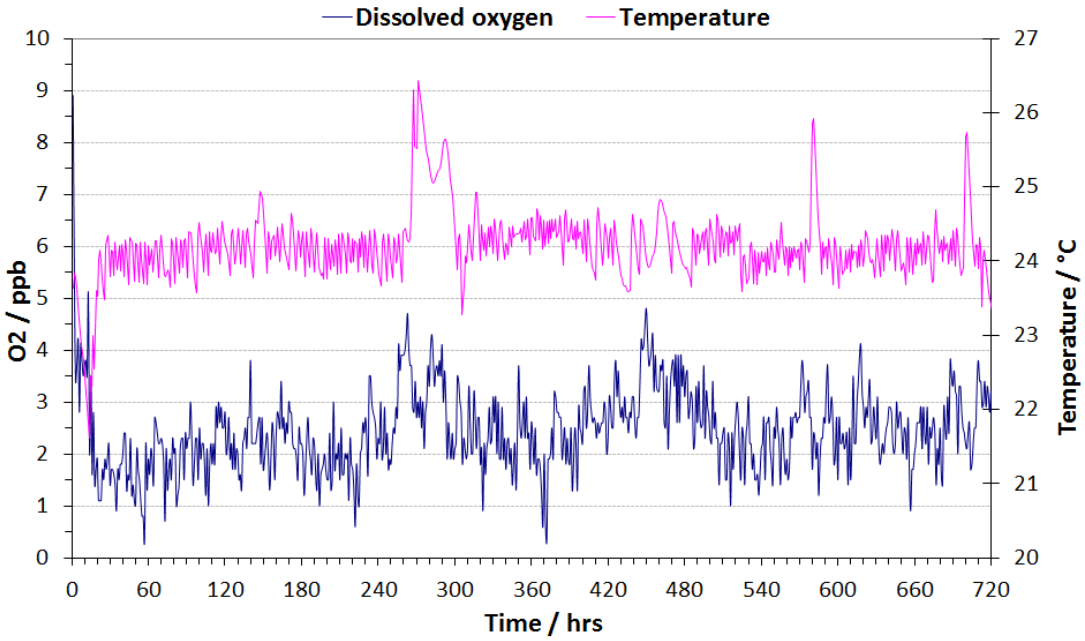

Figure A2.1 Oxygen & temperature measurements for 24 °C tests

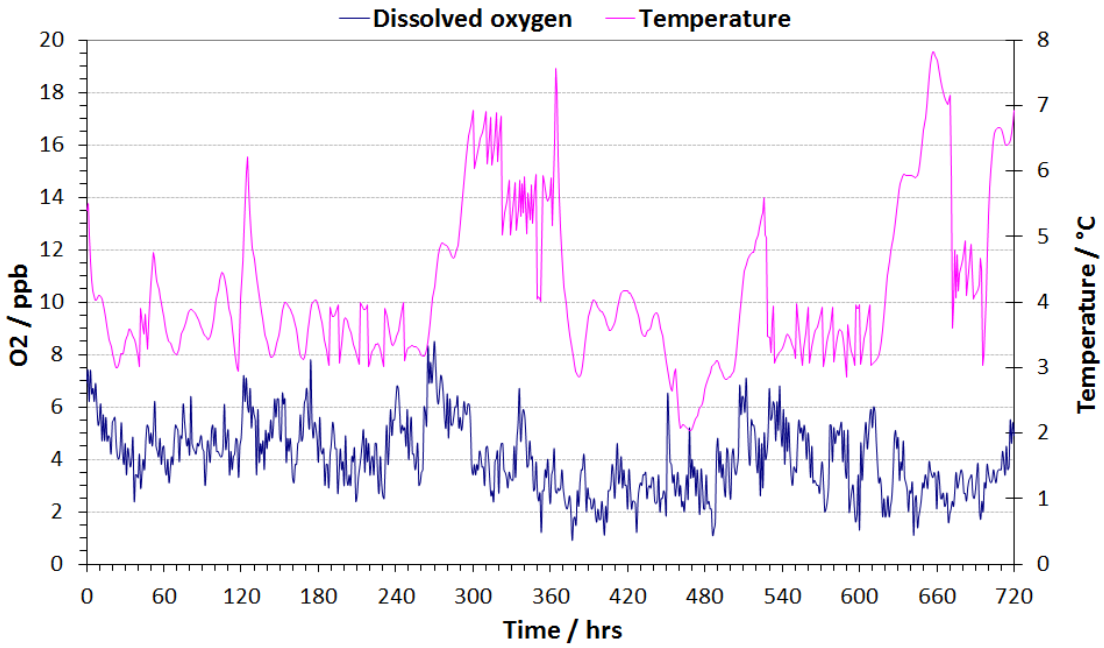

Figure A2.2 Oxygen & temperature measurements for 5 °C tests

A2.2 Produced Water 35 mbar H_2S

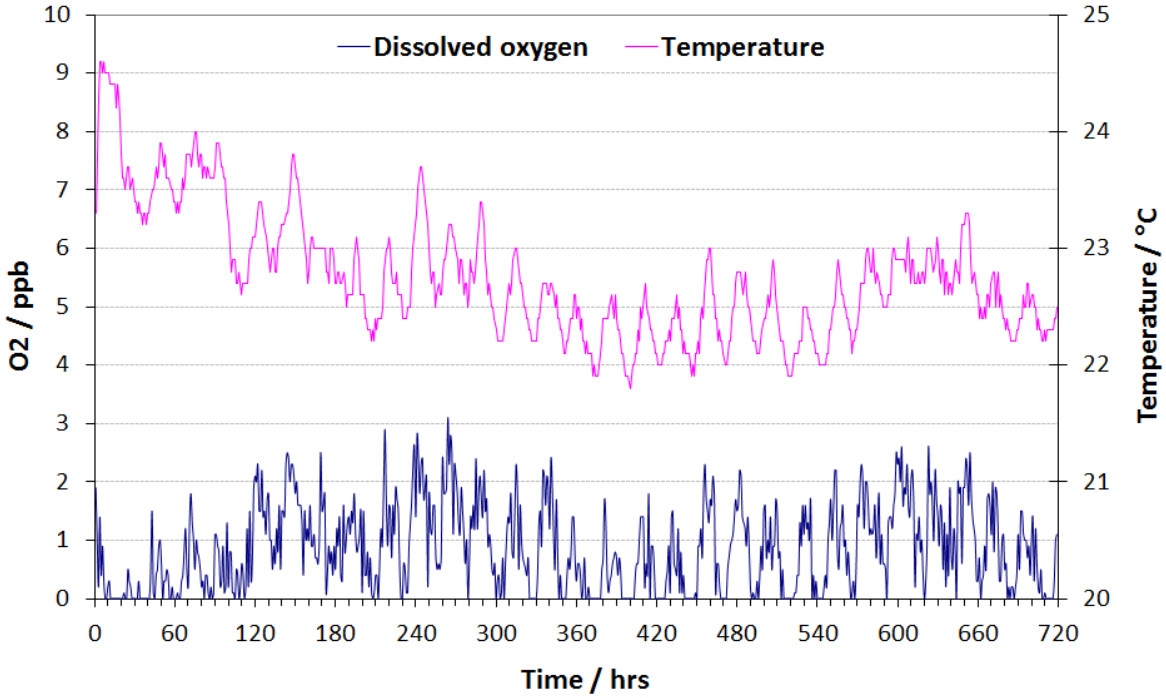

Figure A2.3 Oxygen & temperature measurements for 24 °C tests

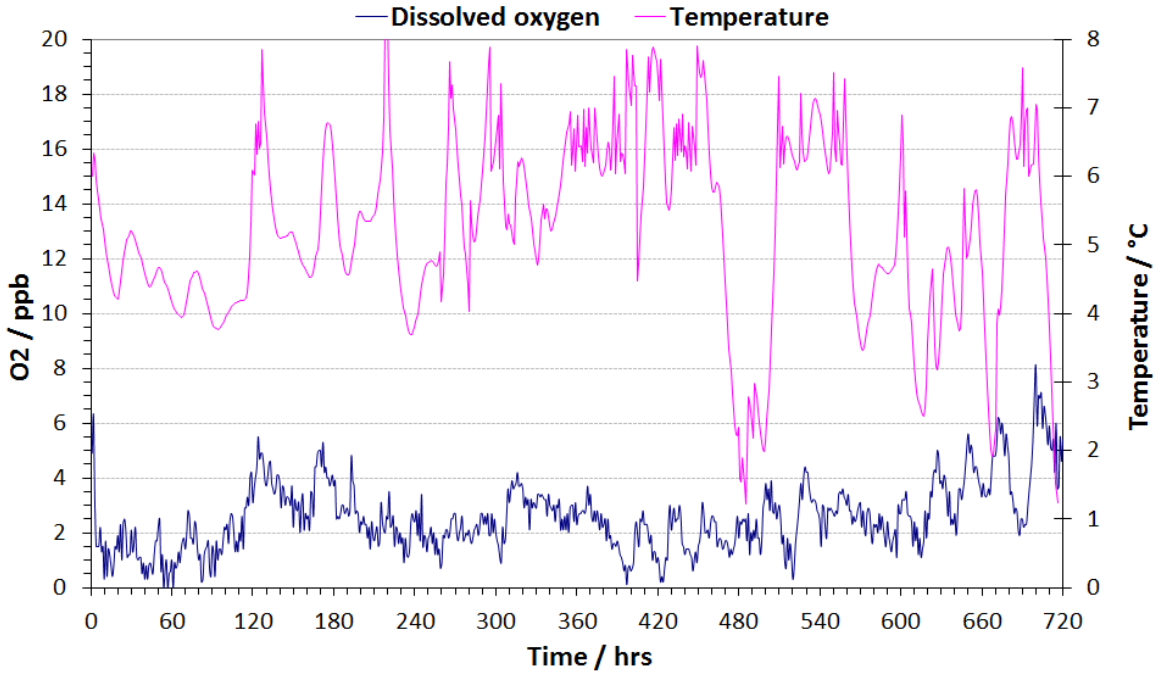

Figure A2.4 Oxygen & temperature measurements for 5 °C tests

A2.2 Condensed Water 69 mbar H_2S

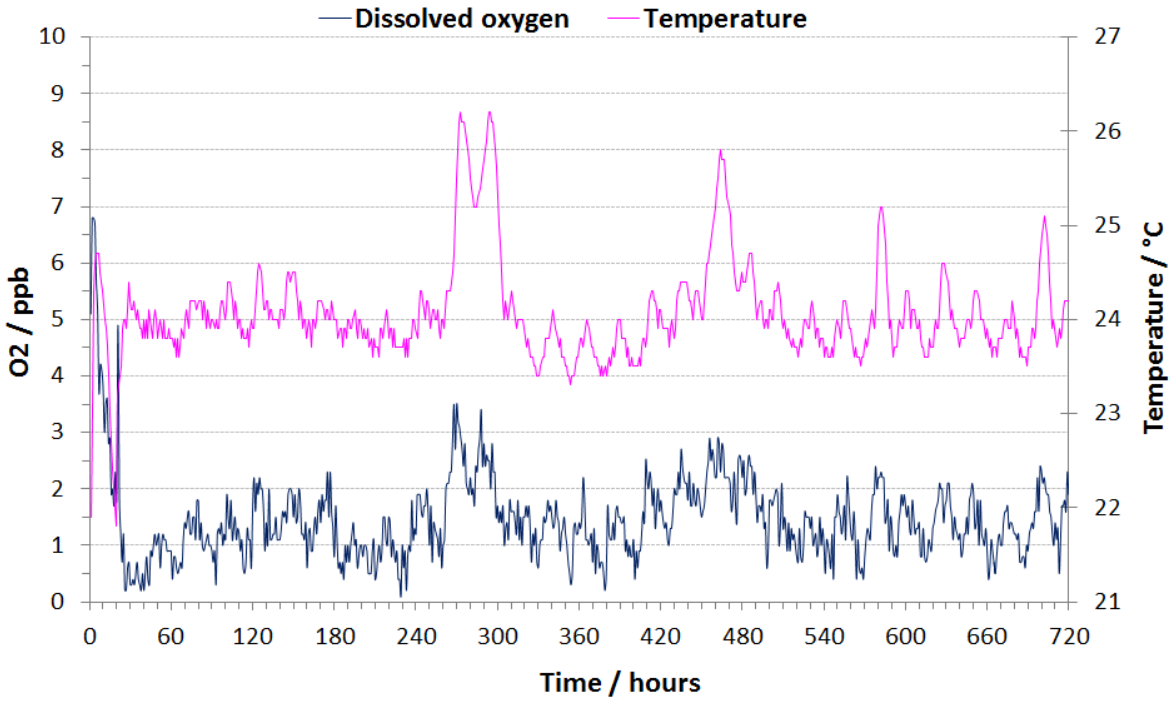

Figure A2.5 Oxygen & temperature measurements for 24 °C tests

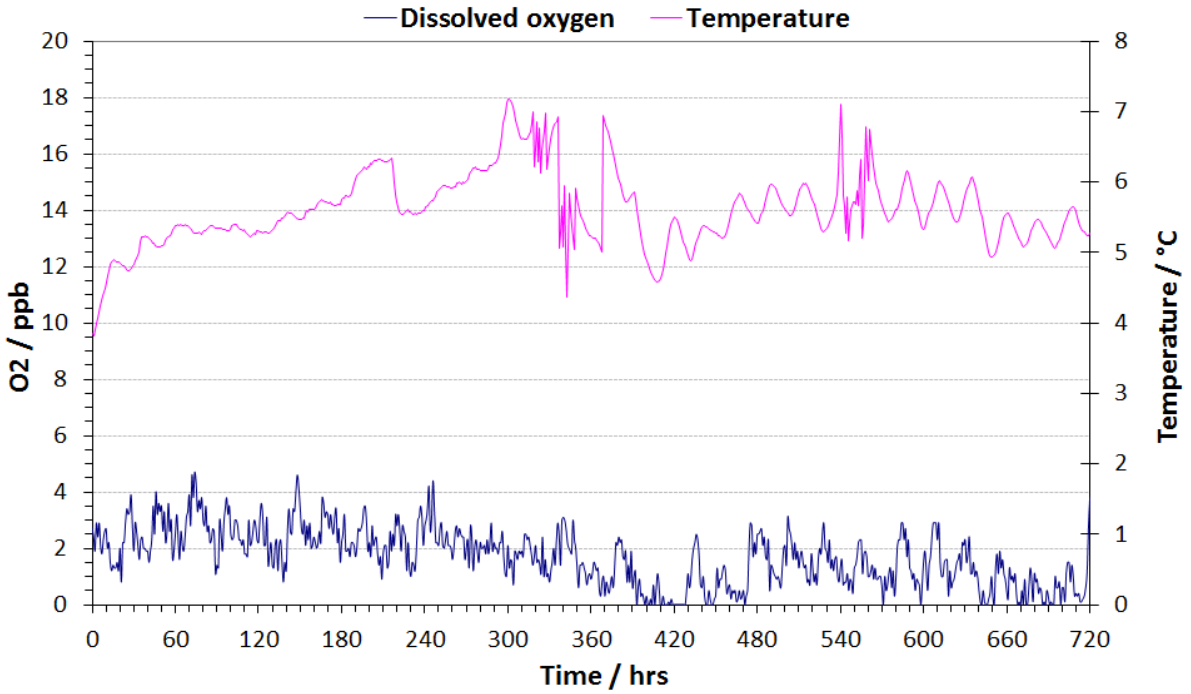

Figure A2.6 Oxygen & temperature measurements for 5 °C tests

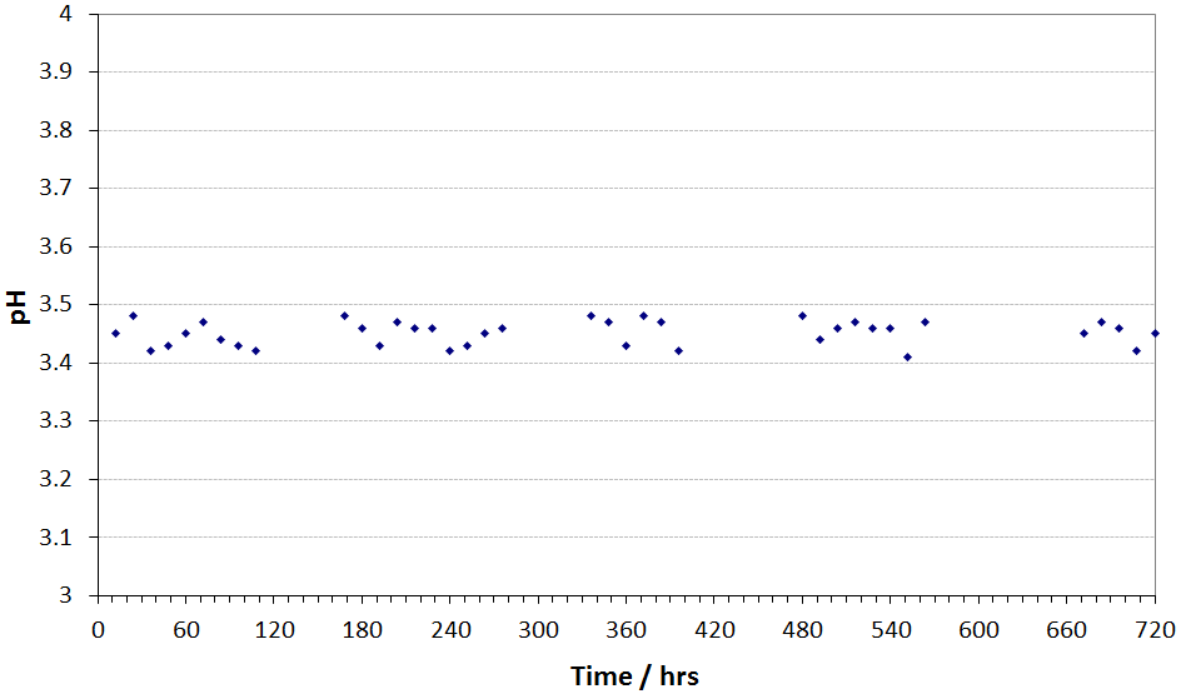

Figure A2.7 Condensed water pH measurements for 24°C tests

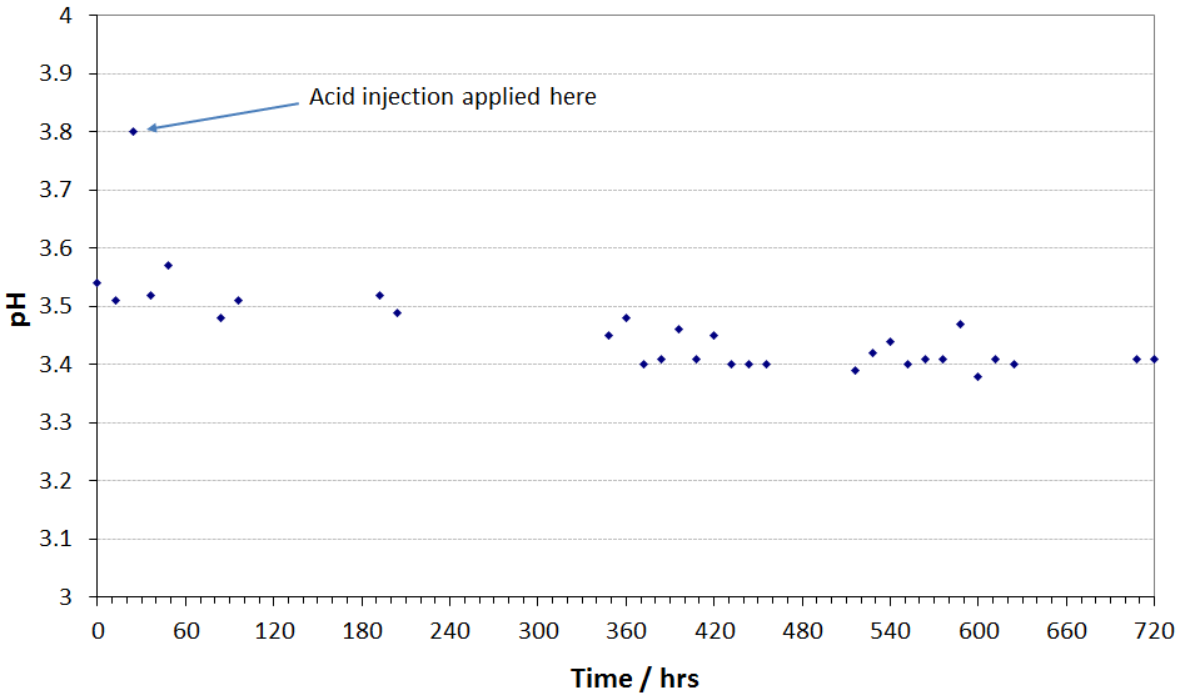

Figure A2.8 Condensed water pH measurements for 5°C tests

LIST OF REFERENCES

1 FMC Technologies. ‘Woodside Echo Yodel’. URL:www.fmctechnologies.com: Accessed Feb 2012

2 Thistle D. ‘The deep-sea floor: an overview’. Elsevier Science 2003; p. 5-37

3 Exova report ref: C500126. Unpublished work, Bodycote 2005

4 NACE MR0175/ISO 15156. 'Petroleum and natural gas industries – Materials for use in H2S-containing Environments in oil and gas production'. NACE/ANSI/ISO 2003

5 Craig BD. 'Oilfield Metallurgy and Corrosion'. 3rd ed. USA: MetCorr; 2004

6 Total. ‘Sour gas, a history of expertise’. The know-how series, March 2007

7 EFC Publications No.17. 'Corrosion Resistant Alloys for Oil and Gas Production - Guidance on General Requirements and Test Methods for H2S Service'. 2nd ed. The Institute of Materials 2002

8 Davenport A. ‘Aqueous Corrosion’. Lecture notes distributed in Environmental Degradation of Alloys EngD module at the University of Birmingham, on 01 April 2009

9 Piron DL. 'The electrochemistry of corrosion'. 2nd ed. USA: NACE International 1994

10 Kane RD, Cayard MS. 'Roles of H2S in the behaviour of engineering alloys: a review of literature and experience'. NACE International, Corrosion 98; Paper No. 274

11 Horner DA, Connolly BJ, Zhou S, Crocker L, Turnbull A. ‘Novel images of the evolution of stress corrosion cracks from corrosion pits’. Corrosion Science 2011; 53:3466-3485.

12 Morana R, Piccolo EL, Scoppio L, Nice PI. ‘Environmental Cracking Performance of Super Martensitic Stainless Steels “13-5-2” (grades 110ksi and 125ksi) for Tubing Applications in High Chloride Reservoir Fluids Containing H2S/CO2’. NACE International, Corrosion 2010: Paper No. 10314

13 Dawson JL. ‘Electrochemical Corrosion Theory & Practice, Polarisation & Corrosion Rates’. Lecture notes distributed at Exova Corrosion Centre, 2009.

14 Olsen S, Enerhaug J. ‘Common Pitfalls During SSC and Pitting Testing of Supermartensitic Stainless Steels for use in Pipelines’. NACE International, Corrosion 2002: Paper No. 02038

15 Dean FWH. 'A Review of Hydrogen Flux Promoters'. NACE International, Corrosion 2010: Paper No. 10182

16 Kim WK, Jung HG, Hoh SU, Kim KY. ‘The Effect of Metallurgical Factors on SOHIC in HIC Free Linepipe Steels’. Proceedings of the Eighteenth (2008) International Offshore and Polar Engineering Conference, Vancouver, BC, Canada July 6-11, 2008

17 Turnbull A, Carroll MW, Ferriss DH. ‘Analysis of Hydrogen Diffusion and Trapping in a 13% Chromium Martensitic stainless Steel’ Acta Metallurgica 1989; 37(7):2039-2046

18 Adams M, Gossett JL. 'Sulfide Stress Cracking and the Commercial Application of NACE MR0175-84'. Fischer Controls 1999; Technical Monograph 34

19 Ghosh DP. ‘Wet H2S Cracking Problem in Oil Refinery Processes – Material Selection and Operation Control Issues’ Tri-service Corrosion Conference 2007.

20 Cooling PJ, Kermani MB, Martin JW, Nice PI. 'The Application limits of Alloyed 13%Cr Tubular Steels for Downhole Duties'. NACE International, Corrosion 98: Paper No. 94

21 Crolet JL, Bonis MR. 'Revisiting Hydrogen in Steel, Part 1: Theoretical Aspects of Charging, Stress Cracking and Permeation'. NACE International, Corrosion 2001: Paper No. 01067

22 ASM. Corrosion in Petroleum Production Operations. In: Garverick L, editor. 'Corrosion in the Petrochemical Industry'. First edition ed. Ohio: ASM International; 1994. p. 259-295

23 Kondo K, Ogawa K, Amaya H, Ueda M, Ohtani H. 'Development of weldable super 13Cr martensitic stainless steel for flowline'. Proceedings of the Twelfth (2002) International Offshore and Polar Engineering Conference, Vol 4 2002:303-309

24 Bilmes PD, Solari M, Llorente CL. 'Characteristics and effects of austenite resulting from tempering of 13Cr–NiMo martensitic steel weld metals'. Mater Charact 2001; 46(4):285-296

25 Caldwell E, Gibson G, Jordan L. 'Further Analysis on M13Cr-110 NACE TM0177 Method A Test Acceptability Prediction'. NACE International, Corrosion 2011: Paper No.11099

26 Enerhaug J, Kvaale PE, Bjordal M, Drugli JM, Rogne T. 'Qualification of welded super 13%Cr martensitic stainless steels for the Asgard field'. NACE International, Corrosion 99: Paper No. 587

27 Lyons WC, Plisga GJ. 'Standard Handbook of Petroleum and natural gas Engineering'. 2nd ed. UK: Elsevier 2005

28 Huizinga S, Ohm RK. 'Qualification and Application Limits of Weldable Supermartensitic 13Cr Linepipe Steels'. NACE International, Corrosion 2001: Paper No. 01093

29 Cayard MS, Kane RD. 'Serviceability of 13Cr Tubulars in oil and gas Production Environments'. NACE International, Corrosion 98: Paper No. 112

30 Omura T, Ohe T, Ueda M, Nice PI, Martin JW. 'Sulfide Stress Cracking (SSC) Resistance Limits for a 125 KSI Grade High Strength Low Alloy Steel OCTG Developed for Mildly Sour Service'. NACE International, Corrosion 2010: Paper No. 10307

31 Byars HG. 'Corrosion Control in Petroleum Production, Appendix 2A – Solubility of oxygen in water'. TPC Publication 5 (2nd Edition). NACE International. 1999

32 Pargeter RJ. 'Susceptibility to SOHIC for Linepipe and Pressure Vessel Steels - Review of Current Knowledge'. NACE International, Corrosion 2007: Paper No. 07115

33 Kane RD, Cayard MS, Cooke DL. 'An Exploratory Examination of the effect of SOHIC Damage on the Fracture Resistance of Carbon Steels' Corrosion Source 2000, Session 11, Paper No. 1101

34 Nippon Steel & Sumitomo Metal Corporation. 'Seamless Steel Line pipe'. Product datasheet ref P103en_01_201211f. 2012.

35 Amaya H, Kondo K, Taniyama A, Sagara M, Ogawa K. 'Stress corrosion Cracking Sensitivity of Super Martensitic Stainless Steels in High Chloride Concentration Environment'. NACE International, Corrosion 2004: Paper No. 04124

36 Winden H, Toussaint P, Coudreuse L. 'Past, present and future of weldable supermartensitic alloys'. Supermartensitic stainless steel conference 2002

37 Linne CP, Blanchard F, Guntz GC. 'Corrosion Performance of Modified 13Cr for OCTG in Oil and Gas Environments'. NACE International, Corrosion 97: Paper No. 28

38 Turnbull A, Griffiths A. 'Corrosion and cracking of weldable 13 wt-% Cr martensitic stainless steels for application in the oil and gas industry'. Corrosion Engineering Science and Technology 2003; 38(1):21-50

39 Marchebois H, Leyer J, Orlans-Joliet BJ. 'SSC Performance of a Super 13% Cr Martensitic Stainless Steel for OCTG: Three-Dimensional fittness-for-purpose Mapping According to PH2S, pH and Chloride Content'. NACE International, Corrosion 2007: Paper No. 07090

40 Kimura M, Miyata Y, Yamane T, Toyooka Y, Nakano Y. 'Corrosion Resistance of High-strength Modified 13% Cr Steel'. Corrosion 1999; 55(8):756-761

41 Enerhaug J. 'A Study of Localized Corrosion in Super Martensitic Stainless Steel Weldments'. PhD Thesis, The Norwegian University of Science and Technology, 2002

42 Ramirez JE. 'Mechanical Properties and Hydrogen-Induced Stress Corrosion Cracking of Super 13Cr Steel Welded Joints'. NACE International, Corrosion 2006: Paper No. 07140

43 Miyata Y, Kimura M, Koseki T, Toyooka T, Murase F. 'Martensitic Stainless Steel Seamless Linepipe with Superior Weldability and CO2 Corrosion Resistance'. NACE International, Corrosion 97: Paper No. 19

44 Amaya H, Kondo K, Hirata H. 'Effect of Chromium and Molybdenum on Corrosion Resistance of Super 13Cr Martensitic Stainless Steel in CO2 Environment'. NACE International, Corrosion 98: Paper No. 113

45 Bhavsar RB, Montani R. 'Application of Martensitic, Modified Martensitic and Duplex Stainless Steel bar stock for Completion Equipment'. NACE International, Corrosion 98: Paper No. 96

46 Hashizume S, Ono T, Alnuaim T. 'Performance of High Strength low C – 13%Cr martensitic stainless steel'. NACE International, Corrosion 2007: Paper No. 07089

47 Scoppio L, Barteri M, Cumino G. 'Sulphide Stress Cracking Resistance of Supermartensitic Stainless Steel for OCTG'. NACE International, Corrosion 97: Paper No. 23

48 Kimura M, Takanori T, Shimamoto K. 'High Cr Stainless Steel OCTG with High Strength and Superior Corrosion Resistance'. JFE Technical Report No.7, Jan 2006

49 Ueda M, Amaya H, Kondo K, Ogawa K, Mori T. 'Corrosion Resistance of Weldable Super 13Cr Stainless Steel in H2S Containing CO2 Environments'. NACE International, Corrosion 96: Paper No. 58

50 Gregori A, Woolin P, Gestel W. 'Analysis of In-Service Failures in Girth-Welded Supermartensitic Pipes'. Stainless Steel World 2003

51 Rogne T, Lange H, Svenning M, Aldstedt S, Solberg J, Ladanova E, Olsen S. 'Intergranular corrosion/cracking of weldable 13%Cr steel at elevated temperature'. NACE International, Corrosion 2002: Paper No. 02428

52 Enerhaug J, Olsen S, Rorvik G, Mikkelsen A, Rogne T, Rostadsand PA, Haabrekke T. 'Robustness of Supermartensitic Stainless Steel Girth Welds-Experiences from the Kristin Field Development Project'. NACE International, Corrosion 2005: Paper No. 05097

53 Woollin P. 'Understanding and avoiding intergranular stress corrosion cracking of welded supermartensitic stainless steel'. NACE International, Corrosion 2007: Paper No. 07094

54 Smallman RE, Ngan AHW. 'Physical Metallurgy and Advanced Materials. Chapter 7: Mechanical properties II – Strengthening and toughening'. 7th Ed. Butterworth Heinemann 2007

55 Lamb S. 'CASTI Handbook of Stainless Steels & Nickel Alloys'.2nd ed. CASTI Publishing Inc. 2003

56 Bhadeshia HKDH. ‘Worked examples in the Geometry of Crystals’. 2nd ed. Institute of Materials, London: 2001 (updated 2006)

57 Campbell FC. ‘Phase Diagrams - Understanding the Basics’. ASM International. 2012

58 DoITPoMS, University of Cambridge. ‘Displacive v diffusive phase transformations’: URL: http://www.doitpoms.ac.uk/tlplib/superelasticity/displacive.php. Accessed 19/11/2013

59 Bhadeshia H, Honeycombe R. ‘Steels - Microstructure and Properties’. 3rd ed. Elsevier 2006

60 Carrouge D. ‘Transformations in supermartensitic stainless steels’. PhD thesis, University of Cambridge, 2002

61 Carter GF, Paul DE. ‘Materials Science and Engineering’. ASM International 1991

62 Krauss G. ‘Martensite before and after Tempering, Deformation and Fracture of’. Encyclopaedia of materials 1991:5193-5197

63 Ramirez JE. 'Effect of PWHT on the Heat-Affected Zone Properties of Super-Martensitic Stainless Pipe Steels'. NACE International, Corrosion 2004: Paper No. 04136

64 Bain EC. ‘Functions of the Alloying Elements in Steel’. US Steel Corporation, Pittsburgh, Pa. 1939

65 Verhoeven JD. ‘Steel Metallurgy for the non-metallurgist’. ASM International 2007

66 Wu W, Hwu LY, Lin DY, Lee JL. ‘The relationship between alloying elements and retained austenite in martensitic stainless steel welds’. Scripta mater. 2000; 42(11):1071-1076

67 Yamasaki S. ‘Modelling Precipitation of Carbides in Martensitic Steels’. PhD thesis, University of Cambridge, 2004

68 Amaya H, Taniyama A, Ogawa K, Ueda M. ‘Intergranular Stress Corrosion cracking Susceptibility and Precipitation Behavior on grain boundary by Post Weld Heat Treatment of Supermartensitic Stainless Steel. NACE International, Corrosion 2008: Paper No. 08100

69 Amaya H, Taniyama A, Ogawa K. 'Effect of Alloying Element on Intergranular stress Corrosion Cracking Susceptibility of Super Martensitic Stainless Steel Welded Joints in Sweet Environment'. NACE International, Corrosion 2007: Paper No. 07091

70 Ma XP, Wang LJ, Subramanian SV, Liu C. ‘Studies on Nb Microalloying of 13Cr Super Martensitic Stainless Steel’. Metallurgical and material Transactions A. 2012; 43A(12):4475-4486

71 Kimura M, Miyata Y, Toyooka T. ‘Development of a new 13cr steel pipe with high strength and good toughness’. NACE International, Corrosion 2002: Paper No. 02044

72 Meck NS, Chambers B, Skogsberg J, Kane R, Anand T. ‘Sour Service Limits of Martensitic Stainless Steels: A Review of current Knowledge, Test Methods and Development Work’. NACE International, Corrosion 2013: Paper No. 2639

73 Sakamoto S, Maruyama K, Asahi H, Kaneta H. 'Effects of Environmental Factors on SSC Property of Modified 13Cr Steels in Oil and Gas Fields'. NACE International, Corrosion 97: Paper No. 21

74 Hinds G, Zhao J, Griffiths AJ, Turnbull A. 'Hydrogen diffusion in super 13% chromium martensitic stainless steel'. Corrosion 2005; 61(4):348-354

75 Chambers B, Kane RD, Yunovich M. 'Implications of Temperature and Buffering Systems for Laboratory Testing of Carbon Steel and 13Cr Materials in oil and Gas Production Environments'. NACE International, Corrosion 2011: Paper No. 11096

76 Kimura M, Miyata Y, Toyooka T, Nakano Y. 'Effect of Test Method on SSC Performance of Modified 13Cr Steel'. NACE International, Corrosion 98: Paper No. 114

77 Cayard MS, Maldonado JG. 'Use and misuse of laboratory tests'. NACE International, Corrosion 2000: Paper No. 00132

78 Kane R, Skogsberg J, Meng J, Chambers B. 'New Evaluation and Qualification Protocol for Stainless Steel Tubulars for H2S/CO2 service'. EuroCorr 2009; 8065

79 Sidorin D, Pletcher D, Hedges B. 'The electrochemistry of 13% chromium stainless steel in oilfield brines'. Electrochemica Acta 2005; 50(20):4109-4116

80 Kerber S, Tverberg J. 'Stainless Steels Surface Analysis'. Advanced Materials & Processes; November 2000

81 Hashizume S, Inohara Y, Masamura K. 'Effects of pH and PH2S on SSC Resistance of Martensitic Stainless Steels'. NACE International, Corrosion 2000: Paper No. 00130

82 Hara T, Asahi H. 'Effect of δ-Ferrite on Sulfide Stress Cracking in a Low Carbon 13mass% Chromium Steel'. ISIJ International 2000; 40(11):1134-1141

83 Marchebois H, El Alami HAsahi H, Leyer J, Gateaud A. 'Sour Service Limits of 13% Cr and Super 13% Cr Stainless Steels for OCTG: Effect of Environmental Factors'. NACE International, Corrosion 2009: Paper No. 09084

84 Nice PI, Martin JW. 'Application Limits for Super Martensitic and Precipitation Hardened Stainless Steel Bar-Stock Materials'. NACE International, Corrosion 2005: Paper No. 05091

85 Huizinga S, Like WE. 'Limitations for the application of 13Cr steel in oil and gas production environments'. NACE International, Corrosion 97: Paper No. 39

86 Takabe H, Ueda M, Martin JW, Nice PI. 'Application Limits for 110ksi Strength Grade Super 13Cr Steel in CO2 Environments Containing Small Amounts of H2S'. NACE International, Corrosion 2009: Paper No. 09083

87 Takabe H, Ueda M, Ohe T, Martin JW, Nice PI. 'The Effect of Environmental Factors on SSC Resistance of 110ksi Strength Grade Super 13Cr steel'. EuroCorr 2010

88 Crolet JL, Leyer J. 'Use and Abuse of Artificial Acetate Buffering in Standardized and Application Specific Testing'. NACE International, Corrosion 2004: Paper No. 04140

89 Ueda M, Takabe H. 'Effect of Organic Acid on CO2 Corrosion of Carbon and CR Bearing Steels'. NACE International, Corrosion 98: Paper No. 35

90 Pletcher D, Sidorin D. 'A Comparison of the Corrosion of Carbon and 13% Chromium Steels in Oilfield Brines Containing Acetate'. NACE International, Corrosion 2005: Paper No. 05301

91 Amaya H, Ueda M. 'Effect of Test Solution Compositions on Corrosion Resistance of 13Cr Materials in a little Amount of H2S Environment'. NACE International, Corrosion 99: Paper No. 585

92 Augustin C, Marchebois H, Martin JW, Alami HE, Legay F. 'For a better control of pH drift when testing SSC in Fit-For-Purpose conditions'. EuroCorr 2009

93 Drugli JM, Rogne T, Svenning M, Axelsen S, Enerhaug J. 'The Effect of Buffered Solutions in Corrosion Testing of Alloyed 13%Cr Martensitic Stainless Steels for Mildly Sour Applications'. NACE International, Corrosion 99: Paper No. 586

94 Meng J, Skogsberg J, Chambers B, Kimura M. 'Environmentally Assisted Cracking Testing of High Strength 15Cr Steel in Sour Well Environments'. NACE International, Corrosion 2011: Paper No. 11100

95 Vitale DD. 'Effect of Hydrogen Sulfide Partial Pressure, pH, and Chloride Content on the SSC Resistance of Martensitic Stainless Steels and Martensitic Precipitation Hardening Stainless Steels'. NACE International, Corrosion 1999: Paper No. 584

96 Hashizume S, Inohara Y, Masamura K. 'Effect Strength on Stress Corrosion Cracking Resistance of Martensitic Stainless Steels'. NACE International, Corrosion 2001: Paper No. 01085

97 Bilmes PD, Llorente CL, Mendez CM, Gervasi CA. 'Microstructure, heat treatment and pitting corrosion of 13CrNiMo plate and weld metals'. Corrosion Science 2009; 51:876-881

98 Nose K, Asahi H. 'Effect of Microstructure on Corrosion Resistance of a Martensitic Stainless Linepipe'. NACE International, Corrosion 2000: Paper No. 00145

99 Kimura M, Miyata Y, Toyooka T, Kitahaba Y. 'Effect of Retained Austenite on Corrosion Performance for Modified 13% Cr Steel Pipe'. Corrosion 2001; 57(5):433-439

100 Kondo K, Amaya H, Ohmura T, Moriguchi K, Ueda M. 'Effect of Cold Work on Retained Austenite and on Corrosion Performance in low Carbon Martensitic Stainless Steels'. NACE International, Corrosion 2003: Paper No. 03094

101 Bilmes PD, Llorente CL, Huaman LS, Gassa LM, Gervasi CA. 'Microstructure and pitting corrosion of 13CrNiMo weld metals'. Corros.Sci. 2006; 48(10):3261-3270

102 Hashizume S, Nakayama T, Sakairi M, Fushimi K. 'Electrochemical behavior of low C – 13%Cr weld joints by using solution flow type micro-droplet cell'. NACE International, Corrosion 2008: Paper No. 08102

103 Smirnova A, Johnsen R, Nisancioglu K. 'Effect of tensile stress on hydrogen permeation in 13% Cr super martensitic stainless steel'. EuroCorr 2010

104 Meng J, Chambers B, Yunovich M, Kane R. 'What is Really Known About Using 13Cr Tubulars in Sour Service'. Materials Performance August 2011; Vol. 50 No. 8

105 Hashizume S, Masamura K, Yamazaki K. 'Performance of High Strength Super 13%Cr Martensitic Stainless Steel'. NACE International, Corrosion 2003: Paper No. 03095

106 Rogne T, Drugli J, Knudsen O, Olsen S, Enerhaug J. 'Corrosion Performance of 13Cr Stainless Steels'. NACE International, Corrosion 2000: Paper No. 00152

107 Miyata Y, Kimura M, Koseki T. 'Martensitic Stainless Steel Seamless Pipe for Linepipe' JFE Technical report No.7, 2006

108 Fowler C. 'Sour Service Corrosion Testing'. Exova Corrosion Centre presentation 2012

109 NACE. 'Standard Test Method Laboratory Testing of Metals for Resistance to Sulfide Stress Cracking and Stress Corrosion Cracking in H2S Environments'. 1996(TM0177-96)

110 NACE. 'Slow strain rate test method for screening corrosion-resistant alloys (CRAs) for stress corrosion cracking in sour oilfield service'. 2004(TM0198-04)

111 Fowler CM, Bray JA. 'OTI 95 635: A Test Method to Determine the Susceptibility to Cracking of Linepipe Steels in Sour Service'. Health and Safety Executive. 1996

112 Fowler CM, Himeman M. 'The Full Ring Test Enables Detection of Susceptibility to Cracking in Sour Service'. NACE International, Corrosion 99: Paper No. 608

113 ASTM. 'Standard Practice for Preparation and Use of Bent-Beam Stress-Corrosion Test Specimens'. 2005(G39-99 (2005))

114 BSI. 'Corrosion of metals and alloys – stress corrosion testing – Part 2: Preparation and use of bent-beam specimens'. BSI 1995; ISO 7539-2

115 Nimmo B, Griffiths A, Crocker L, Shaw R, Turnbull A. 'Issues in four-point bend testing for assessing stress corrosion cracking susceptibility of welds'. NPL report 2003; MATC(A) 153

116 Turnbull A, Nimmo B. 'Stress corrosion testing of welded supermartensitic stainless gas steels for oil and gas pipelines'. Corrosion Engineering Science and Technology 2005; 40(2):103-109

117 Megson THG. 'Structural and Stress Analysis': 2nd Ed. Elsevier 2005

118 Open University Course material. 'T357 Structural Integrity: designing against failure. Block 1 Stress Analysis Part 6'. Open University 2007

119 Sines G. 'Elasticity and Strength'. Allyn and Bacon Inc. Boston. 1969

120 Oberg EJ, Franklin DH, Holbrook LR, Henry H. 'Machinery's Handbook 28th Ed. P.236 – Properties of Bodies: Moment of Inertia & Section Modulus. Industrial Press Inc. NY. 2008

121 Hearn EJ. 'Mechanics of Materials, Volume 2 - An Introduction to the Mechanics of Elastic and Plastic Deformation of Solids and Structural Materials': 3rd Ed. Elsevier. 1997

122 Rees DWA. 'Basic Engineering Plasticity: An Introduction with Engineering and Manufacturing Applications': 1st Ed. Elsevier. 2006

123 University of Cambridge DoITPoMS. 'Plastic deformation during beam bending'. URL: http://www.doitpoms.ac.uk/tlplib/beam_bending/plastic.php. Accessed July 2013

124 Anon. 'How strain gauges work' URL: www.leanenet.it/download/howsgw.pdf. Accessed Oct 2012

125 Vishay Precision Group. 'Errors due to misalignment of strain gauges'. Tech note TN-511

126 Ajovalasit A, Pitarresi G. 'Strain Measurements on Composites: Effects due to Strain Gauge misalignment'. Strain 2011; 47:e84-e92

127 Lichtenberger R, Schreier H. 'Airbag2004: Contactless and Fullfield 3D-Deformation Measurement for Impact and Crash Tests'. URL: http://www.limess.com/download/airbag2004.pdf. Accessed Dec 2012

128 Lord JD, Roebuck B, Morrell R, Lube T. '25 Year Perspective: Aspects of strain and strength measurement in miniaturised testing for engineering metals and ceramics'. Materials Science and Technology 2010; 26(2):127-148

129 Wang YH, Jiang C, Wanintrudal C, Du, C, Zhou D, Smith LM, Yang LX. 'Whole Field Sheet-Metal Tensile Test Using Digital Image Correlation'. Experimental Techniques, March/April 2010; p 54-59

130 Yang L, Smith L, Gothekar A, Chen X. 'Measure strain Distribution Using Digital Image Correlation (DIC) for Tensile Tests'. The Auto/steel Partnership. Jan 2010

131 Bing P, Hui-min X, Bo-qin X, Fu-long D. 'Performance of sub-pixel registration algorithms in digital image correlation'. Meas. Sci. Technol. 2006; 17:1615-1621

132 Principal of Digital Image Correlation, Correlated Solutions. URL: www.correlatedsolutions.com

133 Sutton MA, Yan JH, Tiwari V, Schreier HW, Orteu JJ. 'The effect of out-of-plane motion on 2D and 3D digital image correlation measurements'. Optics and Lasers in Engineering. 2008; 46:746-757

134 The principals of digital image correlation – Trilion optical test systems presentation. URL: http://trilion.com/digital-image-correlation-theory. Accessed 18/09/2013

135 Cintron R, Saouma V. 'Strain Measurements with the Digital Image Correlation System Vic-2D' Center for Fast Hybrid Testing, Department of civil Environmental and Architectural Engineering, University of Colorado, September 2008

136 Fish J, Belytschko T. 'A First Course in Finite Elements'. England: Wiley; 2007

137 Logan D. 'A First Course in the Finite Element Method'. 2nd ed. USA: International Thompson Publishing 1993

138 Abaqus Inc. 'Abaqus User's manual'. 2006

139 Abaqus Inc. 'ABAQUS / Answers: Answers to Common Abaqus Questions'. Hibbit, Karlsson & Sorenson Inc; 1996

140 Yaghi AH. Lecture notes; Mechanics of Solids 2 – The Finite Element (FE) Method. University of Nottingham, Department of Mechanical, Materials & Manufacturing Engineering

141 Afazov SM, Ratchev SM, Segal J. 'Prediction and experimental validation of micro-milling cutting forces of AISI H13 steels at hardness between 35 and 60 HRC'. Int J Adv Manuf Technol. 2012; 62:887-899

142 Huurman M, Pronk AC. 'Theoretical analysis of the 4 point bending test'. Advanced Testing and Characterization of Bituminous Materials. 2009

143 Zhai T, Xu YG, Martin JW, Wilkinson AJ, Briggs GAD. 'A self-aligning four-point bend testing rig and sample geometry effect in four-point bend fatigue'. International Journal of Fatigue. 1999; 21:889-894

144 Lube T, Manner M, Danzer R. 'The miniaturisation of the 4-point-bend test'. Fatigue & Fracture of Engineering Materials & Structures. 1997; 11:1605-1616

145 Amaya H, Arai Y, Ogawa K, Murata Y, Murase T, Ueda M. 'Welded joints properties of super 13Cr martensitic stainless steel considering applicability to field fabrication'. NACE International, Corrosion 2002: Paper No. 02043

146 Griffiths A, Nimmo B, Roebuck B, Hinds G, Turnbull A. 'A novel approach to characterising the mechanical properties of supermartensitic 13 Cr stainless steel welds'. Materials Science and Engineering A 2004; 384:83-91

147 Bosch C, Liessem A, Kulgemeyer A. 'Full-size four-point bend testing – A new approach to evaluate the SSC resistance of large-diameter pipes for sour service'. NACE International, Corrosion 2004: Paper No. 04130

148 Cullity BD. 'Elements of X-RAY DIFFRACTION'. 2nd ed. USA: Addison-Wesley Publishing 1978

149 ASTM. 'Standard Practice for X-Ray Determination of Retained Austenite in Steel with Near Random Crystallographic Orientation'. 2003(E975-03)

150 International Tables for X-Ray Crystallography, Physical and Chemical Tables, Vol. 3. Birmingham England: Kynoch Press; 1962

151 Dickson MJ. 'The Significance of Texture Parameters in Phase Analysis by X-Ray Diffraction'. J. Appl. Cryst. 1969; 2:176-180

152 ASTM. 'Standard Test Methods and Definitions for Mechanical Testing of Steel Products'. 2009(A370-09a)

153 ASTM. 'Standard Test Methods for Notched Bar Impact Testing of Metallic Materials'. 2002(E23-02a)

154 ASTM. 'Standard Test Method for Microindentation Hardness of Materials'. 2008(E384-08a)

155 Exova Test Procedure. 'Determination of H2S concentration by Idometric Titration'

156 ASTM. 'Standard Practice for Preparing, Cleaning, and Evaluating Corrosion Test Specimens'. 2003(G1-03)

157 Nippon Steel & Sumitomo Metal. 'Material Data Sheet: Martensitic Stainless Steel – SM13CRS-110' http://www.tubular.nssmc.com/product-services/octg/materials/data-sheet/sm13crs-110 Accessed Nov 2012

158 Ashby MF, Jones DRH. 'Engineering Materials 1 - An Introduction to Properties, Applications, and Design (4th Edition)'. Elsevier 2012

159 Song YY, Ping DH, Yin FX, Li XY, Li YY. 'Microstructural evolution and low temperature impact toughness of a Fe-13%Cr-4%Ni-Mo martensitic stainless steel'. Mater.Sci Eng A. 2010; 527:614-618

160 Lee YK, Shin DS, Leem DS, Choi JY, Jin W, Choi CS. 'Reverse transformation mechanism of martensite to austenite and amount of retained austenite after reverse transformation in Fe-3Si-13Cr-7Ni (wt%) martensitic stainless steel'. Mater.Sci Technol. 2003; 19:393-397

161 Bojack A, Zhao L, Morris PF, Sietsma J. 'In-situ determination of austenite and martensite formation in 13Cr6Ni2Mo supermartensitic stainless steel'. Mat Char. 2012; 71:77-86

162 Zhao L, van Dijk NH, Bruck E, Sietsma J, van der Zwaag S. 'Magnetic and X-ray diffraction measurements for the determination of retained austenite in TRIP steels. Mater.Sci Eng A. 2001; 313:145-152

163 Kobayashi K, Omura T, Ueda M, Nakamura K. 'Effect of Testing Temperature on SSC Properties of Low Alloy Steel'. NACE International, Corrosion 2006: Paper No. 06127

164 Oliver WC, Pharr GM. 'An improved technique for determining hardness and elastic modulus using load and displacement sensing indentation experiments' Journal of Materials Research. 1992; 7(6):1564-1583

165 Fischer-Cripps AC. 'Nanoindentation' Chapter 2: Nanoindentation testing. 3rd Edition, Springer 2011

166 Tosha K, Lu J, Gueloroget B, Nagashima E. 'Shot Peening and Grit Blasting – Effects on Surface Integrity'. Conference Proceedings ICSP-9 (pg 400-405) Document Ref: 2005116, 2005

167 Wandell JL. 'New Studies May Help Prevent An Old Problem. Shot Peening: an Answer to hydrogen embrittlement?' Metal Improvement Company Inc. 2005

168 Hinds G, Wickstrom L, Mingard K, Turnbull A. 'Impact of surface condition on sulphide stress corrosion cracking of 316L stainless steel'. Corrosion Science. 2013; 71:43-52

169 Douabul AA, Riley JP. 'The solubility of gasses in distilled water and seawater-V. Hydrogen Sulphide'. Deep-Sea Research. 1978; 26A:259-268

170 Millero FJ, Huang F, Laferiere AL. 'Solubility of oxygen in the major sea salts as a function of concentration ad temperature'. Marine Chemistry. 2002; 78:217-230

171 Murrey CN, Ripley JP. 'The solubility of gases in distilled water and sea water – II. Oxygen'. Deep-Sea Research, 1969; 16:311-320

172 Hay MG. ‘Fitness-for-Purpose Material Testing for Sour Gas Service-An Overview’ NACE International, Corrosion 2000: Paper No. 139

173 Murrey CN, Ripley JP. ‘The solubility of gases in distilled water and sea water – IV. Carbon dioxide’. Deep-Sea Research, 1971; 8:533-541

174 Duan Z, Moller N, Weare JH. ‘Prediction of the solubility of H2S in NaCl aqueous solution: an equation of state approach’. Chemical Geology, 1996; 130:15-20

175 Dent P. MPhil program. ‘Stress Corrosion Cracking of 13 Cr Steels in Sour Gas Environments as a Function of Sub-ambient Temperature’. University of Birmingham 2014

176 Turnbull A, Mingard K, Lord JD, Roebuck B, Tice DR, Mottershead KJ, Fairweather ND, Bradbury AK. ‘Sensitivity of stress corrosion cracking of stainless steel to surface machining and grinding procedure’ Corrosion Science, 2011; 53:3398-3415

177 Turnbull A, Zhou S. ‘Residual stress relaxation in shot peened high strength low alloy steel and its implications for hydrogen assisted cracking’ Materials Science and Technology, 2010;26(7):824-832

178 Turnbull A, Nimmo W. ‘Methodology for determining the resistance of welded corrosion resistant alloys to stress corrosion using the four-point bend method'. NPL report 2004; DEPC MPE 007

179 Baratta FI, Matthews WT, Quinn GD. ‘Errors associated with flexure testing of brittle materials’. Report No. MTL TR 87-35, U.S. Army Materials Technology Laboratory. 1987

180 Turnbull A, Crocker L. ‘Four point bend testing – Finite element analysis of the stress and strain distribution’. NPL report 2014; MAT 63

181 Discussions at the Four-Point Bend Test Procedure working group, Orlando march 2013

182 ASTM ‘Tensile Testing – second edition’. (Product code #05106G). 2004

183 ASTM. 'Standard test Methods for Bend Testing of Metallic Flat Materials for Spring Applications Involving Static Loading'. 2008(E855-08)

184 Hyde TH, Sun W, Williams JA. ‘Requirements for and use of miniature test specimens to provide mechanical and creep properties of materials: a review’. International Material Reviews 2007; 52(4):213-255

185 Hutchings RB, Turnbull A. ‘The Effect of Prior Mechanical Deformation on Hydrogen Transport Through 13% Chromium Martensitic Stainless Steel’. Corrosion Science, 1992: 33:713-728